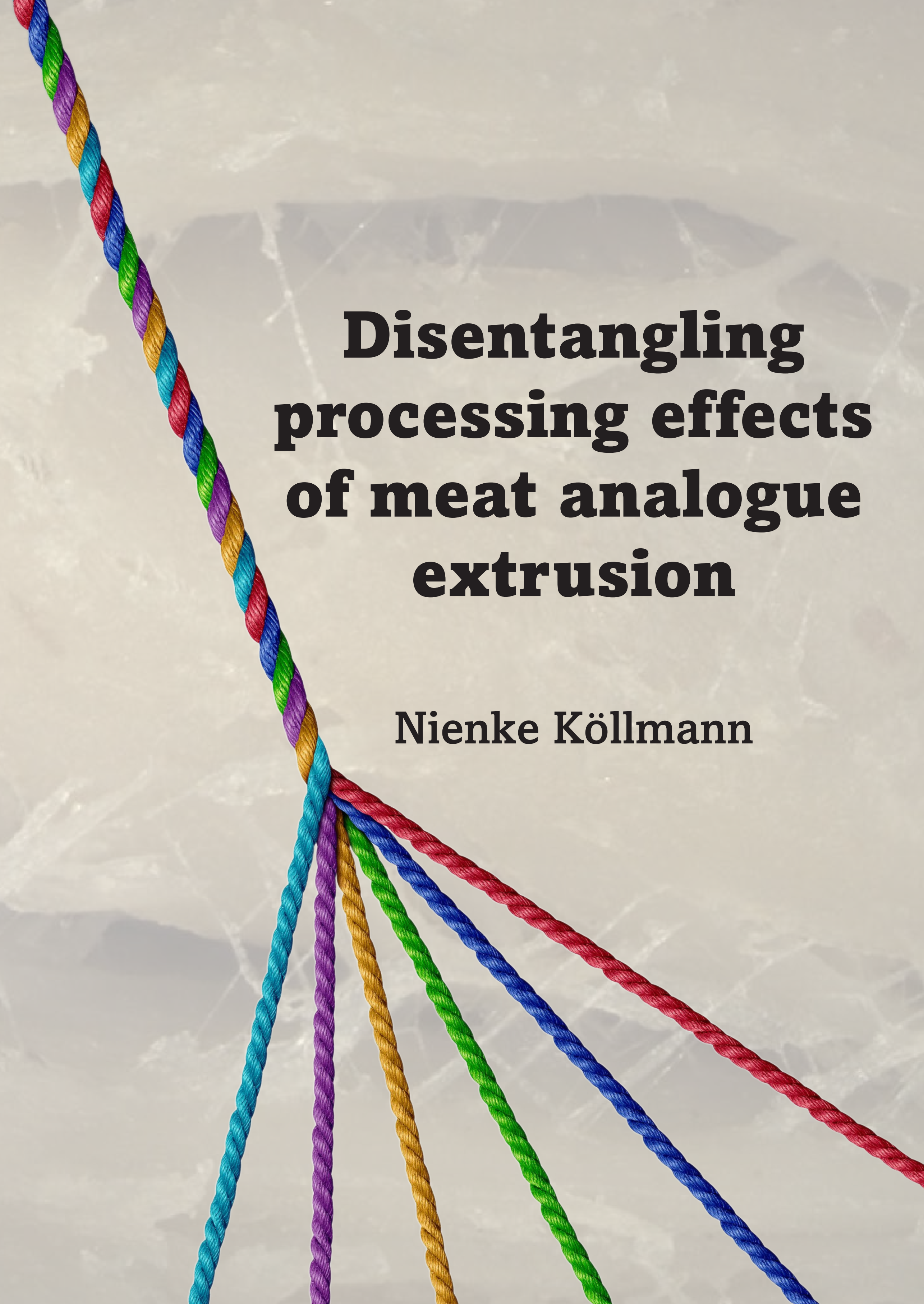

Disentangling processing effects of meat analogue extrusion

Nienke Köllmann

Propositions

1. A simplified process provides more insight in industrial food processes than a simplified product composition.
   (this thesis)

2. To disentangle processing effects, it is necessary to quantify their combined impact.
   (this thesis)

3. Only when specialized scientists have a broad interest, they can solve societal challenges.

4. A productive scientist knows how to balance doing and thinking.

5. The use of a strong hypothesis bears the risk of confirmation bias and missed discoveries.

6. A PhD trajectory resembles a relay race more than a single marathon.

7. Artificial intelligence urges universities to innovate their education.

8. The purpose of meat analogues is to become obsolete.

Propositions belonging to the thesis, entitled

Disentangling processing effects of meat analogue extrusion

Nienke Köllmann
Wageningen, 5 November 2024

Disentangling processing effects of meat analogue extrusion

Nienke Köllmann

Thesis committee

Promotor

Prof. Dr A.J. van der Goot

Personal chair at the Laboratory of Food Process Engineering

Wageningen University & Research

Co-promotor

Dr Lu Zhang

Assistant professor at the Laboratory of Food Process Engineering

Wageningen University & Research

Other members

Prof. Dr J.P.M. van Duynhoven, Unilever, Wageningen University & Research

Prof. Dr A.M. Wagemans, Technische Universität Dresden, Germany

Dr P. Acharya, University of Greenwich, United Kingdom

Dr I. Bodnár, DSM-Firmenich, Geneva, Switzerland

This research was conducted under the auspices of the Graduate School VLAG

(Biobased, Biomolecular, Chemical, Food and Nutrition Sciences)

Disentangling processing effects of meat analogue extrusion

Nienke Köllmann

Thesis

submitted in fulfilment of the requirements for the degree of doctor

at Wageningen University

by the authority of the Rector Magnificus,

Prof. Dr C. Kroeze,

in the presence of the

Thesis Committee appointed by the Academic Board

to be defended in public

on Tuesday 5 November 2024

at 1:00 p.m. in the Omnia Auditorium.

Nienke Köllmann

Disentangling processing effects of meat analogue extrusion

232 pages

PhD thesis, Wageningen University, Wageningen, the Netherlands (2024)

With references, with summaries in English and Dutch

DOI https://doi.org/10.18174/671649

Content

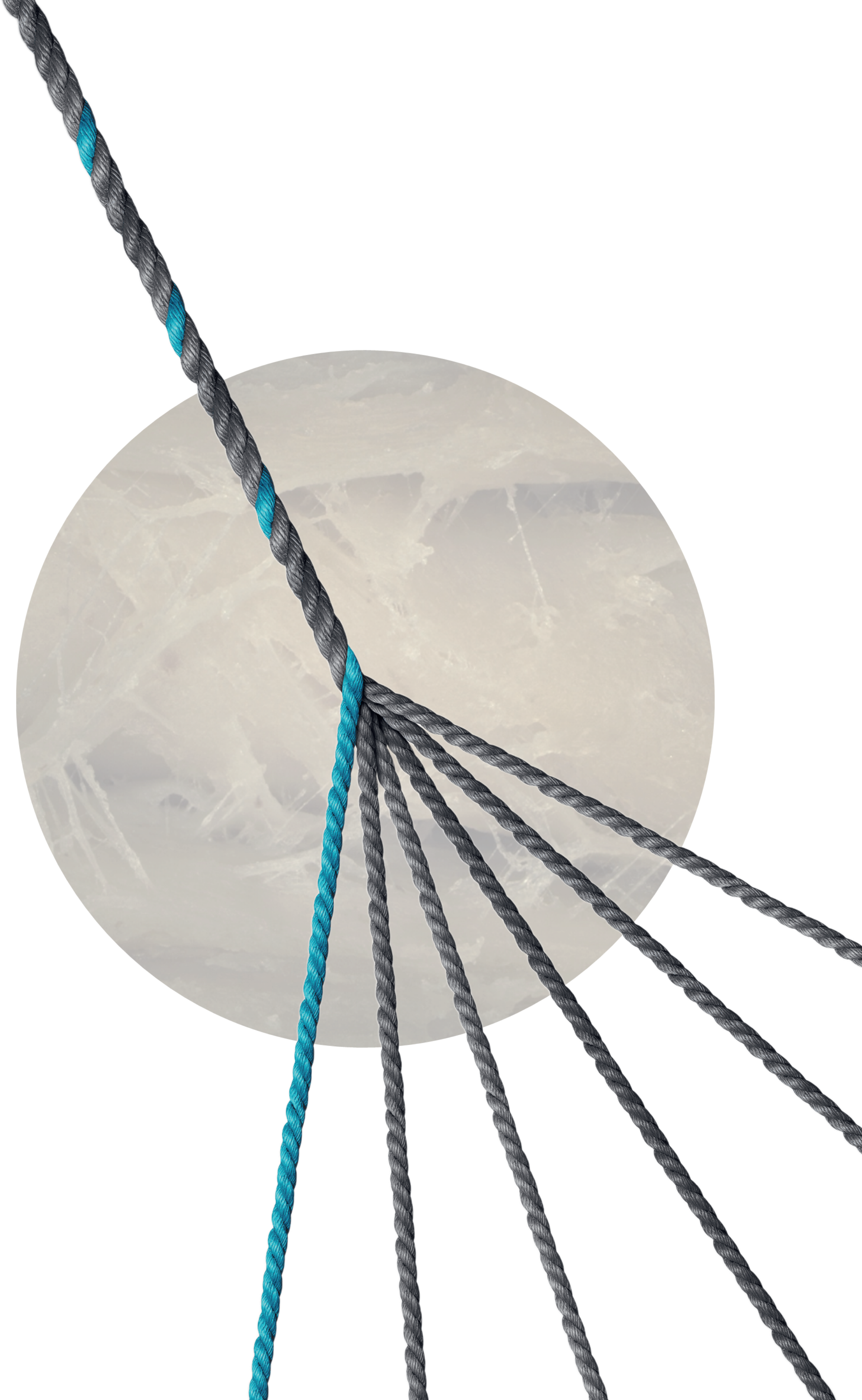

Chapter 1

Introduction and thesis outline

1.1 Plant-based meat analogues

The greenhouse gas emissions and water usage associated with food production can be reduced by moving to a more plant-based diet (Kim et al., 2020). Plant-based meat analogues are often suggested as a means to facilitate the shift to a more plant-based diet (Onwezen et al., 2021). Michel et al. (2021) found that both omnivores and flexitarians prefer plant-based foods that resemble meat. They therefore recommended to focus on the development and production of meat analogues with highest possible similarity in taste and texture compared to animal meat. However, the current meat analogues on the market do not fulfil these consumer expectations fully and often lack the typical fibrous texture of meat (Sha & Xiong, 2020).

There are several methods to produce meat analogues, which were summarized by Dekkers, Boom, et al. (2018). These methods include, but are not limited to extrusion, shear cell structuring, mixing of proteins and carbohydrates, and the use of mycoproteins or cell culturing. More recently, 3D food printing for meat analogues was developed (Ramachandraiah, 2021). On an industrial scale extrusion is still the most applied process (Dekkers, Boom, et al., 2018). During extrusion dense starch-rich or protein-rich materials are pushed forward by a combination of mechanical treatment and pressure, while heated (Maurya & Said, 2014). Depending on the moisture content in the product formulation meat analogue extrusion can be divided into two categories: low-moisture extrusion (LME) (<40% moisture) and high-moisture extrusion (HME) (>40% moisture). The meat analogue products produced through LME are often referred to as texturized vegetable protein (TVP). These TVPs have a porous spongy structure and must be hydrated before they are used as meat analogue (Riaz, 2011; Samard et al., 2019). HME products have a structure that resembles the structure of whole muscle products more, which is the main advantage of using HME instead of LME (Samard et al., 2019). This thesis therefore focuses on the use of HME for meat analogue production.

1.2 Challenges in understanding extrusion process for meat analogue production

Even though HME of meat analogues has been studied intensively since the 1990s there is no full consensus about the mechanism for fibrous structure formation. Recently, van der Sman & van der Goot (2023), Cornet et al. (2022) and Schmid et al. (2022) gave overviews of the different hypotheses that explain the formation of fibrous structure formation during HME.

The extrusion process consists of three main processing operations: (1) mixing and hydrating, (2) thermomechanical treatment, and (3) cooling (Cornet et al., 2022). Mixing and hydrating and thermomechanical treatment take place in the screw section of the extruder by heating of the barrel and rotation of one or two screws. For LME both a single and a twin-screw can be used, whereas for HME a twin-screw extruder is more commonly applied (Noguchi, 1989). After leaving the screw section, the material enters the die and is cooled to create the final product structure (Emin & Schuchmann, 2017). During LME a porous structure is formed because of moisture evaporation when the material exits the die. For HME a long cooling die is used to prevent or limit product expansion. Furthermore, the cooling of the material increases its viscosity and therefore allows pressure build-up in the extrusion barrel (Noguchi, 1989). The long cooling die is often thought to be responsible for the formation of a layered structure during HME (Cheftel et al., 1992; Sandoval Murillo et al., 2019; Tolstoguzov, 1993). However, recently several authors found that the formation of an anisotropic structure already occurs at the transition from the extrusion barrel to the cooling die (Garina et al., 2024; Wittek, Ellwanger, et al., 2021). A schematic representation of a twin-screw extruder with a long cooling die is shown in Fig. 1.1.

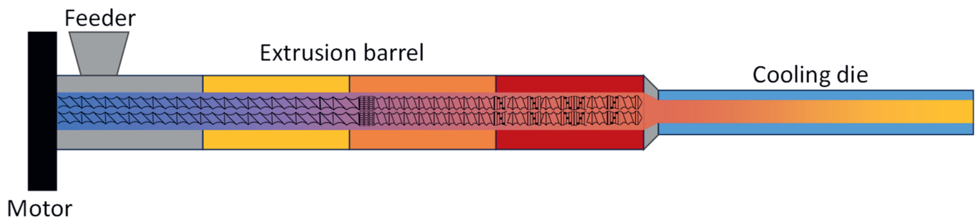

Fig. 1.1 Schematic representation of a co-rotating twin screw extruder with a long cooling die. Please note that this figure is not to scale.

Understanding structure formation during HME is challenging due to several reasons. Firstly, the effects of thermomechanical stresses on the reaction behaviour of proteins have mainly been studied for dilute protein dispersions (<50%) or at mild temperatures (<100 °C) (Emin et al., 2017), which can be explained by the limitations of most analytical techniques to handle the dense protein dispersions relevant for HME. Besides, the extruder does not allow for in-line measurements other than pressure and temperature. For this reason, dead-stop experiments are conducted to collect the protein material at different locations along the extruder barrel and cooling die. However, cooling, which is inevitable when opening the extruder, can lead to changes in the protein material. Another factor that hinders the understanding of the structuring process during HME is the fact that processing parameters are interlinked. The effect of a single process variable can therefore not be studied in isolation (Schmid et al., 2022). An overview of interactions between the different processing variables and intermediate processing conditions is shown in Fig. 1.2.

To solve the problem of interlinked process parameters and processing conditions Meuser & van Lengerich (1984) proposed a system analytical model for the extrusion of starch. This model describes the target parameters (e.g. swelling power) as a function of structure parameters (e.g. deformation of starch granules), which are a result of the action of system parameters (e.g. residence time). The system parameters are determined by the process parameters (e.g. mass flow). In addition to the effects of system parameters, knowledge of the reaction kinetics of the physicochemical changes that occur during HME is required to gain complete insights in the structure formation process (Emin & Schuchmann, 2017). These physicochemical changes include but are not limited to gluten polymerization, disulfide bond formation and protein aggregation (Garina et al., 2024; Pietsch et al., 2018).

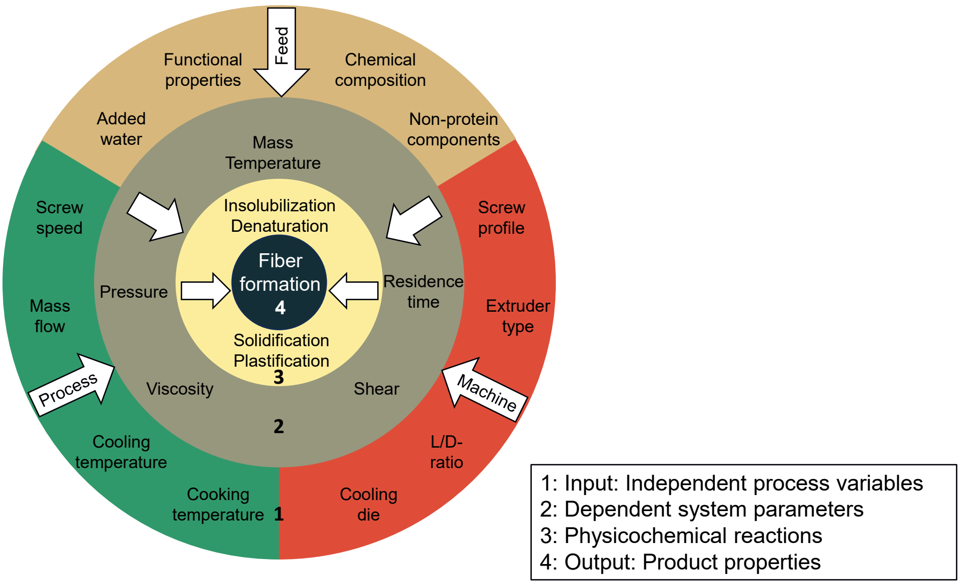

Fig. 1.2 Overview of the input variables and dependent variables on the fibrous structure formation taken from Osen & Schweiggert-Weisz (2016) who adapted this figure from Camire (1991).

1.3 Approach used in this thesis to study the extrusion process

To gain more insight into the effects of thermomechanical treatment on the reactions that occur during extrusion, such as starch degradation or amylase inactivation, the so-called "shear cell" was developed at Wageningen University (van den Einde et al., 2004; van der Veen et al., 2004). This device provides simple shear flow and allows the separation of the effects of shear force, shear rate, temperature, and time during thermomechanical treatment of dense dispersions (van den Einde et al., 2004). In subsequent studies it was discovered that it is possible to create fibrous structures using calcium caseinate (Manski et al., 2007) and plant-based materials (Grabowska et al., 2014) by means of the shear cell. After these discoveries the high-temperature shear cell (HTSC) was explored as a novel production method for plant-based meat analogues (Dekkers et al., 2016; Grabowska et al., 2016; Schreuders et al., 2019). Recently, the HTSC has mainly been used to study the effect of ingredient composition on the final product structure (Ma et al., 2024; Snel et al., 2024; Taghian Dinani et al., 2024).

The processing steps when structuring dense plant-based protein mixtures in the HTSC are similar as those used during extrusion. These steps are mixing and hydrating, thermomechanical treatment, and cooling (Cornet et al., 2022). The similarity in processing steps provides an opportunity to study the effects of the processing parameters during the HME process separately. So far, this approach has not been applied to structure formation phenomena during HME of meat analogues yet. In this thesis the HTSC is therefore used to study the effects of the relevant processing parameters on the final product structure for the different processing steps during HME.

In addition to the use of the HTSC to study the structure formation mechanism during HME off-line, it remains relevant to study the processing conditions during the HME process with in-line methods. For example, it was previously shown that an infrared sensor can be used to reveal large temperature fluctuations during HME that are not captured by the standard thermocouples just before the cooling die (Emin et al., 2016). However, such measurements with an infrared sensor provide only limited insight in what is happening inside the extruder (Emin, 2022). Therefore, the development of a technique that quantifies the combined effect of the thermal stresses on the physicochemical changes that take place during HME would be highly relevant. One technique that is promising for this application is near-infrared (NIR) spectroscopy. NIR spectroscopy relies on the absorption of the NIR radiation (750-2500 nm) of CH, NH and OH and can therefore be used to measure the protein, oil, and water content of food products (Pasquini, 2018). NIR spectroscopy was previously used to measure the end-point temperature of meat products using the fact that the NIR spectrum is influenced by changing protein-water interactions upon heating (Ellekjaer & Isaksson, 1992; Uddin et al., 2002). Furthermore, NIR spectroscopy has already been applied to classify extruded pea protein samples according to their processing intensity during extrusion (Ben-Hdech et al., 1993) and to estimate the thermal load during the heating of fish gels (Elmasry & Nakauchi, 2015). NIR spectroscopy is also used to determine the composition of food products. In case of meat analogues produced with HME, the quantification of the oil content is of interest, because the exact oil content can differ from the added amount due to expelling of oil from the protein matrix (Cheftel et al., 1992; Kendler et al., 2021). This makes exploring NIR spectroscopy for rapid and accurate analysis of the oil content highly relevant.

1.4 Research aim and thesis outline

The aim of this thesis is to better understand the effects of processing conditions on the properties of dense plant-based products made through HME. To this end HTSC processing is applied to disentangle the effects of processing parameters **(Chapters 2 & 3)** on structuring during HME. Then, NIR spectroscopy is investigated as rapid and non-destructive technique to measure the composition of dense plant-based products (**Chapters 4 & 5)**. In **Chapter 6** the HTSC and NIR spectroscopy is combined to quantify the thermal process intensity during extrusion. A schematic overview of the different thesis chapters is shown in Fig. 1.3.

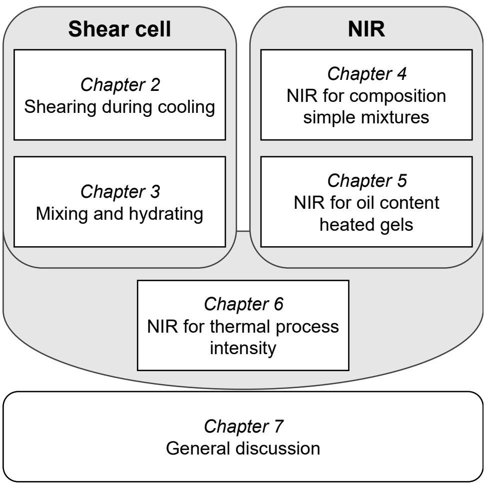

Fig. 1.3 Schematic overview of the outline of this thesis.

As mentioned in section 1.1 the cooling die is often considered the main structuring region of the HME process. For this reason, the effect of deformation during cooling is described in **Chapter 2.** In this chapter the HTSC is used to systematically vary the shear applied on a pea protein isolate-wheat gluten mixture during cooling. The properties of these products are evaluated by visual observations and tensile testing. To evaluate the effect of shear during cooling, the products sheared during cooling are compared with products sheared during heating, which is the standard procedure for HTSC processing.

In **Chapter 3** the effects of mixing and hydrating time prior to shear cell processing on the dough and final product properties are described. The properties of the dough are evaluated by the torque profile during mixing and the rheological properties of the doughs. The properties of the final shear cell products are evaluated by visual observation and tensile testing. To explore the interactions between ingredient properties and processing conditions three commonly used plant-based protein ingredients or mixtures are used: soy protein concentrate, soy protein isolate-wheat gluten and pea protein isolate-wheat gluten.

Chapters 4, 5 & 6 describe the use of NIR spectroscopy for non-destructive measurement of the composition and thermal process intensity of meat analogues. In **Chapter 4** a simple model dispersion consisting of pea protein isolate, sunflower oil and water is used to explore the potential of NIR spectroscopy for the quantification of sunflower oil content and pea protein isolate content. However, the application of NIR spectroscopy for compositional analysis of meat analogues is complicated by the effect of heating on the NIR spectra, which is due to changed interactions between water and protein through heating. The effect of the heating conditions (temperature and time) on the measurement of oil content in pea protein isolate gels is therefore described in **Chapter 5.**

The effect of heating conditions on the NIR spectra was studied further in **Chapter 6**. In this chapter the combined effect of mechanical and thermal treatment on the thermal process intensity during HME of soy protein concentrate is quantified with the use of NIR spectroscopy. To be able to measure the thermal process intensity with NIR spectroscopy the HTSC is used to obtain a calibration curve for processing temperature under controlled conditions. This calibration curve is subsequently applied to extrudates to calculate their so-called “shear cell equivalent temperature”. The equivalent shear cell temperature is used to summarize the combined effect of variations in the screw profile (with or without kneading elements), screw speed and barrel temperatures on the total thermal process intensity.

Furthermore, the equivalent shear cell temperature is used to describe the effect of the used processing parameters on the degree of texturization of the extrudates.

The thesis ends with a discussion of the new insights resulting from the work presented in this thesis and an outlook to possible future research directions resulting from these insights in **Chapter 7.**

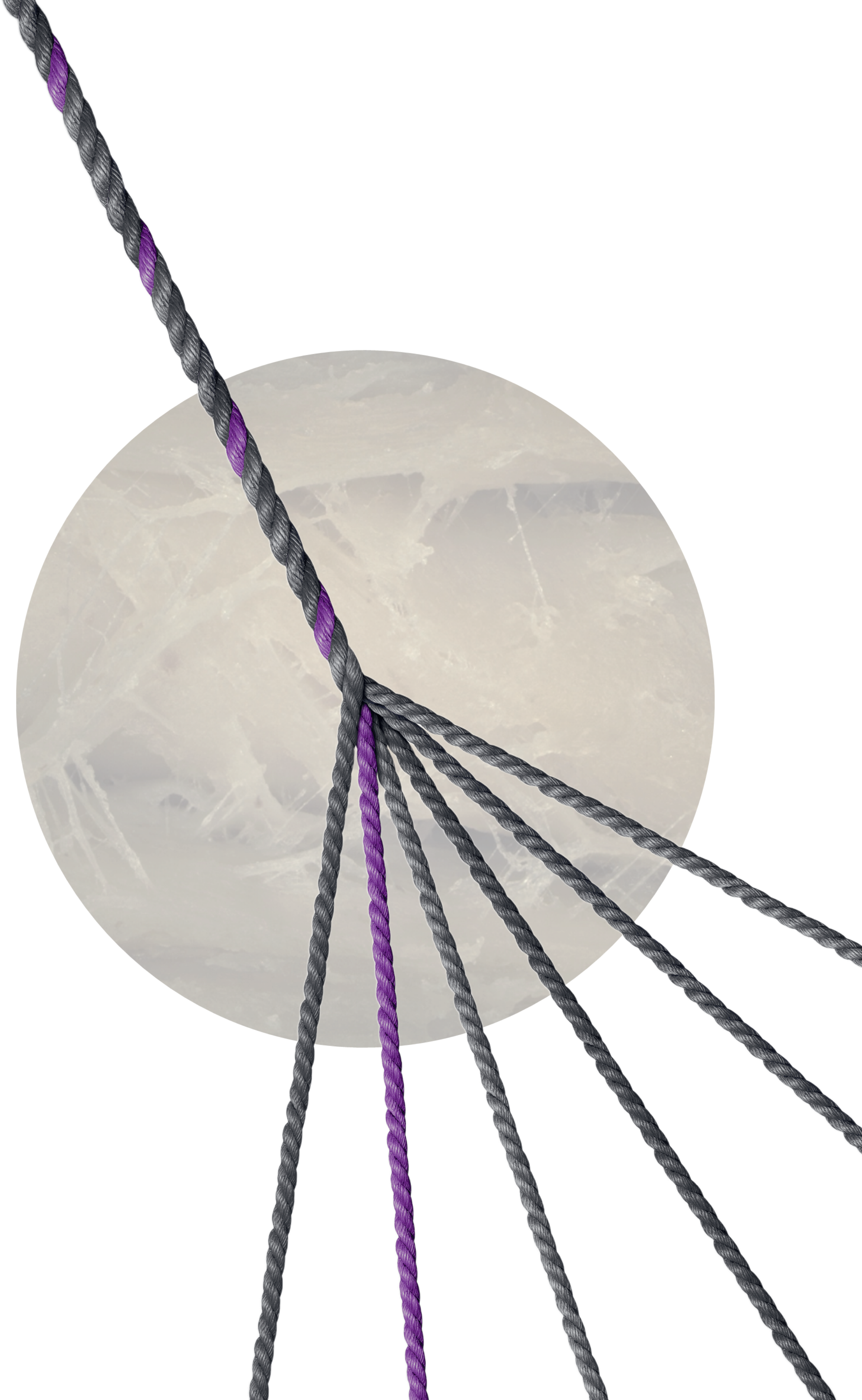

Chapter 2

On the importance of cooling in structuring processes for meat analogues

This chapter has been published as Köllmann, N., Schreuders, F. K. G., Zhang, L., & van der Goot, A. J. (2023). On the importance of cooling in structuring processes for meat analogues. *Journal of Food Engineering*, *350*, 111490.

2.1 Abstract

High moisture extrusion (HME) is a common method to produce meat analogues. This process requires cooling of the product in the die and is associated with a high mechanical energy input. Here, we use high-temperature shear cell (HTSC) technology to better understand the importance of cooling while shearing for the formation of fibrous products upon thermomechanical processing. The maximal rotational speed for fibrous structure formation from a pea protein isolate-wheat gluten (PPI-WG) blend was found to be the same (<30 rpm) when shearing during heating or cooling. However, shearing during cooling was not beneficial for making visually fibrous products in the HTSC and it weakened the products, while simultaneously inducing mechanical anisotropy. Additionally, we found that the mechanical energy necessary to produce these fibrous structures is only a fraction of the mechanical energy input currently used for HME. We therefore conclude that the HME process for production of meat analogues could still be improved.

2.2 Introduction

The development of plant-based meat analogues with a fibrous structure could stimulate the transition towards a more plant-based diet among consumers (Michel et al., 2021). High moisture extrusion (HME) and high-temperature shear cell (HTSC) technology rely on thermomechanical processing to create fibrous products from plant-based ingredients. Both processing techniques have similarities in their basic three unit operations, which are mixing/hydration, thermomechanical treatment and cooling (Cornet et al., 2022). Unfortunately, even today, the structure formation process in HME is still poorly understood because parameters such as the shear rate, temperature and pressure in the extruder are highly correlated and their effects on food materials' behaviours are difficult to disentangle. In the HTSC though, these parameters can be controlled separately (van den Einde et al., 2004). Therefore, HTSC was developed as a useful tool to study the effects of processing parameters on the quality of products, to better understand the effects of thermomechanical treatment on materials.

The mechanism of fibrous structure formation during HME and HTSC processing has been explained with several hypotheses and is thought to have a similar basis. Most of these hypotheses consider the presence of two different phases in the heated protein-rich material as a prerequisite for structure formation. However, researchers hold different opinions on the nature and origin of the formation of two phases and why such multi-phase material is needed (Cornet et al., 2022). In case of extrusion, fibrous structure formation is thought to mostly occur during cooling when materials pass through a long die and are subjected to shear flow (Cheftel et al., 1992; Sandoval Murillo et al., 2019; Tolstoguzov, 1993). For structuring in the HTSC it is often assumed that the fibrous structure formation is a result of deformation of the dispersion of biopolymers upon shearing (Dekkers, Boom, et al., 2018). For the pea protein isolate (PPI)-wheat gluten (WG) blend used in the current work, Cornet et al. (2021) hypothesized PPI acted as the dispersed phase while WG acted as the continuous phase. However, Schreuders et al. (2020) found indications that the PPI-WG blend formed a bi-continuous phase using the polymer blending law.

As stated above, cooling is thought to be essential to make fibrous products with HME. Therefore, it is also interesting to explore whether shear treatment during cooling can also lead to fibrous structure formation in plant-based materials using the HTSC. During cooling, the material is expected to become more viscous and might even solidify as the temperature decreases sufficiently. Shear rate or stress applied to material will influence structure formation in HTSC, which is related to the processing parameter of rotational speed (rpm). The application of shear during cooling might enhance structure formation through shear-induced deformation because mechanical forces can be better transferred to the two phases in the product as the material solidifies. However, the application of too high shear stresses during cooling will result in structural breakdown. Therefore, shear-induced deformation in a two-phase system needs to be well in balance with the extent of solidification for optimal fibrous structure formation during cooling.

This study aims to better understand the importance of cooling during shearing for thermomechanical processing of plant-based proteins. To investigate the effect of cooling on structure formation, PPI-WG blends were processed using different shearing time and shear rate combinations during heating and cooling. Subsequently, the obtained products were evaluated in terms of fibrous structure formation by visual observation and textural properties by tensile test analysis.

2.3 Materials and methods

2.3.1 Materials

Pea protein isolate (PPI) (Nutralys S85F) and vital wheat gluten (WG) (Vitens CWS) were both purchased from Roquette (Lestrem, France). The manufacturer's specifications indicated the PPI contained, 83-88% protein, 1 wt.% dietary fibre, 9 wt.% lipids, 5 wt.% ash; and WG contained 10 wt.% starch, 0.5 wt.% cellulose fibre, 3 wt.% lipids and 1 wt.% ash. PPI and WG had an average dry matter content of 93.8 wt.% and 92.8 wt.%, respectively. Sodium chloride was obtained from Sigma-Aldrich (Zwijndrecht, Netherlands).

2.3.2 Preparation of proteinaceous materials

A protein blend of PPI–WG at mass ratio 1:1 was prepared with a final dry matter content of 40 wt.%. The sample preparation procedure has been previously described by Grabowska et al. (2014) and Schreuders et al. (2019). First, 1 wt.% sodium chloride was dissolved in distilled water to prepare a saline solution. Then, PPI was added to this solution, followed by mixing this dispersion by hand using a spatula until a homogeneous paste was obtained. The protein material was then hydrated at room temperature for 30 min. Finally, WG was mixed into the hydrated PPI dispersion with a spatula immediately before use.

2.3.3 High-temperature shear cell

The PPI-WG blends were treated in a high-temperature shear cell (HTSC) (Wageningen University, Netherlands) that was developed in house (Grabowska et al., 2016). For all treatment conditions, the blends were heated at 120 °C for 15 min in the pre-heated HTSC and were sheared at 5-100 rpm (corresponding to shear rates of 6.5-130 s^{-1}). This shearing was performed at various shear rates i) for 15 min during heating, ii) from the 8th minute onwards during heating and iii) for 8 min during cooling. After the shear treatment the products were cooled until they reached a temperature of around 30 °C, using an external oil bath of which the temperature was set to 25 °C. An overview of the experimental design can be seen in Fig. 2.1.

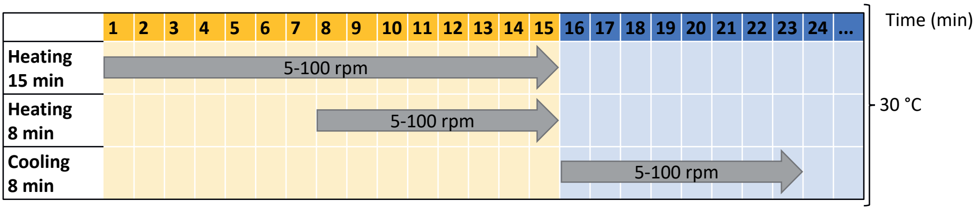

Fig. 2.1 Experimental design of the current study: the heating and cooling periods were indicated by yellow and blue colour, respectively, and the material was sheared in a range from 5 to 100 rpm.

The average temperature of the protein blend during shearing was measured at the upper non-rotating cone of the HTSC and was 110-115 °C when shearing during heating (Fig. S.2.1A and B). The temperature depended on the shear rate used. A higher shear rate led to a higher temperature, probably due to increased viscous dissipation. The average temperature during the shear treatment when shearing during cooling was 80-90 °C (Fig. S.2.1 C).

All products were left at room temperature in a closed plastic bag for at least one hour before further measurements were performed. All products were prepared in triplicate.

The torque measured during the HTSC treatment by the Haake Polylab QC drive (Germany) was used to calculate the specific mechanical energy (SME in J/kg) of the process (Eq. *3.2.*1).

$$SME = \frac{\int_{t=0}^{t_f} \omega . M(t) . dt}{m} \qquad Eq.\ 2.1$$

In which t_f is the final time, t=0 is the start time, ω is the rotor speed (s^{-1}), M is the torque (Nm) and m is the mass of the material loaded in the HTSC (kg) (=0.1 kg) (Peighambardoust et al., 2004).

2.3.4 Visual observation of macrostructure

The fibrousness of the products produced in the HTSC was assessed visually by bending the products parallel to the shear flow direction to obtain a tear at the middle of the product. The bent pieces were placed onto a metal pin and the fracture surface was photographed using a digital microscope with 34x magnification (Smartzoom 5, Carl Zeiss, Germany).

2.3.5 Tensile test

Tensile tests were performed with a Texture Analyzer (TA.XTPlusC, TA Instruments, USA) using a trigger force of 0.001 N. A uniaxial tensile test was performed at room temperature with a displacement rate of 1 mm/s. Tensile bars were taken from the product with a dog bone-shaped mould in parallel and perpendicular to the shear flow direction. The measured tensile strength was normalized based on the dimensions of the tensile bar. The ends of the tensile bars were placed into the two clamps such that 15.5 mm was the initial length of the sample. Tensile stress and tensile strain at fracture were calculated from the force and displacement measured using the equations for the Hencky stress and strain for uniaxial extension as explained in Macosko (1994) and used by Schreuders et al. (2019). The strain (ε) and tensile stress (σ) were be calculated using the following equations:

$$\epsilon = ln\frac{h(t)}{h_0} \qquad \text{Eq. 2.2}$$

$$\sigma(t) = \frac{F}{A} \qquad \text{Eq. 2.3}$$

In which:

$$A = \frac{h_0}{h(t)} * A_0 \qquad \text{Eq. 2.4}$$

In which *h(t)* (m) is the sample length at fracture, h_0 (m) is the sample length at the start of the measurement, *F* (N) is the force at fracture, *A* (m^2) is the cross-section area, A_0 (m^2) is the cross-section of the sample at the start of the measurement and *l* and *w* (m) are the length and width of the sample cross-section measured before the start of the measurement. The Young's modulus (Pa) was calculated at the initial slope of the stress-strain curve until a 1.5 mm extension was achieved.

For every product, three parallel and three perpendicular specimens were taken. Therefore, in total nine parallel and nine perpendicular specimens per treatment were measured.

2.3.6 Statistical analysis

All experiments were performed in triplicate unless stated otherwise. Values are represented as the mean ± standard deviation. Tukey's HSD test was performed to evaluate the statistical significant differences between samples at a significant level of 95% ($P < 0.05$) analysed using SPSS statistics Version 25.0.0.2 (IBM, Armonk, NY). The results of the statistical analysis can be found in Tables S.2.1, S.2.2 and S.2.3.

2.4 Results and discussion

2.4.1 Visual observations

Anisotropy in a product can be defined in two manners: visual fibrousness and mechanical anisotropy. Visual observations of the HTSC products were used to assess the visual fibrousness of the HTSC products. HTSC products produced at rotational speeds below 30 rpm were more fibrous than products prepared at higher shear rates (Fig. 2.2). This effect was visible for all temperature conditions used. However, the fibrous structures formed during cooling appeared to be more "flaky" and showed less distinguishable fibres compared to the products sheared during heating. For treatments with rotational speeds above 30 rpm texturization of the products was still visible, but no clear fibres could be observed.

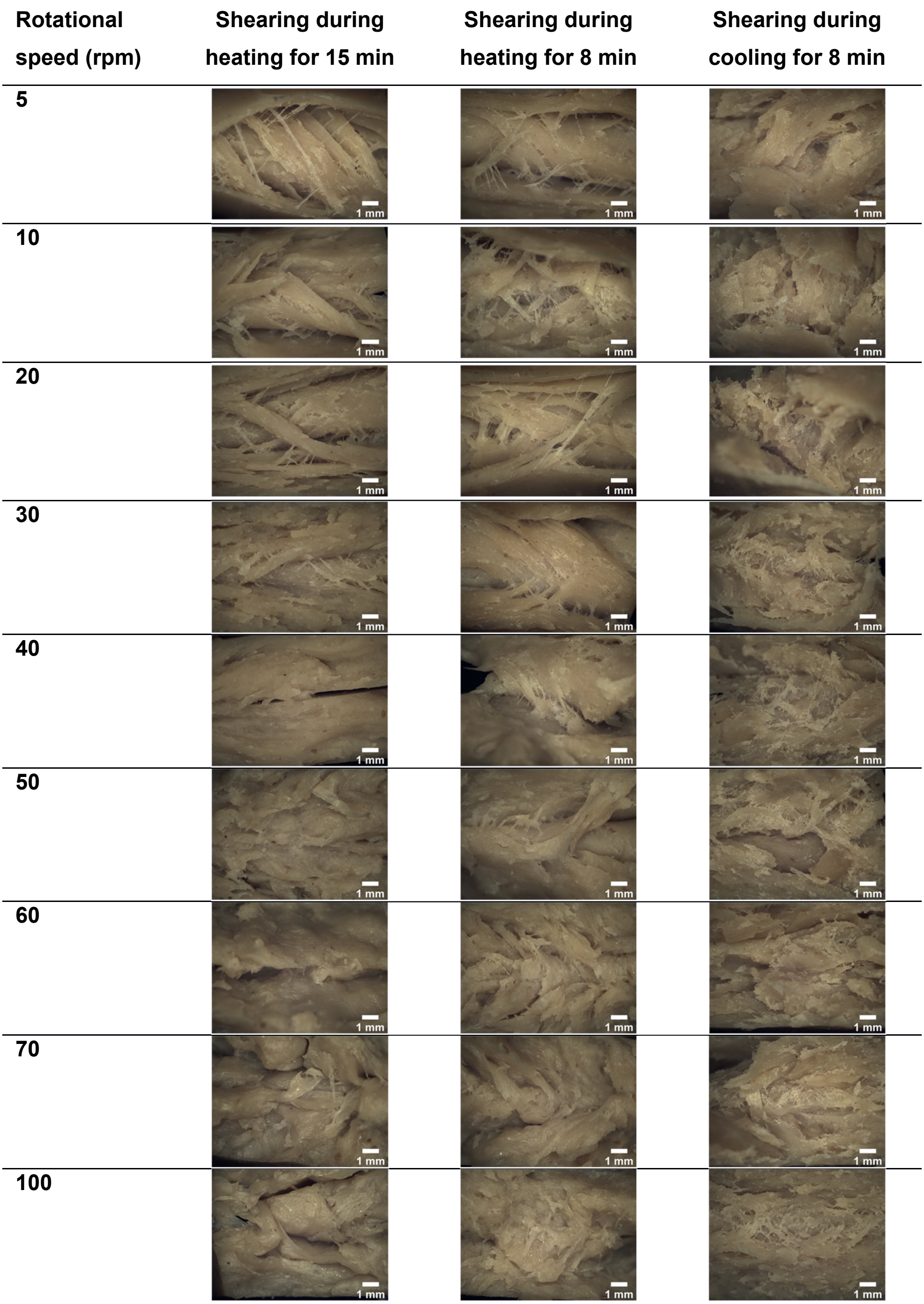

Fig. 2.2 Representative digital microscopy pictures with 34x magnification of HTSC product structures sheared at different shear rates for 15 min during heating, 8 min during heating or 8 min during cooling.

2.4.2 Tensile test

Tensile tests in the parallel and perpendicular direction to the shear flow were used to quantify the anisotropy in the textural properties of the different HTSC products. Generally, HTSC products are stronger in parallel direction than they are in perpendicular direction. Products sheared during cooling had a lower tensile strain compared to products sheared during heating, especially in perpendicular direction at rotational speeds below 30 rpm (Fig. 2.3). The tensile strain of these products sheared at a rotational speed below 30 rpm and above 30 rpm during cooling clearly differed (Fig. 2.3C). Above 30 rpm parallel tensile strain of products sheared during cooling increased when the rotational speeds (Fig. 2.3C). In contrast, the perpendicular tensile strain only increased slightly with an increasing shear rate. As a result, the difference between the tensile strain in parallel and perpendicular direction was larger for products sheared at a rotational speed of 40 rpm or higher. This indicates that the HTSC products reached a higher mechanical anisotropy at higher rotational speeds, while not showing visual fibrousness (Fig. 2.2). This increase in tensile strain anisotropy at high rotational speeds was only observed for products sheared during cooling. Remarkably, the effect of rotational speed on the tensile strain of products sheared during heating was small, even though the products' structures were visually very different and only showed visual fibrousness when processed using rotational speeds below 30 rpm (Fig. 2.2 and 2.3A, B).

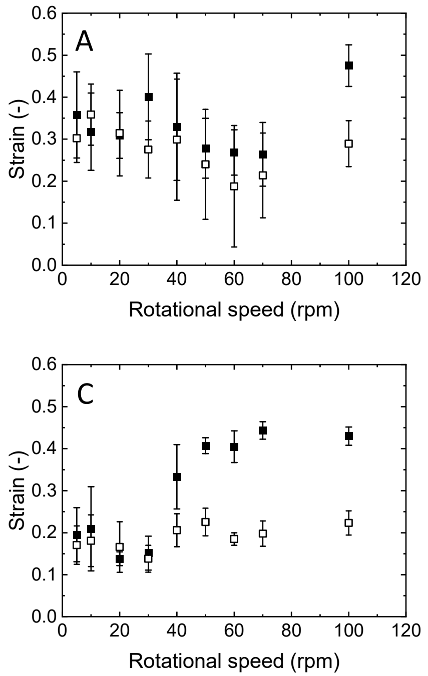

Fig. 2.3 Tensile strain at fracture plotted against shear rate in parallel (▪) and perpendicular (□) direction for products sheared for A. 15 min during heating, B. 8 min during heating, C. 8 min during cooling.

It is remarkable that the variation in strains is higher for samples that were sheared during heating, especially when shearing at high rotational speeds for 15 min. Obviously, the structure of these products is more heterogeneous at the length scale of the measurement. This corresponds to the more clearly fibrous structures that were observed for the product sheared during heating. The variation in the tensile properties of HTSC products might therefore be a better indicator of fibroussness compared to the anisotropy index that does not always correspond with visual fibrousness (Schreuders, Schlangen, et al., 2022).

Similarly to the tensile strain, the tensile stress was lower for products sheared during cooling, especially in perpendicular direction (Fig. 2.4). These products had a higher tensile stress in parallel direction for rotational speeds above 40 rpm (Fig. 2.4C). This means that similar to the tensile strain also the tensile stress indicated a more anisotropic structure at higher shear rates, while no clear fibrous structures were visible. Both visual fibrousness as mechanical anisotropy can therefore be obtained when shearing during cooling depending on the rotational speed that is used, which gives new opportunities to obtain a HTSC product with desired visual or mechanical properties. This was not observed for the products sheared during heating. The parallel tensile stress of the products sheared for 8 min during heating slightly increased at rotational speeds higher than 30 rpm (Fig. 2.4B). The tensile stress in perpendicular direction did not change significantly for these products. However, for products sheared for 15 min during heating, the tensile stress was not affected by rotational speed, except for a slight increase at 100 rpm compared to the other rotational speeds (Fig. 2.4A). The tensile stress results overall showed the same trend as the tensile strain results. The standard deviation of the tensile stress and strain was higher for products sheared for 15 min during heating compared to the other temperature conditions. This could be an indication that the products sheared for 15 min had a more heterogeneous structure at the length scale of the measurement.

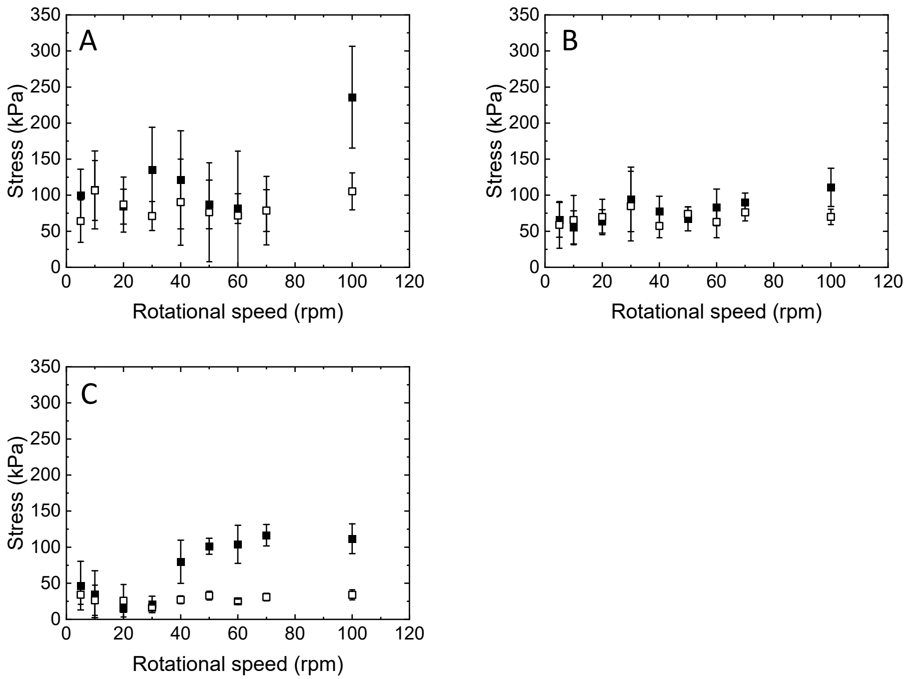

Fig. 2.4 Tensile stress at fracture plotted against rotational speed in parallel (▪) and perpendicular (□) direction for products sheared for A. 15 min during heating, B. 8 min during heating, C. 8 min during cooling.

The Young's modulus indicates the elasticity of the HTSC products. The Young's moduli of products sheared during cooling were lower compared to those during heating (Fig. 2.5). The Young's modulus of products sheared during cooling was not affected by rotational speed. However, for the products sheared for 8 min during heating the Young's modulus slightly increased with an increasing rotational speed (Fig. 2.5B). The Young's modulus of the products sheared for 15 min during heating increased with an increasing rotational speed in perpendicular direction, while in parallel direction no significant changes were found (Fig. 2.5A). An increase in Young's modulus can be linked to an increase in rigid structures both on molecular as on macroscopic levels (Cuq et al., 2000). WG polymerization can lead to more rigid protein chains because of the formation of disulfide bonds. The higher rigidity of HTSC products sheared at increasing rotational speeds during heating could therefore be the result of the more extensive deformation and orientation during WG polymerization (Pietsch, Werner, et al., 2019).

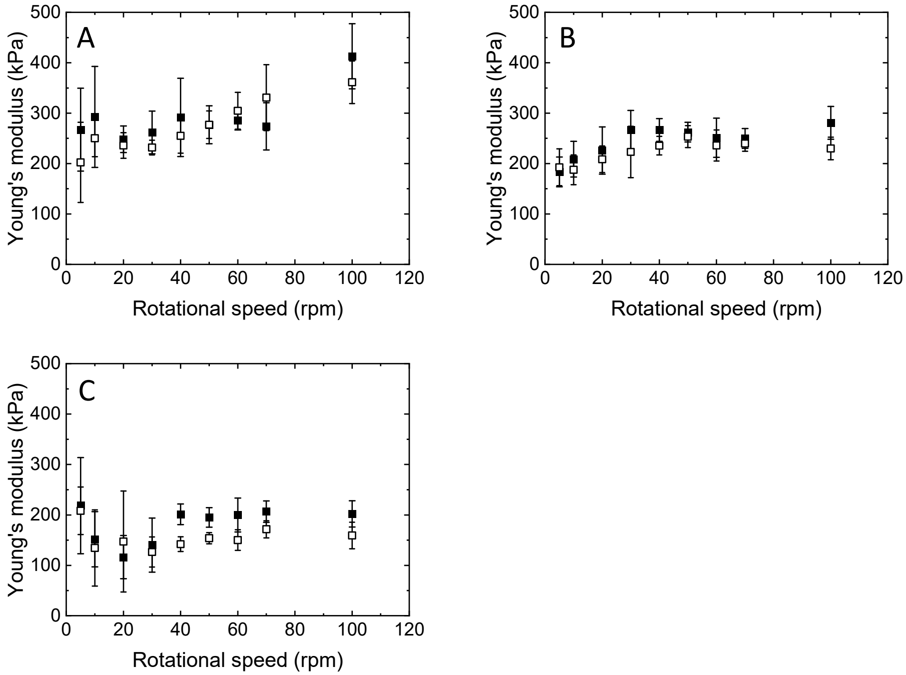

Fig. 2.5 Young's modulus plotted against rotational speed in parallel (▪) and perpendicular (□) direction for products sheared for A. 15 min during heating, B. 8 min during heating, C. 8 min during heating.

From these observations we can conclude that shearing during cooling weakened the HTSC products as indicated by a lower tensile stress and strain and Young's modulus and was detrimental for visual fibrousness. Furthermore, it was possible to create HTSC products from the same PPI-WG blend with different visual and mechanical characteristics, by changing the processing conditions. Especially during cooling structures with either visual fibrousness or mechanical anisotropy could be created depending on the rotational speed during shearing, resulting in a wider range of product properties. However, it remains difficult to predict the product properties based on a single processing parameter (i.e. rotational speed). As mentioned in the introduction, we hypothesized that the application of shear during cooling would either enhance structure formation, because mechanical forces can be better transferred to the product or could cause structural breakdown as a result of deforming a solidified material. The weaker products that were produced when shearing during cooling compared to shearing during heating indicated that structural breakdown was important for the PPI-WG system.

In a previous study, fibrous products using a PPI-WG blend were formed in the HTSC at a rotational speed of 30 rpm (Cornet et al., 2021; Schreuders et al., 2019). Here, we observed the most pronounced fibrous structure in products produced at a rotational speed of < 20 rpm (Fig. 2.2) which was somewhat lower. We attribute this observation to the slightly different functional properties of PPI used in the current study (Nutralys® S85F) and the previous one (Nutralys® F85M). Nutralys® S85F has a smaller particle size and is more soluble than Nutralys® F85M according to the manufacturer's specifications. This difference in functional properties of the raw ingredients may have influenced the overall behaviour of the blend during thermomechanical treatment.

2.4.3 Specific mechanical energy (SME)

The total mechanical input to HTSC products during the process can be quantified by calculating the specific mechanical energy (SME). The SME is often considered a measure to describe the intensity of HTSC processing and high moisture extrusion (HME) (Cornet et al., 2022; Peighambardoust et al., 2004). SME is indirectly affected by temperature through the rheological properties of the material. An increased temperature is known to reduce viscosity, which results in a reduced resistance to deformation and therefore a lower torque and SME (Palanisamy et al., 2019). We used SME to compare the different processing conditions. In all processes, the total time and overall temperature profile were kept constant, but rotational speed, shearing time and moment of shearing were varied. The temperature during shearing was therefore different in case shearing was applied at constant temperature during heating or during cooling. SME of the different shear treatments ranged from 1.6 to 163 kJ/kg (Fig. 2.6). The SME was not much affected by cooling at low rotational speeds. At higher rotational speeds, the SME was slightly higher during cooling. This was probably due to a higher viscosity of the protein blend inside the HTSC as the temperature dropped.

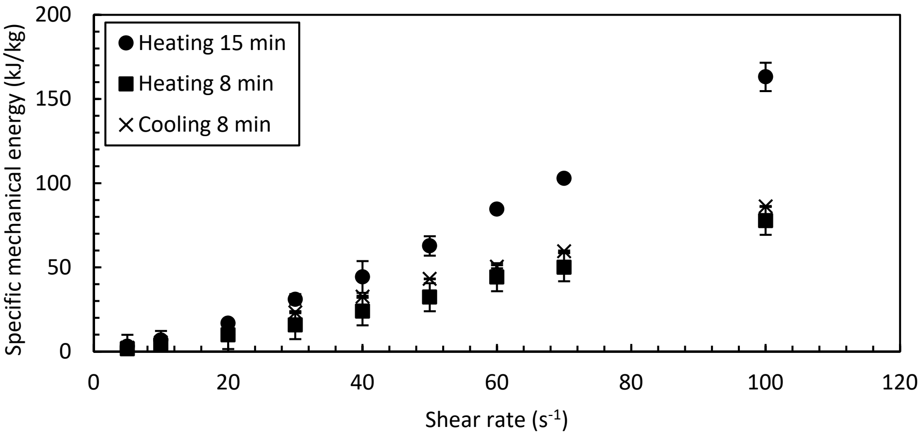

Fig. 2.6 Specific mechanical energy of the shear treatments under different conditions.

The SME used to create visually fibrous products ranged from 1.6-16.8 kJ/kg (Fig. 2.2 and 2.6) which is lower compared to what was previously reported for structuring with the Couette cell device (8.6-59.9 kJ/kg) and HME (32-1276 kJ/kg) (Krintiras et al., 2016; Maung et al., 2021; Pietsch, Werner, et al., 2019; H. Wang et al., 2022; Zahari et al., 2021). The low SME required for structuring in the shear cell could mean that the intensity during HME processing could be lower, while still giving good products.

To better correlate the SME during processing and the textural properties of the HTSC products, texture maps were created (Fig. 2.7). Texture maps are used to describe the structure of food gels and correlate the tensile strain and stress with textural properties (Ersch et al., 2015; Schreuders, Sagis, et al., 2021; Shand et al., 2008). Products that fall in the top left and right corner of the texture map are classified as tough and brittle, respectively. Products that fall in the lower left and right corners can be classified as mushy and rubbery, respectively (Kim et al., 2005; Schreuders, Sagis, et al., 2021). At first glance, all the data points were located in the diagonal line of the texture map that connects the “mushy” and “tough” corners (Fig. 2.7D). This indicates that the HTSC products produced varied in texture, i.e. more towards “mushy” or “tough”, depending on the temperature or SME during processing. For comparison: the middle region of the diagonal line lies in the same range as the tensile stress (100 kPa perpendicular, 44 kPa parallel) and strain (0.3 perpendicular, 0.2

parallel) of cooked chicken reported by Schreuders et al. (2019). Data points of products sheared during cooling are spread out over the diagonal, while the data points of samples sheared during heating were more clustered in the middle of the texture map and were slightly tougher (Fig. 2.7A, B, C). No clear correlation between SME and the position of the samples in the texture map was found. This indicates that SME cannot completely explain the variation in product characteristics that can be achieved by using different processing conditions.

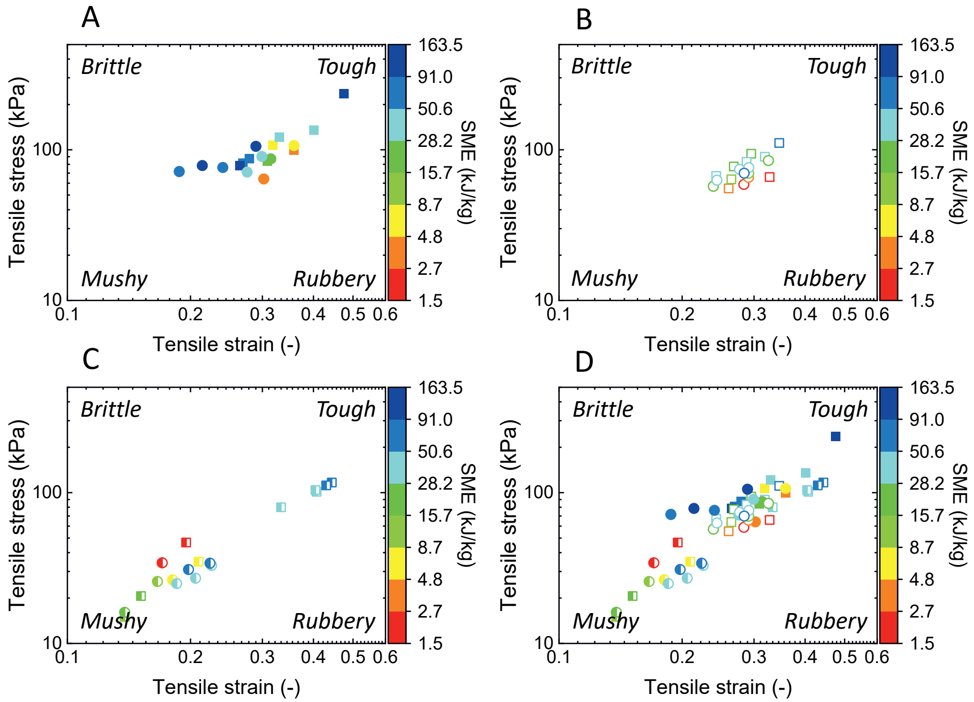

Fig. 2.7 Texture map with tensile stress plotted against tensile stress in parallel (□) and perpendicular direction (○) for shear cell products sheared for A. 15 min during heating (filled symbols), B. 8 min during heating (open symbols), C. 8 min during cooling (half-filled symbols) and D. All treatment conditions.

2.4.4 Implications for the importance of cooling during extrusion

Deformation during cooling is often thought to be essential for fibrous structure formation using HME (Cheftel et al., 1992; Sandoval Murillo et al., 2019; Tolstoguzov, 1993). However, our research revealed that shear application during cooling is not a requirement for visual fibrous structure formation. We found that visually fibrous products could be produced using a low shear rate (<30 rpm or <39 s^{-1}). The apparent shear rates in the cooling die range from 1-46 s^{-1} (Cornet et al., 2022), which is comparable to the lower shear rates at which visual fibrous structures were found in this study. Additionally, products sheared during heating were visually more fibrous and had a higher tensile strain and stress, which suggests that a higher temperature during shear application in the cooling die could lead to stronger extrudates. Ramos Diaz et al. (2022) indeed showed that a higher cooling die temperature (40-80 °C) resulted in increased hardness, as measured using texture profile analysis (TPA), and cutting strength of HME extrudates made from oat fibre concentrate and PPI. However, Kantanen et al. (2022) did not find this correlation for mixtures of faba protein concentrate and isolate, possibly because it was overshadowed by the effect of mixture composition. Even though increasing the cooling die temperature could be beneficial for fibrous structure formation, the product temperature at the end of the cooling die should remain below 100 °C to prevent product expansion (Maningat et al., 2022). Furthermore, the use of a long cooling die remains imperative for HME as it enables upstream pressure generation, the use of high temperature, channel filling and the continuity of the extrusion process (Cheftel et al., 1992).

2.5 Conclusion

In this study, we report on the importance of cooling to produce fibrous products using HTSC and HME. It was found that shearing during cooling can be used to create product structures that differ from structures obtained without shearing during cooling. Cooling of PPI-WG in the HTSC was not beneficial for visual fibrous structure formation. The structure of the product could be described best as “flaky”. Besides, products sheared during cooling were weaker compared to products sheared during heating. However, shearing at higher rotational speeds during cooling did lead to increased mechanical anisotropy and could therefore be used to obtain HTSC products with a specific desired texture. It was therefore concluded that deformation during cooling is not essential for structure formation. When overviewing all results, it was found that fibrous products could be obtained at low SME conditions in the HTSC. This finding suggests that it is still possible to further optimise the HME process towards lower SME-inputs.

2.6 Appendix

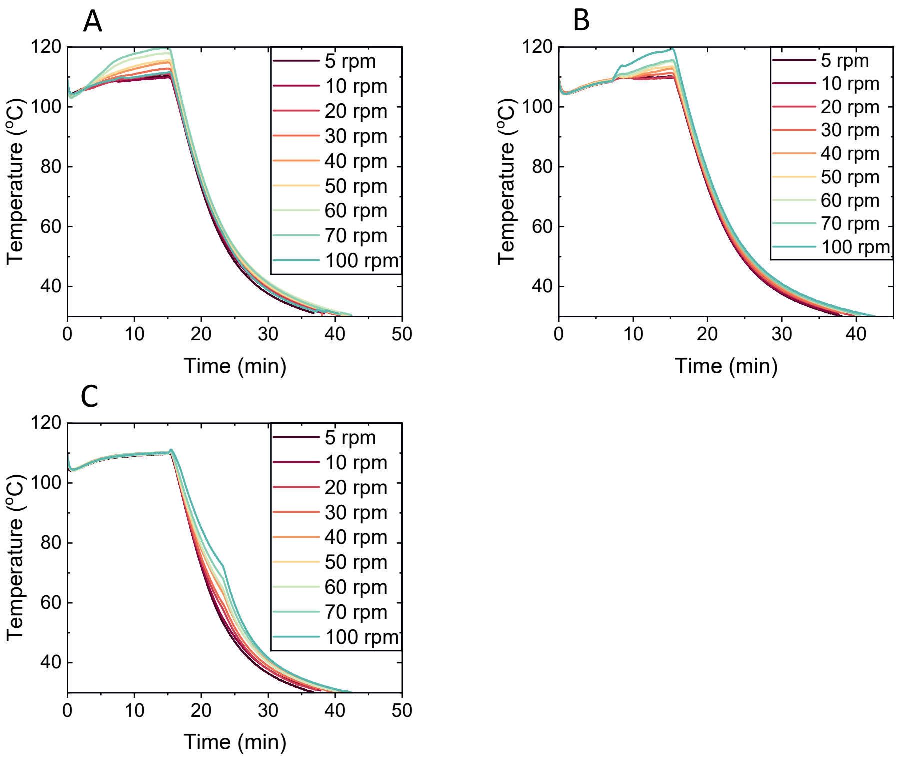

Fig.S.2.1 Temperature profile at different rotational speeds when shearing for 15 min during heating (A), when shearing for 8 min during heating (B) and when shearing for 8 min during cooling (C).

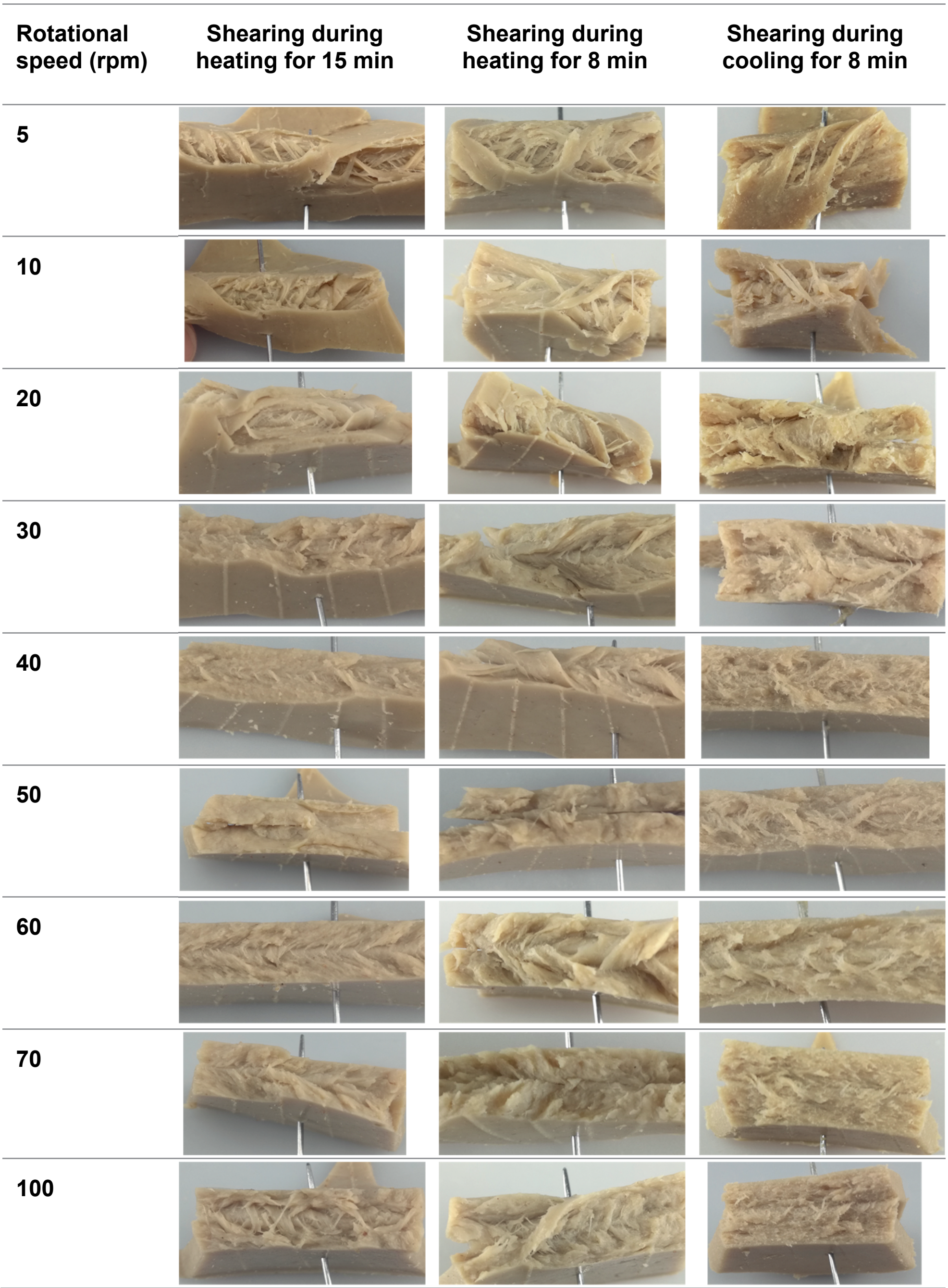

Fig.S.2.2 Digital pictures of the fibrous structures of HTSC products sheared for 15 min during heating, for 8 min during heating or for 8 min during cooling at different rotational speeds. These pictures were taken with the inbuilt camera of a smartphone (P9 Lite, Huawei, China).

Table S.2.1 Statistical analysis of the homogeneous subgroups with a Tukey HSD test at 95% significance ($P<0.05$) of tensile test properties of HTSC products sheared for 15 min during heating. Means with the same letter within a column were not significantly different.

	Tensile strain		Tensile stress		Young's modulus	
	Parallel	Perpendicular	Parallel	Perpendicular	Parallel	Perpendicular
5 rpm	a,b,c	a,b	a	a	a	a
10 rpm	a,b	b	a	a	a	a,b,c
20 rpm	a,b	a,b	a	a	a	a,b
30 rpm	b,c	a,b	a	a	a	a,b
40 rpm	a,b	a,b	a	a	a	a,b,c
50 rpm	a,b	a,b	a	a	a	b,c,d
60 rpm	a	a	a	a	a	c,d,e
70 rpm	a	a,b	a	a	a	d,e
100 rpm	c	a,b	b	a	b	e

Table S.2.2 Statistical analysis of the homogeneous subgroups with a Tukey HSD test at 95% significance ($P<0.05$) of tensile test properties of HTSC products sheared for 8 min during heating. Means with the same letter within a column were not significantly different.

	Tensile strain		Tensile stress		Young's modulus	
	Parallel	Perpendicular	Parallel	Perpendicular	Parallel	Perpendicular
5 rpm	a,b	a	a	a	a	a,b
10 rpm	a,b	a	a	a	a,b	a
20 rpm	a,b	a	a	a	a,b,c	a,b,c
30 rpm	a,b	a	a,b	a	c,d	a,b,c
40 rpm	a,b	a	a,b	a	c,d	a,b,c
50 rpm	a	a	a	a	b,c,d	c
60 rpm	a,b	a	a,b	a	b,c,d	b,c
70 rpm	a,b	a	a,b	a	b,c,d	c
100 rpm	b	a	b	a	d	a,b,c

2

Table S.2.3 Statistical analysis of the homogeneous subgroups with a Tukey HSD test at 95% significance ($P<0.05$) of tensile test properties of HTSC products sheared for 8 min during cooling. Means with the same letter within a column were not significantly different.

	Tensile strain		**Tensile stress**		**Young's modulus**	
	Parallel	Perpendicular	Parallel	Perpendicular	Parallel	Perpendicular
5 rpm	a	a,b	a,b	b	c	b
10 rpm	a	a,b	a	a,b	a,b,c	a
20 rpm	a	a,b	a	a,b	a	a,b
30 rpm	a	a	a	a	a,b	a
40 rpm	b	b	b,c	a,b	b,c	a,b
50 rpm	b,c	b	c	a,b	a,b,c	a,b
60 rpm	b,c	a,b	c	a,b	b,c	a,b
70 rpm	c	a,b	c	a,b	b,c	a,b
100 rpm	c	b	c	a,b	b,c	a,b

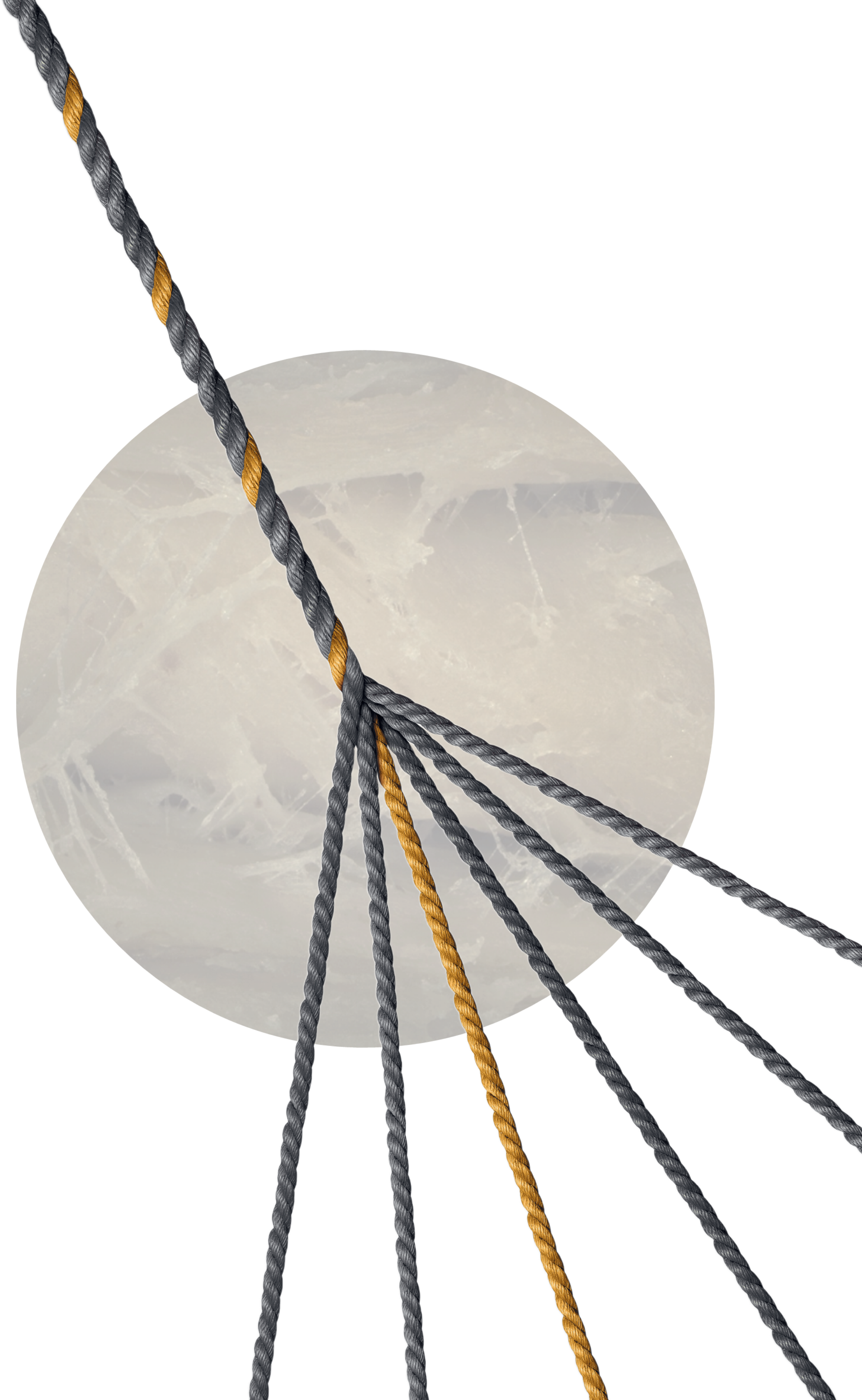

Chapter 3

Effect of mixing and hydrating time on the structural properties of high-temperature shear cell products from multiple plant-based ingredients

This chapter has been published as Köllmann, N., Sivakul, K., Zhang, L., & van der Goot, A. J. (2024). Effect of mixing and hydrating time on the structural properties of high-temperature shear cell products from multiple plant-based ingredients. *Journal of Food Engineering*, *369*, 111911.

3.1 Abstract

Mixing and hydrating plant-based ingredients to form a dough is an essential step to produce meat analogues using high-temperature shear cell (HTSC) technology. In this study the effect of mixing and hydrating time on the structural properties of soy protein concentrate (SPC), pea protein isolate (PPI)-wheat gluten (WG) and soy protein isolate (SPI)-WG doughs and HTSC products was investigated. Our results showed mixing and hydrating time minimally affected the structural properties of the dough and corresponding HTSC products of SPC. For both PPI-WG and SPI-WG mixtures, longer mixing resulted in tougher doughs. Additionally, for PPI-WG, mixing the dough to the optimal dough development time led to higher tensile strength of HTSC products. The same effect was not observed for SPI-WG, which showed the importance of ingredient properties in determining structural properties of plant-based meat analogues. These findings offer insights for optimizing processes for meat analogue production through tailored mixing strategies.

3.2 Introduction

Mixing is an essential unit operation during food processing. Its main purpose is to combine multiple ingredients, but it is also used to modify the structure of food products such as (bread) dough, cream, and margarine (Cullen & O'Donnell, 2009). Mixing and hydrating are vital to produce meat analogues from plant-based ingredients using high-moisture extrusion (HME) or high-temperature shear cell (HTSC) technology (Cornet et al., 2022). However, for both processes the effect of mixing on the final product properties remains unclear. In case of HME this is because mixing occurs in in the first part of the barrel, which cannot be separated from the thermomechanical treatment in the subsequent part of the barrel. It should be noted though that mixing can also occur before the extruder barrel through pre-mixing of the dry ingredients, possibly in combination with pre-hydrating (Giezen et al., 2014). In case of HTSC processing, mixing is always separated from thermomechanical processing, as mixing is done outside of the HTSC. The standard mixing method used before HTSC processing is hand-mixing (Taghian Dinani, Charles Carrillo, et al., 2023). Mixing could therefore be influenced by operator changes, though by experience we know these effects are limited. For the upscaled version of the HTSC, the Couette Cell, a z-blade mixer was already successfully applied to prevent this (Krintiras et al., 2016). A similar mixer, such as a farinograph, can therefore be used to mix the proteinaceous doughs systematically before HTSC processing. This makes HTSC an interesting tool to study the effect of mixing and hydrating during thermomechanical processing of meat analogues.

One of the ingredients that is commonly used to produce meat analogues using HME or HTSC is gluten (Sha & Xiong, 2020). It is well known that gluten network formation in bread doughs is heavily impacted by the initial mixing step of the bread making process. During mixing of bread dough, the mechanical input results in a distribution of the flour components and enables new interactions between these components resulting in an increase in the dough cohesion. However, its shearing effect also results in the fracturing of organized structures, which reduces the dough cohesion, especially during longer mixing times. As a result, it is known that bread dough can be under- and over-mixed, which both results in a lower bread volume (Cuq et al., 2003; Dobraszczyk & Morgenstern, 2003). The optimum kneading time lies at the equilibrium of the effects of creating new interactions and fracturing of structures (Cuq et al., 2003). The cohesive structure that is formed during bread kneading is formed by the gluten in the dough (Dobraszczyk & Morgenstern, 2003). Gluten network formation is also important for the creation of fibrous structures in HTSC products produced from a protein isolate-wheat gluten (WG) mixture, in which the protein isolate acts as a filler (Cornet et al., 2021). We therefore expect that mixing intensity would influence the final product properties of protein isolate-WG HTSC products in similar way at it does in bread doughs and both under- and overmixing were expected to be detrimental for the formation of fibrous structures. However, the protein isolate that is used affects the properties of the final HTSC products. The elastic modulus of the protein isolate influences the visual fibrousness of the final product (Schlangen et al., 2023; van der Sman & van der Goot, 2023). Furthermore, the used protein isolate determines the mechanical strength of the meat analogue (Schreuders et al., 2019). The protein isolate that is used in combination with WG was therefore expected to have an influence on the effect of mixing on the final HTSC product.

Hydrating the protein dough is also an important step during HTSC processing. One of the protein ingredients is hydrated with a NaCl or $CaCl_2$ solution for 30 min after which a second protein or carbohydrate is added (Schreuders, Schlangen, et al., 2022; Taghian Dinani, Allaire, et al., 2023). Up till now, it is assumed that the ingredients form a dispersion with two or more phases upon mixing and that molecular mixing is not likely to occur under these mixing conditions (van der Sman & van der Goot, 2023). Schreuders et al. (2020) described how water distributed among the two different phases in pea protein isolate (PPI)-WG and soy protein isolate (SPI)-WG mixtures. The pea and soy protein phases take up more water, which makes the WG gluten phase more concentrated. This influenced the rheological behavior of these mixtures at temperatures relevant for HTSC processing and is therefore expected to influence the structuring properties of the mixture during HTSC processing. Taghian Dinani, Charles Carrillo, et al. (2023) also found an influence of hydrating and hypothesized that hydrating iota-carrageenan before adding it to PPI and WG was detrimental for fibrous structure formation because of the reduced amount of water available for gluten network formation. Hydrating of WG after mixing could therefore influence the final products structure.

Nevertheless, the effect of mixing and hydrating of the proteinaceous dough before HTSC processing has not been systematically investigated yet. Therefore, the effect of mixing and subsequent hydrating time on the structural properties of proteinaceous doughs and the corresponding HTSC products were investigated in this study. Three different protein doughs were investigated: soy protein concentrate (SPC) to investigate the effect of mixing and hydrating on non-gluten containing doughs and PPI-WG and SPI-WG to explore the effect on gluten containing doughs. Systematic mixing of the protein doughs was performed in a farinograph after which the doughs were processed in a HTSC. The rheological properties of the dough were analyzed in a closed cavity rheometer (CCR). The quality of the HTSC products was analyzed by visual observations of their fibrousness and tensile testing. Finally, this study describes the effect of mixing time on the properties of proteinaceous doughs and the structural properties of HTSC products.

3.3 Materials and methods

3.3.1 Materials

Soy protein concentrate (SPC) (ALPHA 8 IP) and soy protein isolate (SPI) (SUPRO EX 37 HG IP) were purchased from Solae (St. Louis, USA). Pea protein isolate (PPI) (Nutralys S85F) and vital wheat gluten (WG) were purchased from Roquette (Lestrem, France). The dry matter contents of SPC, SPI, PPI and WG were 93.9wt.%, 94.6wt.%, 94.2wt% and 93.4 wt%, respectively. The protein contents of SPC, SPI, PPI and WG as measured with the Dumas combustion method were 62.0wt% (Nx5.71), 80.2wt% (Nx5.71), 72.2wt% (Nx5.52) and 77.4 wt% (Nx5.7) based on dry matter, respectively. Sodium chloride was obtained from Sigma- Aldrich (Zwijndrecht, Netherlands).

The water holding capacity (*WHC*) was measured according to the method described by Jia et al. (2021). To determine the *WHC* of the insoluble fraction 1 g of material and 49 g of deionized water were placed in a 50-mL Falcon tube and hydrated for 24 h while rotating at a speed of 20 rpm in a rotator (Bibby Scientific Stuart Rotator Disk SB3, Thermo Fisher Scientific, Waltham, MA, USA). Subsequently, the dispersion was centrifuged at a speed of 15,000 ×g at 25 °C for 10 min. The pellet was transferred dried in an oven at 105 °C for 24 h. The mass of the wet pellet and dry pellet were determined and denoted as *Mwet pellet and Mdry pellet*. The *WHC* was calculated using Eq. 3.1.

$$WHC = \frac{M_{wet\ pellet} - M_{dry\ pellet}}{M_{dry\ pellet}} \qquad \textit{Eq. 3.1}$$

3.3.2 Preparation of proteinaceous doughs

Three different types of proteinaceous doughs were prepared, SPC, PPI-WG and SPI-WG. These blends were used, because these are well-known to form fibrous products, contrary to blend containing only SPI or PPI (Grabowska et al., 2016; Schreuders et al., 2019; Snel et al., 2024). All proteinaceous dough had total dry matter content of 40 wt.% consisting of 39 wt% protein ingredient(s) and 1 wt% sodium chloride (NaCl). The PPI-WG andSPI-WG mixtures had a 1:1 mass ratio. The preparation of the mixtures was adapted from Schreuders et al. (2019) and Jia et al. (2021). The total weight of one mixing batch in the farinograph was 300 g. For all materials the NaCl was first dissolved in distilled water to prepare a saline solution.

In case of SPC, the protein ingredient was placed in a farinograph (Brabender GmbH &Co KG, Duisburg, Germany) before the saline solution was added and the material was mixed for 2, 4, 5, 7, 10, and 30 min at 50 rpm at 30 °C. Mixing of SPC in the farinograph before HTSC processing was performed once for every mixing time to validate that mixing of a single protein ingredient with water did not have a large effect on the dough and HTSC product properties.

In case of the PPI-WG and SPI-WG mixtures, the PPI and SPI were hand-mixed with the saline solution and hydrated for 30 min to mimic the standard high temperature shear cell (HTSC) process (Schreuders et al., 2019). After hydrating the PPI or SPI paste was placed in the farinograph. Subsequently, WG was added, and the dough was mixed for an additional 2, 4, 5, 7, 10, and 30 min at 50 rpm at 30 °C. Mixing of PPI-WG and SPI-WG before HTSC processing was performed in duplicate to get a more reliable insight in the effect of mixing and hydrating on the dough and final product properties.

The specific mechanical energy (*SME* in J/kg) required for mixing in the farinograph was calculated from the torque recorded by the WinMix software (version 3.2.14, Brabender GmbH &Co KG, Duisburg, Germany).

$$SME = \frac{\int_{t=0}^{t_f} \omega . M(t) . dt}{m} \qquad \textit{Eq. 3.2}$$

In which t_f is the final time, t=0 is the start time, ω is the rotor speed (s^{-1}), M is the torque (Nm) and m is the mass of the material loaded in the farinograph (kg) (=0.3 kg) (Peighambardoust et al., 2005).

To investigate the effect of hydrating after mixing and to allow water migration from PPI or SPI to WG the protein dough was further hydrated in a zip-lock bag after mixing for 60, 140 or 220 min. starting from the moment WG was added to the protein isolate before it was used in the HTSC. This means total hydrating times of 90, 170 or 250 min. for PPI or SPI. To ensure that all protein doughs had the same total hydrating time, the SPC dough was hydrated for an additional 30 min. resulting in the same total hydrating times of 90, 170 or 250 min. from the moment of water addition to SPC until HTSC processing. In the rest of this paper the total hydrating time will be indicated as hydrating time. Hand-mixed samples were prepared as a control sample for all product compositions used and all hydrating times.

3.3.3 Closed cavity rheometer

The rheological properties of the protein materials were measured with a closed-cavity rheometer (CCR) (RPA Elite, TA instruments, New Castle, DE, USA) (Emin et al., 2017). However, the preparation of the proteinaceous doughs slightly differed from what was described in section 2.2. Approximately 50 g of the dough was removed from the farinograph after 2, 5, 10 and 30 min of mixing. The doughs were hydrated until the total hydrating time was 90 min, which means that the PPI-WG and SPI-WG doughs were hydrated for 60 min. after WG addition. The protein doughs were vacuumized to prevent the effect of air in the sample on the rheological measurements (Wittek, Walther, et al., 2021). Approximately 6 g was placed in between two plastic films in the closed cavity, which was sealed with a closing pressure of 4.5 bar to prevent water evaporation at high temperature.

The geometry of the CCR has a radius of 22.5 mm, the maximum height of the inner cavity is 4 mm and a biconical opening has an angle of 3.35◦ to allow homogeneous transmission of the shear stress to the protein materials. The grooves on the surface of the cones prevent slippage. In this setup, the lower cone oscillates in strain-controlled mode while the upper cone remains stationary.

First, the protein material was heated for 2 min at the measurement temperature (i.e., 30 °C, 120 °C or 140 °C) without a shear treatment. Subsequently, strain sweep (1%–1000%) experiments were performed at 30 °C (all doughs), 120 °C (PPI-WG and SPI-WG) or 140 °C (SPC) at a constant frequency (1 Hz). All strain sweeps were performed in duplicate. The strain sweep experiments were used to determine the yield stress and the flow stress of the materials. The yield stress is defined as the value of the shear stress at the end of the linear viscoelastic (LVE) regime. Here, we define this stress as the point where G’ ′differs more than 5% from its strain-independent value in the LVE regime (Schreuders, Sagis, et al., 2021). The flow stress is defined as the value of shear stress at the crossover point where the storage modulus is equal to the loss modulus (G’=G”) (Schreuders, Sagis, et al., 2021).

3.3.4 High temperature shear cell

The protein doughs were treated in a high-temperature shear cell (HTSC) (Wageningen University, Netherlands) that was developed in house (Grabowska et al., 2016). Heating and cooling were done using an external oil bath. The hydrated protein doughs were transferred to the pre-heated HTSC and sheared for 15 min. at 30 rpm at 140 °C for SPC and 120 °C for

PPI-WG and SPI-WG. The different temperatures for SPC and PPI-WG, SPI-WG mixtures was used to enable fibrous structure formation (Grabowska et al., 2016; Schreuders et al., 2019). The SME of the mechanical treatment was calculated from the torque measured by the DO-Corder E330 (Brabender GmbH &Co KG, Duisburg, Germany) using Equation 2. After the shear treatment the material the products were cooled down until the temperature measured at the centre of the upper cone reached 35 °C using an external oil bath set to 25 °C. SPC products were prepared once to validate that mixing with water did not have a large effect on the properties of products produced from a single ingredient. PPI-WG and SPI-WG products were prepared in duplicate to get a more reliable insight in the effect of mixing and hydrating on gluten network formation.

3.3.5 Visual observations

The fibrousness of the products produced in the HTSC was assessed visually by bending the products parallel to the shear flow direction to obtain a tear at the middle of the product. The bent pieces were placed onto a metal pin and the fracture surface was photographed using a digital microscope with 36×magnification using the extended depth of field (EDF) option (Smartzoom 5, Carl Zeiss, Germany).

3.3.6 Tensile test

Tensile tests were performed with a Texture Analyzer (TA.XTPlusC, TA Instruments, USA) using a trigger force of 0.001 N. A uniaxial tensile test was performed at room temperature with a displacement rate of 1 mm/s. Tensile bars were taken from the product with a dog bone-shaped mould in parallel and perpendicular to the shear flow direction. The measured tensile strength was normalized based on the dimensions of the tensile bar. The ends of the tensile bars were placed into the two clamps such that 15.5 mm was the initial length of the sample. Tensile stress and tensile strain at fracture were calculated from the force and displacement measured using the equations for the Hencky stress and strain for uniaxial extension as explained in Macosko (1994) and used by Schreuders et al. (2019). The strain (ε) and tensile stress (σ) were be calculated using the following equations:

$$\epsilon = ln\frac{h(t)}{h_0} \qquad \textit{Eq. 3.3}$$

$$\sigma(t) = \frac{F}{A} \qquad \textit{Eq. 3.4}$$

In which:

$$A = \frac{h_0}{h(t)} * A_0 \qquad \textit{Eq. 3.5}$$

In which $h(t)$ (m) is the sample length at fracture, h_0 (m) is the sample length at the start of the measurement, F (N) is the force at fracture, A (m^2) is the cross-section area, A_0 (m^2) is the cross-section of the sample at the start of the measurement and l and w (m) are the length and width of the sample cross-section measured before the start of the measurement. The Young's modulus (Pa) was calculated at the initial slope of the stress-strain curve until a 1.5 mm extension was achieved.

For every product, three parallel and three perpendicular specimens were taken.

3.3.7 Statistical analysis

All values are represented as the mean ± standard deviation. A factorial ANOVA was performed to evaluate the effect of mixing time, hydrating time and their interaction a significance level of 95% ($P < 0.05$) analysed using SPSS statistics Version 28.0.1.1 (IBM, Armonk, NY, USA). A one-way ANOVA per hydrating time and ingredient combination was used to test the effect of mixing time. Tukey HSD was used to find differences between samples at a significance level of 95% ($P<0.05$) Levene's test ($P<0.05$) was used to check the assumption of equal variances. The results of the statistical analysis can be found in Tables S.3.1-S.3.15.

3.4 Results and discussion

3.4.1 Dough formation

The torque profile of the different proteinaceous doughs during 30 min of mixing in the farinograph is shown in Fig. 3.1. The torque profile of wheat gluten (WG) containing doughs had a similar shape to the typical farinograph curves during mixing of bread doughs. In these curves first, the torque increases suggesting the development of the gluten network. Subsequently, the optimal dough development time is reached, and the dough has its maximal strength. Finally, the torque decreases, which is generally interpreted as a disruption of the gluten network (Létang et al., 1999; Li et al., 2020). The torque profile of pea protein isolate (PPI)-WG showed similarities to this typical farinograph pattern of bread doughs with respect to having an optimum and continued breakdown after the maximum peak. The time to peak, which the case of wheat dough is referred to as optimal dough development time, was around 4.5 min. Mixing the soy protein isolate (SPI)-WG dough resulted in a higher torque and longer optimal dough development time around 8 minutes compared with the torque and development time of PPI-WG doughs. The higher energy input required to deform the SPI-WG dough is probably due to the more elastic and tougher nature of SPI-WG blends compared with PPI-WG (Schreuders, Sagis, et al., 2021). Part of the explanation for the shorter dough development time and dough stability of PPI-WG compared with SPI-WG is the lower WHC of PPI compared with SPI (Table 3.1). This leaves more water available for the WG in the PPI-WG dough compared with the WG in the SPI-WG dough (Schreuders et al., 2020). Jia et al. (2022) found that a higher water content in the wheat flour doughs made it more susceptible to mixing and thus resulted in a faster development and breakdown of the gluten network. However, the opposite effect of the water content on the development of the gluten network is also reported in literature (Dufour et al., 2024; Koksel & Scanlon, 2012). We expect these conflicting results were caused by the relatively low water to gluten protein ratio used in the study of Jia et al. (2022) (4-6) compared to those of Dufour et al. (2024) (8-15) and Koksel & Scanlon (2012) (7-31). The water:gluten ratio used by Jia et al. (2022) was more comparable to the one used in this study (4) and we therefore expect the effects reported in that study to be the most relevant for our doughs. However, other differences between PPI and SPI, such as their protein content, gelling capacity, amino acid composition or non-protein components (Shrestha et al., 2023), also play a role in the observed difference in the torque profile during farinograph mixing.

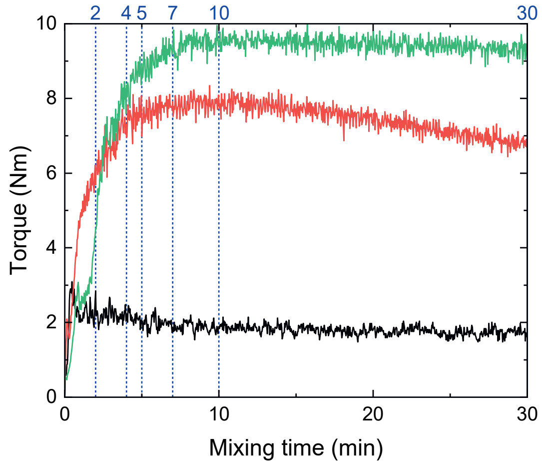

Fig. 3.1 Torque profile during mixing of SPC (black), PPI-WG (red) and SPI-WG (green). The blue dotted lines indicate the mixing times that were used in the high temperature shear cell (HTSC).

Table 3.1 Water holding capacity of the ingredients used in this study. Letters indicate homogeneous subgroups at $p<0.05$ using Tukey's HSD.

	SPC	PPI	SPI	WG
Water holding capacity (g/g)	6.73 ± 0.26^{b}	9.34 ± 0.09^{c}	20.99 ± 0.27^{d}	1.69 ± 0.13^{a}

Mixing of soy protein concentrate (SPC) resulted in a different torque profile, probably due to the absence of WG. Because of the low water holding capacity of SPC (Table 3.1) network formation does not occur upon hydrating, which explains the low torque measured. During the initial mixing phase (<1 min), a minor torque increase was observed, which can be attributed to the initial force required to start the mixing process.

3.4.2 Rheological properties of the protein doughs

Strain sweeps were performed in a closed cavity rheometer (CCR) to study the effect of mixing on the rheological properties of the protein doughs. The obtained rheological properties were summarized in texture maps in which the shear stress is plotted against the strain at the end of the linear viscoelastic (LVE) regime or the cross-over point (Fig. 3.2). The different corners in these texture maps indicate different textural properties of the material (Schreuders, Sagis, et al., 2021).

The rheological properties measured at 30 °C provide information about the behaviour of the dough during and after mixing. It was found that the rheological properties at the end of the LVE were not influenced by mixing for all protein doughs (Fig. 3.2A). In case of the WG containing doughs, this implies that changes in the gluten network are not reflected in the rheological properties in the LVE regime (Meerts et al., 2017). However, at the cross-over point longer mixing times resulted in tougher behaviour of the WG containing doughs and slightly mushier behaviour of SPC (Fig. 3.2.B). The increased toughness could indicate that mixing induced aggregation of the gluten (Jia et al., 2022). The effect of mixing on the rheological properties of the PPI-WG and SPI-WG doughs at the cross-over point showed a similar trend. However, a longer mixing time resulted in a larger shift in the texture map for PPI-WG doughs compared with SPI-WG doughs (Fig. 3.2B). This indicates that PPI-WG doughs were affected by mixing more than SPI-WG doughs. This difference was also visible in the torque profile during farinograph mixing (Fig. 3.1), in which it was shown that SPI-WG had a higher dough stability. As explained in section 3.4.1 the reason for this different behaviour could be the difference in water distribution between the protein isolate and WG for these two doughs, but other differences between PPI and SPI could also play a role.

The WG containing doughs were rubberier than SPC at the end of the LVE and the cross-over point (Fig. 3.2A&B). This can be explained by the gluten network that is present in these doughs. SPI-WG had a slightly higher stress compared with PPI-WG at the end of the LVE. However, at the cross-over point SPI-WG was tougher compared with the PPI-WG dough. The same trend was seen by Schreuders, Sagis, et al. (2021). The rheological properties measured at 120 and 140 °C provide information about the behaviour of the dough during HTSC processing. Mixing did not influence the rheological properties at the end of the LVE (Fig. 3.2C). As can be seen, the hand-mixed control showed different behaviour compared with the doughs in the farinograph for the doughs containing gluten. In case of PPI-WG the hand-mixed dough was mushier than the farinographs doughs while, in case of SPI-WG the hand-mixed dough was tougher compared with the doughs that were mixed in the farinograph. The PPI-WG dough showed one deviating point after 2 min mixing, which turned out to be very mushy compared with the other mixing conditions. At the cross-over point no consistent effect of mixing was seen for SPC and SPI-WG (Fig. 3.2D). However, mixing increased the toughness of PPI-WG.

At 120 or 140 °C more differences between the different ingredients were observed at the end of the LVE than at 30 °C (Fig. 3.2A&C). Clearly SPI-WG was tougher than PPI-WG. For SPC no clear LVE could be determined, which is why no data points at the end of the LVE are given for this dough. At the cross-over point the same trend was visible but the clusters were closer together. SPC was the mushiest and SPI-WG the toughest (Fig. 3.2D). PPI-WG lied in the middle of these two extremes.

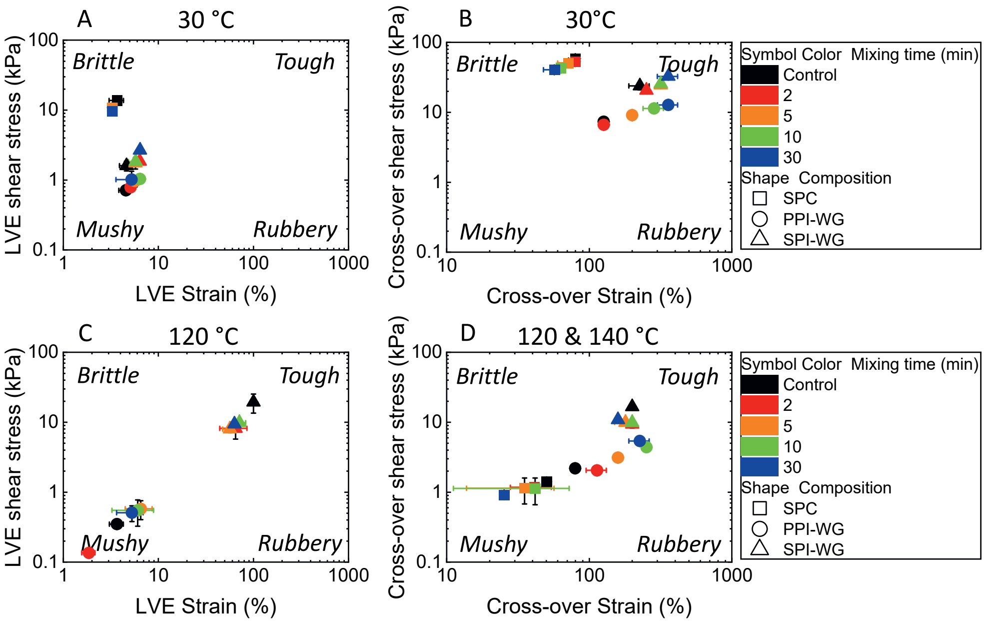

Fig. 3.2 Texture maps of at the end of the linear viscoelastic regime (LVE) (A&C) and at the cross-over (B&D) point of SPC (■), PPI-WG (●) and SPI-WG (▲) at 30 °C (A&B), 120 (PPI-WG&SPI-WG) and 140 °C (SPC) (C&D). The colour of the datapoints indicates the mixing time in the farinograph. The control treatment is shown in black.

It remains difficult to link these fundamental rheological properties of the doughs to the HTSC product properties. However, previous studies show that rheology can be used to obtain more insights in differences between proteins and effects of processing such as extrusion and HTSC processing (De Angelis et al., 2023; Ji et al., 2023; Schreuders et al., 2020; Snel et al., 2023). The effect of mixing at the end of the LVE and cross-over point was small compared with the effect heating and cooling of the PPI-WG or SPI-WG blends that was reported by Schreuders, Sagis, et al. (2021). However, the changes induced by mixing PPI-WG were similar to those induced by heating mixtures of PPI or SPI with cellulose or pectin (Schreuders, Schlangen, et al., 2022). Mixing can therefore be considered to have a relevant influence on the rheological properties of the protein doughs and is therefore be expected to influence the final HTSC product properties.

3.4.3 Specific mechanical energy (SME) of mixing and thermomechanical processing

As was discussed in the previous section (section 3.4.2), mixing affected the rheological properties of PPI-WG at the cross-over point measured at temperatures relevant for HTSC structuring. It was therefore hypothesized that mixing can affect the mechanical input required to deform the material in the HTSC. The hydrating time after mixing might also influence the behaviour of the dough in the HTSC. Fig. 3.3 shows the specific mechanical energy (SME) input during mixing in the farinograph and thermomechanical treatment in the HTSC for the different combinations of ingredients and mixing conditions investigated in this study. Separate figures with only mixing SME or HTSC SME including statistical differences can be found in Fig. S.3.1. and S.3.2.

The thermomechanical SME ranged from 23.2 kJ/kg (PPI-WG 4 min mixing 250 min hydrating) to 50.0 kJ/kg (SPC 10 min mixing 90 min hydrating) (Fig. 3.3). The mixing and hydrating times used in this study did not significantly affect the thermomechanical processing SME in the HTSC, even though different rheological properties were observed at the cross-over point in the CCR in cases of PPI-WG (Fig. 3.2).

It is interesting to compare the SME of mixing to the SME during the thermo-mechanical treatment in the HTSC. The mixing SME ranged from 0.7 kJ/kg (SPC 2 min mixing) to 43.6 kJ/kg (SPI-WG 30 min mixing). The SME of mixing was lower compared with the SME of thermomechanical processing, except for PPI-WG mixed for 30 min. The combined SME of the mixing and thermomechanical processing ranged from 27.0 kJ/kg (PPI-WG 5 min mixing 250 min hydrating) to 93.0 kJ/kg (SPI-WG 30 min mixing 250 min hydrating). This is on the low end of the SME during high-moisture extrusion (HME) 42.8-1276 kJ/kg (Maung et al., 2021; H. Wang et al., 2022; Zahari et al., 2021; Zhang et al., 2023). This means that HTSC processing including the mixing step is relatively mild compared with HME.

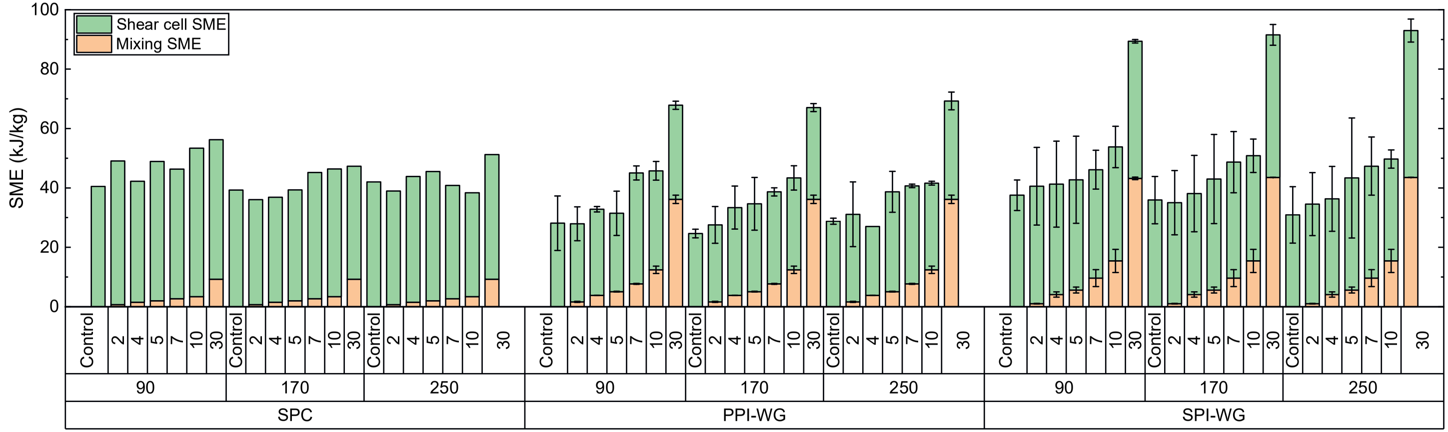

Fig. 3.3 Specific mechanical energy (SME) of mixing in the farinograph (orange) and thermomechanical processing in the HTSC (green) of the SPC, PPI-WG, and SPI-WG mixed for 2, 4, 5, 7, 10 or 30 minutes the control treatment and a hydration time of 90, 170 or 250 min.

3.4.4 Visual observations of HTSC products

Fig. 3.4-3.6 show the macrostructures of the HTSC products produced after different mixing conditions. The use of the different ingredient formulations and mixing conditions led to a wide range of (fibrous) structures including small-fibres, thick fibres, layers and flaky structures. Some products showed combinations of these structural elements.

In case of SPC, anisotropic structures were visible for all mixing and hydrating combinations (Fig. 3.4). Surprisingly, the hand-mixed control treatment with a hydrating time of 90 minutes appeared the least fibrous and longer hydrating of the hand-mixed control led to thicker fibres. No consistent effect of mixing or hydrating time was observed, although 7 and 10 min of mixing led to many small fibres and 5 min mixing time showed the least fibrous structures. A longer hydrating after mixing of 4 to 7 min appears to be favourable for fibrous structure formation, but this effect was not observed for other mixing times.

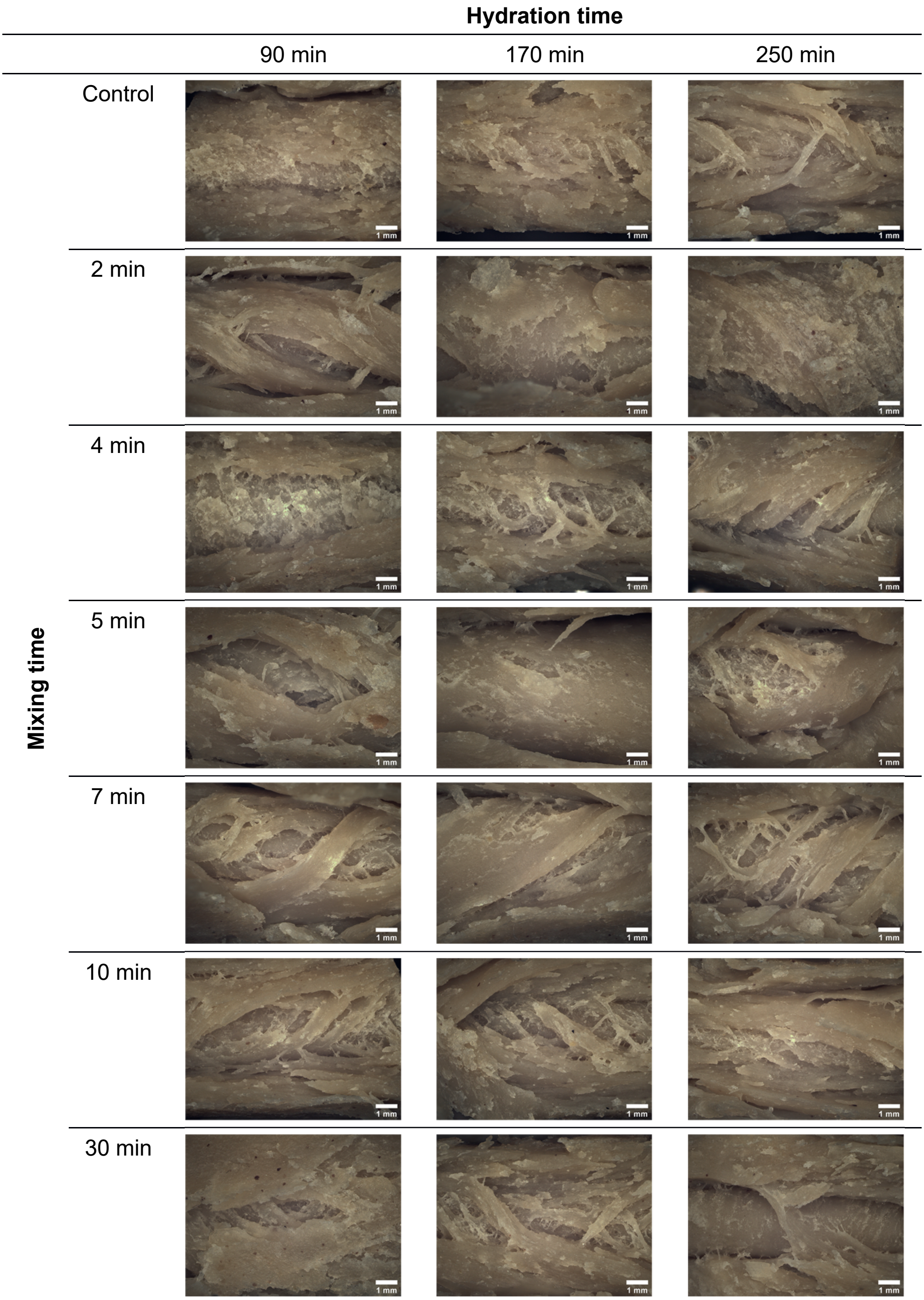

Fig. 3.4 Representative extensive depth of field (EDF) images of SPC HTSC products processed after different mixing and hydration times taken with a SmartZoom digital microscope at 36x magnification.

The WG containing products had structures that can best described as layered and were less clearly fibrous compared with the SPC products (Fig. 3.5 and 3.6). The hydrating times used in this study had no clear effect on the structures of both PPI-WG and SPI-WG products. Additionally, the composition of the HTSC products appeared to have a larger effect on the visual fibrousness compared to the mixing and hydrating conditions.

The limited visual fibrousness of PPI-WG products corresponds to our previous results with this protein mixture where the optimal shear rate for fibrous structure formation in the HTSC of this protein mixture was lower than the rotational speed of 30 rpm used in this study (Chapter 2). Mixing time appeared to have an influence on the visual macrostructure of the PPI-WG products. At mixing times up to 5 minutes the structures were clearly layered, whereas at longer mixing times this layered structure became less clear (Fig. 3.5).

The visually observed macrostructure of the SPI-WG products was less fibrous than expected from the results of Schreuders et al. (2019) and Cornet et al. (2021) Here, the control did not show a clearly fibrous structure. This difference with previous research might be caused by batch-to-batch variations in the ingredients used, the higher process temperature (140 °C) and lower dry matter content (30wt%) that were used by Cornet et al. (2021). Although the SPI-WG products appear to be more gel-like compared with SPC or PPI-WG products, they still were visually anisotropic (Fig. 3.4-3.6). Longer mixing times, for example 10 min mixing and 250 min hydrating and 30 min mixing 90 min hydrating did result in the formation of small fibres (Fig. 3.6).

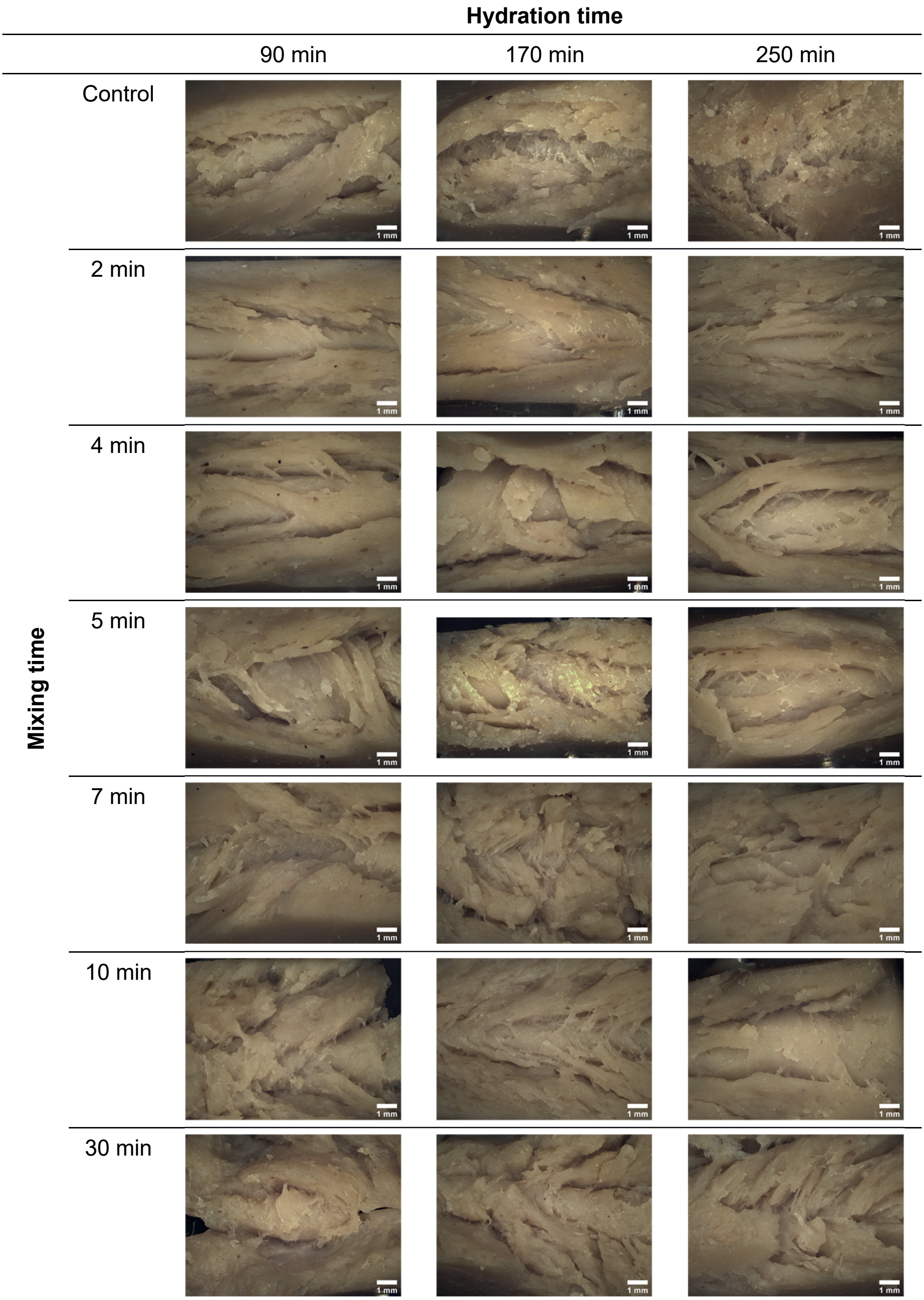

Fig. 3.5 Representative extensive depth of field (EDF) images of PPI-WG HTSC products processed after different mixing and hydration times taken with a SmartZoom digital microscope at 36x magnification.

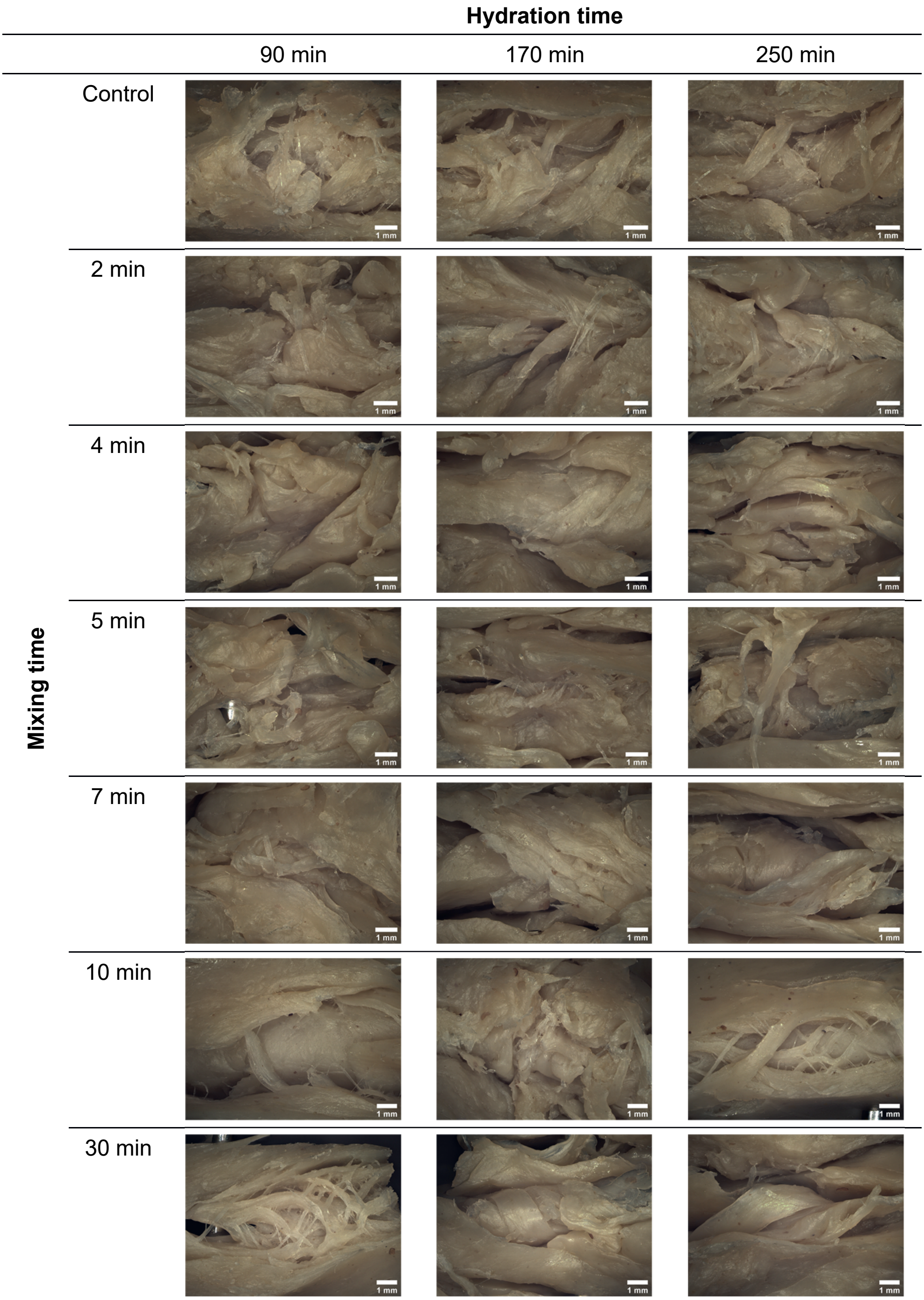

Fig. 3.6 Representative extensive depth of field (EDF) images of SPI-WG HTSC products processed after different mixing and hydration times taken with a SmartZoom digital microscope at 36x magnification.

3.4.5 Tensile test

To determine the effect of mixing and hydrating time on the mechanical properties of the products a tensile test was performed. In case of SPC mixing time did not influence the tensile test properties to a large extent (Fig. 3.7A1, 3.7A2, 3.7A3). This limited effect of mixing was also seen in the rheological properties (Fig. 3.2) and visual observations (Fig. 3.4). This is probably caused by the absence of network formation in SPC during mixing, because of its low WHC and the absence of WG.

However, in case of PPI-WG mixing influenced tensile test properties (Fig. 3.7B1, 3.7B2, 3.7B3). The strain and stress in parallel and perpendicular direction were higher after 5 min of mixing compared with other products. The Young's modulus was not influenced by mixing. The increase of the tensile stress and strain that was observed for a mixing time of 5 minutes at corresponds with the optimal dough development time observed in the torque profile (Fig. 3.1). This indicates that the optimal dough development corresponds with an increased tensile strength, suggesting that how gluten network is formed during mixing remains relevant when processing the blend in the HTSC, despite the higher SME of the thermomechanical treatment (Fig. 3.3). This corresponds with the work of Peighambardoust et al. (2005) who showed that the glutenin macropolymer was broken down during mixing of bread dough in a farinograph, but not during shear cell treatment. Thus, the dough properties measured during mixing in a farinograph type mixer could be used to control the mechanical properties of the final meat analogue product. However, the maximum in the tensile stress and strain did not correspond with clear changes in the visual macrostructure (Fig. 3.5). For the most constant product properties a mixing time longer than the optimal dough development time might be beneficial, as the product properties are expected to be less affected by small changes in the mixing conditions. Optimization of the mixing process could be used to produce stronger HTSC products without the use of additional ingredients or more intensive processing in the HTSC, which could reduce the cost and energy usage of the process.

Mixing time only significantly influenced the Young's modulus in case of SPI-WG (Fig. 3.7C1, 3.7C2, 3.7C3). The Young's modulus in parallel direction was higher after 4 minutes of mixing compared with the control. In perpendicular direction the Young's modulus after 4,5,7 or 30 min was higher compared with the control. Unlike for the PPI-WG no maximum was measured for the tensile test properties. This corresponds with the more subtle effect of mixing in the torque profile and rheological properties of SPI-WG compared with PPI-WG (Fig. 3.1 and 3.2). As was already speculated in section 3.4.1, a possible explanation is a difference in available water for gluten in the two doughs. However, Schreuders et al. (2019) reported the fibrous structure formation was less affected by temperature for SPI-WG in comparison with PPI-WG and attributed this the higher gelling capacity of SPI compared with PPI. This could also influence the effect of mixing on these products.

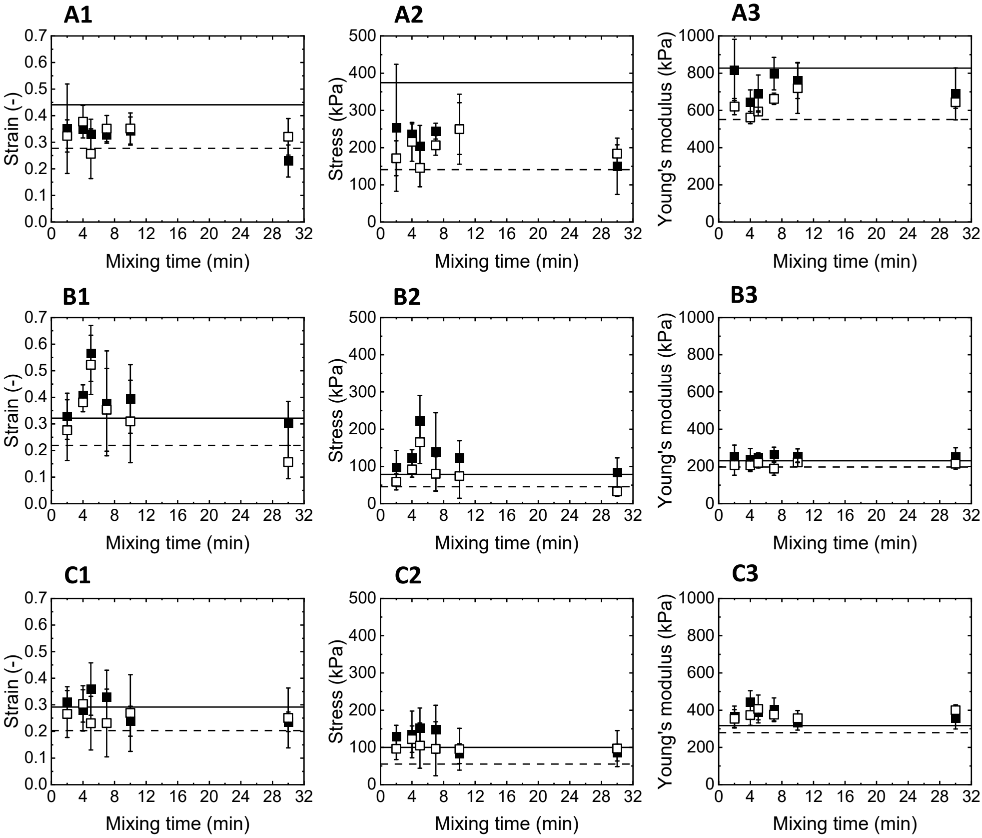

Fig. 3.7 Tensile strain (1), stress (2) and Young's modulus (3) in parallel (closed symbols) or perpendicular (open symbols) direction for SPC (A), PPI-WG (B) and SPI-WG (C) products after 90 min. hydration. The horizontal lines represent the control treatment at the same hydration time in parallel (filled line) and perpendicular (dashed line) direction.

In the range of hydrating times used in this study, hydrating time did not have a significant effect on the tensile test properties of the different ingredients used, except for the Young's modulus in parallel direction for PPI-WG (Table S.3.3-S.3.5). Because of this only the tensile test results of a hydrating time of 90 min were discussed here. The results for the other hydrating times can be found in Fig. S.3.3 and S.3.4. The limited effect of hydrating time on the tensile test properties indicates that the water distribution from PPI or SPI to the WG phase was already completed within 60 min after the addition of WG. However, at shorter hydrating times, water distribution could still have an influence on the structuring properties of the protein dough, which we would like to exclude in this study. Further research on the effect of hydrating at shorter hydrating times therefore remains necessary.

Fig. 3.8 summarizes the textural properties of the HTSC products based on the measured tensile stress and strain. For all product compositions changes in mixing intensity resulted in a shift in behaviour on the diagonal line between the bottom left corner, which indicates mushy behaviour, to the top right corner, which indicates tough behaviour.

The PPI-WG products show a wider range of textural properties compared with SPC and SPI-WG products. The cluster of SPI-WG products fell in the middle of the range for the PPI-WG products. This indicates that the mechanical properties of SPC and SPI-WG were hardly influenced by the mixing time compared to those of PPI-WG products. This aligns with the observation that the rheological properties of SPC and SPI-WG doughs and visual fibrousness of SPC and SPI-WG HTSC products were also hardly different as a result of different mixing times (Fig. 3.2). Additionally, Schreuders et al. (2019) found the structure of SPI-WG products was less affected by the processing temperature in the HTSC than PPI-WG. Furthermore, in our previous study (Chapter 2), varying rotational speed (0-100 rpm) or shearing time (8 or 15 min) during HTSC processing of PPI-WG yielded similar variations in the tensile stress and strain of the products, as the variations presented in this study. This could indicate that SPI-WG is generally more robust to changes in the process conditions compared with PPI-WG.

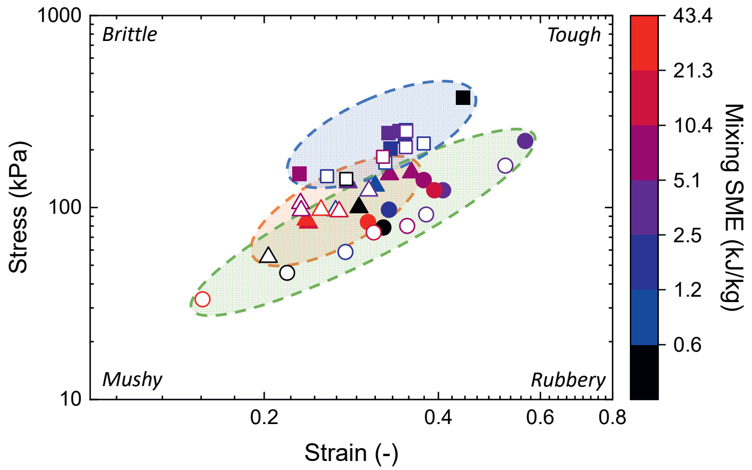

Fig. 3.8 Texture map tensile stress plotted against tensile strain for SPC (■), PPI-WG (●) and SPI-WG (▲) in parallel (closed symbols) and perpendicular (open symbols) direction for products of which the dough was hydrated for 90 minutes. Shades indicate are of tensile test properties of SPC (blue), PPI-WG (green) and SPI-WG (orange).

This study gives more insight in the effect of mixing and hydrating time on mixtures of protein isolates with WG and protein concentrates mixed with water. However, this information is not sufficient to optimize the mixing strategy before HTSC processing, as additional variables such as mixer type, mixing speed and mixing temperature should be further studied to do so. Furthermore, protein isolates can also be mixed with carbohydrates such as dietary fibres (e.g. pectin or cellulose) instead of gluten, to create fibrous structures in the HTSC (Schreuders, Schlangen, et al., 2022), but these ingredients were not included in this study. We expect that mixing of the dough will also influence the final product properties for protein-carbohydrate HTSC products. Mixing might lead to break up of the dispersed carbohydrate phase, like the break-up of the pectin phase in a SPI-pectin mixture at higher shear rates in the HTSC that was observed by Dekkers, Hamoen, et al. (2018). However, the mechanical deformation during HTSC processing might overshadow the effect of mixing in this case. Furthermore, we do not expect a clear optimal dough development time to be visible in the farinograph curves of these mixtures since no network formation takes place. We therefore expect a similar torque profile as was seen for SPC in this study (Fig. 3.1) and for other pulse ingredients (Bresciani et al., 2022). However, to the best of our knowledge the farinograph properties of pulse ingredients with the addition of fibres or hydrocolloids has not been investigated previously. Therefore, further research on the effect of mixing on protein-carbohydrate doughs and their resulting properties remains necessary before general mixing guidelines can be developed.

Additionally, this research provides more insight in the effects of mixing in the extrusion process. However, the total SME of mixing and HTSC processing was low compared with HME processing (section 3.4.3). We therefore expect the subtle effects of mixing on the final product structure that were found in this study to be overshadowed during HME. This corresponds with previous research in which screw speed was found to have a minor effect compared to for example moisture content or barrel temperature (Omohimi et al., 2014; Samard et al., 2019).

3.5 Conclusion

This study described the effect of mixing and hydrating soy protein concentrate (SPC), pea protein isolate (PPI)-wheat gluten (WG) and soy protein isolate (SPI)-WG doughs and on the properties of the properties of HTSC products. The effect of mixing depended on the composition of the dough. For SPC mixing had a limited effect on the rheological properties of the doughs and the visual and tensile test properties of the HTSC products. In case of SPI-WG, prolonged mixing resulted in a slightly tougher dough, but prolonged mixing had no effect on the final product properties. However, mixing did influence the final product properties in case of PPI-WG, for which a highest tensile strength was observed when applying a mixing time of 5 minutes. This could be related to the limited formation of a gluten network at short mixing times and break-down of the gluten network when using mixing times longer than 5 minutes. Hydrating the protein doughs after mixing did not result in large changes in the final HTSC product properties.

The effect of mixing on final product was remarkable as the specific mechanical energy input of the subsequent thermomechanical treatment in the HTSC is substantially higher than the SME input during mixing. However, the different effects of mixing on the final product properties of SPC, PPI-WG and SPI-WG products highlights the importance of considering the ingredient properties when optimizing the processing parameters for HTSC products.

3.6 Appendix

3.6.1 Statistical analysis SME

Specific mechanical energy of mixing in the farinograph

A full factorial ANOVA was conducted to compare the main effects of dough composition (PPI-WG or SPI-WG) and mixing time as well as their interaction effects on the mixing SME. The Levene's test showed that the variances of the groups were not equal ($F(11,15)=22.038$, $p<0.001$). Dough composition ($F(1,15)=12.726$, $p=0.003$) and mixing time ($F(5,15)=346.889$, $p<0.001$) were significantly significant. The interaction effect was not significant ($F(5,15)=3.902$, $p=0.018$).

Table S.3.1 Homogeneous subsets effect of mixing time on the mixing SME according to Tukey's HSD with $p<0.05$.

Mixing time (min)	**Homogeneous subsets mixing SME**
2	a
4	a,b
5	b,c
7	c
10	d
30	e

*Assumption of homogeneity of variance is violated as tested with the Levene's test with $p<0.05$

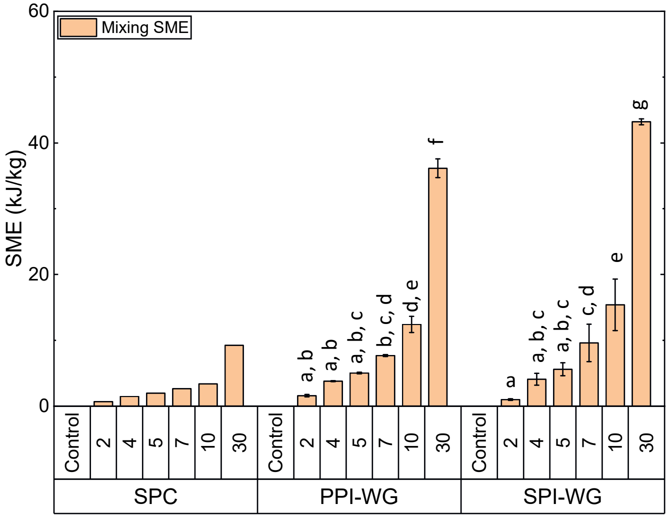

Fig. S.3.1 Specific mechanical energy (SME) of mixing for SPC, PPI-WG and SPI-WG mixed for different times. Letters indicate homogeneous subsets according with Tukey's HSD at P<0.05. Levene's test for equal variance is violated (P<0.001). SPC was not included in statistical analysis as only single measurements were performed.

Specific mechanical energy of thermomechanical processing in the high-temperature shear cell

A full factorial ANOVA was conducted to compare the main effects of dough composition (SPC, PPI-WG or SPI-WG), mixing time and hydration time as well as their interaction effects on the mixing SME. The Levene's test showed that the variances of the groups were not equal ($F(40,57)=4.978$, $p<0.001$). The effect of dough composition was significant ($F(2,57)=19.832$, $p<0.001$).. Whereas the effect of mixing time ($F(6,57)=1.289$, $p=0.277$) and hydration time ($F(2,57)=1.446$, $p=0.244$) and the interaction effects were not.

Table S.3.2 Homogeneous subsets of the effect of protein dough composition on thermomechanical processing SME according to Tukey's HSD with p<0.05

Dough composition	**Homogeneous subsets**
SPC	b
PPI-WG	a
SPI-WG	b

*Assumption of homogeneity of variance is violated as tested with the Levene's test with p<0.05

3

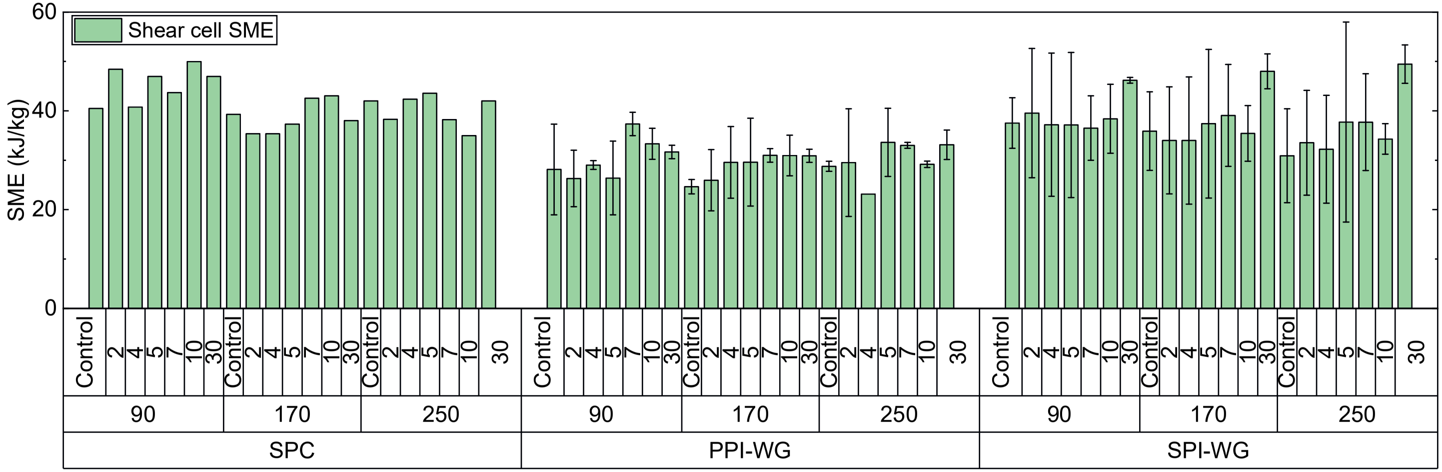

Fig. S.3.2 Specific mechanical energy (SME) during HTSC processing of SPC, PPI-WG and SPI-WG for different mixing and hydration times. Statistical analysis for the SME of PPI-WG and SPI-WG processing did not result insignificant differences at p<0.05.

3.6.2 Statistical analysis tensile test

Full factorial ANOVA tensile test

A full factorial ANOVA was conducted to compare the main effects of mixing time and hydration time as well as their interaction effects on the tensile test properties of HTSC products (parallel and perpendicular stress, strain and Young's modulus) for every dough composition.

Table S.3.3 SPC full factorial ANOVA mixing time and hydration time and their interaction. Bold p-values indicate significance at p<0.05.

	Mixing time	**Hydration time**	**Mixing * hydration**
Parallel stress*	$F(6,111)=1.784$ $p=0.109$	$F(2,111)=1.108$ $p=0.334$	$F(12,111)=1.947$ $\mathbf{p=0.036}$
Perpendicular stress	$F(6,111)=1.751$ $p=0.116$	$F(2,111)=0.669$ $p=0.514$	$F(12,111)=1.564$ $p=0.113$
Parallel strain*	$F(6,111)=0.873$ $p=0.518$	$F(2,111)=0.622$ $p=0.239$	$F(12,111)=1.516$ $p=0.129$
Perpendicular strain*	$F(6,111)=1.499$ $p=0.185$	$F(2,111)=0.336$ $p=0.715$	$F(12,111)=1.905$ $\mathbf{p=0.041}$
Parallel Young's modulus	$F(6,111)=7.744$ $\mathbf{p<0.001}$	$F(2,111)=0.875$ $p=0.420$	$F(12,111)=3.508$ $\mathbf{p<0.001}$
Perpendicular Young's modulus*	$F(6,111)=7.432$ $\mathbf{p<0.001}$	$F(2,111)=2.312$ $p=0.104$	$F(12,111)=1.478$ $p=0.143$

*Assumption of homogeneity of variance is violated as tested with the Levene's test with p<0.05

3

Table S.3.4 PPI-WG full factorial ANOVA mixing time and hydration time and their interaction. Bold p-values indicate significance at p<0.05.

	Mixing time	**Hydration time**	**Mixing * hydration**
Parallel stress*	F(6,129)=10.649 **p<0.001**	F(2,129)=1.695 p=0.188	F(11,129)=2.018 **p=0.032**
Perpendicular stress*	F(6,129)=9.738 **p<0.001**	F(2,129)=1.016 p=0.365	F(11,129)=2.094 **p=0.025**
Parallel strain*	F(6,129)=9.484 **p<0.001**	F(2,129)=2.108 p=0.126	F(11,129)=2.431 **p=0.009**
Perpendicular strain*	F(6,129)=10.483 **p<0.001**	F(2,129)=0.750 p=0.475	F(11,129)=1.824 p=0.056
Parallel Young's modulus*	F(6,129)=2.796 **p=0.014**	F(2,129)=11.692 **p<0.001**	F(11,129)=1.924 **p=0.042**
Perpendicular Young's modulus*	F(6,129)=2.346 **p=0.035**	F(2,129)=0.880 p=0.417	F(11,129)=0.808 p=0.632

*Assumption of homogeneity of variance is violated as tested with the Levene's test with p<0.05

Table S.3.5 SPI-WG full factorial ANOVA mixing time and hydration time and their interaction. Bold p-values indicate significance at p<0.05.

	Mixing time	**Hydration time**	**Mixing * hydration**
Parallel stress*	F(6,111)=1.784 p=0.109	F(2,111)=1.108 p=0.334	F(12,111)=1.947 **p=0.036**
Perpendicular stress	F(6,111)=1.751 p=0.116	F(2,111)=0.669 p=0.514	F(12,111)=1.564 p=0.113
Parallel strain*	F(6,111)=0.873 p=0.518	F(2,111)=0.622 p=0.539	F(12,111)=1.516 p=0.129
Perpendicular strain*	F(6,111)=1.499 p=0.185	F(2,111)=0.336 p=0.715	F(12,111)=1.905 **p=0.041**
Parallel Young's modulus	F(6,111)=7.744 **p<0.001**	F(2,111)=0.875 p=0.420	F(12,111)=3.508 **p<0.001**
Perpendicular Young's modulus*	F(6,111)=7.432 **p<0.001**	F(2,111)=2.312 p=0.104	F(12,111)=1.478 P=0.143

*Assumption of homogeneity of variance is violated as tested with the Levene's test with p<0.05

One-way ANOVA for mixing time per hydration time and per composition

A one-way ANOVA was conducted to evaluate the effect of mixing intensity per dough composition and per hydration time. In case of a significant effect of mixing time a Tukey post-hoc test with a significance level of 0.05 was used to determine the homogeneous subsets.

Table S.3.6 SPC one-way ANOVA for effect of mixing time for different hydration times. Bold p-values indicate significance at p<0.05.

	90 min	**170 min**	**250 min**
Parallel stress	F(6,13)=2.045 p=0.132*	F(6,14)=2.845 p=0.050*	F(6,11)=1.338 p=0.319
Perpendicular stress	F(6,13)=1.154 p=0.387	F(6,14)=1.040 p=0.441	F(6,11)=1.740 p=0.202
Parallel strain	F(6,13)=1.861 p=0.164*	F(6,14)=2.082 p=0.121	F(6,11)=0.321 p=0.913*
Perpendicular strain	F(6,13)=1.092 p=0.417	F(6,14)=0.860 p=0.546*	F(6,11)=0.612 p=0.717
Parallel Young's modulus	F(6,13)=1.092 p=0.408	F(6,14)=7.062 **p=0.001**	F(6,11)=2.439 p=0.095
Perpendicular Young's modulus	F(6,13)=1.297 p=0.325*	F(6,14)=6.750 **p=0.002**	F(6,11)=2.254 p=0.115

*Assumption of homogeneity of variance is violated as tested with the Levene's test with p<0.05

Table S.3.7 Homogeneous subsets for SPC tensile test parameters for which mixing time had a significant effect with a Tukey HSD test at p<0.05.

	170 min Parallel Young's modulus	**170 min Perpendicular Young's modulus***
Control	a	a, b
2 min	b	b
4 min	a	a
5 min	b	b
7 min	a, b	b
10 min	b	a, b
30 min	a, b	b

*Assumption of homogeneity of variance is violated as tested with the Levene's test with p<0.05

3

Table S.3.8 PPI-WG one-way ANOVA for effect of mixing time for different hydration times. Bold p-values indicate significance at $p<0.05$. Products hydrated for 250 min and sheared for 30 min in perpendicular direction were too weak to measure and were not included.

	90 min	**170 min**	**250 min**
Parallel stress	$F(6,44)=6.443$ **$p<0.001$***	$F(6,44)=4.062$ **$p=0.003$***	$F(5,41)=4.404$ **$p=0.003$***
Perpendicular stress	$F(6,44)=10.386$ **$p<0.001$***	$F(6,44)=3.472$ **$p=0.007$**	$F(5,41)=2.597$ **$p=0.039$***
Parallel strain	$F(6,44)=5.177$ **$p<0.001$***	$F(6,44)=3.450$ **$p=0.007$**	$F(5,41)=6.403$ **$p<0.001$***
Perpendicular strain	$F(6,44)=8.733$ **$p<0.001$***	$F(6,44)=4.048$ **$p=0.003$**	$F(5,41)=2.693$ **$p=0.034$**
Parallel Young's modulus	$F(6,44)=0.419$ $p=0.863$*	$F(6,44)=4.856$ **$p<0.001$***	$F(5,41)=2.571$ **$p=0.041$**
Perpendicular Young's modulus	$F(6,44)=0.538$ $p=0.776$*	$F(6,44)=3.899$ **$p=0.003$**	$F(5,41)=0.826$ $p=0.538$

*Assumption of homogeneity of variance is violated as tested with the Levene's test with $p<0.05$

Table S.3.9 Homogeneous subsets for PPI-WG at a hydration time of 90 min. tensile test parameters for which mixing time had a significant effect with a Tukey HSD test at $p<0.05$.

	Parallel stress*	**Perpendicular stress***	**Parallel strain***	**Perpendicular strain***
Control	a	a	a	a,b
2 min	a	a	a	a,b
4 min	a	a	a,b	b,c
5 min	b	b	b	c
7 min	a,b	a	a	b,c
10 min	a	a	a,b	a,b
30 min	a	a	a	a

*Assumption of homogeneity of variance is violated as tested with the Levene's test with $p<0.05$

Table S.3.10 Homogeneous subsets for PPI-WG at a hydration time of 170 min. tensile test parameters for which mixing time had a significant effect with a Tukey HSD test at $p<0.05$.

	Parallel stress*	Perpendicular stress	Parallel strain	Perpendicular strain	Parallel Young' s modulus*	Perpendicular Young' s modulus
Control	a,b	a,b	a,b	a,b	a	a,b,c
2 min	c	a,b	b,c	b,c	a,b	a,b,c
4 min	c	b	c	c	b	a,b,c
5 min	b,c	a,b	b,c	a,b,c	a,b	b,c
7 min	a,b,c	a,b	a,b,c	a,b,c	a,b	a,b
10 min	a,b,c	b	b,c	b,c	a,b	c
30 min	a	a	a	a	a,b	a

*Assumption of homogeneity of variance is violated as tested with the Levene's test with $p<0.05$

Table S.3.11 Homogeneous subsets for PPI-WG at a hydration time of 250 min. tensile test parameters for which mixing time had a significant effect with a Tukey HSD test at $p<0.05$. Products sheared for 30 min in perpendicular direction were too weak to measure and were not included.

	Parallel stress*	Perpendicular stress*	Parallel strain*	Perpendicular strain	Parallel Young's modulus
Control	a	a	a	a	a
2 min	b	a	b	a	a
4 min	b	a	b	a	a
5 min	b	a	a,b,c	a	a
7 min	a,b	a	b	a	a
10 min	b	a	b,c	a	a
30 min	a,b	-	a,b	-	a

*Assumption of homogeneity of variance is violated as tested with the Levene's test with $p<0.05$

Table S.3.12 SPI-WG one-way ANOVA for effect of mixing time for different hydration times according to Tukey's HSD test with p<0.05.

	90 min	**170 min**	**250 min**
Parallel stress	$F(6,41)=2.932$ **p=0.018**	$F(6,37)=0.987$ p=0.448*	$F(6,33)=1.745$ p=0.141*
Perpendicular stress	$F(6,41)=1.813$ p=0.120	$F(6,37)=0.610$ p=0.721	$F(6,33)=3.593$ **p=0.008**
Parallel strain	$F(6,41)=2.444$ **p=0.041**	$F(6,37)=0.946$ p=0.475*	$F(6,33)=0.999$ p=0.442*
Perpendicular strain	$F(6,41)=0.910$ p=0.498	$F(6,37)=1.564$ p=0.185	$F(6,33)=3.066$ **p=0.017**
Parallel Young's modulus	$F(6,41)=5.677$ **p<0.001**	$F(6,37)=3.349$ **p=0.010**	$F(6,33)=4.583$ **p=0.002**
Perpendicular Young's modulus	$F(6,41)=6.404$ **p<0.001**	$F(6,37)=2.988$ **p=0.018***	$F(6,33)=2.448$ **p=0.045***

*Assumption of homogeneity of variance is violated as tested with the Levene's test with p<0.05

Table S.3.13 Homogeneous subsets for SPI-WG at a hydration time of 90 min. tensile test parameters for which mixing time had a significant effect with a Tukey HSD test at p<0.05.

	Parallel stress	**Parallel strain**	**Parallel Young's modulus**	**Perpendicular Young's modulus**
Control	a	a,b	a	a
2 min	a	a,b	a,b,c	a,b
4 min	a	a,b	c	b
5 min	a	b	a,b,c	b
7 min	a	a,b	b,c	b
10 min	a	a,b	a,b	a,b
30 min	a	a	a,b	b

*Assumption of homogeneity of variance is violated as tested with the Levene's test with p<0.05

Table S.3.14 Homogeneous subsets for SPI-WG at a hydration time of 170 min. tensile test parameters for which mixing time had a significant effect with a Tukey HSD test at $p<0.05$.

	Parallel Young's modulus	Perpendicular Young's modulus*
Control	a	a
2 min	a,b	a
4 min	a	a
5 min	b	a
7 min	a	a
10 min	a,b	a
30 min	a,b	a

*Assumption of homogeneity of variance is violated as tested with the Levene's test with $p<0.05$

Table S.3.15 Homogeneous subsets for SPI-WG at a hydration time of 250 min. tensile test parameters for which mixing time had a significant effect with a Tukey HSD test at $p<0.05$.

	Perpendicular stress	Perpendicular strain	Parallel Young' s modulus	Perpendicular Young' s modulus*
Control	a	a	a	a,b
2 min	a,b	a	a	a,b
4 min	a,b	a	a,b	a,b
5 min	a,b	a	b	a,b
7 min	a,b	a	a,b	a,b
10 min	a	a	a,b	a
30 min	b	a	a,b	b

*Assumption of homogeneity of variance is violated as tested with the Levene's test with $p<0.05$

3

3.6.3 Tensile test results 170 and 250 min hydration

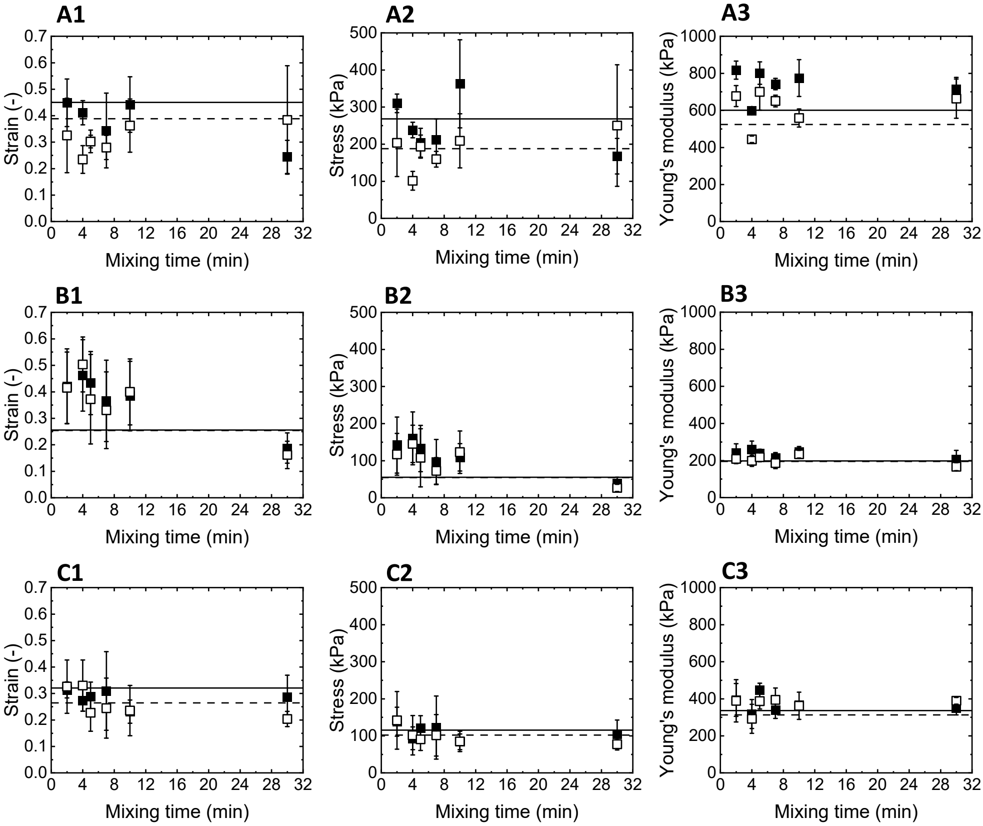

Fig. S.3.3 Tensile strain (1), stress (2) and Young's modulus (3) in parallel (closed symbols) or perpendicular (open symbols) direction for SPC (A), PPI-WG (B) and SPI-WG (C) products after 170 min. hydration. The horizontal lines represent the control treatment at the same hydration time in parallel (filled line) and perpendicular (dashed line) direction.

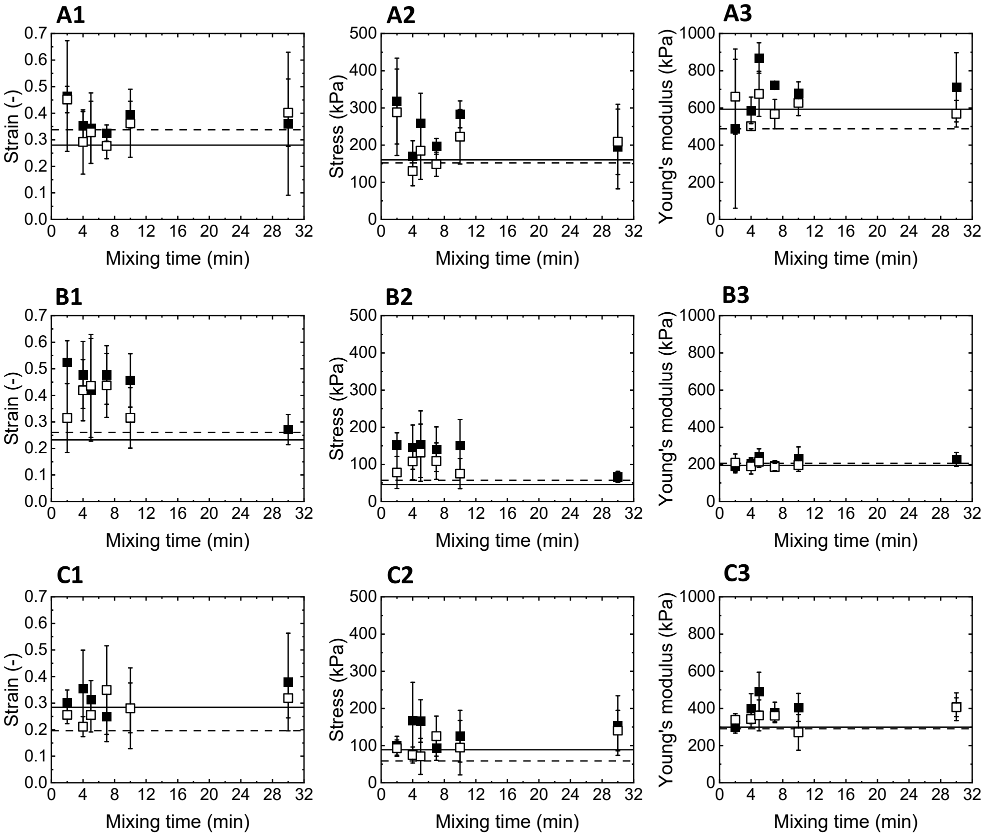

Fig. S. 3.4 Tensile strain (1), stress (2) and Young's modulus (3) in parallel (closed symbols) or perpendicular (open symbols) direction for SPC (A), PPI-WG (B) and SPI-WG (C) products after 250 min. hydration. The horizontal lines represent the control treatment at the same hydration time in parallel (filled line) and perpendicular (dashed line) direction.

3.6.4 Effect mixing on other type of PPI mixed with WG

In addition to the results discussed in the main manuscript the effect of mixing and hydration time on another grade of PPI: Nutralys F85M was also investigated. According to the supplier this ingredient had a larger particle size. However, this difference in particle size was not found in particle size measurements: Nutralys S85F $D_{4,3}$ 105.33 µm, Nutralys F85M 104.33 µm. The particle size distribution of the used ingredients was determined with laser diffraction using a Mastersizer 3000 (Malvern Instrument Ltd., Worcestershire, UK) equipped with a dry dispersion unit (Aero S) and a high energy venturi dispenser. A dispersion pressure of 2 bar was and the volume-based particle size distribution was estimated using the Mie theory, using a refractive index of 1.46 (Ramos Diaz et al., 2022) and an absorption index of 0.1. The particle size distribution of each sample was measured in triplicate.

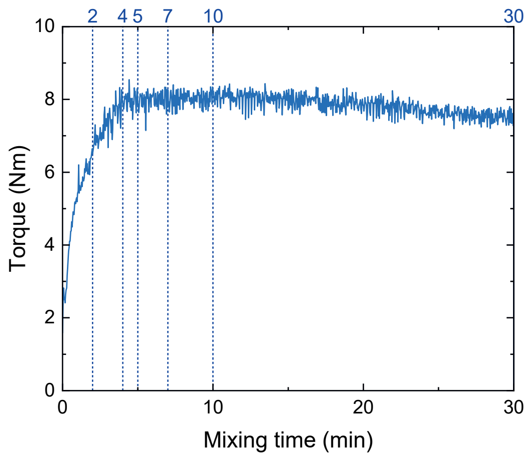

Fig. S. 3.5 Torque profile during mixing of Nutralys F85M-WG.

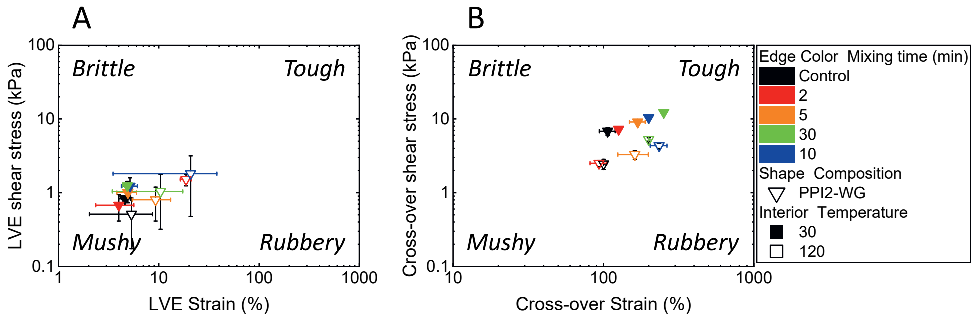

Fig. S. 3.6 Texture maps of at the end of the linear viscoelastic regime (LVE) (A) and at the cross-over (B) point at 30 °C (closed symbols) 120 °C (open symbols) for Nutralys F85M-WG. The colour of the datapoints indicates the mixing time in the farinograph, ranging from blue to red. The control treatment is shown in black.

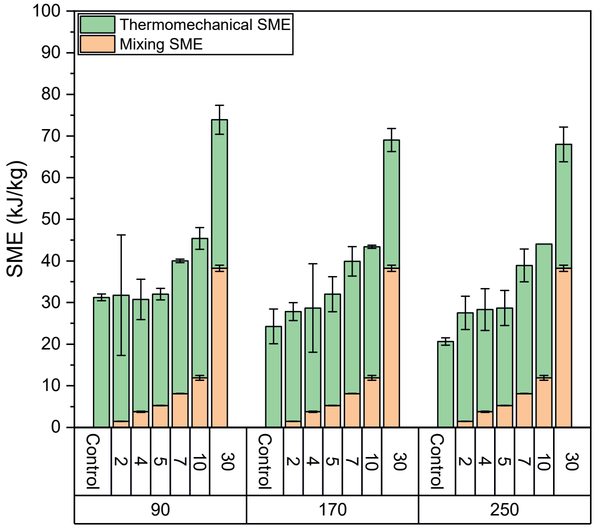

Fig. S. 3.7 Mixing SME and thermomechanical processing SME Nutralys F85M-WG.

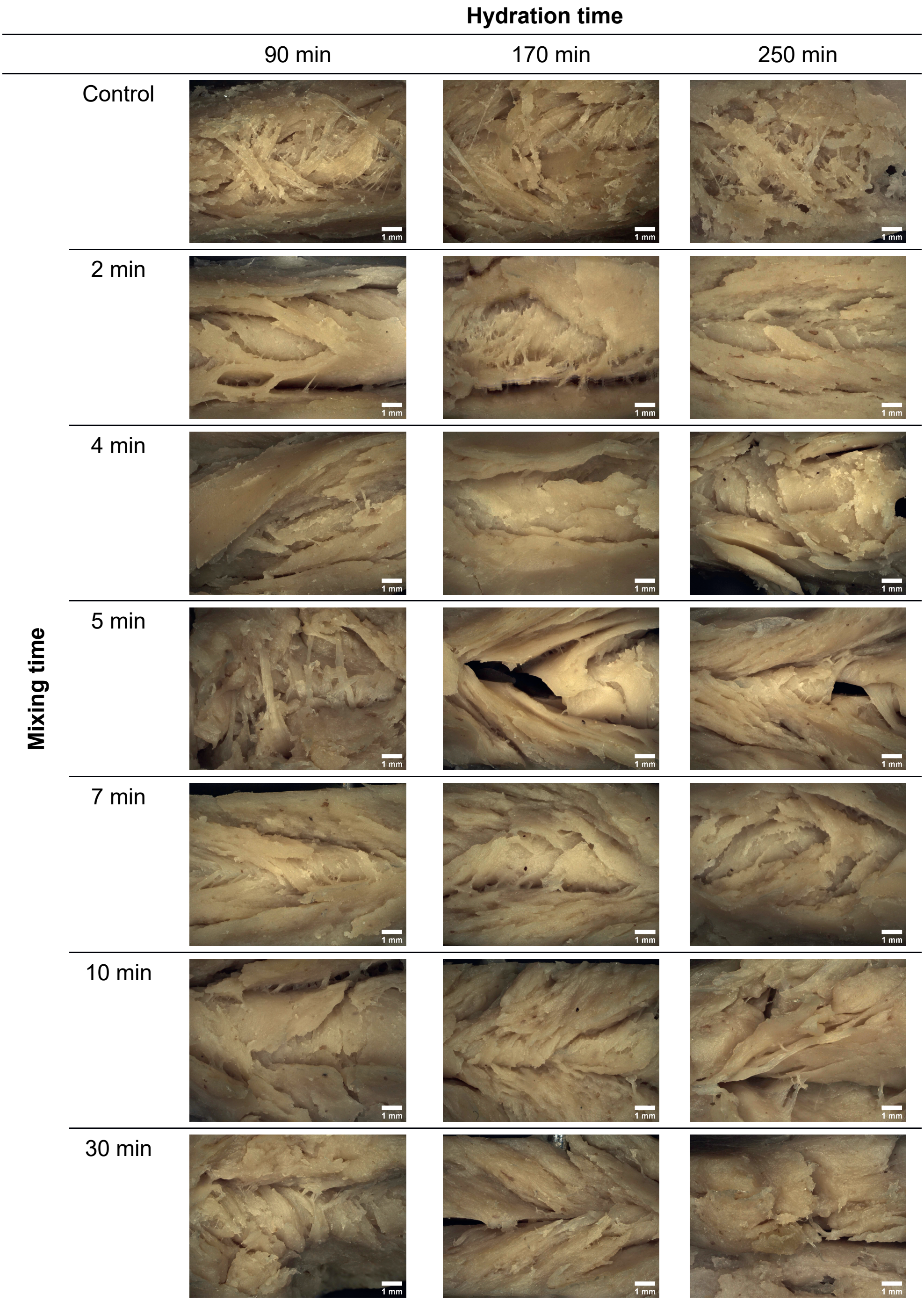

Fig. S. 3.8 Representative extensive depth of field (EDF) images of SPC HTSC products processed after different mixing and hydration times taken with a SmartZoom digital microscope at 36x magnification.

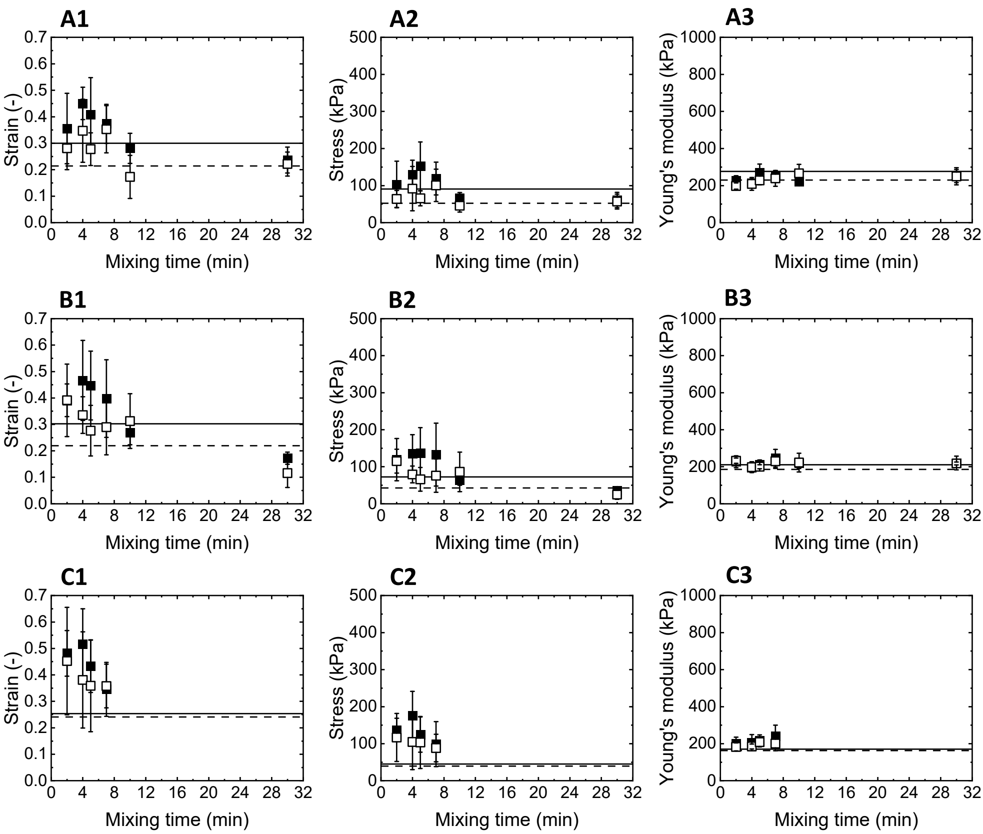

Fig. S.3.9 Tensile strain (1), stress (2) and Young's modulus (3) in parallel (closed symbols) or perpendicular (open symbols) direction for Nutralys F85M-WG, hydrated for 90 (A), 170 (B) or 250 min (C). The horizontal lines represent the control treatment at the same hydration time in parallel (filled line) and perpendicular (dashed line) direction.

Table S.3.16 Nutralys F85M-WG full factorial ANOVA mixing time and hydration time and their interaction. Bold p-values indicate significance at p=0.05.

	Mixing time	Hydration time	Mixing*hydration
Parallel stress*	F(6,90)=8.077 **p<0.001**	F(2,90)=0.107 p=0.899	F(10,90)=1.032 p=0.424
Perpendicular stress*	F(6,90)=3.778 **p=0.002**	F(2,90)=1.333 p=0.269	F(10,90)=1.278 p=0.255
Parallel strain*	F(6,90)=10.662 **p<0.001**	F(2,90)=0.238 p=0.789	F(10,90)=0.795 p=0.633
Perpendicular strain*	F(6,90)=5.391 **p<0.001**	F(2,90)=3.223 **p=0.044**	F(10,90)=1.256 p=0.268
Parallel Young's modulus*	F(6,90)=3.045 **p=0.009**	F(2,90)=12.039 **p<0.001**	F(10,90)=2.346 **p=0.016**
Perpendicular Young's modulus*	F(6,90)=3.220 **p=0.007**	F(2,90)=10.904 **p<0.001**	F(10,90)=1.658 p=0.103

*Assumption of homogeneity of variance is violated as tested with the Levene's test with p<0.05

Table S.3.17 Nutralys F85M-WG one-way ANOVA for effect of mixing time for different hydration times.

	90 min	170 min	250 min
Parallel stress	F(6,34)=3.117 **p=0.015***	F(6,32)=2.833 **p=0.025***	F(4,29)=6.354 **p=0.001**
Perpendicular stress	F(6,34)=2.198 p=0.067*	F(6,32)=3.340 **p=0.011***	F(4,29)=1.668 p=0.190*
Parallel strain	F(6,34)=3.403 **p=0.010***	F(6,32)=3.988 **p=0.004***	F(4,29)=7.185 **p<0.001***
Perpendicular strain	F(6,34)=4.039 **p=0.004**	F(6,32)=4.651 **p=0.002**	F(4,29)=1.467 p=0.243
Parallel Young's modulus	F(6,34)=3.824 **p=0.005**	F(6,32)=1.691 p=0.155*	F(4,29)=2.169 p=0.103
Perpendicular Young's modulus	F(6,34)=2.497 **p=0.041**	F(6,32)=2.088 p=0.082*	F(4,29)=2.259 p=0.093

*Assumption of homogeneity of variance is violated as tested with the Levene's test with p<0.05

Table S.3.18 Homogeneous subsets for Nutralys F85M-WG at a hydration time of 90 min. tensile test parameters for which mixing time had a significant effect with a Tukey HSD test at significance level p<0.05.

	Parallel stress*	Parallel strain*	Perpendicular strain	Parallel Young's modulus	Perpendicular Young's modulus
Control	a,b	a,b	a,b	b	a,b
2 min	a,b	a,b	a,b	a,b	a
4 min	a,b	b	b	a	a,b
5 min	b	a,b	a,b	a,b	a,b
7 min	a,b	a,b	b	a,b	a,b
10 min	a	a,b	a	a,b	b
30 min	a	a	a,b	a,b	a,b

*Assumption of homogeneity of variance is violated as tested with the Levene's test with p<0.05

Table S.3.19 Homogeneous subsets for Nutralys F85M-WG at a hydration time of 170 min. tensile test parameters for which mixing time had a significant effect with a Tukey HSD test at significance level p<0.05.

	Parallel stress*	Perpendicular stress*	Parallel strain*	Perpendicular strain
Control	a	a	a	a,b
2 min	a	b	a,b	c
4 min	a	a,b	b	b,c
5 min	a	a,b	b	a,b,c
7 min	a	a,b	b	b,c
10 min	a	a,b	a,b	b,c
30 min	a	a	a,b	a

*Assumption of homogeneity of variance is violated as tested with the Levene's test with p<0.05

Table S.3.20 Homogeneous subsets for Nutralys F85M-WG at a hydration time of 250 min. tensile test parameters for which mixing time had a significant effect with a Tukey HSD test at significance level p<0.05. Products sheared for 10 or 30 minutes were too fragile to measure and were not included.

	Parallel stress	**Parallel strain***
Control	a	a
2 min	b	b,c
4 min	b	c
5 min	a,b	b,c
7 min	a,b	a,b
10 min	-	-
30 min	-	-

*Assumption of homogeneity of variance is violated as tested with the Levene's test with $p<0.05$

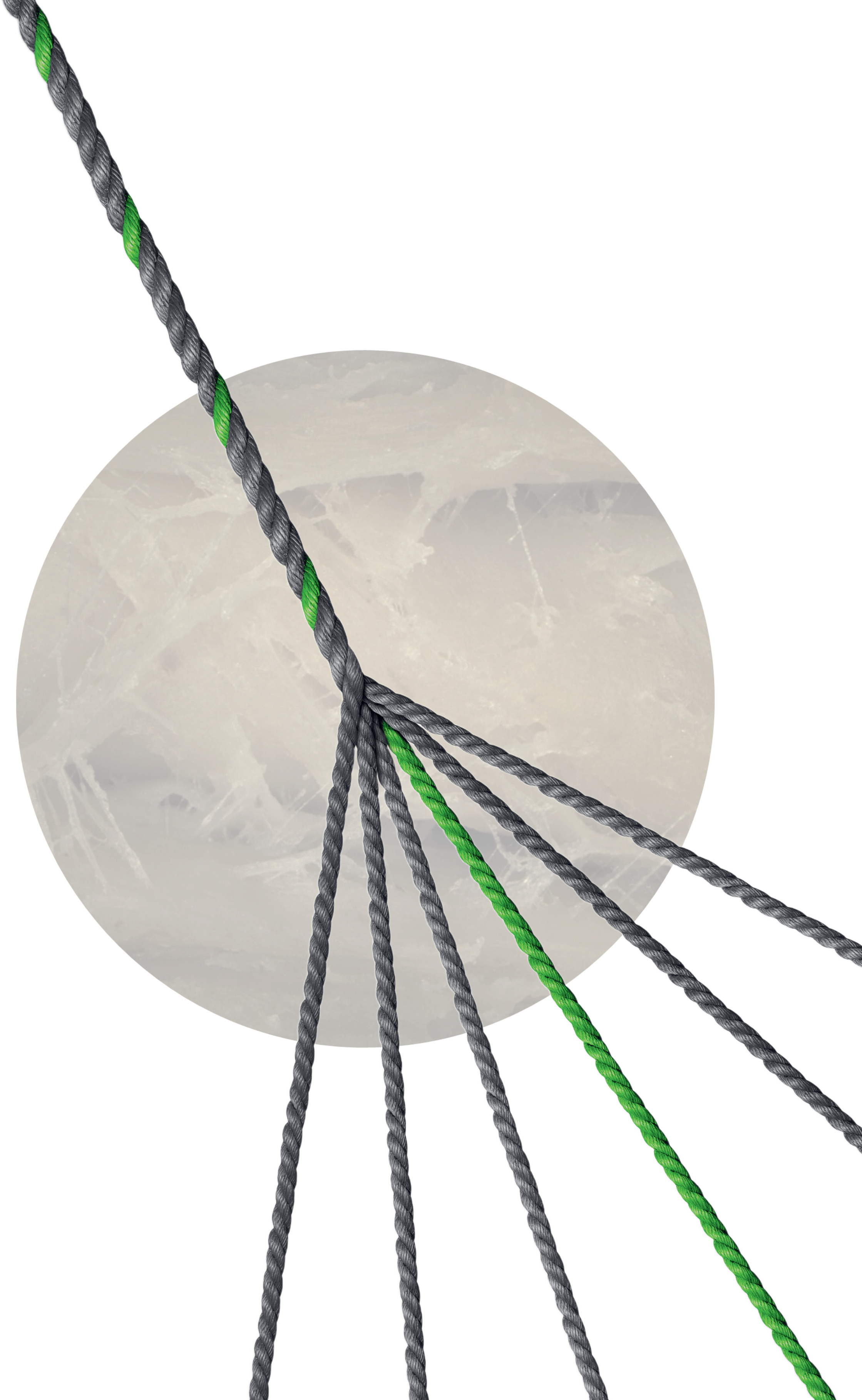

Chapter 4

Near-infrared spectroscopy-based quantification of sunflower oil and pea protein isolate in dense mixtures for novel plant-based products

This chapter has been published as Köllmann, N., Schreuders, F. K. G., Mishra, P., Zhang, L., & der Goot, A. J. van. (2023). Near-infrared spectroscopy-based quantification of sunflower oil and pea protein isolate in dense mixtures for novel plant-based products. *Journal of Food Composition and Analysis*, *121*, 105414.

4.1 Abstract

Techniques to quantify oil and protein in plant-based products are laborious and environmentally harmful. This study explores the potential of near-infrared (NIR) spectroscopy as an alternative method for rapid and non-destructive quantification of oil and protein in mixtures with known content of sunflower oil and pea protein isolate (PPI). Accurate calibrations with partial least square regression (PLSR) were possible for sunflower oil (Root Mean Standard Error of the Test (RMSET) set, 0.33%; coefficient of determination of the test set (R^2_t), 0.99) and PPI content (RMSET, 1.24%; R^2_t, 0.99). Prediction of an extrapolated validation set was less accurate for sunflower oil (Root Mean Standard Error of the Validation (RMSEV) set, 2.65%; coefficient of determination of the validation set (R^2_v), 0.70), but was successful for PPI content (RMSEV, 2.43%; R^2_v, 0.93). Wavelength range reduction for CH/NH bonds improved the predictions of the PLSR models for oil but not for PPI. Wavelength selection using the Covariance Selection (CovSel) algorithm reduced the number of wavelengths from 2151 to 3 without loss of prediction accuracy within the calibration range. Wavelength range reduction gave the best model for oil; wavelength selection was best for PPI. NIR spectroscopy is a promising tool to determine oil and protein in plant-based foods rapidly and with sufficient accuracy.

4.2 Introduction

There has been increasing demand for plant-based products in the past 5 years (Good Food Institute, 2022). Consumers want to reduce their consumption of animal-based products for health and environmental reasons (Atta-Delgado et al., 2023; Cheah et al., 2020). Replacement of animal-based products is thought to be facilitated by plant-based products that are similar in texture and taste to the animal-product they intend to replace (Jaeger et al., 2023; Michel et al., 2021). Protein and oil are important contributors to the sensory and the nutritional profile of these new plant-based products (Kyriakopoulou et al., 2021). However, it is not easy to obtain the desired levels of oil in those products with a concentrated protein matrix. For example, it has been reported that oil is expelled from the protein matrix if more than 4–5 wt.% oil is added before or during extrusion of meat analogues (Cheftel et al., 1992; Kendler et al., 2021). Thus, the oil content in the final product might differ from the amount added, making analysis of the oil and protein levels in dense plant-based products of special interest.

Current measurement techniques for oil and protein content are laborious, require many samples and large sample amounts, and are hazardous and environmentally harmful (Pallone et al., 2018; Prevolnik et al., 2011; Tøgersen et al., 2003). Organic solvent extraction is the traditional method of determining oil content in meat and meat analogues. The official Soxhlet extraction method recommended by the AOAC (Townshend, 1987) is widely used for determining oil content in food products. However, previously, we found that some oil remains encapsulated in the food matrix at the end of the extraction process (Berghout et al., 2014), making accurate analysis of the oil content difficult. Similarly, the analysis of protein content in the food matrix is also not straightforward; the protein content measured is dependent on the method used. Amino acid analysis gives the most accurate results, because it is least affected by non-protein components in the sample (Mæhre et al., 2018). However, the cost of this method is high. For this reason, the most frequently used methods for protein determination are based on the total nitrogen content of the sample: Kjeldahl's method and the Dumas method (Mæhre et al., 2018; McClements et al., 2021).

Near-infrared (NIR) spectroscopy has the potential to quantify the oil and protein content in plant-based products non-destructively. It is a rapid, low-cost, non-destructive, accurate, and reliable method, requires minimal or no sample preparation before analysis, and can analyse multiple attributes simultaneously (Klaypradit et al., 2011; Stubbs et al., 2010; Wu et al., 2008). Oil, protein, and moisture can be identified through the overtones and combinations related to CH, NH, and OH bonds captured in the NIR range of the electromagnetic spectrum (Osborne, 2000). NIR spectroscopy has already been applied to protein ingredients commonly used in plant-based products, such as soy, pea, and gluten (Aykas et al., 2020; Cai, 2017; Hughes et al., 2001; Mourya et al., 2016; Sato et al., 2002), and is therefore expected to be a suitable technique for the measurement of oil and protein content in plant-based products. Furthermore, NIR spectroscopy has been applied to measure the fat and protein content of different types of meat, fish and cheese (Ayvaz et al., 2021; Dixit & Reis, 2023; Goi et al., 2022; Kucha et al., 2022; Mishra et al., 2021; Reis et al., 2022). However, to the best of our knowledge, NIR spectroscopy has been used only for texturized vegetable proteins (TVPs) (Squeo et al., 2022), not yet for dense plant-based products that have a higher water content.

NIR spectroscopy data are multivariate in nature with several peaks overlapping (Pasquini, 2018). Chemometric modelling is therefore used to resolve the broad peaks in NIR spectra (Pasquini, 2018). Latent variable (LV) extraction methods are often used to extract the relevant chemical components to perform tasks such as regression and classification. Partial least squares regression (PLSR) is commonly used for this (Wold et al., 2001). In addition to the extraction of LVs from the complete spectrum, the use of a reduced wavelength range or specifically selected wavelengths further simplifies and improves the measurement and calibration model. Reduction of the wavelength range or the number of variables results in better prediction because the effect of irrelevant noise on the model is reduced (Barbin et al., 2013; Z. Wang et al., 2022). Variable selection is used to identify which specific wavelengths are important for analysis. The use of a reduced number of wavelengths increases the speed of the analysis, which is relevant when using NIR for inline or online measurements. In this study, wavelength selection was done using the covariates selection (CovSel) approach (Roger et al., 2011).

In the present work, dense sunflower oil/pea protein isolate (PPI)/water mixtures were used as a simplified model mixture for dense plant-based products. NIR spectroscopy was used to determine the content of sunflower oil and PPI in these mixtures. Models based on the 1st and 2nd CH overtones and 1st and 2nd NH overtones in the NIR region were separately developed for the prediction of the sunflower oil and PPI content, respectively. To do this, data were analysed by PLSR. Variable selection with the CovSel approach was used to identify the most significant wavelengths that explain the sunflower oil and PPI prediction in the mixtures. Finally, the most important factors that need to be considered before applying NIR spectroscopy to processed plant-based products will be discussed.

4.3 Materials and methods

4.3.1 Materials

Pea protein isolate (PPI) (NUTRALYS S85F) was obtained from Roquette Frères S.A., (Lestrem, France). PPI had a dry matter content of 93.6 wt.% and consisted of 74.7 wt.% protein (N × 5.58) on a dry matter basis. Sunflower oil (Albert Heijn, Zaandam, the Netherlands) was purchased from a local supermarket. Before use, the sunflower oil was stored at room temperature in a closed cabinet for 9 months. According to the supplier, the sunflower oil contained 10% saturated and 82% unsaturated fats.

4.3.2 Sample preparation

To construct the sunflower oil calibration curve, dispersions of sunflower oil (0–10 wt.%) and PPI (40 wt.% on a dry weight basis) in water (50–60 wt.%) were manually mixed until visually homogeneous. The ingredients were added to the mixture in the following order before mixing: PPI, water, sunflower oil. Water was replaced by sunflower oil in steps of 1 wt.%. In addition, seven dispersions of sunflower oil (5 wt.%) and 30–60 wt.% PPI in water (35–65 wt.%) were prepared for the PPI calibration curve. Water was replaced by PPI in steps of 5 wt.%. Finally, a validation set was prepared with eight different dispersions of 30–55.6 wt.% PPI and 0–10 wt.% sunflower oil in 35.9-65 wt.% water. The validation set was based on an inscribed Central Composite Design (Ranade & Thiagarajan, 2017) with 30%–60% as limits for PPI content and 0%–10% for sunflower oil content. The extreme point with a PPI content of 60%, sunflower oil content of 5% and water content 35% was not used, because it was not possible to obtain a homogeneous mixture with this composition. Fig. 4.1 gives an overview of the mixture composition as it was weighed and rounded off to one decimal place. Unrounded numbers were used for all subsequent analyses.

The mixtures were then hydrated for 30 min. All mixtures were divided into three different cups with an internal diameter of 2.7 cm and a height of 1.5 cm until they were filled. The samples were slightly compressed to ensure a smooth surface and reduce air in the sample cup. Before measurement, the mixtures were stored in closed zip-lock bags to prevent evaporation of moisture.

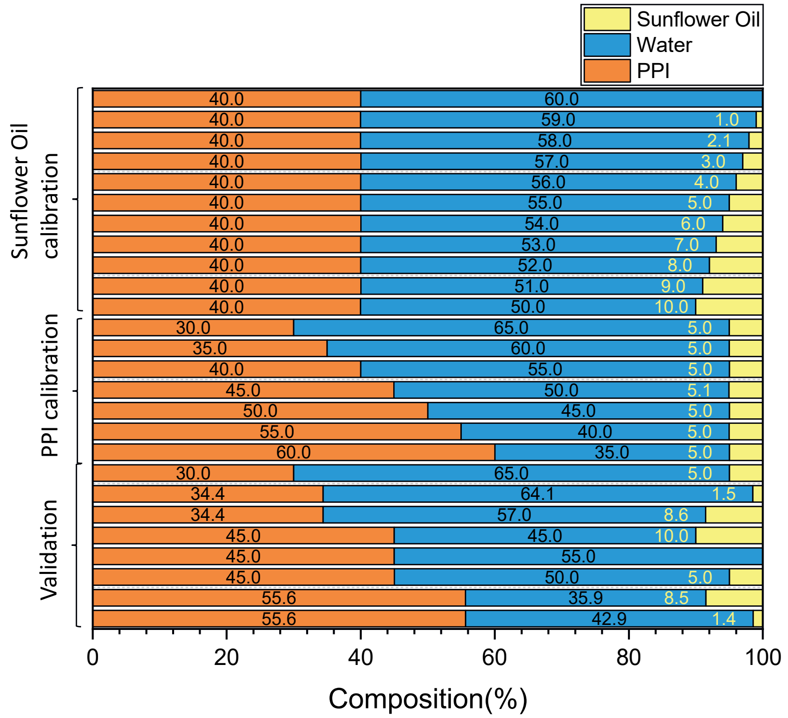

Fig. 4.1 Composition of the mixtures used for sunflower oil calibration, PPI calibration and validation based on weight.

4.3.3 NIR spectroscopy measurements

Near-infrared (NIR) spectral measurements were performed using a Hi-Res, ASD LabSpec spectrometer (Malvern Panalytical, Malvern, UK). The measurements were performed using an area scan probe (Hi-Brite probe) with a spot size of 10 mm. The probe was placed in a tripod and positioned above the sample as close as possible without touching the mixtures. The probe has an in-built 6.5 W halogen light source for illumination and optical fibres were used to capture the reflected light. The instrument was controlled using the Indico Pro software (Malvern Panalytical, Malvern, UK). The integration time was optimized automatically by the Indico Pro software and was set at 15 ms. The Indico Pro software automatically provided the average of ~5 consecutive measurements and radiometric calibration with white and dark references.

4.3.4 Spectral pre-processing

Several pre-processing steps were applied to the reflectance spectra before regression modelling. First, the reflectance was converted to absorbance. Scattering in the NIR reflectance spectra was reduced using standard normal variate (SNV) correction. In SNV correction, each spectrum is centred and divided by its standard deviation, resulting in a common scale for all spectra (Barnes et al., 1989). The spectra were smoothened using the Savitzky-Golay (SAVGOL) algorithm (Savitzky & Golay, 1964) and the 1st derivative was estimated to reveal underlying peaks. A window size of 31 was used for smoothening. Covariates selection (CovSel) was applied to the raw reflectance spectra.

4.3.5 PLSR modelling

Partial least square regression (PLSR) is a commonly used chemometric technique for interpretation of NIR spectral data (Wold et al., 2001). PLSR deals with the multi-co-linearity in the multivariate signal by extracting the underlying peaks to find the inherent latent variables (LVs). PLSR starts by extracting a set of new variables (known as scores), which are based on the projection of the data into the direction of LVs. Because of this, the LVs have maximum covariance with the response variables. In the present work, PLSR was implemented with MATLAB's default plsregress function. For each mixture composition, the spectra of two of the sample cups were used to prepare the calibration curves and one sample cup was used as a test set. The calibration set consisted of $2 \times 11 = 22$ samples for sunflower oil content and $2 \times 7 = 14$ samples for PPI content. A default leave-one-out cross-validation approach was integrated to optimize the LVs. The LVs were then selected by identifying the inflection point. Figs. S.4.1 and S.4.2 show the LV selection results.

4.3.6 Variable selection with CovSel

The CovSel method is a popular chemometric technique for filtering important wavelengths (Roger et al., 2011). The CovSel algorithm performs wavelength selection by iterating two steps. The first step is a search for the variable index that is closest to the response variables. As a second step, the selected wavelength is removed from the predictor and response matrix using orthogonal projection. The process is then repeated for a specified number of wavelengths. The resulting explained variation plotted as a function of the wavelengths extracted was used to decide on the optimal number of variables. Our CovSel implementation was performed using code developed in-house (Roger et al., 2011). CovSel was applied to the raw reflectance spectra without pre-processing to ensure rapid analysis in real-life applications. Once the wavelengths were selected, multiple linear regression, implemented using the plsregress function in MATLAB, was run to achieve the final calibration model.

4.3.7 Data analysis

All data analysis was performed using MATLAB 2019b (Natick, WA, USA). The analysis was a combination of in-built functions from MATLAB's toolboxes and in-house code. The calibration and prediction results were analysed in terms of the root mean standard error of calibration (RMSEC), root mean standard error of the test set (RMSET), regression coefficient of calibration ($R^2{}_c$) and regression coefficient of the test set ($R^2{}_t$). The extrapolation of the model was analysed in terms of the root mean standard error of validation (RMSEV) and the regression coefficient ($R^2{}_v$) estimated on a new independent validation set generated in a new experiment.

4.4 Results and discussion

4.4.1 PLSR calibration for prediction of sunflower oil content

Fig. 4.2 shows the mean spectral profiles of the mixtures that were used for the sunflower oil calibration curve in the complete visible and near-infrared (NIR) spectrum (350–2500 nm), in the 1st CH overtone region (1600–1800 nm) and in the 2nd CH overtone region (1100–1250 nm). These mixtures had increasing sunflower oil content (0–10 wt.%) and decreasing water content (60–50 wt.%) but had a constant pea protein isolate (PPI) content (40 wt.%). All sunflower oil calibration mixtures exhibited similarities in spectral absorbance patterns with differences in the magnitude of absorbance throughout the NIR range (350–2500 nm). The differences observed in spectral absorbance of the mixtures are related to the changes in the composition (0–10 wt.% sunflower oil and 60–50 wt.% water). The absorbance in the oil overtones region increased as the sunflower oil content increased. This indicates increased absorption of NIR radiation by the sunflower oil. For this reason, the spectral data were considered suitable for further analysis using partial least square regression (PLSR). The change in absorbance is linked to the overtones and stretching of the CH bonds present in oil (Brøndum et al., 2000; Cozzolino & Murray, 2004; Ding & Xu, 2000; Hoving-Bolink et al., 2005; Skibsted et al., 2005).

The absorption in the 1st overtone region of the OH bonds (1400–1500 nm) (Shaw & Mantsch, 2006) decreased with increasing sunflower oil content (Fig. S.4.3). The oil content and water content in the samples were inversely correlated. The decreased absorption with an increasing water content therefore indicated an increased adsorption by the water in the sample. However, this effect is not clearly visible in the 2nd overtone region of the OH bonds (950–1100 nm) (Shaw & Mantsch, 2006).

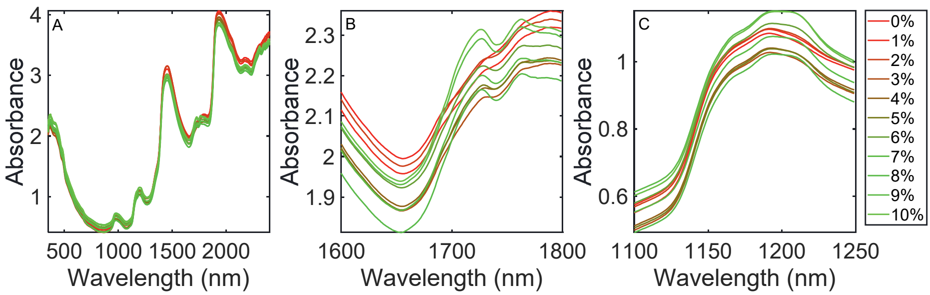

Fig. 4.2 Average spectral profiles of the meat analogue mixes. The sunflower oil content in the mixes is indicated with colours ranging from red to green. (A) Complete spectra, (B) 1st overtones region for CH bonds (1600–1800 nm), and (C) 2nd overtones region for CH bonds (1100–1250 nm).

A PLSR model for the content of sunflower oil was constructed based on the complete visible and NIR range (350–2500 nm), based on the range of the 1st CH overtone (1600–1800 nm) and the 2nd CH overtone (1100–1250 nm). Fig. 4.3 shows the fit of the PLSR models. The regression coefficient of calibration (R^2_c) and regression coefficient of the test set (R^2_t) of these models were 0.99–1.00 for the different wavelength ranges. This indicates that the models have a similar quality when comparing the model outcomes with the measurement of oil content in plant-based or animal products (Aykas et al., 2020; Dixit & Reis, 2023; Fowler et al., 2021; Squeo et al., 2022). However, R^2 depends on the variance of the dataset used, which makes direct comparison of the models based on different datasets complicated (Kjeldahl & Bro, 2010). In this study, we were able to control the distribution of the sample compositions, which distinguishes this approach from studies using products with biological variation such as meat or fish.

The selection of a narrower wavelength range allowed an improved prediction of the sunflower oil content in the mixtures in the test set. The root mean standard error of the test set (RMSET) of the models based on the 1st (0.19%) and 2nd (0.11%) overtones were lower compared with the RMSET of the model based on the complete spectrum (0.33%). In addition, the necessary number of latent variables (LVs) was lower for the models based on the overtone regions (6 or 4 instead of 9 LVs). Models based on the 1st and 2nd overtones could also predict the values for the extrapolated validation set rather well, with the models on the 2nd overtone giving best predictions (root mean standard error of validation (RMSEV) 1.31% 1st overtones and 0.92% 2nd overtones). The spread of the predicted sunflower oil

4

content of samples in the external validation set with the same sunflower oil content was larger than that of the predictions of the calibration and test set samples. This can be explained by the different PPI and water contents in the validation set compared with the calibration set. Wavelength range reduction for the 1st and 2nd overtone regions of the CH bonds reduced the spread of the sunflower oil content predictions for both the calibration and test sets and the external validation set.

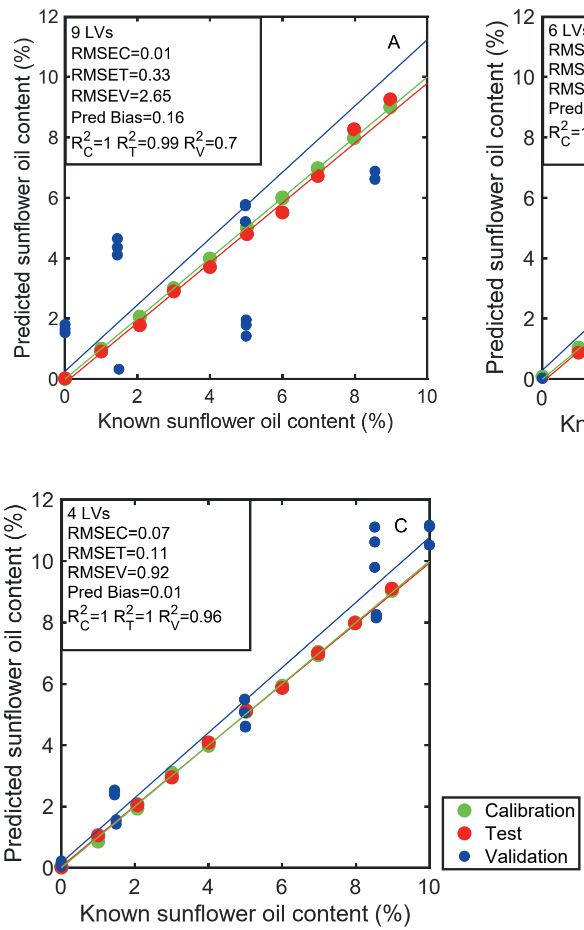

Fig. 4.3 PLSR calibration of sunflower oil content for different spectral ranges. (A) Complete visible and NIR spectroscopy (350–2500 nm) spectra, (B) 1st overtones region for CH bonds (1600–1800 nm), and (C) 2nd overtones region for CH bonds (1100–1250 nm). The points in green are the calibration set, points in red are the test set and points in blue are the validation set.

Fig. 4.4 shows the regression coefficients of the PLSR models for sunflower oil content based on the complete spectrum and the 1st and 2nd overtone regions. The regression coefficients of PLSR models show which wavelengths contributed most to the prediction. From the regression coefficients obtained for the model based on the complete spectrum, we concluded that the 1st and 2nd overtones are indeed important wavelength ranges for the prediction of the sunflower oil content in these mixtures. However, the wavelengths in the combination region of the spectrum (2200–2500 nm) also contributed to the regression coefficient of the entire spectrum. This was not considered as a separate wavelength range because of the weaker signal in the combination region of the spectrum compared with the overtone regions (Ozaki & Morisawa, 2021).

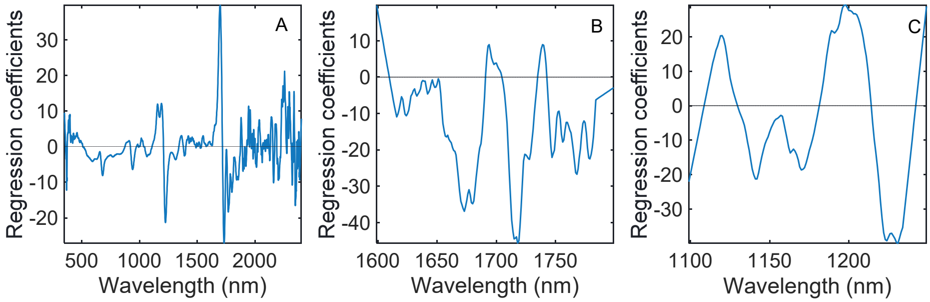

Fig. 4.4 Regression coefficients from PLSR calibration for different spectral ranges. (A) Complete visible and NIR spectroscopy (350–2500 nm) spectra, (B) 1st overtones region for CH bonds (1600–1800 nm), and (C) 2nd overtones region for CH bonds (1100–1250 nm).

4.4.2 PLSR calibration for PPI content

The mean spectra of the mixtures with varying PPI content had peaks at the same positions as the spectra measured for mixtures with different sunflower oil content. However, Fig. 4.5 shows the intensity of absorbance varied more with changes in PPI content compared with the spectra for sunflower oil content (Fig. 4.2). This was most likely caused by the larger variation in composition of the mixtures within the PPI calibration set compared with the sunflower oil calibration set. The absorption in the NH overtones decreased as the PPI content increased, which was not expected. This decreased absorption was possibly related to the decreasing water content (65–35 wt.%) of mixtures with increasing PPI content (30–60 wt.%), which might have overshadowed the absorption by the PPI. The overtones of the OH and NH bonds lie in the same wavelength region (Shaw & Mantsch, 2006), which explains this effect. Similarly, Barbin et al. (2013) reported that the effect of NH stretching was indeed suppressed by water when applying NIR to measure the composition of pork.

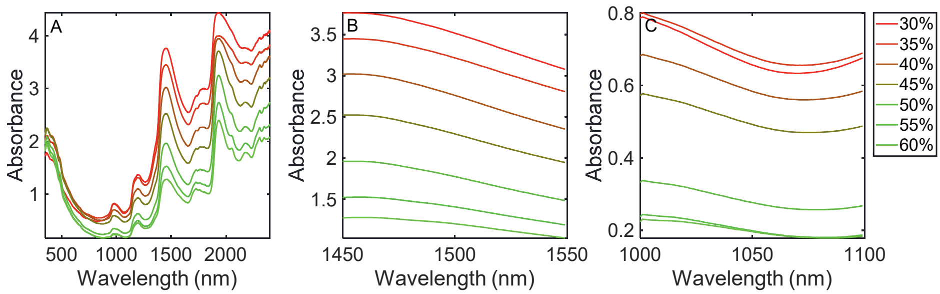

Fig. 4.5 Spectral profiles of the meat analogue mixes. The initial PPI content in the mixes is indicated with colours ranging from red to green. (A) Complete spectra, (B) 1st overtones region for NH bonds (1450–1550 nm), and (C) 2nd overtones region for NH bonds (1000–1100 nm).

Just like the PLSR models for the sunflower oil content, PLSR models for the PPI content of the PPI calibration dataset were constructed based on the complete spectrum (350–2500 nm), on the 1st NH overtones (1450–1550 nm) and on the 2nd NH overtones (1000–1100 nm). Fig. 4.6 shows the R^2_t of these models was 0.99, indicating that the quality of the calibration models for the PPI content and sunflower oil content was similar. R^2_t indicates that the performance of our models was similar to that in earlier research in which NIR spectroscopy was used to the determine the protein content of soybeans, texturized vegetable proteins (TVPs) or pork (Aykas et al., 2020; Barbin et al., 2013; Mishra et al., 2021; Squeo et al., 2022). However, as discussed in Section 4.4.1, our products with a pre-defined composition have a more controlled variation than real-life products, which hinders exact comparison of the models.

Reduction of the wavelength range only improved the prediction of the PPI content when the 2nd overtone region of the NH bond was used (RMSET 0.94% instead of 1.24%) and decreased the model quality when the PLSR model was based on the 1st overtones (RMSET 3.43%). The PPI content of the external validation set was better predicted by the PLSR model based on the complete wavelength range compared with the PLSR model based on the 1st and 2nd overtone ranges (RMSEV 2.43% compared with 5.43% or 2.86%). The predicted PPI content of the samples in the external validation set had a larger spread compared to the calibration and test set samples, especially at a PPI content of 35%. This can be explained by the different sunflower oil and water contents of these samples compared to the calibration set. A reduction of the wavelength range did not reduce this spread in the predicted PPI content. This indicates that wavelength range reduction for PPI was a less successful approach than for sunflower oil. However, it was found that only 3 LVs instead of 5 or 8 were necessary to construct the PLSR model based on the 2nd overtone region. In addition, the prediction bias of the 2nd overtone model was the lowest (−0.12 compared with 0.38 or 1.91). This means that wavelength range selection is still beneficial.

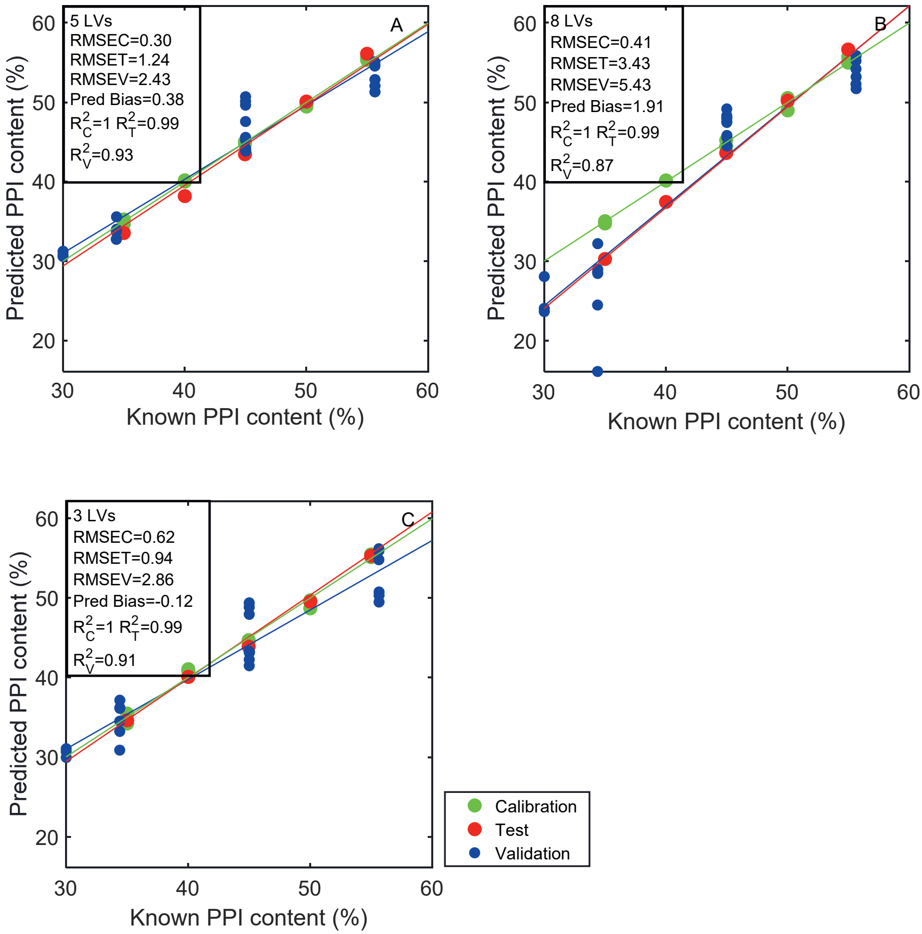

Fig. 4.6 PLSR calibration of PPI content for different spectral ranges. (A) Complete visible and NIR spectroscopy (350–2500 nm) spectra, (B) 1st overtones region for NH bonds (1450–1550 nm), and (C) 2nd overtones region for NH bonds (1000–1100 nm). The points in green are the calibration set, points in red are the test set and points in blue are the validation set.

Fig. 4.7 shows the regression coefficient of the PLSR model based on the complete spectral range. Some of the main wavelengths on which the prediction is based (458, 499, 2036 and >2300 nm) are not in the NH overtone regions, which explains why the models based on the 1st overtones performed worse than the model based on the complete spectrum. Even though the important wavelengths in the complete spectrum were not directly associated with NH overtones, wavelengths >2300 nm have been reported previously as a part of the wavelengths that are predictive for protein content of wheat (Chen et al., 2018; Ranzan et al., 2015) or lamb (Pu et al., 2014).

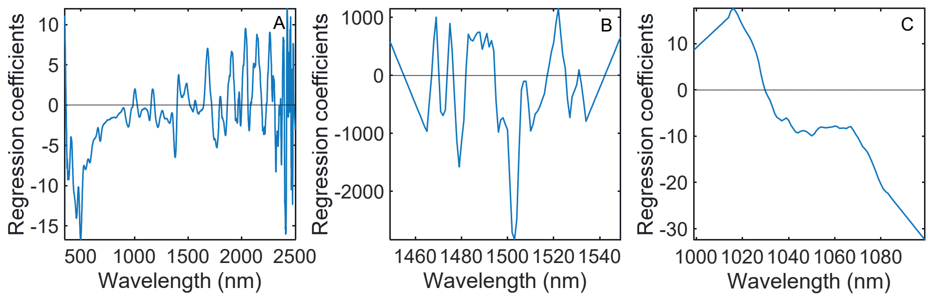

Fig. 4.7 Regression coefficients from PLSR calibration of PPI content for different spectral ranges. (A) Complete visible and NIR spectroscopy (350–2500 nm) spectra, (B) 1st overtones region for NH bonds (1450–1550 nm), and (C) 2nd overtones region for NH bonds (1000–1100 nm).

4.4.3 Selecting key features for predicting sunflower oil and PPI content

The CovSel approach was applied to reduce the complexity of the model by identifying key wavelengths. The wavelengths selected by the algorithm allow the development of low-cost spectral sensors, thereby increasing the speed of both the measurement and the processing time of the PLSR model. This simplification is beneficial when NIR is used for quality control in a food production environment. Figs. 4.8 and 4.9 show the results for the application of covariates selection (CovSel) for the prediction of sunflower oil and PPI content, respectively. Application of CovSel showed that only 3 wavelengths instead of the 2151 in the complete wavelength range were sufficient to adequately predict the sunflower oil or PPI content of the mixtures, implying a complexity reduction of 717 times. The RMSET of the prediction of the sunflower oil content slightly decreased after wavelength selection (from 0.33% to 0.29%) (Fig. 4.3A and Fig. 4.8C) compared with the PLSR model based on the complete spectral range. However, the PLSR models based on the CH overtones performed better (RMSET 0.19% and 0.11%) compared with the model based on the selected wavelengths. Selection of a wavelength range was therefore a more successful approach to reduce model complexity for sunflower oil content prediction. Furthermore, the prediction of the sunflower oil content in the validation set worsened after wavelength selection (RMSEV 3.55% instead of 2.65%). This indicates that the simplification of the model for sunflower oil content by wavelength selection reduces its applicability to samples outside the calibration range.

For quantification of the PPI content, wavelength reduction with the CovSel approach led to an increased RMSET for all spectral regions investigated (0.89% instead of 1.24%, 3.43% or 0.94%). Furthermore, the prediction of the PPI content of the validation set improved slightly after the use of CovSel (RMSEV 1.45% instead of 2.43%, 5.43% or 2.86%). The CovSel approach was therefore beneficial for the accuracy of the prediction of PPI content.

The positive effect of wavelength selection on PLSR models has been described previously by many other authors. Generally, it was found that the influence of noise and interfering factors was reduced when selecting variables specifically linked to the component of interest (Barbin et al., 2013; Z. Wang et al., 2022). The high quality of the PLSR models for sunflower oil content based on the CH overtones indicates that wavelength range reduction successfully reduced the influence of interfering factors. This could explain why wavelength selection with CovSel did not result in a further improvement of the model, compared to wavelength range reduction. However, for PPI content wavelength range reduction was less successful. This was caused by the large influence of the water content on the absorbance in the NH overtone regions of the NIR spectrum (Fig. 4.5). This might explain why the application of CovSel improved the prediction of PPI content compared with the models based on the NH overtones.

In this study, the CovSel approach was applied to the raw reflectance data to ensure rapid analysis during real-life application and to be able to identify the key wavelengths in the reflectance data. However, pre-processing of the NIR spectra could reveal the underlying peaks in the spectral data. The effect of pre-processing on our PLSR models and the models after wavelength selection is shown in Tables S.4.1, S.4.2, S.4.3 and S.4.4.

The application of CovSel facilitates the use of NIR spectroscopy for quality control during the production of plant-based products. Inline use of NIR has already been successfully applied for cereal extrusion (Dodds & Heath, 2005; Evans et al., 1999). Inline measurements are only feasible for use in industry when the scanning of the sample is fast enough, and the probe is affordable. Fast measurements can be achieved through the application of monochromators, but those can only be applied when sufficient information can be extracted when measuring a small wavelength range. Wavelength selection is therefore an important tool to improve online use of this technique (Dodds & Heath, 2005). In this study, we showed that models based only 3 wavelengths already predicted the content of sunflower oil and PPI reasonably well, which means NIR has strong potential as an inline measurement method during the production of plant-based products.

Figs. 4.8B and 4.9B show the most important wavelengths related to sunflower oil and PPI content. Remarkably, the wavelengths around 1211 nm that were selected here were also found to be important for the prediction of fat content in minced pork (1211 nm) (Barbin et al., 2013) and lamb (1212 nm) (Fowler et al., 2021; Pu et al., 2014). Apparently, this wavelength is very strongly linked to the oil content in different matrices. We did not find such a characteristic wavelength in previous studies that reported on protein content.

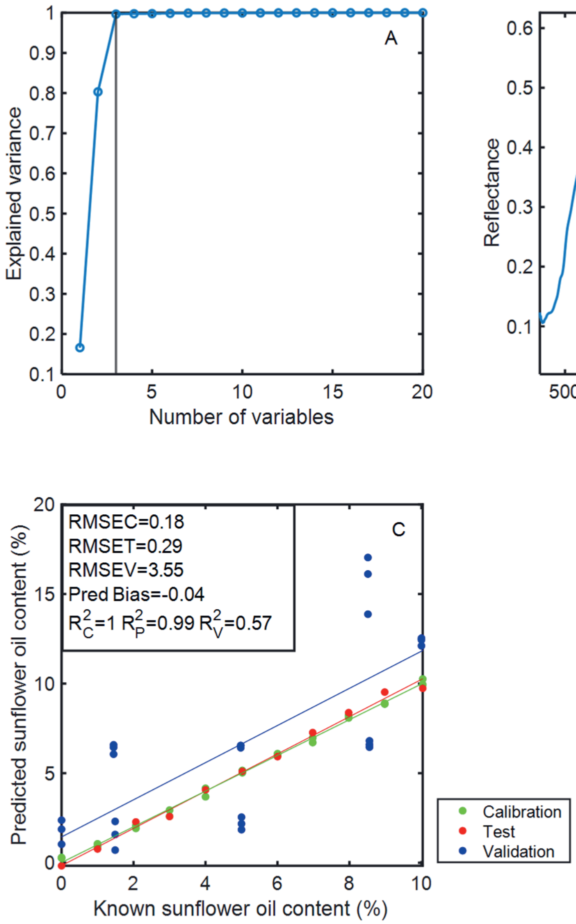

Fig. 4.7 CovSel variable selection and calibration models with the selected variables for the sunflower oil content. CovSel variable selection and calibration models with the selected variables. (A) Selection of the necessary number of wavelengths, (B) selected wavelengths plotted with the average spectrum of all samples in the sunflower oil calibration set. (C) The calibration plot with the selected wavelengths obtained in (A) and (B) with the calibration (green), test (red) and validation (blue) sets.

4

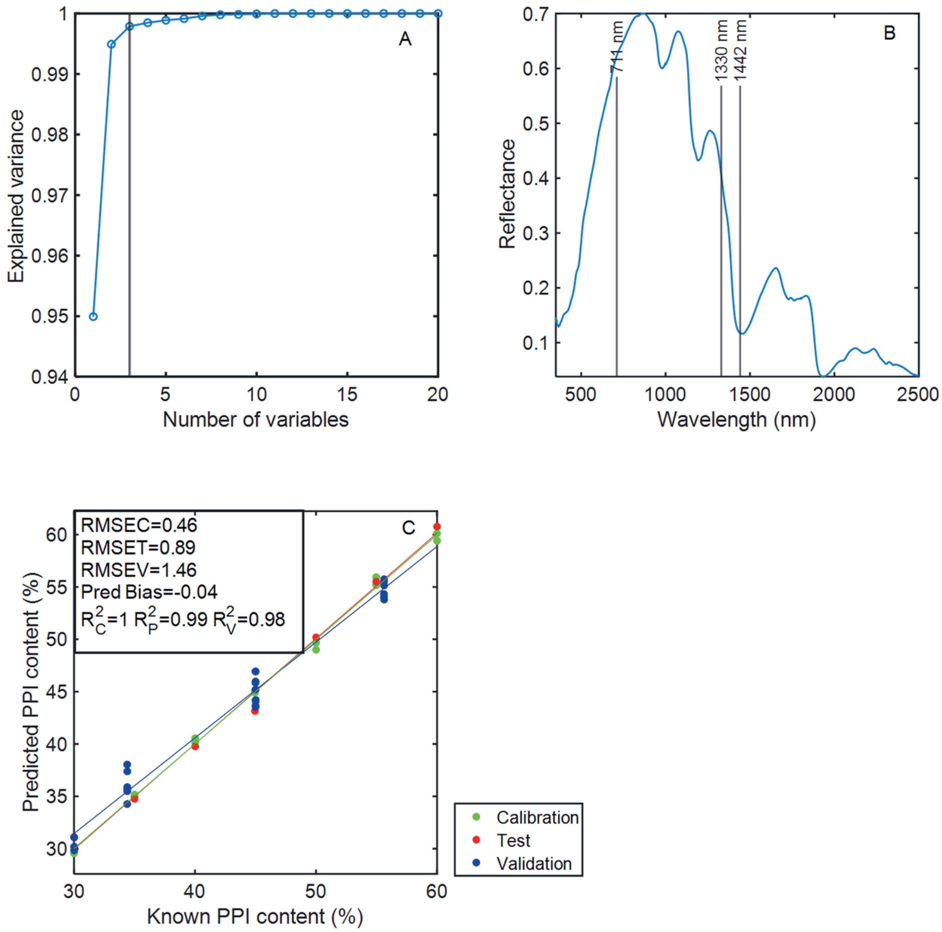

Fig. 4.8 CovSel variable selection and calibration models with the selected variables for the pea protein isolate (PPI) content. CovSel variable selection and calibration models with the selected variables. (A) Selection of the necessary number of wavelengths, (B) selected wavelengths plotted with the average spectrum of all samples in the PPI calibration set. (C) The calibration plot with the selected wavelengths obtained in (A) and (B) with the calibration (green), test (red) and validation (blue) sets.

4.4.4 Perspectives for the use of NIR spectroscopy for the compositional measurement of plant-based foods

In this study, we showed that NIR spectroscopy can be used to measure the sunflower oil and PPI content of simple sunflower oil/PPI/water model mixtures. However, commercial plant-based products have a more complex composition and texture compared to these simple mixtures. Before NIR spectroscopy can be applied to dense plant-based products such as meat analogues, several factors should be considered.

First, only one source of oil (sunflower) and one protein ingredient (PPI) were studied. Most likely, calibration curves need to be constructed for different protein sources, because the visible part of the vis-NIR spectrum is affected by the protein source of pulse flours (Sivakumar et al., 2022). Furthermore, commercial plant-based products have a more complex composition compared to the three-component mixtures studied here. Meat analogues for example also contain flavourings, binding agents, and colouring agents (Kyriakopoulou et al., 2021). These additional ingredients could influence the vis-NIR spectra and should therefore be included when a calibration curve for the final product is created. It is well known that the robustness of NIR spectroscopy is low with changes in temperature, sample composition and the physical structure of the sample. This means calibration models need to be updated regularly (Zeaiter et al., 2006). Several methods to facilitate updating of the calibration models and reduce the need for re-calibration have been explored (Mishra & Nikzad-Langerodi, 2021; Zeaiter et al., 2006), but it remains one of the main limitations of the use of NIR spectroscopy.

Second, the simple mixtures that were measured in this study were not heated, unlike meat analogues. Thermal treatment is known to affect the NIR spectra to a large extent, and NIR spectroscopy has even been used to measure the temperature during heat treatment of animal products (O'Farrell et al., 2011; Skåra et al., 2014; Uddin et al., 2006; Wold et al., 2020). The effect of thermal treatment on these products remained measurable after they cooled down (Uddin et al., 2006; Skåra et al., 2014). The effect of thermal treatment on the NIR spectra is caused by differences in the hydrogen-bonded water structure (Büning-Pfaue, 2003). This causes a shift in the absorption bands of water (Wold et al., 2020). Furthermore, changes in protein confirmation due to thermal denaturation can also result in changes in the NIR spectra (Uddin et al., 2002). Therefore, the PLSR models prepared in this study cannot be used directly for final meat analogue products. However, for meat products and TVPs, it has been shown that NIR spectroscopy can be applied to measure the composition of cooked products (Bajawa & Apple, 2011; Ma et al., 2018; Squeo et al., 2022). A next step could be to apply this method to processed mixtures after the creation of a new PLSR model based on previously heated products.

Another challenge for the measurement of the composition of meat analogues is their fibrous nature, which affects the scattering pattern of NIR radiation. Grinding could overcome this problem, as already shown for meat (Cozzolino et al., 2000; Gaitán-Jurado et al., 2008). However, this would add additional sample preparation steps.

In summary, our results show that NIR spectroscopy is a promising technique to measure the oil and protein content of dense protein mixtures with a composition similar to meat analogues. To analyse processed meat analogues, dedicated calibration curves should be created before this technique can be applied in real-life situations. However, with those calibration curves, a sound estimation of meat analogue compositions can be expected using the procedures described in this paper.

To produce successful plant-based products, not only the total oil content but also the distribution of the oil is important. In our simple PPI/water/oil mixtures, we expected the oil distribution to homogeneous. For processed meat analogues, in which this is not the case, hyperspectral imaging could be applied to visualize the distribution of oil, as has already been done for salmon (Dixit & Reis, 2023), pork (Kucha et al., 2022) and TVPs (Squeo et al., 2022). Therefore, hyperspectral imaging is a promising technique to show the distribution of oil and protein in the final meat analogue product.

4.5 Conclusion

Near-infrared (NIR) spectroscopy offers a rapid and non-destructive method for measuring the contents of sunflower oil and pea protein isolate (PPI) in dense sunflower oil/PPI/water mixtures. PLSR showed that the sunflower oil and PPI content could be predicted accurately. Wavelength range reduction and wavelength selection with the covariates selection (CovSel) approach could be used to simplify the model and improve the model quality. Wavelength range reduction was the most successful approach for oil content, but the CovSel approach was more successful for PPI content. The key wavelengths were 670, 1315 and 1211 nm for prediction of the sunflower oil content and 1330, 711 and 1442 nm for prediction of the PPI content. The selected wavelengths allow development of a cheap multi-spectral spectrometer for rapid analysis of oil or protein content in plant-based products. This would allow better quality control during the production of plant-based products and could therefore aid in the production of high-quality plant-based products. We expect that the method could be extended to other dense plant-based products before and after thermo-mechanical processing.

4.6 Appendix

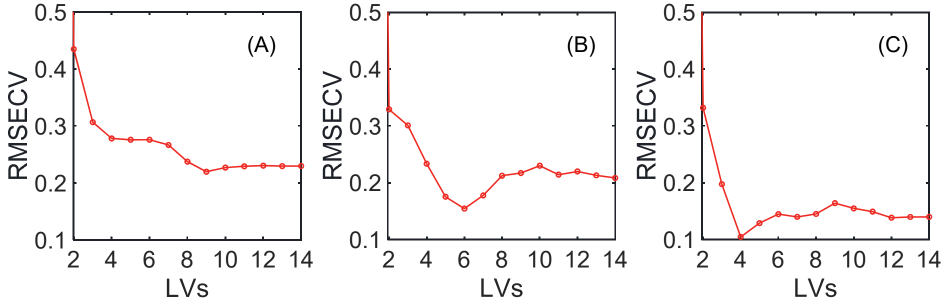

Fig. S.4.1 LV selection for PLSR models for sunflower oil content based on cross validation for the for the complete spectra (A), 1st CH overtones (B) and 2nd CH overtones (C).

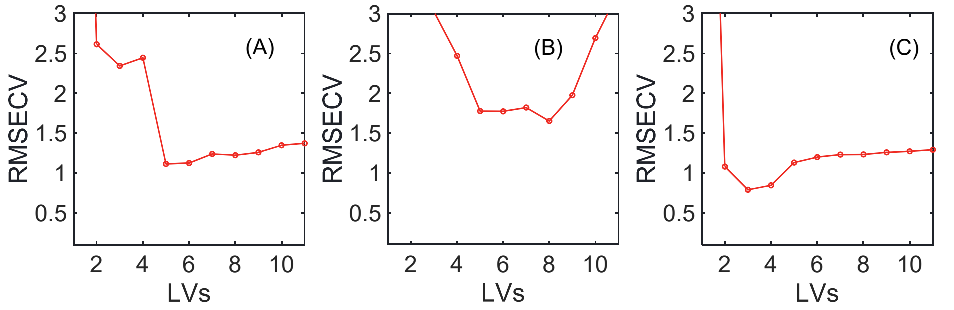

Fig. S.4.2 LV selection for PLSR models for protein content based on cross validation for the complete spectra (A), 1st NH overtones (B) and 2nd NH overtones (C).

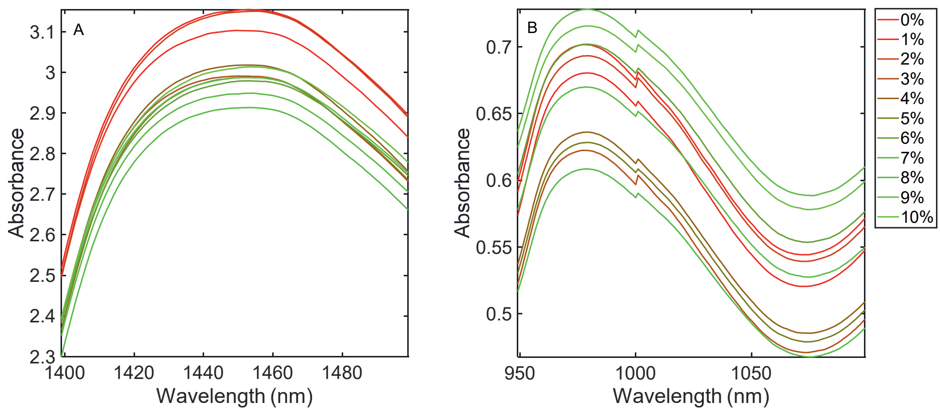

Fig. S.4.3 Average spectral profiles of the meat analogue mixes for the OH overtones. The sunflower oil content in the mixes is indicated with colours ranged from red to green. (A) 1st overtones region for OH bonds (1400-1500 nm), and (B) 2nd overtones region for OH bonds (950-1100 nm).

Table S.4.1 Overview of the parameters that were used to evaluate the PLSR models for sunflower oil content based on the pre-processing method that was applied (Raw reflectance + SNV + 2nd derivative or Absorbance + SNV + 1st derivative) and the spectral range on which the model was based. Cells highlighted in green indicate the pre-processing method that was most favourable per criterium and wavelength range, cells highlighted in red indicate the least favourable pre-processing method.

	Raw reflectance + SNV + 2nd derivative	Absorbance + SNV + 1st derivative	Raw reflectance + SNV + 2nd derivative	Absorbance + SNV + 1st derivative	Raw reflectance + SNV + 2nd derivative	Absorbance + SNV + 1st derivative
	Complete spectral range		1st overtones		2nd overtones	
LVs	2	9	4	6	3	4
RMSEC	0.13	0.01	0.19	0.08	0.09	0.07
RMSET	0.17	0.33	0.38	0.19	0.11	0.11
RMSEV	2.84	2.65	3.94	1.31	0.81	0.92
Pred. Bias.	-0.02	0.16	-0.03	0.02	0	0.01
R^2_C	1	1	1	1	1	1
R^2_T	1	0.99	0.99	1	1	1
R^2_V	0.63	0.7	0.45	0.95	0.97	0.96

4

Table S.4.2 Overview of the parameters that were used to evaluate the PLSR models for PPI content based on the pre-processing method that was applied (Raw reflectance + SNV + 2nd derivative, raw reflectance +SNV or Absorbance + SNV + 1st derivative) and the spectral range on which the model was based. Cells highlighted in green indicate the pre-processing method that was most favourable per criterium and wavelength range, cells highlighted in red indicate the least favourable pre-processing method.

	Raw reflectance + SNV + 2nd derivative	Raw reflectance + SNV	Absorbance + SNV + 1st derivative	Raw reflectance + SNV + 2nd derivative	Raw reflectance + SNV	Absorbance + SNV + 1st derivative	Raw reflectance + SNV + 2nd derivative	Raw reflectance + SNV	Absorbance + SNV + 1st derivative
	Complete spectrum			1st overtones			2nd overtones		
LVs	2	4	5	3	3	8	2	2	3
RMSEC	0.92	0.3	0.3	1.03	0.69	0.41	0.67	0.62	0.62
RMSET	1.54	0.73	1.324	1.35	1.52	3.43	1.09	1.04	0.94
RMSEV	1.41	1.58	2.43	2.91	2.71	5.43	2.38	2.64	2.86
Pred. Bias.	0.6	0.19	0.38	1.08	1.02	1.91	0.01	-0.09	-0.12
R^2_C	0.99	1	1	0.99	1	1	1	1	1
R^2_T	0.98	1	0.99	1	1	0.99	0.99	0.99	0.99
R^2_V	0.98	0.97	0.93	0.92	0.93	0.87	0.94	0.91	0.91

Table S.4.3 Overview of the parameters that were used to evaluate the models for sunflower sunflower oil content that were based on the wavelengths selected with the CovSel approach with and without application of pre-processing. Cells highlighted in green indicate the pre-processing method that was most favourable per criterium, cells highlighted in red indicate the least favourable pre-processing method.

	Raw reflectance	Absorbance + SNV + 1st derivative
	Complete spectral range	
number of wavelengths	3	2
RMSEC	0.18	0.23
RMSET	0.29	0.24
RMSEV	3.55	1.29
Pred. Bias.	-0.04	0
R^2_C	1	0.99
R^2_T	0.99	0.99
R^2_V	0.57	0.91

Table S.4.4 Overview of the parameters that were used to evaluate the models for PPI content that were based on the wavelengths selected with the CovSel approach with and without application of pre-processing. Cells highlighted in green indicate the pre-processing method that was most favourable per criterium, cells highlighted in red indicate the least favourable pre-processing method.

	Raw reflectance	Absorbance + SNV + 1st derivative
	Complete spectral range	
number of wavelengths	3	11
RMSEC	0.46	0.12
RMSET	0.89	2.55
RMSEV	1.48	5.08
Pred. Bias.	-0.04	0.31
R^2_C	1	1
R^2_T	0.99	0.94
R^2_V	0.98	0.74

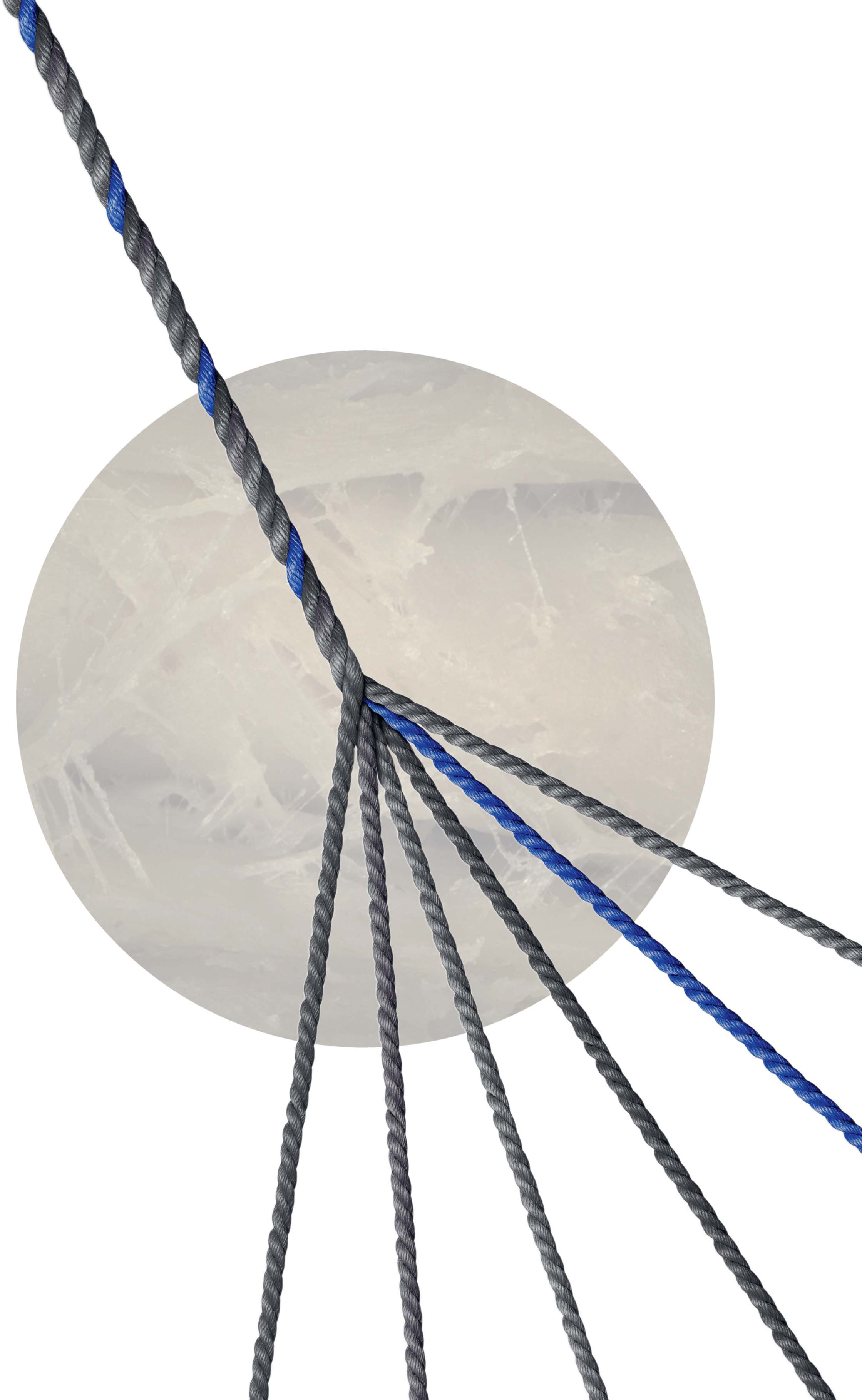

Chapter 5

Wavelength selection enables robust oil content quantification with near-infrared spectroscopy in pea protein gels produced under varying heating conditions

This chapter is submitted as Köllmann, N., Hageman, J., Groot Nibbelink, D., Zhang, L. & van der Goot, A.J. Wavelength selection enables robust oil content quantification with near-infrared spectroscopy in pea protein gels produced under varying heating conditions.

5.1 Abstract

Thermal processing influences the near-infrared (NIR) spectra of food products, causing inaccuracy in quantification of the product composition. In this study the effect of thermal processing on the NIR measurement of the oil content in pea protein isolate (PPI) gels was investigated. Analysis of variance (ANOVA) confirmed that heating temperature (30-120 °C) and time (2.5-15 min) during the production of PPI gels influenced parts of the NIR spectra. Stepwise multiple linear regression (SW-MLR) was used to select a combination of 5 wavelengths that was suitable to create a robust model for the prediction of oil content (Q^2=0.9928±0.002, RMSE=0.2806±0.0423 wt.%). The combination of these wavelengths was shown to reduce the effect of thermal process history on the measurement, improving the accuracy of oil content quantification. This approach, therefore, can be applied for inline quantification of the oil content of food products subjected to varying heating conditions using specialized sensors.

5.2 Introduction

Oil is an important contributor to the taste, texture, and nutritional properties of many food products, including plant-based foods (Godschalk-Broers et al., 2022; Mefleh et al., 2022). Accurate and rapid measurement of oil content in food products is therefore very relevant. The oil content in food products is conventionally determined with solvent extraction or gas chromatography methods (Holman et al., 2019; Tao & Ngadi, 2018). However, these standard methods for oil analysis are laborious, require harmful chemicals and are destructive (Tao & Ngadi, 2018). Furthermore, oil can remain encapsulated in the food matrix (Berghout et al., 2014), which leads to underestimations in the oil content analysis when using solvent based methods. Alternatively, near-infrared (NIR) spectroscopy is used to determine the oil content in food products (Krepper et al., 2018; Squeo et al., 2022; Zhang et al., 2020). NIR spectroscopy has several advantages over traditional methods for the determination of product composition. It is simple since generally no sample preparation is required, and the measurement itself can be done in a few seconds (Osborne, 2006; Porep et al., 2015). Furthermore, the measurements are non-destructive and allow simultaneous analysis of multiple components.

NIR spectroscopy is based on the absorption of electromagnetic radiation by vibrating molecules in the NIR region (750-2500 nm) (Osborne, 2006; Pasquini, 2018). The NIR spectra are mainly influenced by the OH, NH, CH, and SH bonds present in foods (Osborne, 2006; Pasquini, 2018). Therefore, NIR is used to quantify the protein, carbohydrate, water and fat content in food samples. Such determinations are based on based on calibration models created by chemometric modelling with the NIR spectra of products with a known composition (Pasquini, 2018). These calibration models can subsequently be used to accurately determine the product composition.

Nevertheless, the use of NIR spectroscopy for product composition quantification presents challenges. One major challenge is the influence of the thermal processing conditions during food production on the NIR spectra of the measured samples (Ben-Hdech et al., 1993; Ellekjaer & Isaksson, 1992; Wold et al., 2020; Chapter 6). Heat treatment influences the protein-water interactions of the material, affecting the resulting NIR spectra (Ellekjaer & Isaksson, 1992). The effect of heat treatment on the NIR spectra was previously used to measure the end-point temperature of heated meat and fish products and the thermal process intensity during extrusion of meat analogues (Skåra et al., 2014; Wold, 2016; Wold et al., 2020; Chapter 6).

While previous research mostly focussed on the effect of measurement temperature on the NIR-spectra (Campos et al., 2018; Kartakoullis et al., 2019; Xu et al., 2023), the effect of thermal processing on the compositional analysis with NIR spectroscopy has not yet been explored. Hageman et al. (2005) presented an overview of chemometric approaches that reduce the effect of measurement temperature on the results of NIR spectroscopy measurements. It is therefore interesting to investigate whether these approaches could also be applied to reduce the effect of processing temperature on the compositional analysis using NIR. One approach is to develop a calibration model based only on the parts of the spectrum that are not affected by temperature (Hageman et al., 2005). Wavelength selection is a commonly applied method to do so and often improves the model quality. In our previous work we showed that wavelength selection is a suitable tool to improve the oil content prediction in dense plant-based matrices (Chapter 4). Here, wavelength selection using stepwise multiple linear regression (SW-MLR) is applied to select the wavelengths that are most related to the oil content irrespective of the heat treatment. The main advantage of SW-MLR over other wavelength selection techniques is the simplicity and interpretability of its models (Xiaobo et al., 2010).

This study investigates the use of NIR spectroscopy to measure the oil content in plant-based products, i.e. pea protein isolate (PPI) gels, produced under varying heating conditions. The effect of heating is studied by using different combination of temperatures (30-120 °C) and times (2.5-15 min) during the production of these gels and the NIR spectra of these gels are recorded after they are cooled. First, principal component analysis (PCA) and analysis of variance (ANOVA) are used to quantify the influence of oil content, heating temperature and time and their interactions on the spectral variation and each individual wavelength. Subsequently, SW-MLR is applied to select the most relevant wavelengths for oil content measurement and create a robust model based on these wavelengths. Finally, we examine the correlation of the model residuals with oil content and temperature for models based on an increasing number of selected wavelengths. This provides information about the effect of the selected wavelengths on the robustness of the oil quantification.

5.3 Materials and methods

5.3.1 Materials

Pea protein isolate, PPI (NUTRALYS® S85F) was obtained from Roquette (Lestrem, France). It had a dry matter content of 93.7 wt.% ±0.1 and a protein content of 74.7 wt.% ±0.1 on dry matter basis, as determined by the Dumas combustion method (N×5.58). Sunflower oil (Albert Heijn, Zaandam, the Netherlands) was purchased from a local supermarket. According to the supplier, the sunflower oil contained 10% saturated and 82% unsaturated fats.

5.3.2 Preparation of the protein gels

First PPI was mixed with demineralized water to obtain a 40 wt.% PPI dispersion (on dry matter basis) Subsequently, sunflower oil was added to reach a final concentration of 0, 2, 4, 6, 8 or 10 wt.% in the final mixture, while the PPI dispersion was set to be 100, 98, 96, 94, 92 or 90 wt.% of the total mixture, correspondingly. The mixture was manually mixed with a spoon until it appeared to be homogeneous and after that mixing was continued for another 2 minutes. This mixture was left to hydrate for 30 minutes and vacuumized, after which the sample was placed in metal cups with a diameter of 25 mm and height of 5 mm. A schematic visualisation of the metal cups is given in Fig. 5.1. The gels were heated in a water or oil bath in a range of temperatures (30 °C, 60 °C, 80 °C, 99.9 °C, 120 °C) for a specific time (2.5, 5, 10, 15 min). A water bath was used to heat samples at temperatures below 100 °C, while an oil bath was used for the samples heated at 120 °C. The final gels were trimmed, to create a smooth surface. Each gel was prepared in triplicate and stored in the freezer (-20 °C) prior to analysis. Before further analysis, the gel samples were left to thaw in the refrigerator (4 °C) overnight. The samples were taken out of the refrigerator at least one hour prior to analysis to reach room temperature.

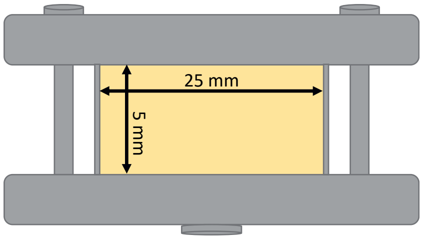

Fig. 5.1 Schematic visualisation of a metal cup, used to create protein gel discs (as depicted in yellow). Please note that the image is not to scale.

5.3.3 NIR measurement

The near-infrared (NIR) spectroscopy measurements were performed by a Hi-Res LabSpec spectrometer (ASD Inc., Boulder, CO, USA), using the area scan probe (Hi-Brite probe, ASD Inc., Boulder, CO, USA) with a spot size of 10 mm. A 6.5 W halogen light source was present in the probe and the probe used optical fibres to capture reflected light. The probe was placed in a tripod and the height was adjusted to ensure that the probe was as close as possible to the gel surface without touching it (maximum distance between gel surface and probe was approximately 1 mm). The spectrometer was controlled by Indico Pro Software (ASD Inc., Boulder, CO, USA). The integration time was automatically optimized by the Indico Pro software and was initially set at 15 ms. Each measurement was an average of ~ 5 consecutive measurements automatically performed by the Indico Pro software. For each gel 1 measurement was made. The radiometric calibration with white and dark reference was performed by the Indico Pro software automatically.

5.3.4 Pre-processing of spectral data

Prior to analysis of the NIR reflectance spectra were transformed to absorbance (-log(reflectance)). Subsequently, scattering in the NIR reflectance spectra was reduced using standard normal variate (SNV) correction. In SNV correction, each spectrum is centred and divided by its standard deviation, resulting in a common scale for all spectra (Barnes et al., 1989). Finally, the absorbance data was pre-treated with smoothening using the Savitsky-Golay (SAVGOL) (Savitzky & Golay, 1964) algorithm and the 2nd derivative was estimated to reveal underlying peaks. A window size of 51 was used for smoothening.

5.3.5 Statistical analysis

To reduce the data dimensionality and visualize the variation in the data, a principal component analysis (PCA) was carried out on auto-scaled pre-processed data. The significance of the factors oil content (wt.%), heating temperature (°C) and heating time (min) and their two-way and three-way interactions on each individual wavelength was quantified using analysis of variance (ANOVA). The method of Benjamini and Hochberg was used to control the false discovery rate. Stepwise multiple linear regression (SW-MLR) was applied to select the most relevant wavelengths for the prediction of oil content from the pre-processed NIR spectra using forward selection. The number of selected wavelengths was determined using 10-fold cross validation (Fig. S.5.1). Predictive abilities of the resulting models for unknown spectra were determined using a separate test set and expressed as a Q^2 value and root mean standard error of the test set (RMSET). The Q^2 value is defined as the coefficient of determination (R^2) for out of bag objects (i.e., the gels that were not included in the data set used to train the model). The variability resulting from a random split in a training and test set and the 10-fold cross validation was investigated by repeating this procedure 10 times.

The statistical analysis was performed using R (version 4.3.2) (R Core Team, 2023) and R-studio (2023.09.1) (RStudio Team, 2020). The R-packages FactoMineR (version 2.11) (Lê et al., 2008) was used for PCA and the packages leaps (version 3.1) (Lumley, 2024) and caret (version 6.0.94) (Kuhn, 2008) for SW-MLR and package pls (version 2.8-3) (Mevik & Wehrens, 2007) for PLS.

5.4 Results and discussion

5.4.1 Overview of the absorbance data

The average absorbance of the pea protein isolate (PPI) gels with varying oil contents (0-10 wt.%) heated at different temperatures (30-120 °C) and for different times (2.5-15 min) before and after pre-processing is shown in Fig. 5.2. The raw absorbance spectra showed peaks at 980, 1200, 1450 1920 nm, which corresponds with OH, CH and NH_2 overtones (van Staveren, 2020) of the water, oil, and protein of which the gels were constituted (Fig. 5.2A). The spectra of the heated gels were similar to the spectra of unheated PPI/water/sunflower oil mixtures measured in our previous work (Chapter 4), with the exception that the absorbance of the wavelengths >2100 nm was higher for the heated gels. These wavelengths are related to the combination bands of NH_2 (van Staveren, 2020). These changes could therefore be induced by heating, which causes changes in the protein structure (Uddin et al., 2002). At wavelengths above 2300 nm the data contained a lot of noise, which was also observed by Laurens & Wolfrum (2013) and is most likely caused by the decreasing signal-to-noise ratio of the spectrometer at higher wavelengths (Teixeira Dos Santos et al., 2013).

The average absorbance observed in Fig. 5.2A decreased with higher oil content, which seems counterintuitive. Normally, an increased absorbance correlates with an increased oil content. This trend was caused by baseline shifts which were therefore removed with spectral pre-processing with standard normal variate (SNV) correction and calculation of the 2nd derivative (Fig. 5.2B). Similarly, Wold et al. (2011) observed a decreased absorbance with an increased fat content of beef, which could also be solved with SNV correction. Pre-processing resulted in peaks located at 1405, 1670 and 1716 nm that were clearly correlated with oil content, which fall into the first and second overtone regions of CH bonds (van Staveren, 2020). The correlation of the pre-processed spectra with oil content confirms that near-infrared (NIR) spectroscopy is suitable for the measurement of the oil content of PPI gels heated at different processing conditions.

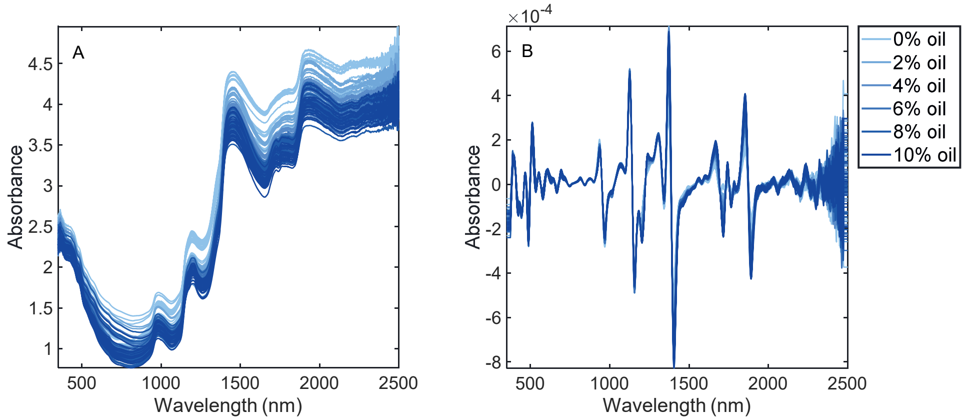

Fig. 5.2 Average absorbance spectra before (A) or after pre-processing using SNV and 2nd derivative (B) of the PPI gels with oil contents ranging from 0-10 wt.% and processed at increasing temperature (30-120 °C) and time (2.5-15 min). The colours, ranging from light to dark blue, indicate an increasing oil content, processing temperature and time, respectively.

5.4.2 Influence of oil content and heating conditions on spectral variation

A principal component analysis (PCA) was performed for the pre-processed absorbance spectra as a first indication of the effect of oil content and heating conditions on the spectral variation. The PCA revealed that the main variation in the NIR spectral data is caused by the oil content (Fig. 5.3A), as was expected from the average pre-processed absorbance spectra (Fig. 5.2B). However, part of the spectral variation is explained by the heating temperature (Fig. 5.3B). The effect of heating time was limited compared to the other experimental factors (Fig. 5.3C).

The limited effect of heating time on the complete sample indicates that the effect of time is temperature dependent. To verify this, separate PCAs were performed for each individual heating temperature. For gels heated at 30 and 60 °C no effect of time was observed for the first 4 principal components (PCs). However, time did influence PC 2 for 100 and 120 °C and PC 3 for 80 and 100 °C (Fig. S.5.2). The influence of time seen in PC 2 of gels heated at 100 and 120 °C indicates that the influence of time increased with an increasing temperature. This increased time effect could imply that changes in the NIR spectra are caused by chemical reactions with Arrhenius type behaviour. This Arrhenius type behaviour leads to an exponential increase of the reaction rate at higher temperatures and is often used to describe reactions of plant-based protein (Pietsch et al., 2018). Nevertheless, when considering the complete range of heating conditions used in this study, the effect of heating time on the NIR spectra was limited compared with the effects of oil content and heating temperature, as indicated by the PCA results. Therefore, the effect of heating time on the calibration model to predict oil content in heated PPI gels will not be discussed further. The influence of oil content and heating temperature on the NIR spectra and the consequences for creating a robust calibration model for the oil content will be the focus of the rest of the results and discussion.

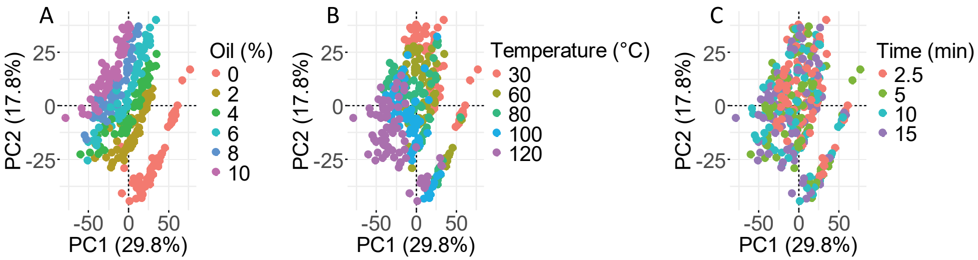

Fig. 5.3 PCA analysis based on pre-processed NIR spectra for PPI gels with different oil contents processed at varying temperatures and time. Colour indicates oil content (A), heating temperature (B) or heating time (C).

An analysis of variance (ANOVA) was performed for each individual wavelength of the pre-processed spectra to get more detailed information about the effect of oil content, heating temperature, and their interactions on each specific wavelength of the NIR spectrum. The ANOVA results are shown in Fig. 5.4. A line with a green colour indicates an interrelated effect of oil and temperature on a specific wavelength, which we refer to as oil:temperature interaction. A line with a red or blue colour was drawn to indicate that the effect of oil or temperature on a specific wavelength was statistically significant, respectively (Fig. 4). When there was a significant effect of the oil:temperature interaction on a specific wavelength, the main effect of a single factor is not interpretable and thus is no longer shown (Ståhle & Wold, 1989).

The interaction between oil and temperature affected the largest part of the spectrum. No interactions between oil and temperature were found for several wavelength ranges >2000 nm. Similarly, Uddin et al. (2005) reported changes in the NIR spectra of kamaboko gels between 1100-2100 nm after the application of different heat treatments. The effect of the interaction in the visual wavelength area (<750 nm) aligns with the decrease in the browning index for gels with a lower oil content or increasing processing temperature found in this study (Fig. S.5.3). The interaction between oil and temperature in the 1st and 2nd NH and OH overtone areas (950-1100 nm and 1400-1550 nm) indicates that the presence of a dispersed oil phase in the protein matrix of the gels influences the changes of the protein properties upon heating. Similarly, Chen et al. (2023) found that the addition of fatty acids affected the protein properties during high-moisture extrusion. The lack of an interaction effect at the highest wavelengths measured in this study is caused by the noise at the highest wavelengths measured (Fig. 5.2).

The main effects of oil content on the NIR spectra were found in the 1st overtone region (1600-1800 nm) and combination bonds (2200-2450 nm) for CH bonds (van Staveren, 2020). This means that the effect of oil content in these spectral regions was not influenced by changes in the heating temperature. This was expected as the 1st overtone region was previously found to be correlated with the oil content of unheated PPI/water/sunflower oil mixtures (Chapter 4).

Many of the wavelengths that were affected by the oil content were also influenced by the heating temperature (Fig. 5.4B and C). This means that oil and temperature both influenced these wavelengths but the effect of oil on these wavelengths was not influenced by temperature and vice versa. However, several parts of the NIR spectrum >2000 nm were only correlated to the oil content and were not influenced by the temperature. This indicates that wavelength selection is a promising technique to create a model that is only based on wavelengths that have explanatory value for the oil content but are not or hardly influenced by the heating conditions.

The ANOVA results for the effect of time and its interactions with oil and temperature can be found in Fig. S.5.4. These results confirm that that only for one wavelength heating time had a limited effect on the NIR spectra compared to oil content and heating temperature.

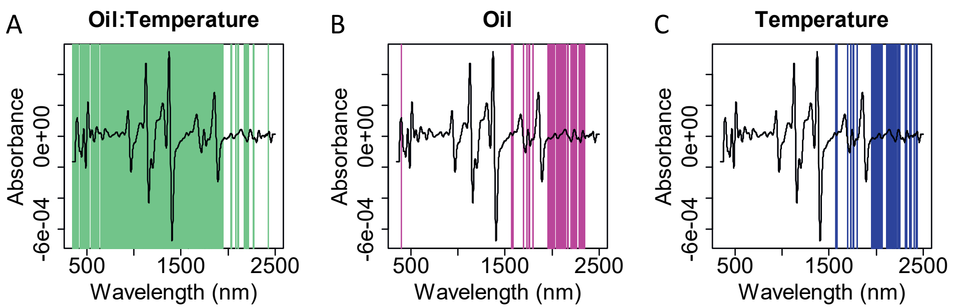

Fig. 5.4 ANOVA for individual wavelengths of the pre-processed NIR spectra of PPI gels produced at varying oil contents (0-10 wt.%), temperatures (30-120 °C) and times (2.5-15 min). The black line is the mean absorbance after SNV correction and calculation of the 2nd derivative. Vertical lines indicate a significant interaction at $p<0.05$ of an oil:temperature interaction (A), oil effect (B) and temperature effect (C). When a significant interaction was found for a wavelength, main effects were no longer considered.

5.4.3 Wavelength selection and modelling

Stepwise multiple linear regression (SW-MLR) was applied to determine the most relevant wavelengths for the measurement of oil content with the use of NIR spectroscopy and to create a model based on these wavelengths. Wavelength selection is commonly used to increase the speed and robustness of the analysis (Dodds & Heath, 2005). In this case SW-MLR was expected to reduce the effect of heating conditions on the oil measurement. An accurate model to predict the oil content for gels produced under different heating conditions was obtained by selecting only 5 wavelengths with SW-MLR (Q^2=0.9915, RMSET=0.2652 wt.%) (Fig. S.5.1, Fig. 5.5). This was more accurate than a partial least squares (PLS) regression model with 6 latent variables based on the same dataset (Q^2=0.9803, RMSET=0.4041 wt.%) (Fig. S.5.5). In our previous study 3 wavelengths were sufficient to predict the oil content of unheated PPI/water/sunflower oil mixtures with a similar composition as was used here (Chapter 4). The higher number of wavelengths required in this study is most likely a result of the additional variation introduced by the heat treatment of the gels.

To make the analysis as rapid and simple as possible, it is possible to measure the oil content using only the first selected wavelength (1219 nm). This leads to an RMSET of 0.37 wt.% oil when such a monochromatic sensor is used, which might be not acceptable for all applications (Fig. S.5.6A).

The 5 wavelengths that were selected by SW-MLR are shown in Fig. 5.5A. The order of inclusion in the model provides information about the relative importance of the wavelengths for the measurement of the oil content. In this case the order of inclusion was as follows: 1219, 1190, 1397, 830 and 1881 nm. The three most important wavelength (1219, 1190 and 1397 nm) corresponded to the 2nd CH overtone (van Staveren, 2020), which was as expected given the fact that these bonds are linked to the oil content. Similar wavelengths of 1211, 1212, 1192 nm were linked to the fat content of meat products in previous research (Barbin et al., 2013; Pu et al., 2014). Surprisingly, all selected wavelengths were affected by the oil:temperature interaction (Fig. 5.4A, Tables S.5.1-S.5.4). This means that the wavelengths that were only influenced by the main effect of oil content were not selected, probably due to the noise associated with these wavelengths (Figs. 5.2B and 5.4B). Apparently, the effect of heating temperature on the selected wavelengths was limited or its effect was reduced by the combination of the different wavelengths in the model. The last two wavelengths that were included in the model (830 and 1881 nm), were linked to 3rd overtone of NH and 1st overtones of CO_2H bonds, respectively (van Staveren, 2020). This means that also bonds that are related to protein contributed to the oil measurement. This could be caused by two effects. Firstly, the protein content was inversely correlated with the oil content because of the experimental design and therefore provides information about the oil content. Secondly, these wavelengths were influenced by the oil:temperature interaction (Fig. 5.4A, Tables S.5.1-S.5.4). This means that these wavelengths are affected by both the oil content and the heating temperature. Because these wavelengths cannot be linked directly to the oil content, it indicates that these wavelengths are included to compensate for the influence of temperature on the prediction caused by the oil:temperature interaction, which also affects the first three wavelengths. We will explore this effect further in section 5.4.4.

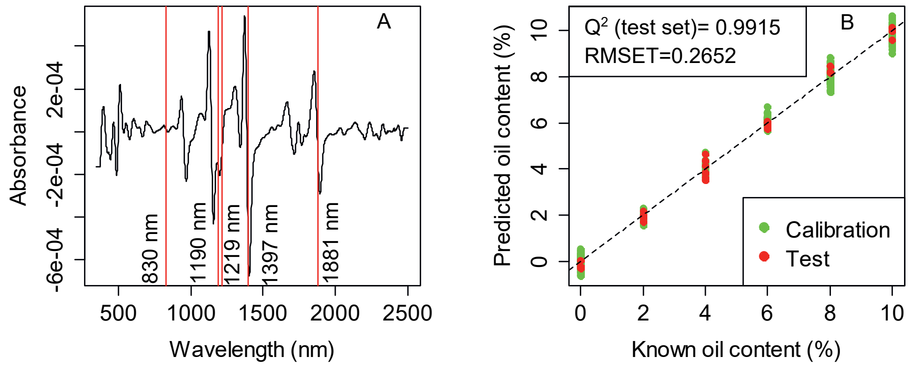

Fig. 5.5 SW-MLR for one model. Selected wavelengths (A) and resulting model prediction (B). The black line in A is the mean absorbance after pre-processing.

When SW-MLR is used for wavelength selection, the specific wavelengths that are selected depend on the calibration set that is used. To get more information about the spectral areas that are suitable for oil content quantification SW-MLR was therefore applied to 10 different splits of the dataset into a calibration and test set. These wavelength areas are suitable to create specific sensors to measure oil content under fluctuating processing conditions. In the 10 different SW-MLR models that were created 13 unique wavelengths were selected (Fig. 5.6). The average Q^2 and RMSET of these models had a small standard deviation of 0.002 and 0.0423, respectively, which indicates that different combinations of 5 out of the 13 wavelengths were equally successful. The selected wavelengths in the models based on different calibration and test set splits were often neighbouring wavelengths, which are highly correlated (Fig. 5.6), leading to models with similar quality. SW-MLR with different calibration and test set splits can therefore be used to find relevant wavelength areas rather than specific wavelengths for oil content quantification.

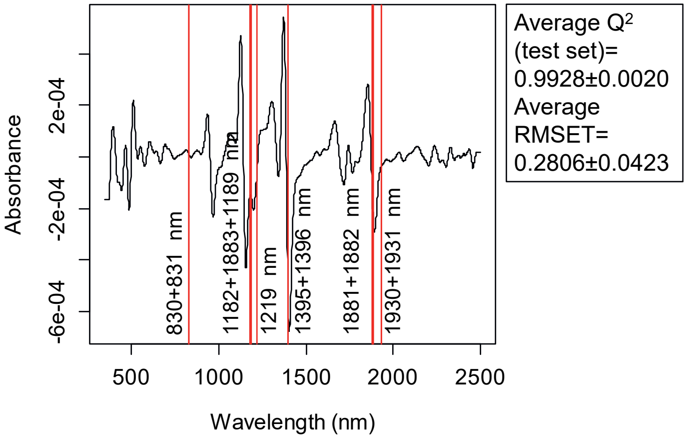

Fig. 5.6 Wavelengths selected by stepwise MLR for 10 different training and test set splits. The black line is the mean absorbance after pre-processing.

5.4.4 Correlation model residuals with oil content and heating temperature

In the previous section it was hypothesized that the SW-MLR model could self-correct for the influence of temperature on the oil content prediction, by using a combination of wavelengths that were all influenced by temperature. To further explore the influence of the heating conditions on the oil content predictions, the correlation of the oil content and heating temperature with the residuals after successively including the selected wavelengths in the model was studied. The Q^2, RMSET and parity plots for these models can be found in Fig.S.5.6. Table 5.1 shows that the a significant interaction of oil and temperature with the model residuals occurs when only 1219 nm is included in the model. This explains the necessity to add the subsequent wavelengths to reduce the effect of the heating temperature on the oil content measurement.

As expected, the correlation of the oil content with the model residuals decreased with each added wavelength. The correlation of the residuals with temperature also decreased when adding additional wavelengths, though the decrease was less consistent than for oil content. The effect of temperature on the oil content measurement was reduced the most when 4 wavelengths were included in the model.

The correlation of the residuals was higher for the oil content compared with the heating temperature, except for the model based on only a single wavelength. This implies that even though heating temperature can influence the measurement, its effect is relatively small. It can therefore be concluded that the use of this combination of 5 selected wavelengths with SW-MLR is suitable to create a model for oil content that is robust against temperature changes.

Table 5.1 Correlation coefficients of the residual error of oil content prediction with the oil content and heating temperature for a model with an increasing number of wavelengths. * Indicates the significance of the correlation coefficient at $p<0.05$. Table S.5.6 shows exact p-values.

Wavelengths included in the MLR model	**Oil**	**Temperature**
1219 nm	0.129*	0.329*
1219 and 1190 nm	0.095	-0.040
1219, 1190 and 1397 nm	0.090	0.049
1219, 1190, 1397 and 830 nm	0.085	-0.010
1219, 1190, 1397, 830 and 1881 nm	0.081	-0.017

5.4.5 Implications for future applications

In this study we presented an approach for a robust measurement of the oil content in PPI gels produced under varying heating conditions. For products with a similar composition and heating conditions the wavelengths selected in this study could be used to develop a specific sensor for this application. However, it should be noted that NIR spectroscopy was performed after the product was cooled down and recalibration is likely necessary before applying this approach to develop a specific inline sensor, as measurement temperature has a significant influence on the recorded NIR spectra (Campos et al., 2018; Kartakoullis et al., 2019; Xu et al., 2023).

To apply the combination of NIR spectroscopy with SW-MLR presented here to a novel industrial application, we created a general workflow. This workflow starts with the development of a calibration curve for the component of interest that is robust to changes in the heating conditions. The first step to obtaining a useful calibration curve is to determine the expected range of product composition and processing conditions that will occur in the final application. Subsequently, an experimental design can be used to determine which samples need to be included in a training set that is sufficiently covering the expected variation. In this study it was possible to manually vary the product composition by adding different amounts of oil. However, for natural products, such as meat or fish, controlling the composition is not possible and a larger sample set is required to obtain sufficient variation. In both cases, the use of an experimental design is useful to determine which processing conditions need to be considered. It should be noted though that the self-correcting effect of the SW-MLR model for the heating conditions that was found in this study might be affected when the size of the dataset is reduced too much.

After creating the experimental design, the NIR spectra need to be recorded at conditions similar to the final application to reduce the influence of the measurement conditions on the NIR spectra. After acquiring the NIR spectra SW-MLR can be used to create a robust calibration curve. When desired, the selected wavelengths by SW-MLR can be used to develop specialized sensors for a specific application. This can increase the speed of the analysis and reduces the cost of analysis (Dodds & Heath, 2005). A well-known limitation of NIR spectroscopy is its limited robustness against changes in the processing conditions or sample composition. This means that the calibration curve needs to be updated regularly to maintain the robustness of the inline measurement (Zeaiter et al., 2006). For the gels presented in this study, it is especially important to recalibrate when the type of oil or protein ingredient is changed.

A final aspect that needs to be considered is the distribution of the component of interest in the product. The area measured with NIR spectroscopy should be representative for the entire product. In case of inhomogeneous distribution of the component of interest, hyperspectral imaging can be used to visualize the distribution of the component throughout the food product and improve the accuracy of its quantification (Squeo et al., 2022; Zhang et al., 2020).

In this study we have shown that NIR spectroscopy is a suitable tool to measure the oil content of heated mixtures containing protein, water and oil. An advantage of NIR spectroscopy is the possibility to measure multiple product properties simultaneously. In our previous work we have also shown that NIR spectroscopy can be applied to measure the thermal process intensity (Chapter 6). Furthermore, NIR spectroscopy could be a suitable tool to measure the structural properties of food products as was already done for noodles (Kwon et al., 2024) and plant-based meat analogues (Dhanapal & Erkinbaev, 2024). NIR spectroscopy is therefore a promising tool to measure the composition, processing conditions and resulting structural properties of heated food products simultaneously.

5.5 Conclusion

In this study the use of near-infrared (NIR) spectroscopy for oil content quantification in pea protein isolate (PPI) gels produced under varying heating conditions was investigated. It was possible to create an accurate model for oil content quantification based on only 5 wavelengths using stepwise multiple linear regression (SW-MLR). The residuals of the models after consecutive inclusion of the selected wavelengths show that all wavelengths added explanatory value for the oil content and reduced the effect of heating temperature on the oil content prediction. The combination of the selected wavelengths therefore reduces the effect of heating conditions on the measurement of oil content even when a large part of the spectrum is influenced by both the oil content and heating conditions. This approach thus shows that selecting wavelength areas allows robust inline analysis of the oil content of food products under varying heating conditions.

5.6 Appendix

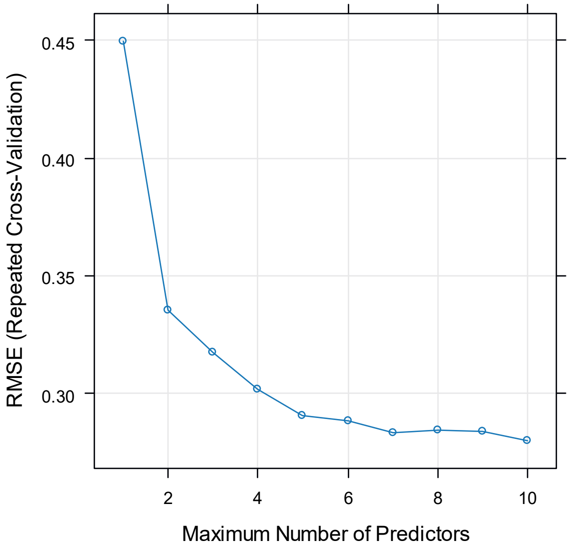

Fig. S.5.1 Residual Mean Square Error (RMSE) of repeated cross-validation plotted against the number of wavelengths included in the stepwise multiple linear regression model (SW-MLR).

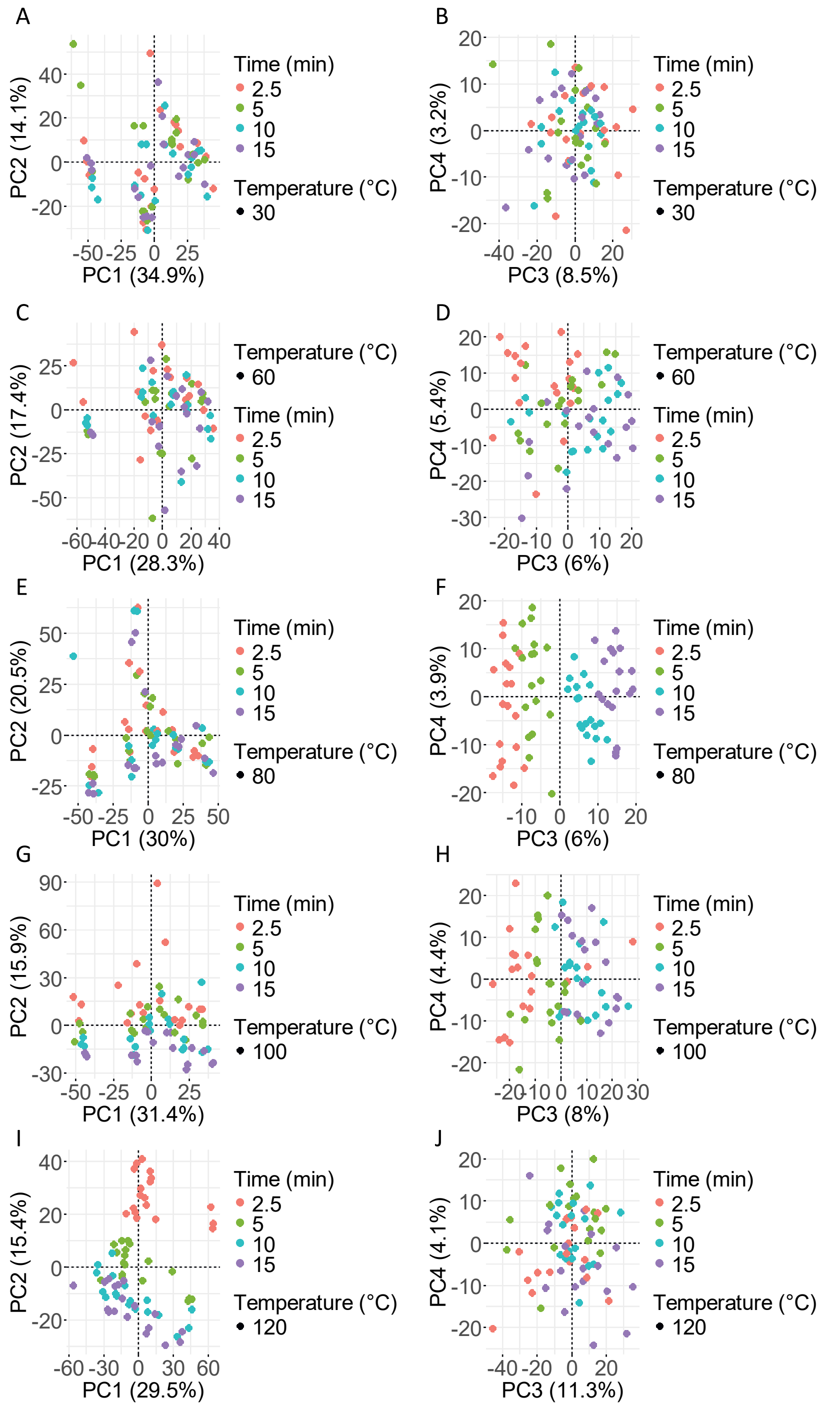

Fig. S.5.2 PCA analysis of time effect heated at different heating temperatures. A&B 30 °C, C&D 60 °C, E&F 80 °C, G&H 100 °C, I&J 120 °C.

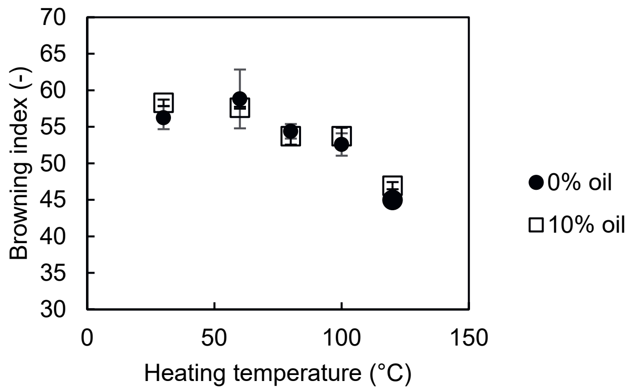

Fig. S.5.3 Browning index calculated from the L*a*b*-values measured with a colorimeter (Chroma Meters CR-400, Konica Minolta Inc., Tokyo, Japan): $\frac{100}{0.17}\left(\frac{a^{*2}+1.75L^{*}}{5.645L^{*}+a^{*}-3.012b^{*}}-0.31\right)$ of PPI gels with 0 wt.% oil (●) or 10 wt.% oil (□) heated for 15 min. at varying heating temperatures.

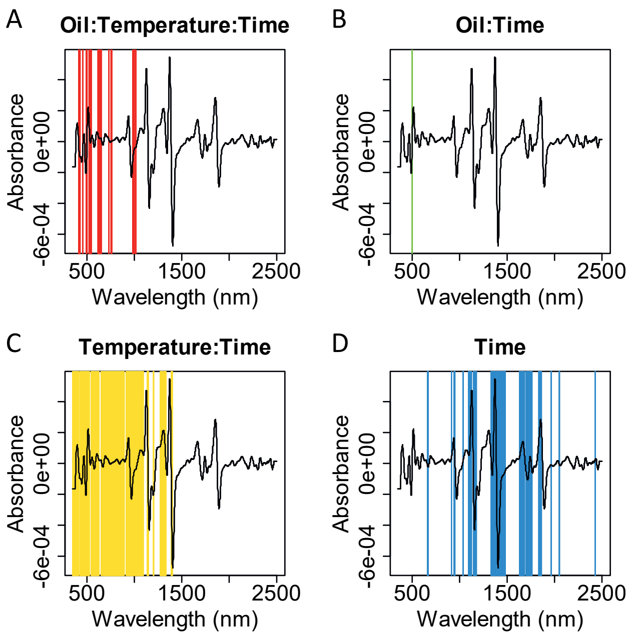

Fig. S.5.4 ANOVA for individual wavelengths of the pre-processed NIR spectra of PPI gels produced at varying oil contents (0-10 wt.%), temperatures (30-120 °C) and times (2.5-15 min). Lines indicate a significant interaction at $p<0.05$ of an oil:temperature:time interaction (A), oil:time interaction (B), temperature:time interaction (C) or time effect (D). When a significant interaction was found for a wavelength, main effects were no longer considered.

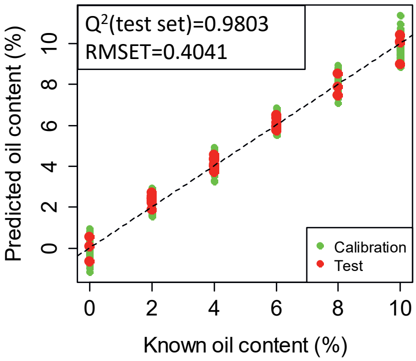

Fig. S.5.5 Result of partial least squares regression with 6 latent variables after pre-processing with SNV and 2nd derivative.

Table S.5.1 Analysis of Variance table for the effects of oil content, heating temperature and time on the NIR signal at 1219 nm after pre-processing with SNV and 2[nd] derivative.

	Df	Sum Sq	Mean Sq	F-value	Pr(>F)
Oil	5	$3.63*10^{-7}$	$7.27*10^{-8}$	9477.20	$<2.2*10^{-16}$ ***
Temperature	4	$1.38*10^{-9}$	$3.45*10^{-10}$	44.96	$<2.2*10^{-16}$ ***
Time	3	$1.00*10^{-11}$	$4.00*10^{-12}$	0.50	0.68
Oil:Temperature	20	$8.50*10^{-10}$	$4.30*10^{-11}$	5.57	$1.069*10^{-11}$ ***
Oil:Time	15	$1.40*10^{-10}$	$9.00*10^{-12}$	1.18	0.28
Temperature:Time	12	$1.50*10^{-10}$	$1.20*10^{-11}$	1.59	0.096.
Oil:Temperature:Time	60	$4.40*10^{-10}$	$7.00*10^{-12}$	0.96	0.56
Residuals	240	$1.84*10^{-9}$	$8.00*10^{-12}$		

Signif. codes: 0 ‘***’ 0.001 ‘**’ 0.01 ‘*’ 0.05 ‘.’ 0.1 ‘ ’ 1

5

Table S.5.2 Analysis of Variance table for the effects of oil content, heating temperature and time on the NIR signal at 1190 nm after pre-processing with SNV and 2nd derivative.

	Df	Sum Sq	Mean Sq	F-value	Pr(>F)
Oil	5	$1.83*10^{-8}$	$3.66*10^{-9}$	226.45	$<2.2*10^{-16}$ ***
Temperature	4	$4.23*10^{-9}$	$1.06*10^{-9}$	65.38	$<2.2*10^{-16}$ ***
Time	3	$4.26*10^{-11}$	$1.42*10^{-11}$	0.88	0.45
Oil:Temperature	20	$1.70*10^{-9}$	$8.51*10^{-11}$	5.26	$6.25*10^{-11}$ ***
Oil:Time	15	$2.56*10^{-10}$	$1.71*10^{-11}$	1.05	0.40
Temperature:Time	12	$3.25*10^{-10}$	$2.71*10^{-11}$	1.67	0.073.
Oil:Temperature:Time	60	$1.26*10^{-9}$	$2.10*10^{-11}$	1.30	0.089.
Residuals	240	$3.88*10^{-9}$	$1.62*10^{-11}$		

Signif. codes: 0 ‘***’ 0.001 ‘**’ 0.01 ‘*’ 0.05 ‘.’ 0.1 ‘ ’ 1

Table S.5.3 Analysis of Variance table for the effects of oil content, heating temperature and time on the NIR signal at 1397 nm after pre-processing with SNV and 2nd derivative.

	Df	Sum Sq	Mean Sq	F-value	Pr(>F)
Oil	5	$4.25*10^{-7}$	$8.50*10^{-8}$	178.79	$<2.2*10^{-16}$ ***
Temperature	4	$1.53*10^{-7}$	$3.81*10^{-8}$	80.25	$<2.2*10^{-16}$ ***
Time	3	$7.28*10^{-9}$	$2.43*10^{-9}$	5.11	0.0019**
Oil:Temperature	20	$5.01*10^{-8}$	$2.51*10^{-9}$	5.28	$5.76*10^{-11}$***
Oil:Time	15	$7.21*10^{-9}$	$4.81*10^{-10}$	1.01	0.44
Temperature:Time	12	$1.69*10^{-8}$	$1.41*10^{-9}$	2.96	0.00073***
Oil:Temperature:Time	60	$2.78*10^{-8}$	$4.63*10^{-10}$	0.97	0.54
Residuals	240	$1.14*10^{-7}$	$4.75*10^{-10}$		

Signif. codes: 0 ‘***’ 0.001 ‘**’ 0.01 ‘*’ 0.05 ‘.’ 0.1 ‘ ’ 1

Table S.5.4 Analysis of Variance table for the effects of oil content, heating temperature and time on the NIR signal at 830 nm after pre-processing with SNV and 2nd derivative.

	Df	Sum Sq	Mean Sq	F-value	Pr(>F)
Oil	5	$1.14*10^{-10}$	$2.28*10^{-11}$	142.36	$<2.2*10^{-16}$ ***
Temperature	4	$1.02*10^{-10}$	$2.54*10^{-11}$	158.37	$<2.2*10^{-16}$ ***
Time	3	$5.97*10^{-12}$	$1.99*10^{-12}$	12.40	$1.44*10^{-7}$***
Oil:Temperature	20	$2.62*10^{-11}$	$1.31*10^{-12}$	8.17	$<2.2*10^{-16}$ ***
Oil:Time	15	$3.09*10^{-12}$	$2.06*10^{-13}$	1.28	0.21
Temperature:Time	12	$2.43*10^{-11}$	$2.02*10^{-12}$	12.61	$<2.2*10^{-16}$ ***
Oil:Temperature:Time	60	$1.38*10^{-11}$	$2.30*10^{-13}$	1.43	0.031*
Residuals	240	$3.85*10^{-11}$	$1.60*10^{-13}$		

Signif. codes: 0 ‘***’ 0.001 ‘**’ 0.01 ‘*’ 0.05 ‘.’ 0.1 ‘ ’ 1

Table S.5.5 Analysis of Variance table for the effects of oil content, heating temperature and time on the NIR signal at 1881 nm after pre-processing with SNV and 2nd derivative.

	Df	Sum Sq	Mean Sq	F-value	Pr(>F)
Oil	5	$4.88*10^{-7}$	$9.76*10^{-8}$	111.73	$<2.2*10^{-16}$ ***
Temperature	4	$2.24*10^{-7}$	$5.59*10^{-8}$	64.00	$<2.2*10^{-16}$ ***
Time	3	$6.14*10^{-9}$	$2.05*10^{-9}$	2.34	0.074.
Oil:Temperature	20	$1.25*10^{-7}$	$6.25*10^{-9}$	7.15	$1.44*10^{-15}$ ***
Oil:Time	15	$1.71*10^{-8}$	$1.14*10^{-9}$	1.30	0.20
Temperature:Time	12	$1.12*10^{-8}$	$9.31*10^{-10}$	1.07	0.39
Oil:Temperature:Time	60	$7.68*10^{-8}$	$1.28*10^{-9}$	1.46	0.024*
Residuals	240	$2.10*10^{-7}$	$8.74*10^{-10}$		

Signif. codes: 0 ‘***’ 0.001 ‘**’ 0.01 ‘*’ 0.05 ‘.’ 0.1 ‘ ’ 1

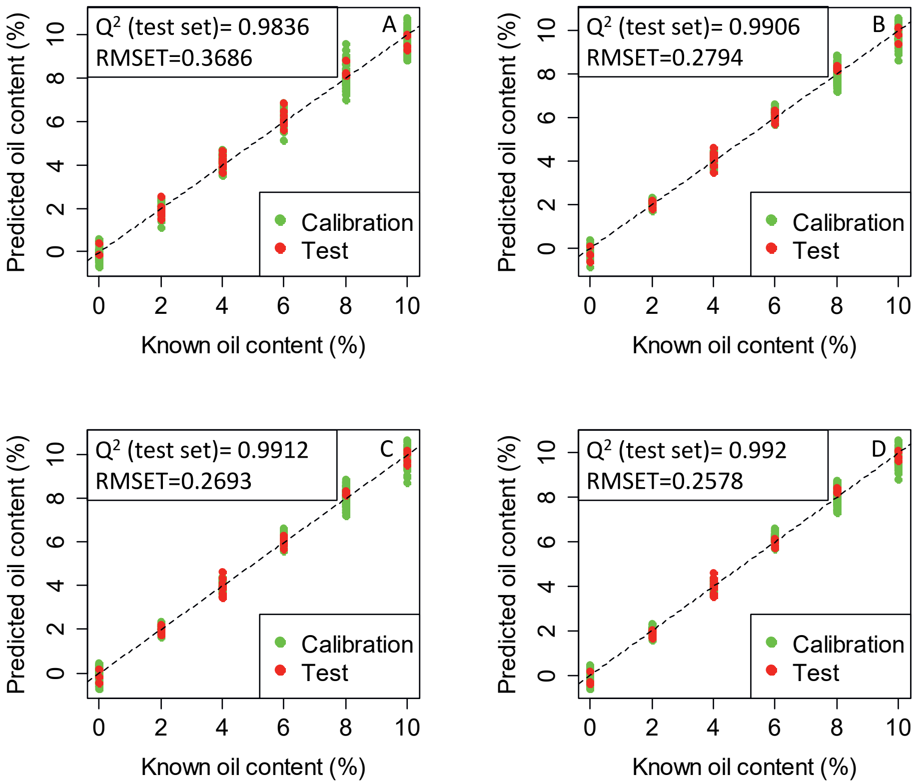

Fig. S.5.6 Predicted oil content plotted against observed oil content for linear regression model based on A. 1219 nm, B. 1219 and 1190, C. 1219, 1190 and 1397 nm, D. 1219, 1190, 1397 and 830 nm.

Table S.5.6 P-values of correlation residuals with oil, temperature and time for multiple linear regression model for oil content based on the subsequent inclusion of the wavelengths selected with SW-MLR.

Wavelengths included in the MLR model	**Oil**	**Temperature**	**Time**
1219 nm	0.020	0.000	0.713
1219 and 1190 nm	0.086	0.475	0.273
1219, 1190 and 1397 nm	0.104	0.382	0.632
1219, 1190, 1397 and 830 nm	0.127	0.851	0.871
1219, 1190, 1397, 830 and 1881 nm	0.143	0.761	0.727

Chapter 6

Near-infrared spectroscopy to quantify overall thermal process intensity during high-moisture extrusion of soy protein concentrate

This chapter has been published as Köllmann, N., Vringer, R., Mishra, P., Zhang, L., & van der Goot, A. J. (2024). Near-infrared spectroscopy to quantify overall thermal process intensity during high-moisture extrusion of soy protein concentrate. *Food Research International*, *186*, 114320.

6.1 Abstract

High-moisture extrusion (HME) is widely used to produce meat analogues. During HME the plant-based materials experience thermal and mechanical stresses. It is complicated to separate their effects on the final products because these effects are interrelated. In this study we hypothesize that the intensity of the thermal treatment can explain a large part of the physicochemical changes that occur during extrusion. For this reason, near-infrared (NIR) spectroscopy was used as a novel method to quantify the thermal process intensity during HME. High-temperature shear cell (HTSC) processing was used to create a partial least squares (PLS) regression curve for processing temperature under controlled processing conditions (root mean standard error of cross-validation (RMSECV)=4.00 °C, coefficient of determination of cross-validation (R^2_{CV})=0.97). This PLS regression model was then applied to HME extrudates produced at different screw speeds (200-1200 rpm) and barrel temperatures (100-160 °C) with two different screw profiles to calculate the equivalent shear cell temperature as a measure for thermal process intensity. This equivalent shear cell temperature reflects the effects of changes in local temperature conditions, residence time and thermal stresses. Furthermore, it can be related to the degree of texturization of the extrudates. This information can be used to gain new insights into the effect of various process parameters during HME on the thermal process intensity and extrudate quality.

6.2 Introduction

High-moisture extrusion (HME) is commonly used to produce fibrous plant-based products with a similar structure to animal meat (Schmid et al., 2022). During this process, plant-based ingredients are mixed with water, sheared, and heated in the extrusion barrel after which the material is pushed through a long cooling die (Opaluwa et al., 2023). Even though extrusion for meat analogue applications was developed already approximately 50 years ago, improvements in the technology seem still possible (Puski & Konwinski, 1976). The development of new extruded products is now mostly based on empirical research, in which the effects of single process parameters on the final product properties are investigated (Emin, 2022). However, the effect of the interactions with other process parameters should be considered as well to better understand the structure formation (Schmid et al., 2022). The hypotheses that are currently available for the mechanisms that cause fibrous structure formation were recently summarized by van der Sman & van der Goot (2023) and Schmid et al. (2022).

One of the prerequisites for fibrous structure formation during HME is the change of physicochemical properties of the ingredients, such as protein denaturation and aggregation or starch gelatinization and degradation (van der Sman & van der Goot, 2023; Z. Zhang et al., 2022). The kinetics of these changes are influenced by the thermal and mechanical treatment of the product inside the extrusion barrel (Pietsch, Schöffel, et al., 2019; Tian et al., 2023). The reactions that take place in the extruder barrel affect the rheological properties and the flow pattern and therefore affect all subsequent steps in the structure formation process (Pietsch, Werner, et al., 2019).

Several authors already investigated the effect of ingredient composition (Chen, Zhang, Liu, et al., 2023; Nasrollahzadeh et al., 2022; Riazi et al., 2023) or processing conditions (Meng et al., 2022; Sun et al., 2022; X. Zhang et al., 2022) on the changes in protein structure during HME. However, evaluating the effect of all process parameters on the possible reactions for all ingredients used would be extremely time-consuming and costly. Furthermore, the effect of a single process parameter cannot be studied in isolation since they often have interlinked effects on the final products, as is the case for barrel temperature and screw speed (Schmid et al., 2022).

Here, we hypothesize that the thermal treatment is critical to ensure the necessary physicochemical changes in the product and thus the required rheological properties and flow pattern to allow structure formation during HME. This hypothesis relies on the premise that the shear rates the plant-based material experiences during HME are insufficient to initiate protein denaturation (Jaspe & Hagen, 2006), whereas it is well-known that thermal treatment has this effect. This is further supported by the minimum texturization temperature as established by Högg & Rauh (2023), which confirms that thermal treatment is the most important factor for HME structuring. However, it should be noted that shear stresses can lower the activation energy for protein denaturation and affect protein aggregation (Pommet et al., 2004; Quevedo et al., 2020; Sharma & Pandey, 2021; Wolz & Kulozik, 2015). A rapid method to determine the combined effect of multiple extrusion parameters on the thermal process intensity would therefore be desired.

An attempt to develop a rapid method to assess the overall effect of process intensity on extruded pea protein has been already made by Ben-Hdech et al. (1993). They successfully used near-infrared (NIR) spectroscopy in combination with principal component analysis (PCA) to rapidly classify extruded pea protein into different categories based on process intensity. NIR spectroscopy is a rapid and non-destructive measurement technique that relies on the absorption of NIR radiation by CH, OH and NH bonds (Ozaki & Morisawa, 2021). The technique has previously been used to successfully assess the end point temperature of sausages (Wold et al., 2020), pâté (O'Farrell et al., 2011) and fish products (Skåra et al., 2014; Uddin et al., 2002, 2005, 2006; Wold, 2016). This applicability of NIR spectroscopy for the measurement of thermal effect mainly relies on the effect of protein denaturation and changes in the protein-water interaction on the NIR spectra (Ellekjaer & Isaksson, 1992; Uddin et al., 2002). NIR measurements of powdered extrudates were previously correlated to the specific mechanical energy input (SME) during cereal extrusion (Guy et al., 1996). However, to the best of our knowledge, NIR has not been applied for the measurement of process intensity of meat analogue products processed by HME yet. This study therefore aims to use NIR spectroscopy to quantify the overall thermal process intensity on products during high-moisture extrusion.

To circumvent the complex interrelated process parameters and high sample amount during HME, high-temperature shear cell (HTSC) processing was used to create a calibration model for thermal process intensity. In this study NIR spectra of HTSC products produced at different processing temperatures were used to create a calibration model for the thermal process intensity using partial least squares (PLS) regression. The influence of processing time (2.5-10 min) on the performance of the calibration model was also quantified, because heating time is known to influence protein denaturation and the NIR spectra of heated protein systems (Skåra et al., 2014). Then, the same calibration model was applied on the NIR spectra of HME extrudates that were produced at different screw speeds (200-1200 rpm), barrel temperatures (100-160 °C) and with two different screw profiles. This method was used to calculate the equivalent shear cell temperature of these extrudates. Subsequently, the effects of these processing parameters on the equivalent shear cell temperature and thus the extent of thermal processing were evaluated. Finally, the relationship between the thermal process intensity and the degree of texturization of the extrudates was explored. This study thus describes a method that quantifies how processing variables influence NIR spectra of HTSC products and extrudates, how these results can be used to generate new insights on the development of inline processing optimisation methods for better quality control of plant-based meat analogues.

6.3 Materials and methods

6.3.1 Materials

ALPHA® 8 IP functional soy protein concentrate (SPC) was purchased from Solae, LCC (St. Louis, MO, USA). The dry matter content of the SPC was 93.9wt.% and protein content as measured with the Dumas combustion method 62.0wt% (Nx5.71) based on dry matter.

6.3.2 High temperature shear cell processing

To prepare the high-temperature shear cell (HTSC) products, first 39wt% SPC (on dry matter basis) was manually mixed with demineralized water. The mixture was subsequently hydrated at room temperature for 30 min. The hydrated SPC was then thermo-mechanically treated in an in-house developed HTSC (Grabowska et al., 2016), driven by a Haake PolyLab QC system (Thermo Fisher Scientific, Waltham, MA, USA), at varying conditions. Prior to the thermo-mechanical treatment, the shear cell was pre-heated to the desired processing temperature using an oil bath. After the heat treatment, an additional oil bath was used to cool the product to 50 °C. After complete cooling to room temperature, the products were stored at -20°C until further usage.

Two different groups of HTSC products were produced by varying processing temperature or time. Firstly, products were produced using a temperature range from 90 to 160 °C with steps of 10 °C at a constant rotational speed of 30 rpm and processing time of 15 min to create the partial least squares (PLS) regression model for processing temperature. Secondly, processing time was varied from 2.5-15 min with steps of 2.5 min at a constant temperature (140 °C) and rotational speed (30 rpm) to evaluate the effect of time on the predicted temperature.

6.3.3 Extrusion

The extrusion experiments were carried out using a TwinLab-F 20/40 (Brabender GmbH & Co KG, Duisburg, Germany) co-rotating twin screw extruder with a modular cooling die (300 x 25 x 7 mm) (Brabender GmbH & Co KG, Duisburg Germany). The extruder was controlled by MetaBridge software (Brabender GmbH & Co KG, Duisburg, Germany). For all experiments, a screw with a diameter of 20 mm and length-to-diameter ratio of 40 was used. Two different screw profiles (A/B) depicted in Fig. 6.1 were used. Screw profile A consisted of conveying elements (SE) only. In screw profile B, three types of screw elements were used: SE, a tooth mixing element (Z), and kneading elements (KBW). SE and KBW elements were built in forwarding (R) and reverse directions (L).

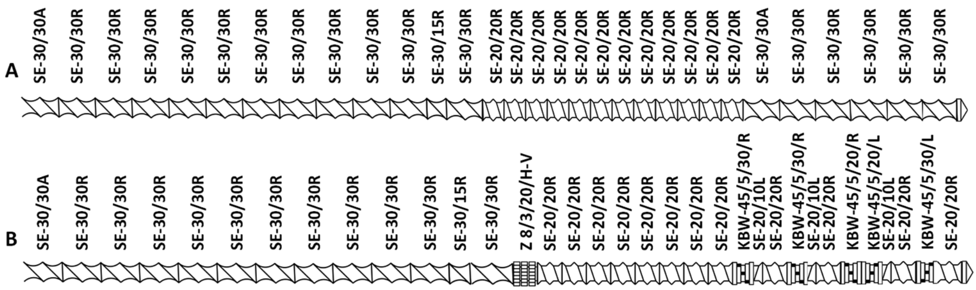

Fig. 6.1 Overview of the screw profiles used during HME. Screw profile A without kneading or reverse screw elements and screw profile and B with kneading and reverse screw elements.

The extrusion barrel was divided into four temperature-controlled zones. Each heating zone was heated separately by an electric cartridge heating system and cooled by a water-cooling system (Weinreich WTD 2es, Weinreich Industriekühliung GmbH, Lüdenscheid, Germany). A modular cooling die (300x25x7 mm) was cooled using a refrigerated water circulator set at 25 °C. The extruder responses, including melt temperature, load (%), and pressure were recorded.

The dry powder was fed into the extruder at a feed rate of 4.5 kg/h and the feed moisture content was fixed at 61wt% (i.e., 39wt% SPC content). The temperature in the final heating zone (°C) and screw profile were varied according to the experimental design shown in Table 5.1. For every temperature profile the screw speed was varied from 200-1200 rpm with steps of 200 rpm.

Table 6.1 Temperature profiles applied for screw profile A and B during high-moisture extrusion (HME).

Temperature (Heating zone 1|2|3|4 °C)	**Screw profile (A/B)**
40|80|100|100	A, B
40|80|110|110	B
40|80|110|120	A, B
40|80|110|130	B
40|80|110|140	A, B
40|80|110|150	B
40|80|110|160	A, B

Sample collection was performed when the extruder had reached a constant melt temperature for at least 2 minutes. The collected samples were stored at -20°C before further analysis.

6.3.4 Near-infrared (NIR) measurements

NIR spectral measurements were performed by a Hi-Res, ASD LabSpec spectrometer (Malvern Panalytical, Malvern, United Kingdom). The measurements were performed using an area scan probe (Hi-Brite probe) with a spot size of 10 mm. The probe was placed in a tripod and placed above the sample as close as possible without touching the HTSC product or extrudate. Before measurement the HTSC product or extrudate was completely thawed and the measurement was performed at room temperature. The NIR spectra of the HTSC products were measured in the middle of the HTSC product radius. NIR-spectra of the extrudates were taken at three different locations within one extrusion sample. The probe had an inbuilt 6.5 W halogen light source for illumination and optical fibres were used to capture the reflected light. The instrument was controlled using the Indico Pro software (Malvern Panalytical, Malvern, United Kingdom). The integration time was automatically optimized by the Indico Pro software and was initially set at 15 ms. Each measurement was an average of ~5 consecutive measurements automatically performed by the Indico Pro software. The radiometric calibration with white and dark reference was performed by the Indico Pro software automatically.

6.3.5 NIR data analysis

Pre-processing

NIR spectra in the wavelength range of 400-2200 nm were used for further data analysis. To reduce the effect of colour changes and the high moisture content of our products the use of a reduced wavelength range of 800-1400 nm was also explored. Prior to analysis of the NIR reflectance spectra were transformed to absorbance using a -log transformation. Subsequently, scattering in the NIR reflectance spectra was reduced using standard normal variate (SNV) correction. In SNV correction, each spectrum is centred and divided by its standard deviation, resulting in a common scale for all spectra (Barnes et al., 1989). Finally, the absorbance data was smoothened using the Savitsky-Golay (SAVGOL) (Savitzky & Golay, 1964) algorithm and the 1st derivative was estimated to reveal underlying peaks. A window size of 51 was used for smoothening.

Partial least squares regression

Partial least squares (PLS) regression modelling is a commonly used chemometric technique for the interpretation of NIR spectral data (Wold et al., 2001). In this study PLS regression was applied to the HTSC products for which the set heating temperature was the independent variable. Of each processing condition, HTSC experiments of SPC samples were performed in triplicate, yielding three independent HTSC products. NIR spectra of two of these HTSC products were used as calibration set (total of 16 samples), and the third set of samples was served as cross-validation set (total of 8 samples). PLS regression was implemented with MATLAB's default 'plsregress' function (MATLAB R2021b, Natick, WA, USA). A default leave-one-out cross-validation was integrated for optimising the latent variables (LVs). The LVs were then selected by identifying the inflection point. The LV selection results can be found in Fig. S.6.1. PLS regression modelling was performed for both the complete (400-2200 nm) and smaller wavelength range (800-2200 m). The calibration and prediction results were analysed in terms of the root mean standard error of calibration (RMSEC), root mean standard error of the cross-validation (RMSECV), coefficient of determination of calibration (R^2_c), coefficient of determination cross-validation (R^2_{cv}) and prediction bias.

6.3.6 Equivalent shear cell temperature

The PLS regression model for the processing temperature of HTSC products based on the reduced wavelength range of 800-1400 nm was used to calculate the equivalent shear cell temperature from the pre-treated NIR spectra of the extrudates. This equivalent shear cell temperature was used as an indicator of the overall thermal process intensity. It indicates the temperature at which a HTSC product would need to be sheared at 30 rpm for 15 min to achieve a similar thermal process intensity as the extrudate that was measured.

6.3.7 Cutting test for extrudates

The force required for cutting the extrudates was measured using a texture analyser with a load cell of 50 N (TA.XT plusC, Stable Micro Systems, Godalming, Surrey, UK) with a guillotine edge blade (HDP/BS). The thawed extrudates were cut to have approximate size of 24×24 mm. Before measurement the texture analyser was set to an initial height of 10 mm. Subsequently, the squared extrudates were compressed to 90% of its original thickness at a cutting speed of 1 mm/s. The maximum cutting force ($Fmax$) was measured in both parallel and perpendicular direction to the extrusion flow in the cooling die. The degree of texturization was calculated using Eq. 6.1.

$$Degree\ of\ texturization = F_{max,\perp}/F_{max,\parallel} \qquad Eq.\ 6.1$$

In which, $F_{max,\perp}$ is the maximum cutting force in perpendicular direction (N) and $F_{max,\parallel}$ the maximum cutting force in parallel direction (N).

6.4 Results and discussion

6.4.1 High-temperature shear cell products

Absorbance spectra

High-temperature shear cell (HTSC) processing was used to study the effect of processing temperature during thermomechanical structuring on the near-infrared (NIR) spectra of the resulting products. Fig. 6.2 shows the average absorbance spectra in the wavelength ranges of 400-2200 nm and 800-1400 nm of HTSC products that were treated at a temperature ranging from 90-160 °C.

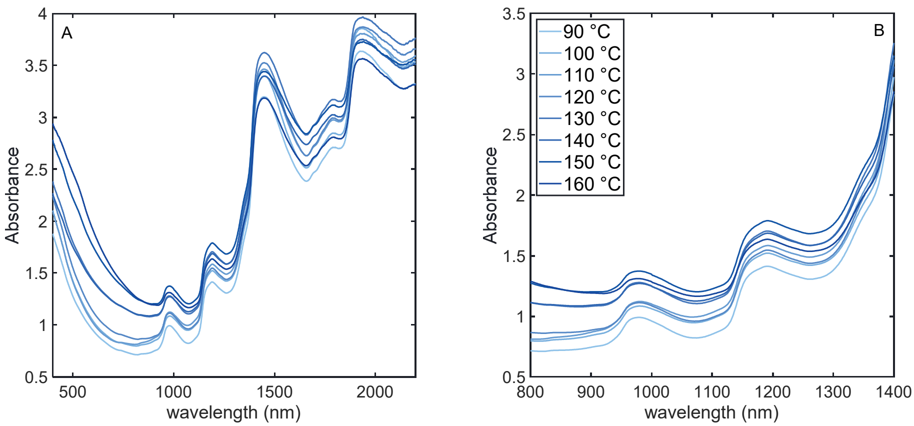

Fig. 6.2 Absorbance spectra in the full (400-2200 nm) (A) and reduced (800-1400 nm) (B) spectral range of HTSC products treated at temperatures ranging from 90-160 °C, as indicated by colours ranging from light to dark blue, at a constant rotational speed (30 rpm) and processing time (15 min).

In the visual wavelength range (400-750 nm) the absorbance increases with an increasing processing temperature (Fig. 6.2A) especially for samples processed at 150 °C and 160 °C. This is in line with the darkened colour of these samples as compared to samples processed at a lower temperature (Fig. S.6.2). The formation of the brown colour could be attributed to Maillard reactions (Taghian Dinani, Charles Carrillo, et al., 2023) and/or sugar caramelization (Schmid et al., 2022). Nevertheless, in some previous studies on high-moisture extrusion (HME) and HTSC processing, Maillard reaction products were not detected in obtained products, which could be due to the low amount of reducing sugars in the ingredients used in these studies and the high moisture content that suppresses these reactions (Osen et al., 2015; Wehrmaker et al., 2022).

The main peaks in the absorbance spectra occur around 980, 1200, 1450, and 1930 nm (Fig. 6.2A). This corresponds with the third overtone of OH, the second overtone of CH, the second overtones of CH, $CONH_2$ and ROH and the first overtone of OH and $CONH_2$ respectively (van Staveren, 2020). These peaks were expected because the products consisted of water, protein, and carbohydrates mainly.

A higher absorbance at around 980 nm was observed when a higher HTSC processing temperature was applied (see Fig. 6.2A), which suggested an increase in water content of the HTSC products. However, this was not confirmed by measuring the moisture content of the products after processing in the HTSC, expect for products produced at 160 °C, which had a lower moisture content (Fig. S.6.3). Furthermore, an increase in absorbance was not observed in the 1st (1900-1960 nm) and 2nd OH overtone (1400-1450 nm) bands. The higher absorbance at around 980 nm at higher processing temperature can be related to a change in the state of the water or it could be a spectral artefact.

At around 1200 nm, the wavelength corresponding to the 2nd overtone of CH bonds, the absorbance increased with an increasing processing temperature. This indicates that the carbohydrate structure changed due to thermal processing, which was also previously suggested for HME extrudates (De Angelis et al., 2023; Pietsch, Bühler, et al., 2019).

In addition, we observed an increase of absorbance at 1450 and 1930 nm (which both correlated to $CONH_2$ bonds) when increasing the processing temperature from 90 °C to 130 °C, which indicated the formation of additional peptide bonds and thus protein aggregation. Interestingly, a further increase of the processing temperature from 130 °C to 160 °C led to a decrease in absorbance at 1450 and 1930 nm, indicating a decrease in the number of peptide bonds. We suspect that changing processing temperature of HTSC process influenced protein-protein interactions of soy protein concentrate (SPC) through a complex mechanism: protein aggregation was induced by the heat treatment, while the peptide bonds broken down when the temperature was further increased. This could be due a shift in the balance between disulphide bonds, hydrophobic and electrostatic interactions which all contribute to thermal aggregation (Ju et al., 2023; Liu & Hsieh, 2007). However, Pietsch, Bühler, et al. (2019) and Wittek, Zeiler, et al. (2021) did not find a change in protein-protein interactions upon heating during HME at a melt temperature of 100-160 °C or 124/135 °C respectively.

Alternatively, the changes in absorbance at 1930 nm can be attributed to the changes in the carbonyl groups of the protein. Previous research has shown a correlation between the carbonyl groups of whey protein isolate and their NIR spectra because of protein oxidation following thermal treatment (Bordignon et al., 2023). Protein oxidation also occurs during HTSC processing as found by Duque-Estrada et al. (2020) and Wehrmaker et al. (2022). It can therefore be concluded that protein oxidation is one of the physicochemical changes induced by HTSC processing reflected by the NIR absorbance spectra.

To reduce the effect of colour changes and the high water content of our HTSC products on the partial least squares (PLS) regression model for processing temperature, the use of a reduced wavelength range of 800-1400 nm was also explored (Fig. 6.2B). Thus, the visual wavelength range of 400-750 nm and the strong NIR absorption bands associated with water around 1400-1440 nm and 1900-1950 nm were not included in the PLS regression model (Büning-Pfaue, 2003). The reduced wavelength range resulted in a clearer trend with processing temperature compared to the complete spectra at wider wavelength ranges (Fig. 6.2). Furthermore, principal component analysis (PCA) analysis showed that the largest part of the variation in these spectra can be related to changes in the processing temperature (Fig. S.6.4).

Summarizing, the effect of temperature on the absorbance spectra indicates that the thermal process intensity indeed affects the protein and carbohydrate properties during the HTSC and HME processes, and that NIR is a suitable technique to capture this effect.

Partial least squares (PLS) regression models

The result of the PLS models based on the complete and reduced wavelength ranges for the processing temperature in the HTSC of products processed at 30 rpm for 15 min are shown in Fig. 6.3. For both wavelength ranges it was possible to create a PLS model (root mean standard error of calibration (RMSEC)=1.05 and RMSEC=3.65) with a low error of cross-validation (root mean standard error of cross-validation (RMSECV)=4.47 and RMESCV=4). This indicates that NIR spectroscopy is a suitable technique for the quantification of thermal effects during HTSC processing. The required number of latent variables (LVs) was higher for the complete spectrum compared to number needed when using the reduced wavelength range. Furthermore, the prediction bias of the model based on the reduced wavelength range was lower (0.89 instead of -2.22). Finally, the difference between the RMSEC and RMSECV was larger for the complete wavelength range compared with the reduced wavelength range which is an indication for overfitting (Shen et al., 2011). For these three reasons the PLS model based on the reduced wavelength range was selected for further analysis of HTSC products and extrudates. This gives an additional advantage being that colour changes and small changes in the water content have a smaller effect on the outcome of the calibration model.

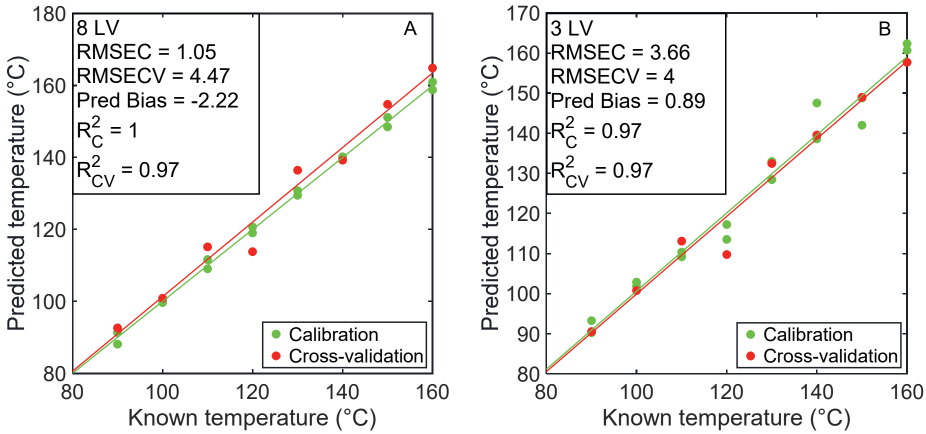

Fig. 6.3 PLS regression calibration model for processing temperature in the HTSC based on standard normal variate (SNV)+1st derivative NIR absorbance of the full (400-2200 nm) (A) and reduced (800-1400 nm) (B) spectral range.

The regression coefficient of the model for the reduced wavelength range is shown in Fig. 6.4 to better understand which wavelengths and chemical components influence the PLS model for HTSC processing temperature the most. These three wavelengths were 945, 1138 and 1028 nm respectively, as indicated by the high absolute values of the regression coefficient. These wavelengths correspond to the 3rd overtone of OH, the 2nd overtone of CH_3 and 3rd overtone of RNH_2 bonds respectively. Because the main effect of protein denaturation on the NIR spectra is a result of changes in protein confirmation and protein-water interactions, it is not surprising that the overtones related to OH and NH_2 groups contributed most to the regression coefficient. The importance of the 2nd overtone of CH_3 confirms the relevance of the CH bonds for the prediction of processing temperature (De Angelis et al., 2023; Pietsch, Bühler, et al., 2019). The results described in this section show that NIR spectroscopy is a suitable technique to measure the thermal effect on the different components in plant-based meat analogues.

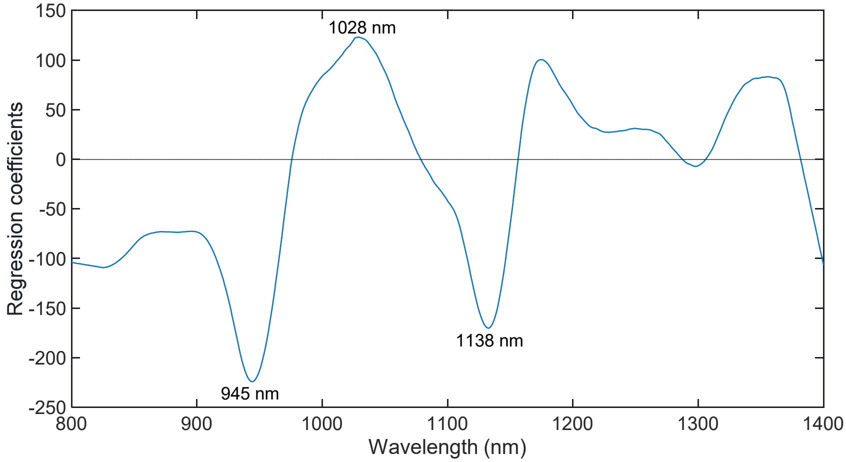

Fig. 6.4 Regression coefficient PLS regression model for processing temperature in the HTSC based on the reduced (800-1400 nm) spectral range. The highest peaks are annotated with wavelength number.

Effect of processing time in HTSC on predicted temperature

Processing time is an important difference between HTSC processing, for which the standard processing time is 15 min, and HME, for which the residence time ranges between 2-5 min (Cornet et al., 2022). Processing time also affects the thermal process intensity, as it influences the extent of protein denaturation, in addition to the heating temperature. Correspondingly, Skåra et al. (2014) reported changes in NIR absorbance of surimi because of both heating temperature and heating time. For this reason, the effect of shorter HTSC processing times (2.5-10 min) on the absorbance spectra and predicted temperature was measured.

The absorbance spectra of the HTSC products produced at shorter processing times showed a similar pattern compared to the HTSC products on which the PLS regression was based, with peaks around 980 and 1200 nm (Fig. 6.2 and Fig. 6.5A). This was expected because the products had the same composition. Nevertheless, the processing time during HTSC processing influenced the absorbance spectra of HTSC products (Fig. 6.5A). At wavelengths above 1300 nm the absorbance spectra of HTSC products processed for 7.5-15 min were very similar. This indicates that for these processing times the protein-water interactions and protein bonds that are formed are very similar, because this wavelength range is linked to NH and OH overtones (van Staveren, 2020). However, at shorter wavelengths the absorbance increases with increasing processing times from 7.5-15 min.

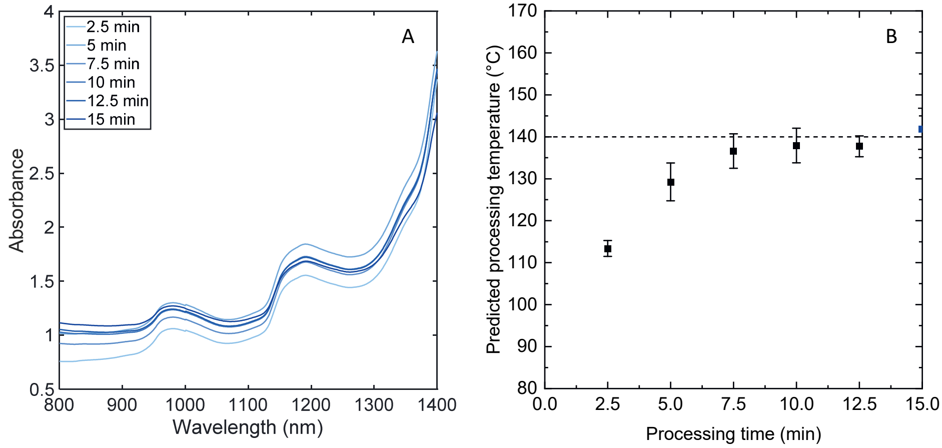

Fig. 6.5 NIR absorbance spectra of HTSC products produced at varying processing time (A) and the predicted processing temperature of these products (B). Dotted line indicates the set processing temperature. The blue point indicates the processing time that was part of the calibration set of the PLS regression model for processing temperature (15 min).

When applying the PLS regression model for processing temperature it can be observed that shorter processing times resulted in a lower predicted processing temperature (Fig. 6.5B). The predicted processing temperature stabilizes at processing times ≥7.5 min, which implicates that physicochemical changes induced by heating mainly occur within the first 7.5 min of the process. This indicates that, to a certain extent, the NIR measurement reflects the time dependency of the reactions that take place during HTSC processing in addition to the effect of temperature and could therefore be used as to quantify the intensity of thermal processing. The typical residence time during HME ranges from 2.5-5 min (Cornet et al., 2022) and residence time is therefore expected to be reflected in the thermal process intensity as measured with NIR spectroscopy with the approach presented in this study.

6.4.2 Application to extrudates

Absorbance spectra

The average absorbance spectra of extrudates produced with screw profile A (without kneading or reverse screw elements) at 100-160 °C and 200-1200 rpm are shown in Fig. 6.6. The absorbance spectrum of these HME extrudates shows peaks at similar locations as HTSC products (Fig. 6.2 and Fig. 6.6), which was expected given their similar composition. Temperature had a limited effect on the absorbance of these extrudates. However, screw speed resulted in a slight decrease in the absorbance, though this effect is reduced by the applied pre-processing (Fig. S.6.5).

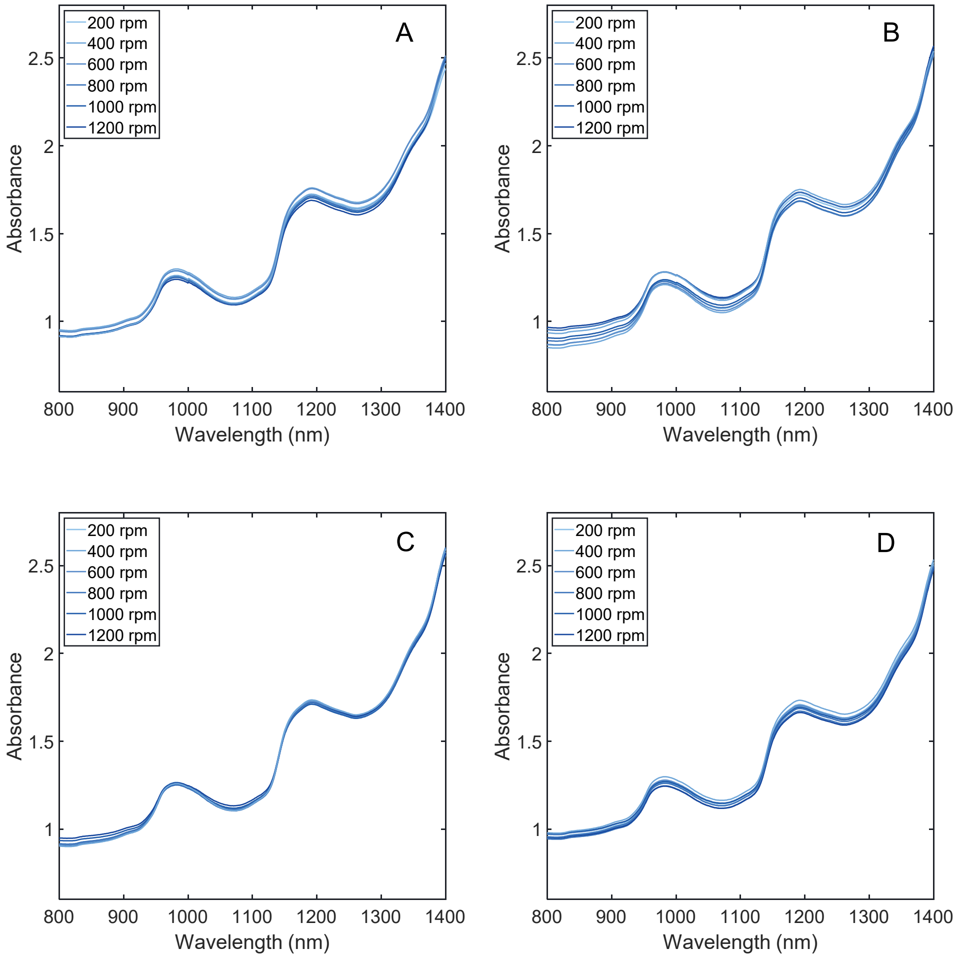

Fig. 6.6 Absorbance spectra of HME extrudates produced with screw profile A at screw speeds of 200-1200 rpm as indicated by colours ranging from light to dark blue at a barrel temperature of 100 (A), 120 (B), 140 (C) or 160 °C (D).

The average absorbance spectra of extrudates produced with screw profile B (with kneading elements) at 100-160 °C and 200-1200 rpm are shown in Fig. 6.7. These absorbance spectra showed a similar pattern to those of extrudates produced with screw profile A (Fig. 6.6). However, here, the screw speed affected the NIR spectra of extrudates more. This was not surprising as an increase in screw speed when using screw B will result in a larger increase in the shear stresses and thus in a larger temperature increase caused by viscous dissipation compared to screw profile A (Ellwanger et al., 2023). It should be noted that both an increase in screw speed and temperature resulted in a decreased absorbance, which is opposite to the trend that was observed for the processing temperature for HTSC products (Fig. 6.2). However, this difference which is most likely caused by baseline shifts is solved by the pre-processing steps applied to the spectra (SNV and 1st derivative) and therefore does not affect the applicability of the PLS regression model (Fig. S.6.6).

It should be noted that pre-processing of the spectral data is crucial for the applicability of the PLS regression model, as it reduces scattering effects caused by structural differences between HTSC products and extrudates. Furthermore, both HTSC and HME products were measured under the same measurement conditions in this study. However, changes in measurement conditions or instrument changes can affect the measured NIR spectra. This should therefore be considered when applying this approach on an industrial scale, for example by standardization of the NIR spectra (Zhang et al., 2019).

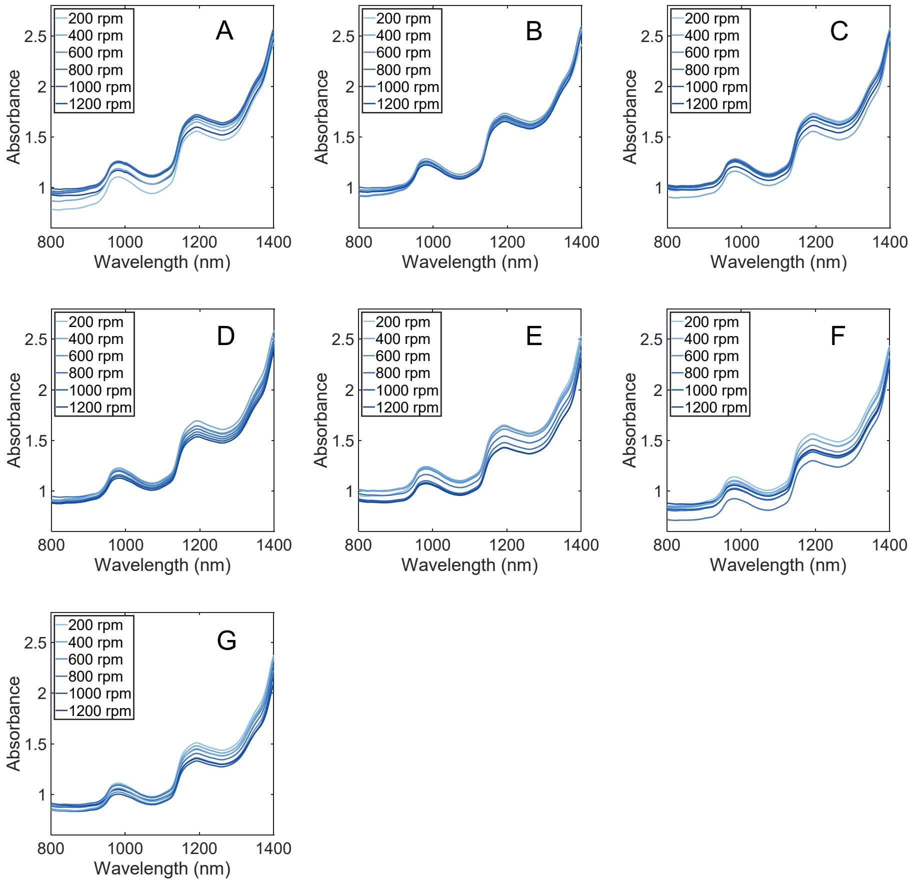

Fig. 6.7 Absorbance spectra of HME extrudates produced with screw profile B at screw speeds of 200-1200 rpm as indicated by colours ranging from light to dark blue at a barrel temperature of 100 (A), 110 (B), 120 (C), 130 (D), 140 (E), 150 (F) or 160 °C (G).

6

Equivalent shear cell temperature of extrudates

The calibration curve created for the processing temperature during HTSC processing was applied to the NIR spectra that were measured for the extrudates, to calculate the so-called "equivalent shear cell temperature". This equivalent shear cell temperature indicates at which processing temperature a product would need to be processed in the HTSC for 15 min at 30 rpm to achieve an equivalent thermal process intensity as during HME. This indicator for thermal processing intensity thus gives insights in the overall process intensity of HME. Thermal process intensity is commonly quantified by the temperature that is measured just before the protein melt enters the cooling die (Ellwanger et al., 2023). For this reason, the equivalent shear cell temperature was plotted versus the measured melt temperature to verify the correlation between these two parameters (Fig. 6.8).

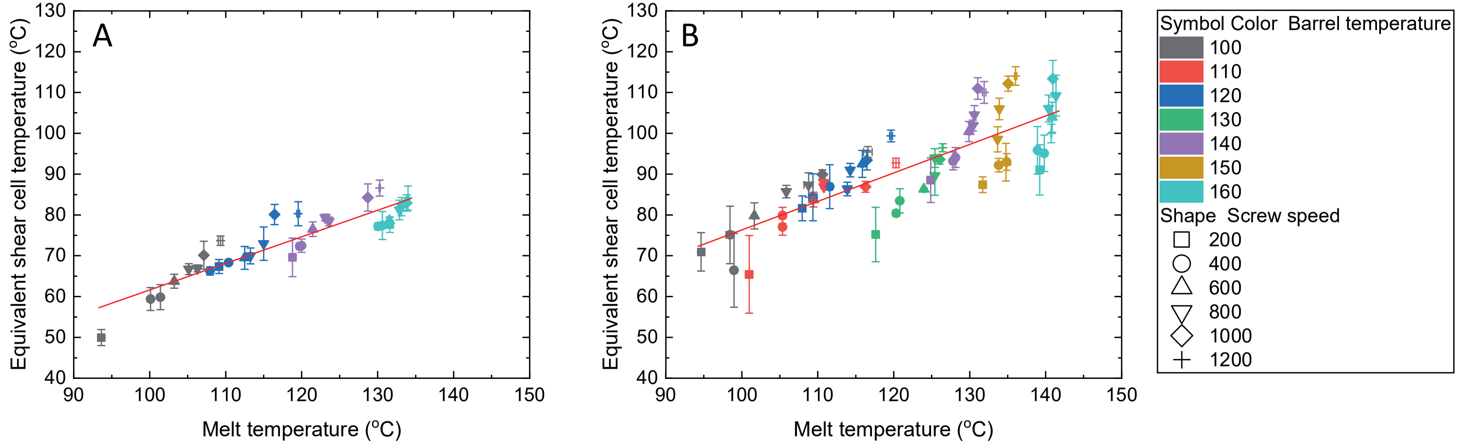

Fig. 6.8 Equivalent shear cell temperature of extrudates produced with screw profile A (A) and B (B) at 100-160 °C (indicated by symbol colour) and 200-1200 rpm (indicated by symbol shape). Red line is a linear fitted trend line for all data points.

6

The equivalent shear cell temperature rose with increasing barrel temperature and screw speed (Fig. 6.8), which is caused by heating from the barrel wall and viscous dissipation (Mateen et al., 2023). The equivalent shear cell temperature showed a correlation with the measured melt temperature (Table 6.2). The coefficient of determination of the prediction (R^2_p) when all temperatures were included was higher for screw A (R^2_p=0.78) than screw B (R^2_p=0.61). Moreover, the correlation between the melt temperature and shear cell temperature depended on the barrel temperature that was used and was highest at 100 °C for screw profile A (R^2_p=0.92) and 130 (R^2_pscrewB=0.82) and 140 °C (R^2_pscrewA=0.85, R^2_pscrewB=0.81) for both screw profiles. Whereas the R^2_p was lower at barrel temperature >140 °C. This can be explained by the limited effect of the screw speed on the melt temperature when the barrel temperature is set to ≥ 140 °C, while this is not the case for the equivalent shear cell temperature. This effect is most prominent for screw profile B. A similar influence of barrel temperature on interaction between screw speed and melt temperature was described by Mateen et al. (2023). They showed that a screw speed increase from 300 to 900 rpm had more effect when the barrel temperature wat set to 110 or 130 °C compared with set temperature 150 °C. Pietsch, Werner, et al. (2019) also observed that screw speed did not significantly contribute to the melt temperature at a barrel temperature of 155 °C, but it did at 100 and 125 °C.

Table 6.2 Overview residual mean square error of prediction (RMSEP), Prediction bias and R^2_p for equivalent shear cell temperature plotted against melt temperature of extrudates.

Barrel temperature	**Screw profile A**			**Screw profile B**		
	RMSEP	Bias	R^2_p	RMSEP	Bias	R^2_p
All temperatures	3.92	0.00	0.78	7.25	0.00	0.61
100 °C	1.98	0.00	0.92	5.02	0.00	0.75
110 °C		-		4.55	-0.03	0.71
120 °C	2.67	0.00	0.77	3.14	0.00	0.73
130 °C		-		3.16	0.00	0.82
140 °C	2.28	0.00	0.85	3.48	0.00	0.81
150 °C		-		7.18	0.00	0.44
160 °C	1.95	0.00	0.62	5.41	0.00	0.55

Contrarily to the melt temperature, the equivalent shear cell temperature increased with screw speed at barrel temperatures ≥ 140 °C (Fig. 6.8). This difference between melt and shear cell temperature is probably caused by the fact that melt temperature only provides information about the thermal process intensity at one position in the process. The shear cell temperature, on the other hand, reflects the total effect of the thermal treatment during HME process and therefore also includes the effect of local temperature maxima. This makes the equivalent shear cell temperature a relevant indicator for overall thermal process intensity, which provides more information than the melt temperature.

Notably, when plotted against melt temperature, the slope of the equivalent temperature increases exponentially with rising barrel temperatures, which is particularly noticeable for extrudates produced at a barrel temperature above 130 °C using screw B. This suggests that mechanical deformation has larger effect on the thermal process intensity than suggested by the melt temperature. This difference can be explained by the influence of local temperature changes resulting from viscous dissipation as was previously described. Additionally, shear stresses could accelerate reactions in the extruder, such as the aggregation and degradation of proteins, as shown for gluten and β-lactoglobulin because shear forces can lower activation energy (Pommet et al., 2004; Quevedo et al., 2020). These changes in chemical properties influence NIR spectra and therefore the equivalent shear cell temperature. However, it should be noted that shear on its own most likely does not cause protein denaturation (Jaspe & Hagen, 2006), but rather reinforces the thermal treatment.

The equivalent shear cell temperature was on average 45 °C lower than the melt temperature for screw A and 30 °C for screw B. The difference between the equivalent shear cell temperature and melt temperature increased with an increase in barrel temperature, which was clearest for screw A. The lower equivalent shear cell T compared to the barrel temperature can probably be attributed to the shorter residence time in the extruder (2-5 min) compared with the HTSC (15 min) (Cornet et al., 2022). This aligns with the effect of processing time on the predicted processing HTSC processing temperature (Fig. 6.5B). Interestingly, the smaller difference between melt temperature and equivalent shear cell temperature for screw B suggests that the product underwent a more intensive process, probably due longer residence time for extrudates processed with this screw and higher temperature due to viscous dissipation in the kneading zones (Ellwanger et al., 2023). The effect of residence time is not reflected in the melt temperature, which makes the equivalent shear cell temperature a valuable additional parameter for comprehensively studying thermal treatment.

Summarizing, the melt temperature and mechanical deformation influence the equivalent shear cell temperature. Because these parameters both influence the rheological properties of the SPC, they also have an influence on the pressure measured at the die entrance (Pietsch, Bühler, et al., 2019). This explains why the equivalent shear cell temperature correlates with the barrel pressure (Fig. S.6.7). A schematic overview of the relation between the processing parameters that were varied in this study and the intermediate processes that finally lead to a change in the equivalent shear cell temperature is shown in Fig. 6.9.

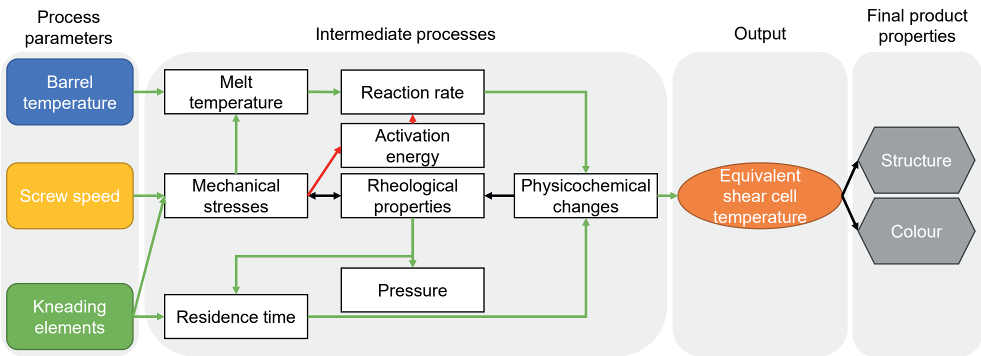

Fig. 6.9 Schematic overview of the effect of barrel temperature, screw speed and kneading elements on the intermediate processing conditions and the equivalent shear cell temperature. Green arrows indicate a positive relationship, red arrows indicate a negative effect and black arrows effects that can be positive or negative depending on the conditions

Effect of thermal process intensity on the structural properties of extrudates

The use of the equivalent shear cell temperature as an indicator for thermal process intensity, rather than the melt temperature, may offer an advantage by providing more information on complete effect of thermal processing on the final product properties. To verify this hypothesis the relation between the melt and equivalent shear cell temperature and the degree of texturization of the extrudates produced in this study was explored (Fig. 6.10). Similar plots for other textural properties (e.g., hardness or cutting strength) can be found in Fig. S.6.8-6.13. The degree of texturization is calculated as the ratio between the peak cutting force in the perpendicular direction and the parallel direction. A degree of texturization-value larger than 1 indicates alignment, whereas a degree of texturization smaller than 1 indicates an isotropic material without a fibrous or layered structure (Shrestha et al., 2024).

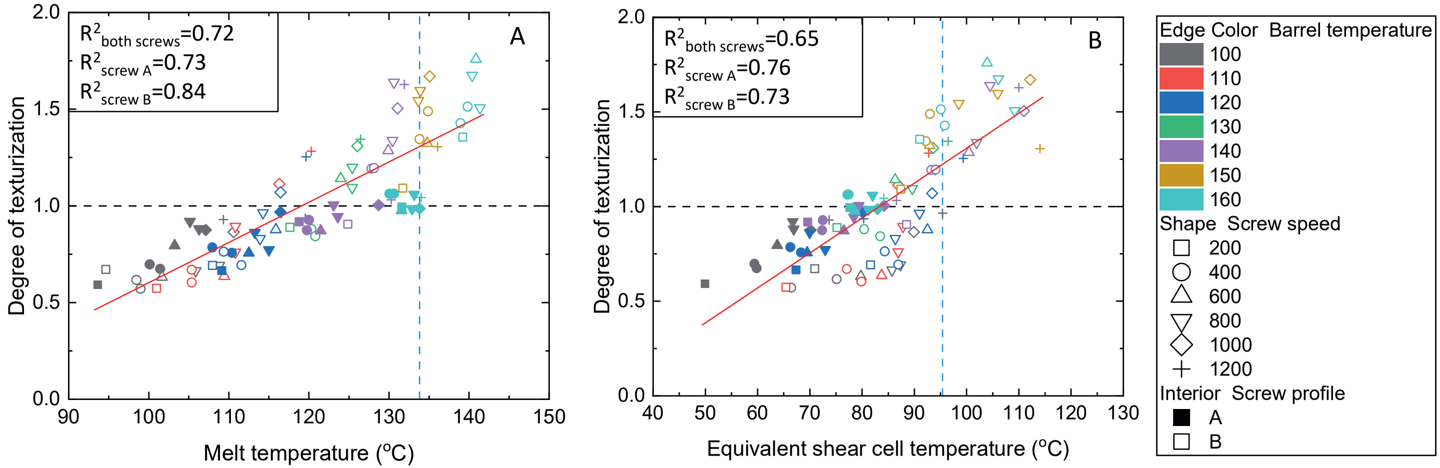

Fig. 6.10 Degree of texturization of extrudates produced with screw profile A (closed symbols) and B (open symbols) at 100-160 °C (indicated by symbol colour) and 200-1200 rpm (indicated by symbol shape) as measured in cutting test plotted against melt temperature (A) or equivalent shear cell temperature (B). Red line is a linear fitted trend line for all data points. The horizontal black dotted line at a degree of texturization of 1 indicates a structure with isotropic properties. The vertical blue dotted line indicates the temperature above which all extrudates had a degree of texturization above 1.

6

The degree of texturization showed a positive correlation with the melt and shear cell temperature (Fig. 6.10). Surprisingly, the linear correlation between temperature and degree of texturization was higher for the melt temperature (R^2=0.72) than the equivalent shear cell temperature (R^2=0.65). When the data of the two screws are split the linear correlation with shear cell temperature for screw A (R^2=0.73) was slightly higher than that with the melt temperature (R^2=0.76). However, this was not the case for screw B. The increasing effect of temperature on the degree of texturization was previously reported for HME of soy protein isolate (SPI) as well (Chen et al., 2010; Maung et al., 2021). This effect of temperature on fibrous structure formation can be explained by two effects. Firstly, temperature directly influences the physicochemical changes in of the material in the extrusion barrel (e.g. protein denaturation and aggregation). And secondly, temperature indirectly influences the flow profile in the cooling die, which results from these physicochemical changes (Wittek, Ellwanger, et al., 2021).

Högg & Rauh (2023) found a minimal texturization temperature of 117.7 °C for HME extrusion of the same type of SPC (Alpha 8) under similar conditions as were used in this study. This is close to the temperature at which the linear trendline for the melt temperature is equal to 1 (119 °C). However, the minimal melt temperature above which all extrudates produced in this study had a texturization index above 1, indicated with the blue dotted line in Fig. 6.10, is higher (134 °C). It should be noted though that when this temperature is used as target temperature for fibrous structure formation, part of the samples produced at lower temperature would be rejected unjustified, because these are fibrous. When using the minimal shear cell temperature (95 °C), fewer products were rejected unjustified and a better separation between products with higher and lower texturization indices was achieved. This indicates that the shear cell temperature is more suitable to find the minimal thermal process intensity required for fibrous structure formation than the melt temperature. A likely explanation for this difference is the fact that the equivalent shear cell temperature reflects the overall effect of processing on thermal process intensity, while melt temperature only captures the thermal process intensity just before the die. Thus, shear cell temperature is more representative for the required physicochemical changes.

Fig. 6.10 shows that extrudates produced with screw A had a higher degree of texturization compared with extrudates produced with screw B at a similar equivalent shear cell temperature. This implies that the physicochemical changes as measured with NIR spectroscopy do not completely explain the structural properties at a larger length scale. However, a degree of texturization slightly above 1 using screw A was only achieved at two processing conditions. A similar trend was observed for the perpendicular cutting strength and other textural properties (hardness, cohesiveness etc.), which indicated stronger products were produced with screw A at temperatures below the minimal temperature for structure formation (Fig. S.6.8-6.13). We hypothesize that the presence of kneading elements is required to achieve a sufficient thermal process intensity for fibrous structure formation. However, at temperatures below the minimal equivalent shear cell temperature for structure formation, kneading elements can lead to a reduction of the size of the protein aggregates formed in the extruder barrel as was hypothesized by van der Sman & van der Goot (2023). This aggregate size reduction, in turn reduces the degree of texturization, because the cutting force perpendicular to the flow direction decreases (Fig. S.6.9). This effect of the screw configuration indicates that thermal process intensity is not the only factor that determines the structure formation during HME. Interestingly, this effect was only observed when plotting the structural properties against the equivalent shear cell temperature and not the melt temperature. This is an additional indication that the equivalent shear cell temperature provides better insights in the factors influencing fibrous structure formation during HME.

Future application

This study demonstrates that NIR in combination with HTSC measurements can be used to get more insight in the processing conditions during HME extrusion of meat analogues. It should be noted though that in this study only a simple formulation consisting of SPC and ~61wt% water was studied. The method can potentially be extended to products that contain more ingredients. To apply this method to these multi-ingredient products, it is necessary to include these formulations in the calibration step and the influence of product homogeneity on the NIR spectra should be considered. This probably means that NIR spectroscopy is interesting for online applications to ensure constant processing conditions during the extrusion process. NIR spectroscopy was already successfully applied online during the extrusion of cereal products (Dodds & Heath, 2005; Evans et al., 1999). Recalibration under processing conditions is required for these in-line measurements. Additionally, the equivalent shear cell temperature is a promising screening tool to find processing conditions that could result in fibrous structures. This is particularly relevant during upscaling from pilot-plant to factory size extruders, as the influence of barrel temperature on the thermal process intensity strongly decreases with larger barrel diameters. In large extruders, heating through viscous dissipation becomes more relevant, while the melt temperature becomes a less accurate measure for the temperature of the product inside the extruder. However, when applying the equivalent shear cell temperature to measure the process intensity of extrudates the NIR measurement conditions of the HTSC products and extrudates should be similar. Finally, NIR spectroscopy can be used as a tool to measure the textural properties of the extrudate in a similar manner as the use of NIR spectroscopy for measurement of the textural properties of animal meat (Schreuders, Schlangen, et al., 2021).

6.5 Conclusion

In this study near-infrared spectroscopy in combination with partial least squares regression was successfully used to create a calibration curve for the processing temperature of high-temperature shear cell (HTSC) products under controlled processing conditions. This model was then used to calculate the equivalent shear cell temperature to assess the thermal process intensity during high-moisture extrusion (HME). The equivalent shear cell temperature reflected the combined effects of shear stresses, (local) temperature effects and the effect of residence time on the thermal process intensity. It was found that the degree of texturization of the extrudates was correlated with the equivalent shear cell temperature. By following a systematic approach this study provides insight into the effect of interrelated processing parameters (e.g., barrel temperature and screw speed) on the thermal process intensity during HME. The knowledge gained could contribute to further optimization of processing conditions to achieve the desired meat analogue products.

6.6 Appendix

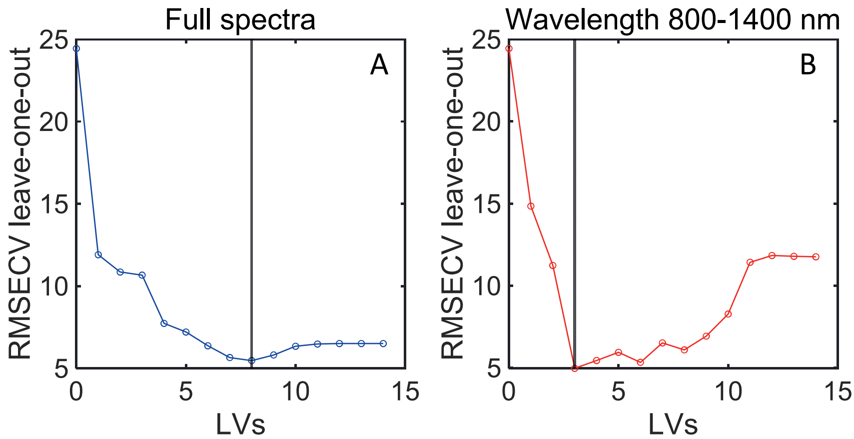

Fig. S.6.1 Latent variable (LV) selection for PLS regression model for the processing temperature of HTSC products for A. the full spectrum (400-2200nm) and B. the reduced spectrum (800-1400 nm).

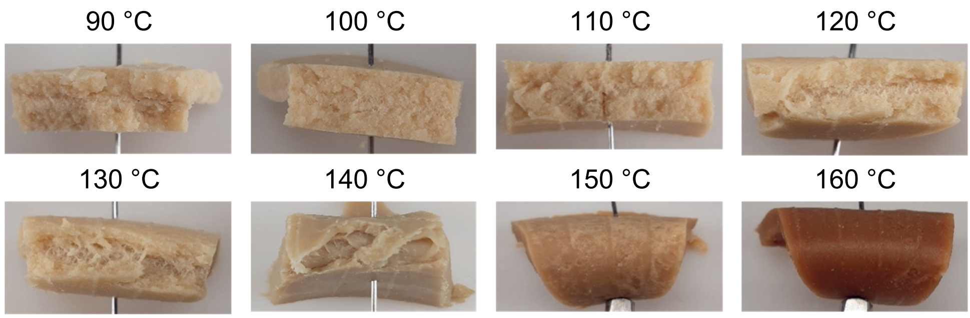

Fig. S.6.2 Visual structure of SPC HTSC products treated at 90-160 °C for 15 min at 30 rpm.

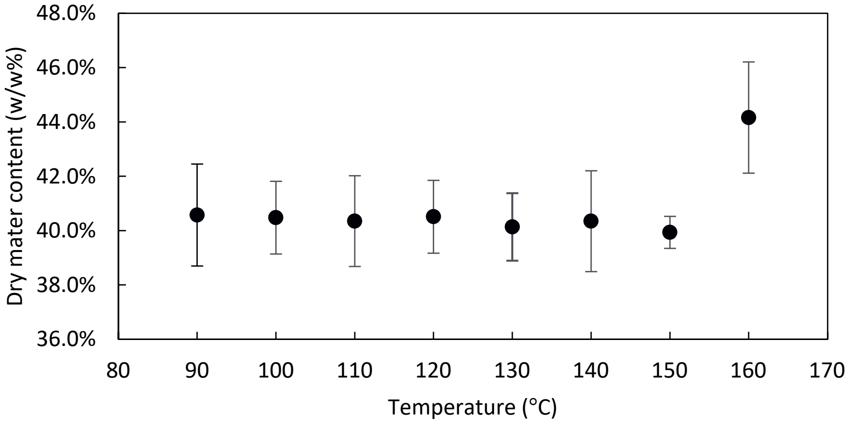

Fig. S.6.3 Dry matter content HTSC products produced at different temperatures and a constant rotational speed and processing time of 30 rpm and 15 min.

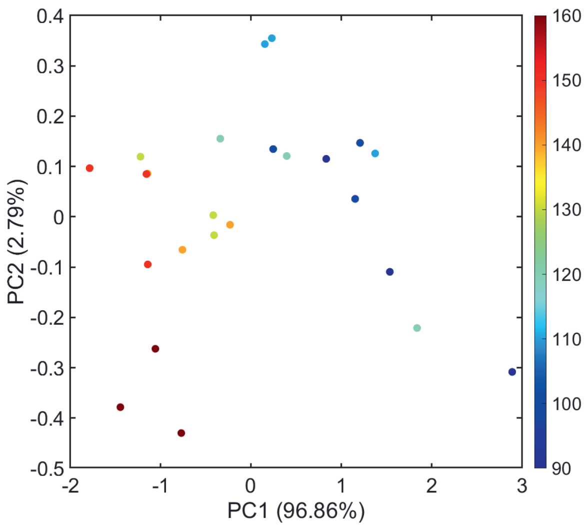

Fig. S.6.4 Principal component analysis based on the reduced NIR absorbance spectra (800-1400 nm) after pre-processing with SNV and Savitzky-Golay 1st derivative of HTSC products treated at 90-160 °C for 15 min at 30 rpm. Colour scale indicates the processing temperature ranging from blue to red.

6

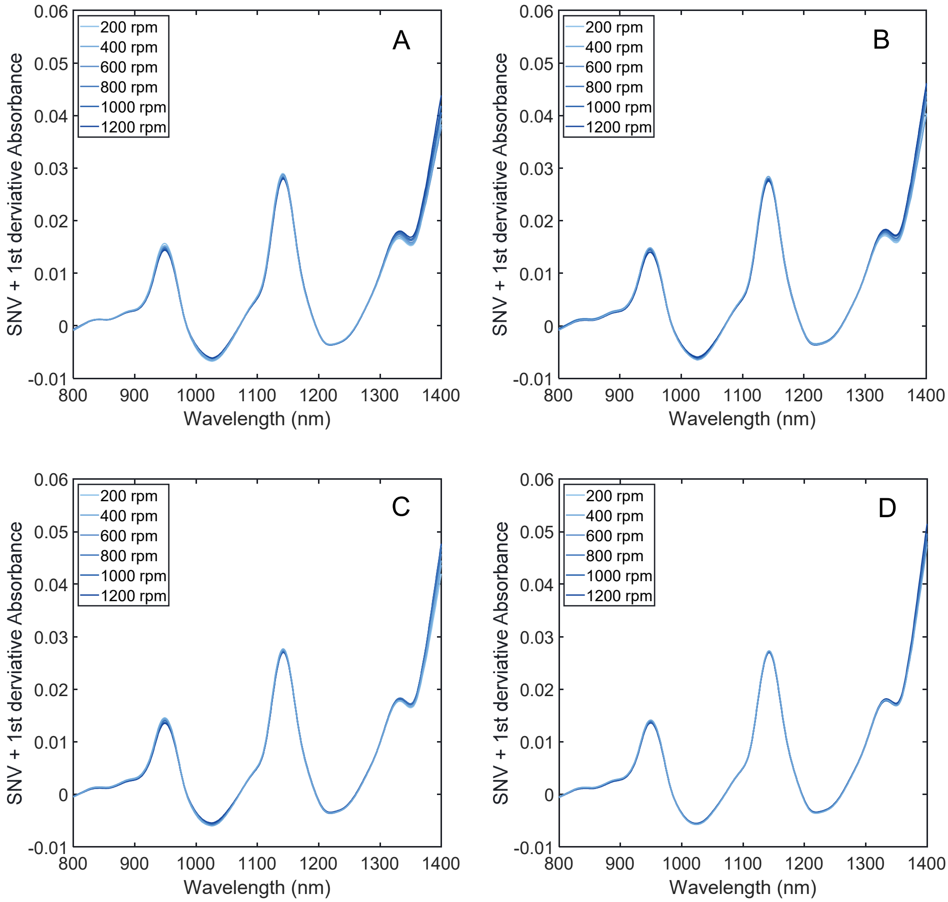

Fig. S.6.5 Average absorbance spectra after pre-procesing with SNV and Savitzky-Golay 1st derivative of extrudates produced with screw profile A at different screw speeds at a barrel temperature of 100 (A), 120 (B), 140 (C), 160 (D) °C.

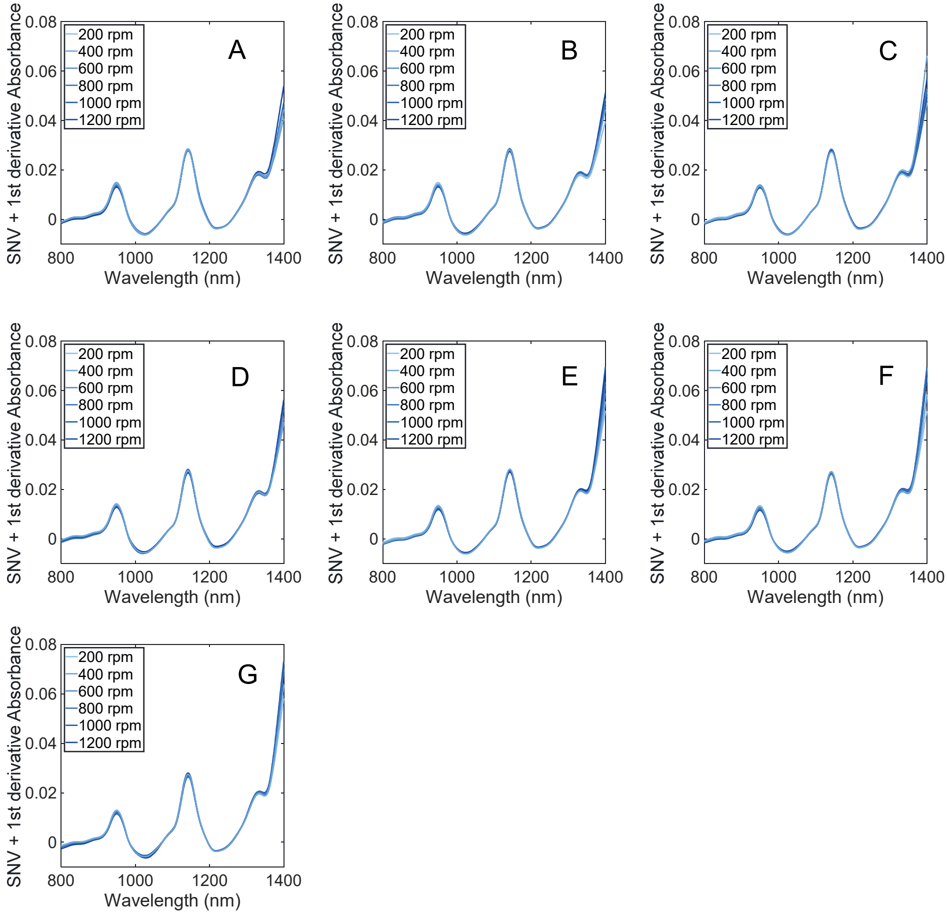

Fig. S.6.6 Average absorbance spectra after pre-procesing with SNV and Savitzky-Golay 1st derivative of extrudates produced with screw profile B at different screw speeds at a barrel temperature of 100 (A), 110 (B), 120 (C), 130 (D), 140 (E), 150 (F), 160 (G) °C.

6

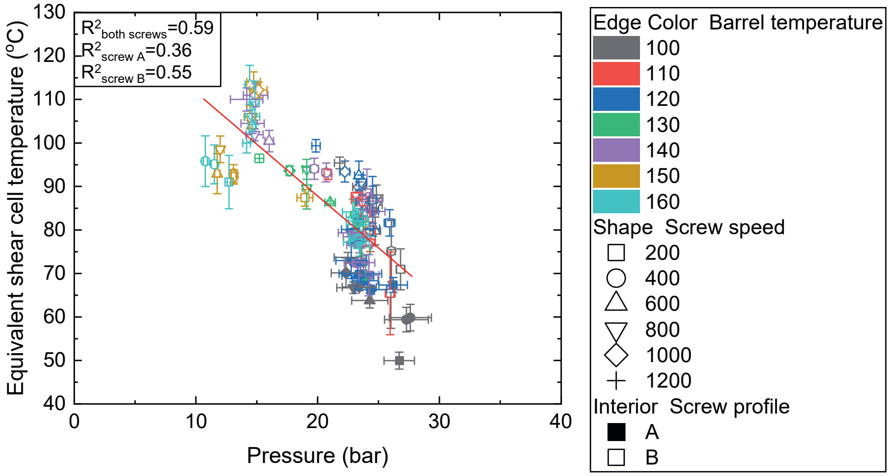

Fig. S.6.7 Equivalent shear cell temperature plotted against pressure measured at the die. The red line represents the linear trendline for all extrudates.

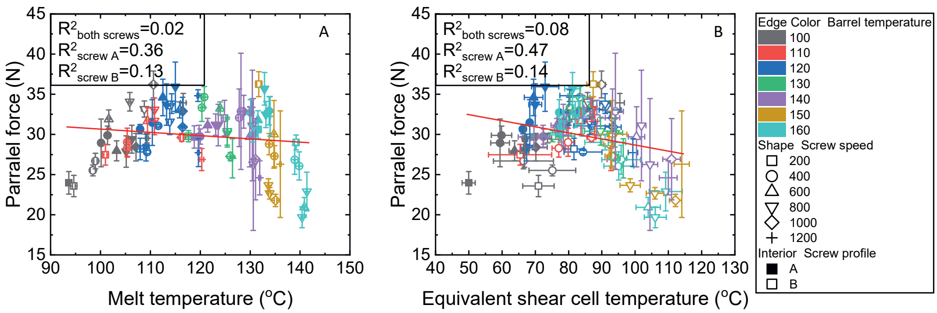

Fig. S.6.8 Maximal cutting force in parallel direction to the flow during HME plotted against melt (A) and shear cell temperature (B). The red line represents the linear trendline for all extrudates.

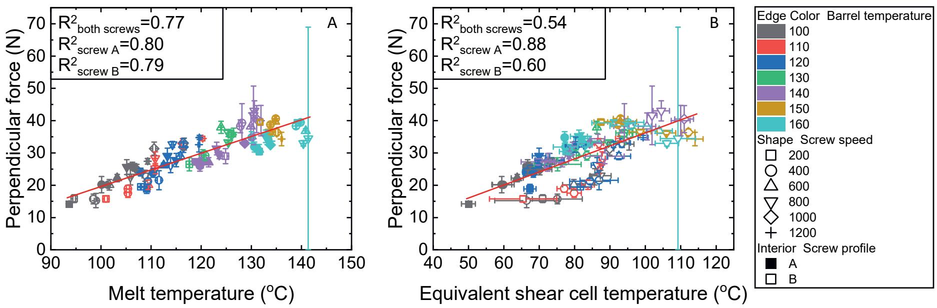

Fig. S.6.9 Maximal cutting force in perpendicular direction to the flow during HME plotted against melt (A) and shear cell temperature (B). The red line represents the linear trendline for all extrudates.

The hardness, cohesiveness, springiness and chewiness were measured with a texture analyser (Model Instron 5564, Instron, Norwood, Massachusetts, USA). The system was calibrated with a 2000N loadcell and the initial height was set at 10mm. The thawed extrudates were cut into a cylindrical shape with a diameter of 20mm. The extrudates were compressed twice, holding time one second, to 50% of its original thickness at a speed of 1mm/s by a compression probe (P/50). A force-time graph was recorded using the software BlueHill 23 Universal (Instron, Norwood, Massachusetts, USA). The maximum peak force (*Fmax*) in the graph is equal to the hardness (N).

$$Hardness\ (N) = F_{max} \qquad Eq.\ S.6.1$$

The cohesiveness is expressed by the ratio of the area under the first and second curve:

$$Cohesiveness\ (-) = A_2/A_1 \qquad Eq.\ S.6.2$$

In which A_2 is the area under the second peak and A_1 is the area under the first peak.

The ratio between the time until the first peak was reached and the second peak is the springiness:

$$Springiness\ (-) = t_2/t_1 \qquad Eq.\ S.6.3$$

In which t_2 is the time until the second peak is reached and t_1 is the time until the first peak is reached.

The chewiness was determined by multiplying hardness, cohesiveness, and springiness values.

$$Chewiness\ (N) = Hardness * Cohesiveness * Springiness = F_{max} * \frac{A_2}{A_1} * \frac{t_2}{t_1} \qquad Eq.\ S.6.4$$

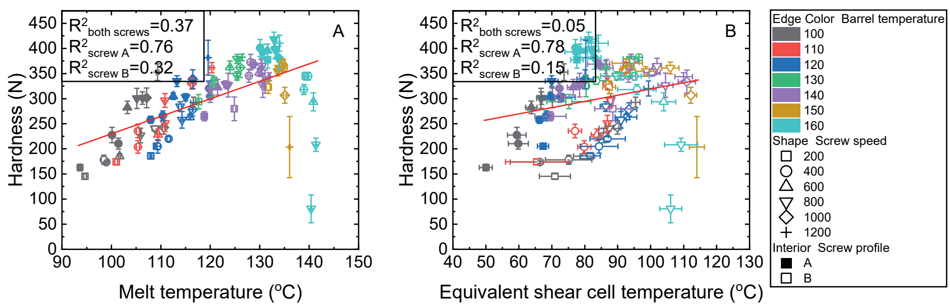

Fig. S.6.10 Hardness as measured with a double compression test plotted against melt (A) and shear cell temperature (B). The red line represents the linear trendline for all extrudates.

6

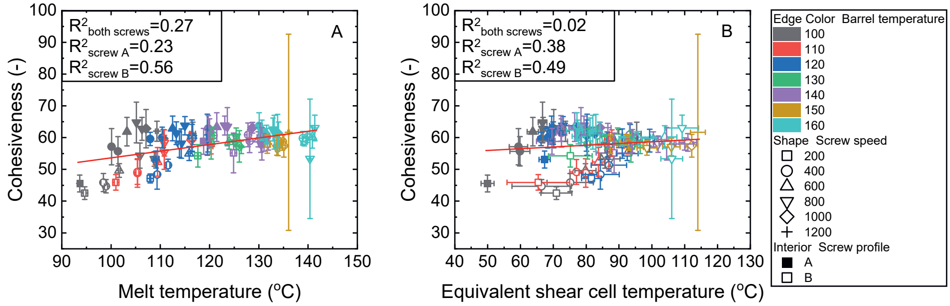

Fig. S.6.11 Cohesiveness as measured with a double compression test plotted against melt (A) and shear cell temperature (B). The red line represents the linear trendline for all extrudates.

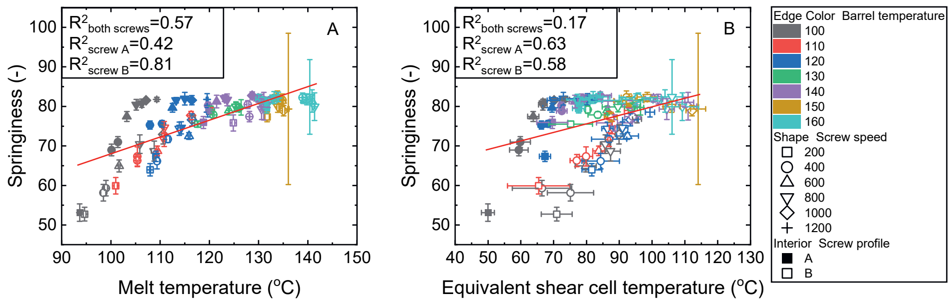

Fig. S.6.12 Springiness as measured with a double compression test plotted against melt (A) and shear cell temperature (B). The red line represents the linear trendline for all extrudates.

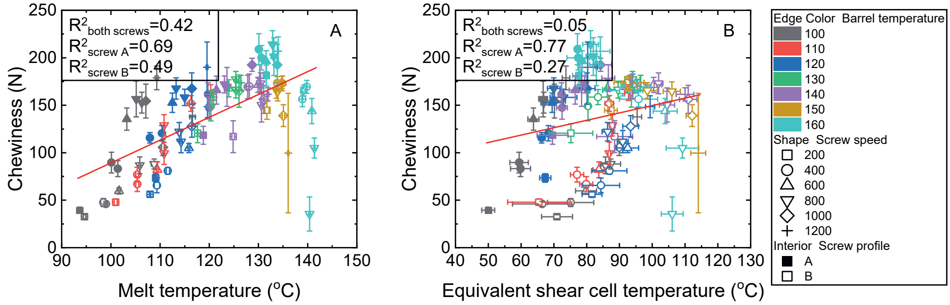

Fig. S.6.13 Springiness as measured with a double compression test plotted against melt (A) and shear cell temperature (B). The red line represents the linear trendline for all extrudates.

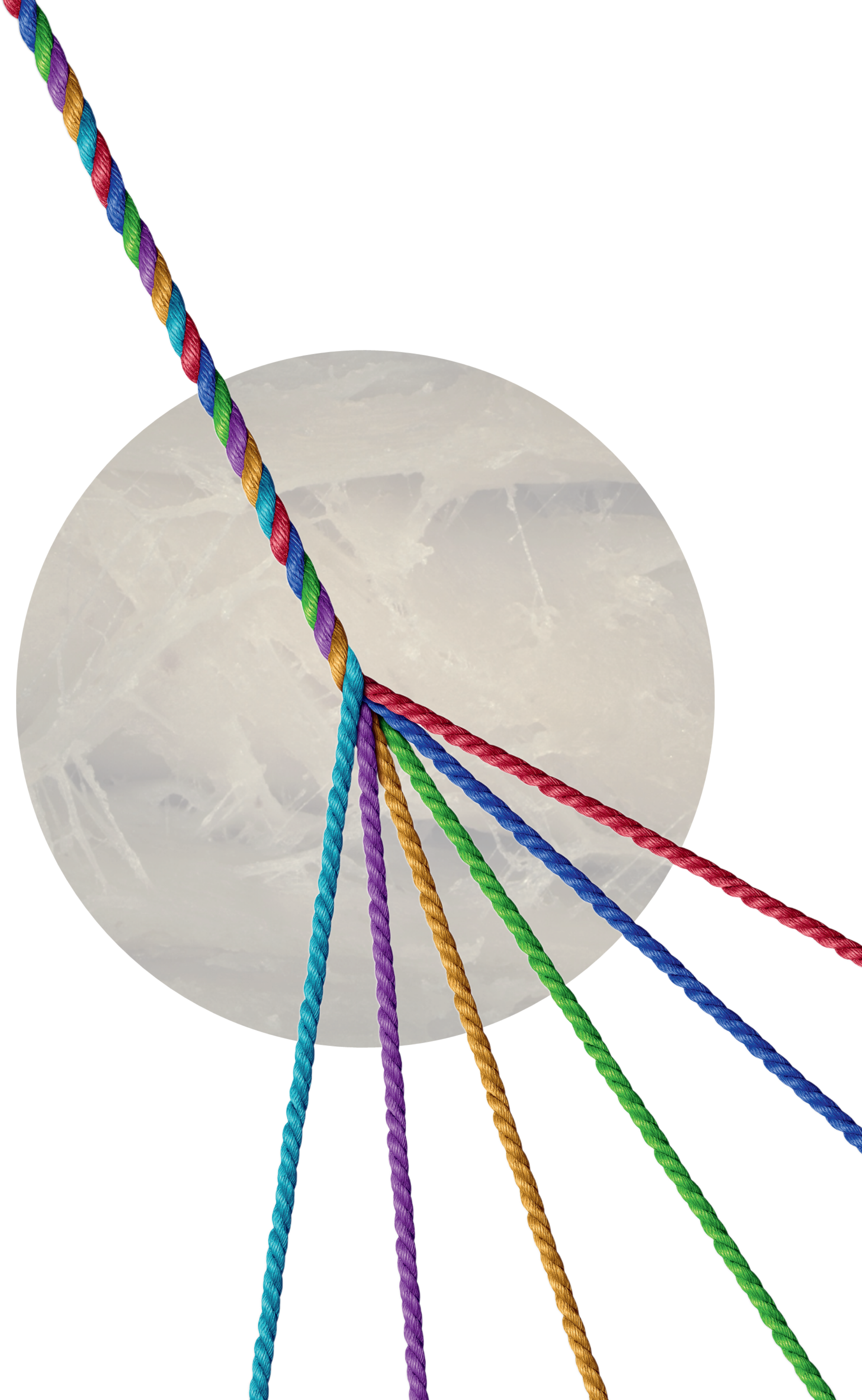

Chapter 7

General discussion

7.1 Introduction

High-moisture extrusion (HME) is commonly used to produce meat analogues with a fibrous appearance to resemble that of meat. However, even though this technique has already been studied for 30 years now, the mechanism for fibrous structure formation is still not fully understood (Guyony et al., 2023; van der Sman & van der Goot, 2023). The main reason for this are the interrelated effects of the different processing parameters.

The aim of this thesis was therefore to systematically investigate the effects of processing conditions on dense plant-based products made through HME. To achieve this goal, the high-temperature shear cell (HTSC) was used to study the effects of the processing parameters separately in **Chapters 2 & 3**. In **Chapters 4 & 5** NIR spectroscopy was used to quantify the composition of plant-based mixtures and gels. In **Chapter 6** the HTSC and NIR spectroscopy were combined to develop a new parameter that describes the thermal process intensity during HME.

This chapter **(Chapter 7)** summarizes the most important findings from the previous chapters and offers suggestions for the future research required for a complete understanding of the fibrous structure formation mechanism during HME.

7.2 Main findings and conclusions

The deformation of extruded material in the cooling die is often thought to be crucial for fibrous structure formation during HME. However, in the standard HTSC process the material is not deformed during cooling. In **Chapter 2** the effect of shearing during cooling on the fibrous structure formation in the HTSC was therefore studied. We found that deformation during cooling was not necessary nor beneficial for fibrous structure formation. Products sheared during heating had a visually more fibrous structure. We hypothesized that other factors, such as the elongational stresses at the die entrance or the temperature gradient in the cooling die, are more important for fibrous structure formation. A higher cooling die temperature could therefore be beneficial for fibrous structure formation during HME. However, use of the cooling die remains crucial to prevent product expansion.

In **Chapter 3** the effects of mixing and hydrating time before HTSC processing were studied for three types of protein dough: soy protein concentrate (SPC), soy protein isolate (SPI)-wheat gluten (WG) and pea protein isolate (PPI)-WG. Mixing time influenced the properties of the dough and the final product structure in some cases, whereas hydrating time only had a limited effect. The effect of mixing time was highly dependent on the ingredients used. For SPC and SPI-WG the effect on the final product structure was limited, while for PPI-WG an optimum mixing time was found based on the tensile properties of the products formed. This optimum mixing time could be correlated with the optimal dough development time as measured during farinograph mixing of the dough. Furthermore, it is remarkable that slight changes in the energy input during the mixing stage resulted in relevant structural changes in the final product. However, for HME the structure formation that occurs in the initial mixing step of the process might be of less importance, because of the more intensive mechanical treatment that follows, which is assumed to destroy the gluten network that is initially formed (van der Sman & van der Goot, 2023).

In **Chapters 2** as well as **Chapter 3** it was found that the investigated parameter influenced the final product properties. This implies that each step in the extrusion process contributes to fibrous structure formation. Remarkably, in some cases only small changes in process conditions led to clear changes in product structures. Most of the findings in this thesis aligned with the hypothesis proposed by van der Sman & van der Goot (2023) who stated that multiple mechanisms contribute to fibrous structure formation during extrusion simultaneously. These mechanisms take place at multiple length scales and locations in the extruder. To fully understand the fibrous structure formation during HME these different mechanisms therefore need to be considered.

In **Chapters 4, 5 & 6** we used NIR spectroscopy for the analysis of meat analogue composition and the thermal process intensity during HME. This technique could be used for in-line measurements during HME because it is a rapid and non-destructive. In **Chapter 4** we showed that NIR spectroscopy is suitable for measurement of the oil and protein content in dense plant-based mixtures. Partial least squares (PLS) regression was used successfully to predict the oil and protein content based on the NIR spectra. Wavelength range reduction and wavelength selection reduced the complexity and improved the quality of these models. However, heating is known to have a large impact on the protein-water interactions in meat analogues, thereby influencing the NIR spectra (Büning-Pfaue, 2003; Uddin et al., 2002; Wold et al., 2020). For this reason, the effect of heating conditions on the oil measurement of heated PPI gels was studied in **Chapter 5**. It was shown that heating conditions indeed influenced the NIR spectra of the protein gels and therefore the oil content measurement.

However, the application of wavelength selection allowed the development of calibration curves for oil content quantification that are robust to fluctuations in the heating conditions.

In **Chapter 6** the effect of heating on the NIR spectra was used to quantify the overall thermal process intensity during HME. First a calibration curve for the processing temperature during HTSC processing was created. Subsequently, this calibration curve was applied to extrudates produced under different processing conditions to calculate the “equivalent shear cell temperature”. The equivalent shear cell temperature was used as an indicator of overall process intensity. With the use of this indicator, it was found that the thermal process intensity during HTSC process was significantly higher compared to HME processing, mainly because of the longer residence time in the HTSC. Additionally, the equivalent shear cell temperature gave insight in the effects of the different processing parameters (i.e., barrel temperature, screw speed and screw profile) on the thermal process intensity. Finally, the thermal process intensity could be related to the degree of fibrous texture formation. It was found that a minimal thermal process intensity is required to ensure the formation of a mechanically anisotropic product. The equivalent shear cell temperature was more suitable to find the minimal thermal process intensity for fibrous structure formation than the melt temperature measured before the die entrance. This implies that the physicochemical changes that occur in the extrusion barrel contribute to the formation of a fibrous structure and the location of structure formation is not limited to the cooling die.

The thermal process intensity was not the only explaining factor for the degree of texturization (**Chapter 6)**. At temperatures below the minimal temperature for fibrous structure formation the addition of kneading blocks led to a lower degree of texturization. This implies that too much mechanical deformation is detrimental for the formation of a fibrous structure. The negative effect of mechanical deformation is probably caused by the break-up of the protein aggregates that are formed in the extrusion barrel (van der Sman & van der Goot, 2023). However, the presence of kneading blocks helped to achieve the minimal thermal process intensity for structuring through viscous dissipation and by increasing the residence time (Ellwanger et al., 2023). This means that the extent of mechanical deformation needs to be balanced to allow a sufficient thermal process intensity and to minimize the breakdown of the protein aggregates formed in the extruder barrel.

7.3 Limitations and outlook for future research

7.3.1 Comparison of the HTSC and HME processes and products

In this thesis the HTSC was used successfully to study the effects of the processing parameters during HME. However, there are some differences between the HTSC and HME process that will be described in this subsection. One of these differences between the HTSC and HME processes is the presence of elongational stresses. During HME these elongational stresses mainly occur at the transition from the extruder barrel to the cooling die. However, during HTSC no elongational stresses act on the product (Wittek, Ellwanger, et al., 2021). Elongational stresses cause break-up and deformation of the dispersed phase of a two-phase mixture even at a high viscosity ratio, whereas simple shear stresses cannot. The deformation of the dispersed phase was proposed to be one of the causes for the fibrous structure formation during HME (Wittek, Ellwanger, et al., 2021). To gain more insight in the impact of these elongational stresses on the fibrous structure formation, we therefore suggest developing a device that can exert elongational stresses on the material.

Another important aspect that complicates the use of the HTSC to study structure formation during HME is the difference in residence time between these processes. The longer residence time for the HTSC process results in a larger thermal process intensity for HTSC processing than HME (**Chapter 6).** It would therefore be interesting to study the use of shorter residence times in the HTSC. It was already shown in **Chapter 2** that a shorter thermomechanical treatment does not have a negative impact on fibrous structure formation. Similarly, pictures of the products for which the residence time was varied in **Chapter 6** showed that the residence time can be decreased to 5 min before losing its fibrous structure. The optimal residence time was around 10 min (Fig. 7.1).

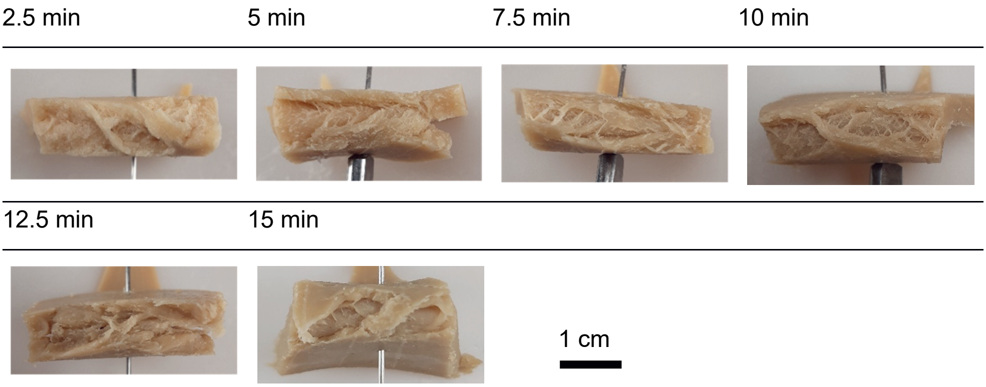

Fig. 7.1 Pictures of HTSC products consisting of 39 wt.% SPC sheared at 30 rpm for different processing times. These products were prepared for Chapter 6, in which more information about their production can be found.

To understand the impact of the differences between the HTSC and the HME processes on their products, the effects of thermal and mechanical treatment on the products' visual and mechanical properties was studied in more detail. The visual macrostructure of HTSC and HME products made with 39 wt.% SPC showed some clear differences (Fig. 7.2). HME products had a structure that can be best described as layered, while HTSC products contains small fibres when broken perpendicular to the flow (Fig. 7.2). This difference between extrudates and HTSC products raises the question whether similar structures with small fibres could be produced with HME. Snel et al. (2022) used a novel rotational cooling die in which simple shear is applied during cooling. The structures produced with this rotational die resembled those of HTSC products more compared with HME products produced with a conventional cooling die. However, the small fibres that are found in HTSC products are still lacking. Nevertheless, the rotating cooling die offers opportunities to structure meat analogues, which needs to be explored further. However, it can be expected that products made with HTSC and HME will remain subtly different in their structures.

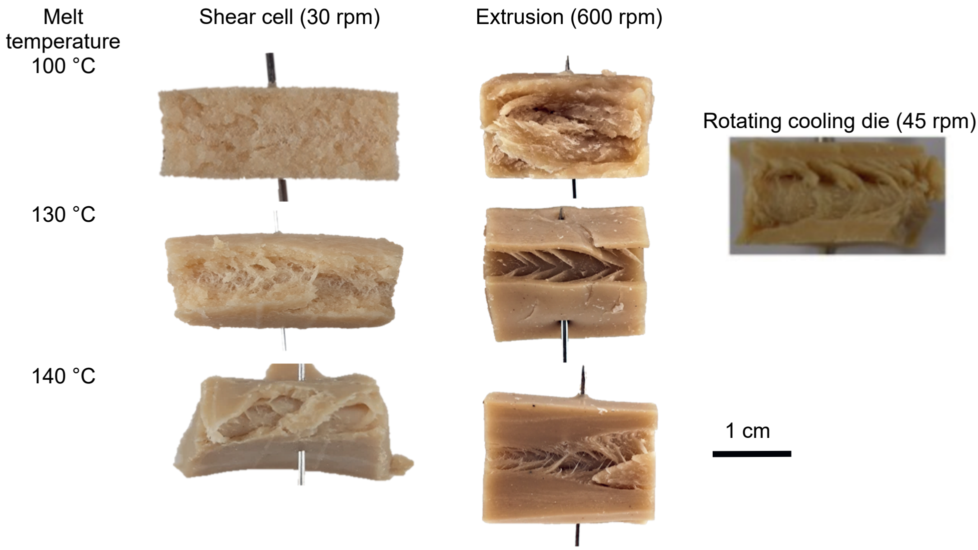

Fig. 7.2 Visual macrostructure of HTSC and HME products after bending (HTSC) or cutting (HME) of the samples and folding them. HTSC and HME products both contain 39 wt.% SPC and were prepared for Chapter 6. HTSC products were sheared at 30 rpm for 15 min. The HME products were produced with screw profile B (containing kneading elements). For reference the visual macrostructure of a SPC product that was produced with a novel rotating cooling die by Snel et al. (2022) was included.

To study the mechanical properties of HTSC and HME products amplitude sweeps in a CCR were used. These results were summarized in texture maps, as was done in **Chapter 3** of this thesis. In all texture maps the measured HTSC and HME products fall into the same area (Fig. 7.2 and 7.3). This indicates that the mechanical properties of products produced with both techniques are similar when applying small oscillatory deformation, despite differences in their macrostructural properties (Fig. 7.2). At the end of the linear viscoelastic regime (LVE) the HTSC and HME products were mushier than commercial products (Schreuders, Sagis, et al., 2022), but similar to mung bean protein extrudates (De Angelis et al., 2023). However, at the cross-over point the HTSC and HME products had similar structural properties compared to commercial meat analogues (Schreuders, Sagis, et al., 2022). This indicates that in the non-linear regime the properties of meat analogues are very similar, and differences between different (commercial) products mainly occur in the LVE region.

Temperature had a limited effect on the final product structure for both HTSC and HME products. Only HTSC products produced at 160 °C deviated in their mechanical properties from the rest of the products, which was caused by moisture evaporation during processing. The limited effect of temperature was surprising, because temperature had a clear effect on the macrostructure of the products (Fig. 7.2). The SME input during extrusion also did not have a large influence on the structural properties of the final product. However, for shear cell products a SME >71 kJ/kg led to a mushier structure that deviates from HTSC products with SME <71 kJ/kg and extrudates. This confirms the structural breakdown at higher SME-inputs, as was also observed in **Chapter 2.** The different deformation applied during HTSC and HME processing could explain the different effects of mechanical energy input for these two processing methods. Additionally, the different effects of SME on the mechanical properties of HTSC and HME products, implies that SME is not the most suitable parameter to quantify mechanical deformation, but rather the maximal shear stress. In case of starch breakdown, it was proven that maximal shear stress had most explaining value (van den Einde et al., 2004), which might hold true for structural breakdown of protein as well.

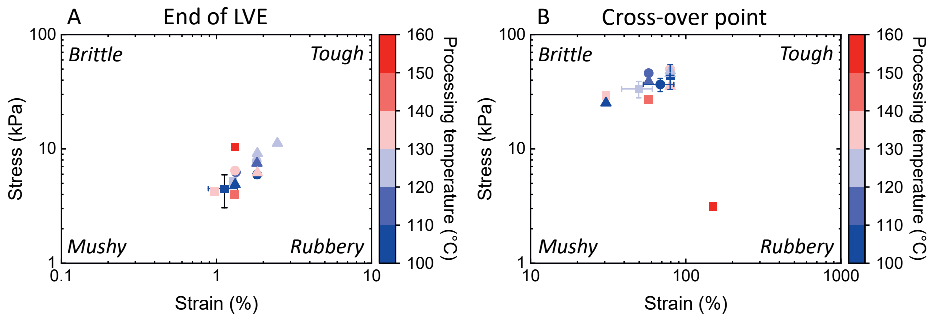

Fig. 7.3 Texture map of HTSC and HME products containing 39 wt.% SPC. HTSC products (■) were sheared at different temperatures (90-140 °C) at 30 rpm for 15 min. HME products were produced with two screw configurations without (●) and with (▲) kneading elements at a rotational speed of 600 rpm at the end of the LVE (A) and cross-over point (B). Colour indicates set temperature during HTSC processing, or the melt temperature recorded during HME.

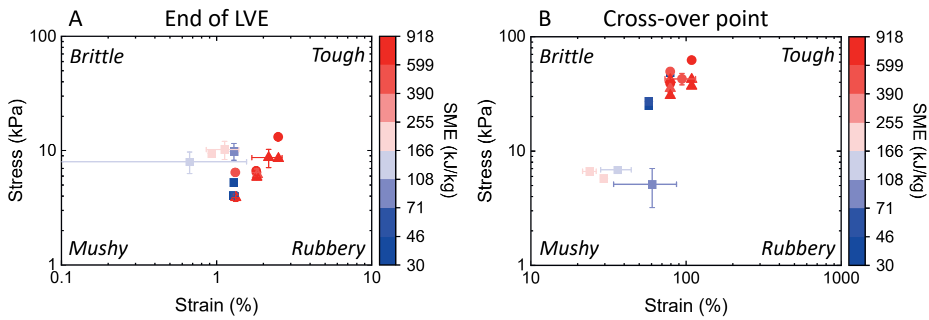

Fig. 7.4 Texture map of HTSC and HME products containing 39 wt.% SPC. HTSC products (■) were sheared at a constant temperature 140 °C at 0-100 rpm for 15 min. HME products were produced with two screw configurations without (●) and with (▲) kneading elements at screw speeds ranging from 200-1200 rpm and barrel temperature ranging from 100-160 °C as was described in Chapter 6, only extrusion conditions resulting in a melt temperature between 130-150 °C were selected here to have a similar processing temperature to the HTSC products. Colour indicates SME during HTSC or HME processing.

A summary of all differences and similarities between the HTSC and HME processes and products discussed in this subsection is shown in Table 7.1.

Table 7.1 Overview of similarities and differences between the HME and HTSC processes and products

	Process		**Products**	
	HTSC	**HME**	**HTSC**	**HME**
Similarities	• Similar processing operations • Similar ingredients suitable for fibrous structure formation		• Anisotropic structure • Similar mechanical properties measured with CCR ○ Temperature has a limited effect on these properties	
Differences	• No elongational stresses • Residence time 15 min • Higher thermal process intensity • Lower SME and maximal shear rate • In standard protocol no deformation during cooling	• Elongational stresses present • Residence time 2-5 min • Lower thermal process intensity • Higher SME and maximal shear rate • Deformation in the cooling die	• Visible macro-structure with small fibres • Mechanical deformation impacts mechanical properties measured with CCR	• Visible macro-structure layered • Mechanical deformation has a limited effect on mechanical properties measured with CCR

Despite differences between HTSC and HME, the HTSC remains a very relevant tool to gain new insights in the extrusion process because HTSC allows decoupling of the effects of the different processing conditions. The new insights described in this thesis can then be tested by further extrusion trials to confirm or dismiss the hypothesized impacts on the structure formation during HME itself. For example, the effect of mixing as was done in **Chapter 3** can be tested by altering the screw configuration. To study the effect of shearing during cooling (**Chapter 2**) the dimensions of the cooling die can be varied (Cornet et al., 2022).

7.3.2 Use of NIR spectroscopy to study thermal reactions

In **Chapter 6** NIR spectroscopy was used to gain more insights in the total effect of the thermal treatment during HTSC processing and HME on the physicochemical changes of SPC. The total effect of thermomechanical processing measured with NIR spectroscopy was influenced by the temperature and the residence time in the HTSC or extruder barrel. This implies that NIR spectroscopy could also be used to quantify the effect of a temperature increase on the reaction rate of the physicochemical changes occurring during HME. Elmasry & Nakauchi (2015) already used NIR spectroscopy to study the combined effect of heating temperature and heating time during the thermal treatment of seafood products. They were able to use the so-called "thermal history" (TH) to quantify the thermal treatment intensity of different time-temperature combinations. They defined thermal history as follows:

$$TH = \int_0^t 10^{\left(\frac{T_h - T_{ref}}{Z}\right)} dt \qquad \textit{Eq. 7.1}$$

In which T_h is the heating temperature (°C) after time t, T_{ref} is the reference temperature (°C) and Z is the temperature increase to result in a 10-fold increase in heating rate (°C). Elmasry & Nakauchi (2015) used a T_{ref} of 100 °C and Z of 25 °C. The *TH* therefore is the time the product needs to be at the reference temperature to achieve the same effect as at the actual heating temperature. The *TH* was linearized by applying a log10 transformation before it was linked to the NIR spectra. This allowed Elmasry & Nakauchi (2015) to create a successful partial least squares (PLS) model for the *TH*.

It was found that also for the non-oil containing PPI gels that were produced in **Chapter 5** a successful PLS model for the *TH* could be obtained based on their NIR spectra (Fig. 7.5), when using of the same T_{ref} and Z-values as were used by Elmasry & Nakauchi (2015). In future research, fitting the Z-value could provide more information about the reaction kinetics during HME processing. It should be noted that the changes that are reflected in the NIR spectra are all physicochemical changes that occur upon extrusion. With the use of the regression coefficient of the PLS model or wavelength selection the most important bonds and therefore most important components that are affected by the heat treatment can be found. This will provide more insight in the reactions underlying the changes in the equivalent shear cell temperature that was presented in **Chapter 6**.

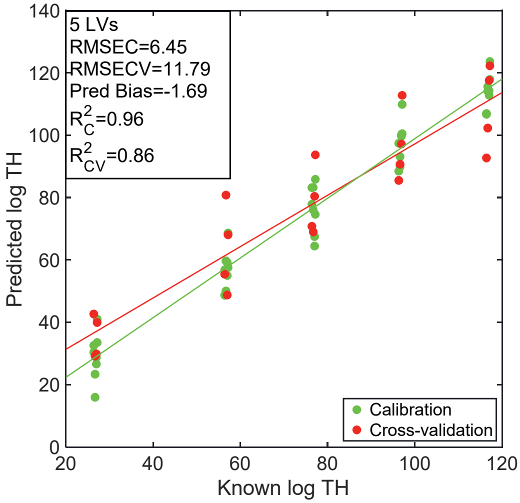

Fig. 7.5 PLS model of thermal history PPI gels without oil. Production of these gels is described in Chapter 5. NIR absorbance was pre-processed with standard normal variate (SNV) correction and Savitzky-Golay 2nd derivative.

In **Chapters 4, 5 and 6** we suggested the use of NIR spectroscopy for the inline measurement of composition and thermal process intensity. Additionally, NIR spectroscopy could be used for the inline measurement of the structural properties of the meat analogues (Dhanapal & Erkinbaev, 2024). The application of NIR spectroscopy in an extruder would therefore offer possibilities to simultaneously analyse the composition, thermal processing history and structure, thereby giving new options for process control.

7

7.3.3 Effect of ingredient properties on structure formation

The work described in this thesis was mainly aimed at understanding the effects of the processing parameters on the final product structure during the different processing steps of HME. However, the extend of the effects of these processing parameters on the final product properties is influenced by the plant-based ingredients used. This was for example shown in **Chapter 3**, in which we showed that the effect of mixing on the final product structure depended on the ingredients used. It is well known that the ingredient properties also influence the processing conditions during extrusion (Emin & Schuchmann, 2017; Kendler et al., 2021; Wittek et al., 2021). It should therefore be noted that the effects of the processing parameters presented **Chapters 2, 3 & 6** of this thesis could be different for different product formulations.

The effect of cooling that was presented in **Chapter 2** could be different for products that do not contain gluten. Potentially, the formation of a gluten network during heating and subsequent breakdown caused by deformation during cooling was responsible for the less fibrous structures that were observed for these products. Additionally, mixing might have a different effect for mixtures of protein isolates and dietary fibres or hydrocolloids compared with the SPC and PPI/SPI-WG products that were studied in **Chapter 3**, as was discussed in subchapter 3.4.5. Finally, the effect of the thermal process intensity described in **Chapter 6** might depend on the product formulation. Because the physicochemical changes and their corresponding changes in the rheological properties of the melt that occur depend on the ingredient properties.

It remains challenging to link the functional properties of the ingredients measured at ambient conditions, such as particle size, solubility, water holding capacity or gelling capacity, measured at ambient conditions to the structuring behaviour of the ingredient. This is caused by the change in these properties above the denaturation temperature (Osen et al., 2014; Samard & Ryu, 2019). Linking the ingredient properties to the final product structure was also difficult in the experiments performed for **Chapter 3** of this thesis, where two different PPI ingredients were mixed with WG. As shown in the supplementary material of **Chapter 3** (Fig. S.3.5-S.3.9) mixing affected the mixtures of these two types of PPI with WG differently. However, there was no significant difference in the protein content, protein solubility, water holding capacity or particle size of these two ingredients (data not shown). Thus, even subtle differences in the ingredient properties and composition impact the structuring properties of the ingredient. This indicates that extensive characterization of the ingredients is necessary to understand its structuring potential. To limit the number of analyses that need to be performed the HTSC can be used as a screening tool for the thermomechanical structuring behaviour of ingredients or ingredient mixtures. This approach was already used by Bühler et al. (2022) and Taghian Dinani, Broekema, et al. (2023) to study the effects of starch or hydrocolloid addition respectively.

Another important meat analogue ingredient that was studied in **Chapters 4 and 5** of this thesis was oil. However, these chapters only focussed on the quantification of the oil content in a mixture with a similar composition and thermal processing history as HME or HTSC products. The effect of oil addition on fibrous structure formation during HME was not considered. The amount and type of oil added influence fibrous structure formation because of its lubricating effect (Chen et al., 2022; Kendler et al., 2021). A change in the way oil is added can mitigate the negative effect on the fibrous structure formation. For example, addition of the oil in the form of an emulsion was found to increase the amount of oil that could be added during extrusion without a negative effect on the fibrous texture from 4 to 8% (H.Wang et al., 2022). Furthermore, Opaluwa et al. (2023) found that the screw configuration that is used before the oil addition point also impacts the oil droplet size, mainly because it influences the rheological properties of the protein matrix. To the best of our knowledge the effect of the screw configuration after the oil addition point was not previously investigated. However, we expect that the mechanical treatment after oil addition influences the homogeneity of the oil distribution in the extrudate. This would therefore a relevant direction for future research.

7.4 Concluding remarks

The aim of this thesis was to better understand the effects of processing conditions on dense plant-based products. It was shown that HTSC processing can be used to study the effects of the processing parameters during the different processing operations of HME. Furthermore, it was shown that NIR spectroscopy is a useful tool for rapid and accurate measurement of oil content in meat analogues, which has potential to be applied for simultaneous in-line process and quality control. Future research could focus on the interrelated effects of ingredient properties and processing conditions on the final product properties. This investigation should consider structure formation mechanisms occur at different length scales and at different locations in the extruder.

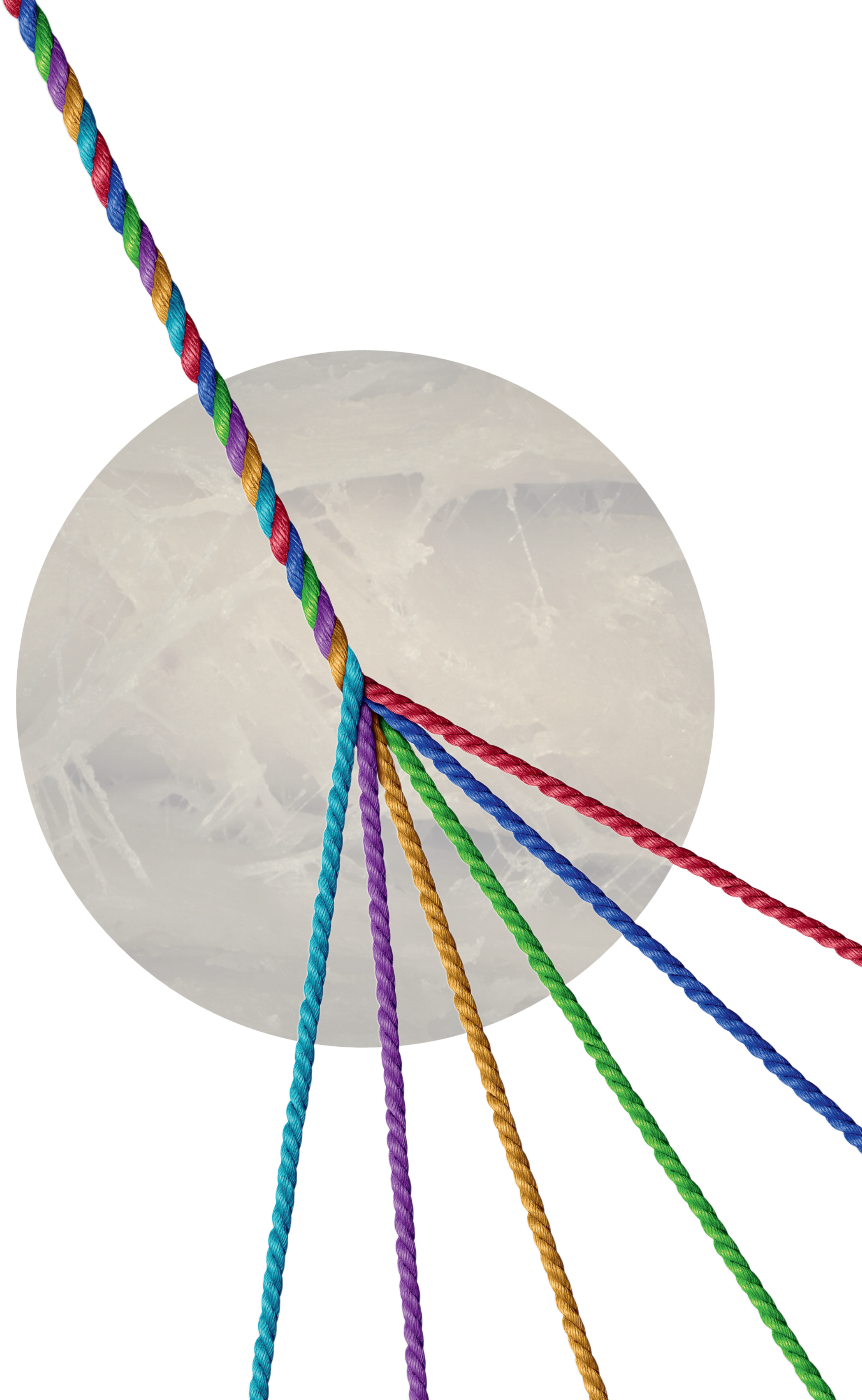

R

References

Atta-Delgado, M. X., Lozano, S. P. G., & Torres, J. A. (2023). A survey on the prevalence of sustainable diets and the eating experience satisfaction. *Innovative Food Science & Emerging Technologies*, *84*, 103305. https://doi.org/10.1016/J.IFSET.2023.103305

Aykas, D. P., Ball, C., Sia, A., Zhu, K., Shotts, M. L., Schmenk, A., & Rodriguez-Saona, L. (2020). In-situ screening of soybean quality with a novel handheld near-infrared sensor. *Sensors (Switzerland)*, *20*(21), 1–19. https://doi.org/10.3390/s20216283

Ayvaz, H., Mortas, M., Dogan, M. A., Atan, M., Yildiz Tiryaki, G., & Karagul Yuceer, Y. (2021). Near- and mid-infrared determination of some quality parameters of cheese manufactured from the mixture of different milk species. *Journal of Food Science and Technology*, *58*(10), 3981–3992. https://doi.org/10.1007/s13197-020-04861-0

Bajawa, S. G., & Apple, J. K. (2011). Non-linear modeling of quality of cooked ground beef patties with visible-NIR spectroscopy. In M.A. Comeau (Eds.), *New Topics in Food Engineering* (pp. 23–44). Nova Science Publishers.

Barbin, D. F., Elmasry, G., Sun, D. W., & Allen, P. (2013). Non-destructive determination of chemical composition in intact and minced pork using near-infrared hyperspectral imaging. *Food Chemistry*, *138*(2–3), 1162–1171. https://doi.org/10.1016/j.foodchem.2012.11.120

Barnes, R. J., Dhanoa, M. S., & Lister, S. J. (1989). Standard normal variate transformation and de-trending of near-infrared diffuse reflectance spectra. *Applied Spectroscopy*, *43*(5), 772–777. https://doi.org/10.1366/0003702894202201

Ben-Hdech, H., Gallant, D. J., Robert, P., & Gueguen, J. (1993). Use of near infrared spectroscopy to evaluate the intensity of extrusion-cooking processing of pea flour. *International Journal of Food Science & Technology*, *28*(1), 1–12. https://doi.org/10.1111/j.1365-2621.1993.tb01246.x

Berghout, J. A. M., Boom, R. M., & van der Goot, A. J. (2014). The potential of aqueous fractionation of lupin seeds for high-protein foods. *Food Chemistry*, *159*, 64–70. https://doi.org/10.1016/j.foodchem.2014.02.166

Bordignon, J. C. S., Badaró, A. T., Barbin, D. F., Mariutti, L. R. B., & Netto, F. M. (2023). Oxidation of whey protein isolate after thermal convection and microwave heating and freeze-drying: Correlation among physicochemical and NIR spectroscopy analyses. *Heliyon*, *9*(7), e17981. https://doi.org/10.1016/J.HELIYON.2023.E17981

Bresciani, A., Annor, G. A., Gardella, M., & Marti, A. (2022). Use of the Farinograph for gluten-free grains. In J. E. Bock & C. Don (Eds.), *The Farinograph Handbook* (Fourth Edition, pp. 111–126). Woodhead Publishing. https://doi.org/10.1016/B978-0-12-819546-8.00012-1

Brøndum, J., Munck, L., Henckel, P., Karlsson, A., Tornberg, E., & Engelsen, S. B. (2000). Prediction of water-holding capacity and composition of porcine meat by comparative spectroscopy. *Meat Science*, *55*(2), 177–185. https://doi.org/10.1016/S0309-1740(99)00141-2

Bühler, J. M., van der Goot, A. J., & Bruins, M. E. (2022). Fibrous Structures from Starch and Gluten. *Polymers 2022, Vol. 14, Page 3818*, *14*(18), 3818. https://doi.org/10.3390/POLYM14183818

Büning-Pfaue, H. (2003). Analysis of water in food by near infrared spectroscopy. *Food Chemistry*, *82*(1), 107–115. https://doi.org/10.1016/S0308-8146(02)00583-6

Cai, J. H. (2017). Near-Infrared Spectrum Detection of Wheat Gluten Protein Content Based on a Combined Filtering Method. *Journal of AOAC International*, *100*(5), 1565–1568. https://doi.org/10.5740/jaoacint.17-0008

Camire, M. E. (1991). Protein functionality modification by extrusion cooking. *Journal of the American Oil Chemists' Society*, *68*(3), 200–205. https://doi.org/10.1007/BF02657770

Campos, M. I., Antolin, G., Debán, L., & Pardo, R. (2018). Assessing the influence of temperature on NIRS prediction models for the determination of sodium content in dry-cured ham slices. *Food Chemistry*, *257*, 237–242. https://doi.org/10.1016/J.FOODCHEM.2018.02.131

Cheah, I., Sadat Shimul, A., Liang, J., & Phau, I. (2020). Drivers and barriers toward reducing meat consumption. *Appetite*, *149*, 104636. https://doi.org/10.1016/J.APPET.2020.104636

Cheftel, J. C., Kitagawa, M., & Queguiner, C. (1992). New Protein Texturization Processes by Extrusion Cooking at High Moisture Levels. In *Food Reviews International* (Vol. 8, Issue 2). Taylor & Francis Group. https://doi.org/10.1080/87559129209540940

Chen, F. L., Wei, Y. M., Zhang, B., & Ojokoh, A. O. (2010). System parameters and product properties response of soybean protein extruded at wide moisture range. *Journal of Food Engineering*, *96*(2), 208–213. https://doi.org/10.1016/j.jfoodeng.2009.07.014

Chen, J., Yang, C., Zhu, H., Li, Y., & Gui, W. (2018). A novel variable selection method based on stability and variable permutation for multivariate calibration. *Chemometrics and Intelligent Laboratory Systems*, *182*, 188–201. https://doi.org/10.1016/J.CHEMOLAB.2018.09.009

Chen, Q., Zhang, J., Liu, H., Li, T., & Wang, Q. (2023). Mechanism of high-moisture extruded protein fibrous structure formation based on the interactions among pea protein, amylopectin, and stearic acid. *Food Hydrocolloids*, *136*, 108254. https://doi.org/10.1016/J.FOODHYD.2022.108254

Chen, Q., Zhang, J., Zhang, Y., Liu, H., Li, T., Wang, Q., & Kaplan, D. L. (2023). Microscopic insight into the interactions between pea protein and fatty acids during high-moisture extrusion processing. *Food Chemistry*, *404*, 134176. https://doi.org/10.1016/J.FOODCHEM.2022.134176

Chen, Q., Zhang, J., Zhang, Y., & Wang, Q. (2022). Effect of fatty acid saturation degree on the rheological properties of pea protein and its high-moisture extruded product quality. *Food Chemistry*, *390*, 133139. https://doi.org/10.1016/J.FOODCHEM.2022.133139

Cornet, S. H. V., Bühler, J. M., Gonçalves, R., Bruins, M. E., van der Sman, R. G. M., & van der Goot, A. J. (2021). Apparent universality of leguminous proteins in swelling and fibre formation when mixed with gluten. *Food Hydrocolloids*, *120*, 106788. https://doi.org/10.1016/j.foodhyd.2021.106788

Cornet, S. H. V., Snel, S. J. E., Schreuders, F. K. G., van der Sman, R. G. M., Beyrer, M., & van der Goot, A. J. (2022). Thermo-mechanical processing of plant proteins using shear cell and high-moisture extrusion cooking. *Critical Reviews in Food Science and Nutrition*, *62*(12), 3264–3280. https://doi.org/10.1080/10408398.2020.1864618

Cozzolino, D., & Murray, I. (2004). Identification of animal meat muscles by visible and near infrared reflectance spectroscopy. *LWT - Food Science and Technology*, *37*(4), 447–452. https://doi.org/10.1016/j.lwt.2003.10.013

R

Cozzolino, D., Murray, I., Scaife, J. R., & Paterson, R. (2000). Study of dissected lamb muscles by visible and near infrared reflectance spectroscopy for composition assessment. *Animal Science*, *70*(3), 417–423. https://doi.org/10.1017/S1357729800051766

Cullen, P. J., & O'Donnell, C. P. (2009). Mixing in the food industry: trends and challenges. In P. J. Cullen (Ed.), *Food mixing Principles and Applications* (pp. 1–5). John Wiley & Sons Ltd.

Cuq, B., Abecassis, J., & Guilbert, S. (2003). State diagrams to help describe wheat bread processing. *International Journal of Food Science & Technology*, *38*(7), 759–766. https://doi.org/10.1046/J.1365-2621.2003.00748.X

Cuq, B., Boutrot, F., Redl, A., & Lullien-Pellerin, V. (2000). Study of the temperature effect on the formation of wheat gluten network: Influence on mechanical properties and protein solubility. *Journal of Agricultural and Food Chemistry*, *48*(7), 2954–2959. https://doi.org/10.1021/jf991339b

De Angelis, D., Opaluwa, C., Pasqualone, A., Karbstein, H. P., & Summo, C. (2023). Rheological properties of dry-fractionated mung bean protein and structural, textural, and rheological evaluation of meat analogues produced by high-moisture extrusion cooking. *Current Research in Food Science*, *7*, 100552. https://doi.org/10.1016/J.CRFS.2023.100552

Dekkers, B. L., Boom, R. M., & van der Goot, A. J. (2018). Structuring processes for meat analogues. In *Trends in Food Science and Technology* (Vol. 81, pp. 25–36). Elsevier Ltd. https://doi.org/10.1016/j.tifs.2018.08.011

Dekkers, B. L., Hamoen, R., Boom, R. M., & van der Goot, A. J. (2018). Understanding fiber formation in a concentrated soy protein isolate - Pectin blend. *Journal of Food Engineering*, *222*, 84–92. https://doi.org/10.1016/j.jfoodeng.2017.11.014

Dekkers, B. L., Nikiforidis, C. V., & van der Goot, A. J. (2016). Shear-induced fibrous structure formation from a pectin/SPI blend. *Innovative Food Science and Emerging Technologies*, *36*, 193–200. https://doi.org/10.1016/j.ifset.2016.07.003

Dhanapal, L., & Erkinbaev, C. (2024). Portable hyperspectral imaging coupled with multivariate analysis for real-time prediction of plant-based meat analogues quality. *Journal of Food Composition and Analysis*, *126*, 105840. https://doi.org/10.1016/j.jfca.2023.105840

Ding, H. B., & Xu, R. J. (2000). Near-infrared spectroscopic technique for detection of beef hamburger adulteration. *Journal of Agricultural and Food Chemistry*, *48*(6), 2193–2198. https://doi.org/10.1021/jf9907182

Dixit, Y., & Reis, M. M. (2023). Hyperspectral imaging for assessment of total fat in salmon fillets: A comparison between benchtop and snapshot systems. *Journal of Food Engineering*, *336*, 111212. https://doi.org/10.1016/j.jfoodeng.2022.111212

Dobraszczyk, B. J., & Morgenstern, M. P. (2003). Rheology and the breadmaking process. *Journal of Cereal Science*, *38*(3), 229–245. https://doi.org/10.1016/S0733-5210(03)00059-6

Dodds, S. A., & Heath, W. P. (2005). Construction of an online reduced-spectrum NIR calibration model from full-spectrum data. *Chemometrics and Intelligent Laboratory Systems*, *76*(1), 37–43. https://doi.org/10.1016/j.chemolab.2004.09.002

Dufour, M., Chaunier, L., Lourdin, D., Réguerre, A.-L., Hugon, F., Dugué, A., Kansou, K., Saulnier, L., & Della Valle, G. (2024). Unravelling the relationships between wheat dough extensional properties, gluten network and water distribution. *Food Hydrocolloids*, *146*, 109214. https://doi.org/10.1016/j.foodhyd.2023.109214

Duque-Estrada, P., Kyriakopoulou, K., de Groot, W., van der Goot, A. J., & Berton-Carabin, C. C. (2020). Oxidative stability of soy proteins: From ground soybeans to structured products. *Food Chemistry*, *318*, 126499. https://doi.org/10.1016/J.FOODCHEM.2020.126499

Ellekjaer, M. R., & Isaksson, T. (1992). Assessment of maximum cooking temperatures in previously heat treated beef. Part 1: Near infrared spectroscopy. *Journal of the Science of Food and Agriculture*, *59*(3), 335–343. https://doi.org/10.1002/jsfa.2740590310

Ellwanger, F., Pernice, L., Karbstein, H. P., & Emin, M. A. (2023). Investigating local residence time and thermomechanical stress profile in twin-screw extrusion of plant proteins by using the moving particle semi-implicit simulation method. *Journal of Food Engineering*, *359*, 111665. https://doi.org/10.1016/J.JFOODENG.2023.111665

Elmasry, G., & Nakauchi, S. (2015). Noninvasive sensing of thermal treatments of Japanese seafood products using imaging spectroscopy. *International Journal of Food Science and Technology*, *50*(9), 1960–1971. https://doi.org/10.1111/ijfs.12863

Emin, M. A. (2022). Key technological advances of extrusion processing. In P. Juliano, K. Knoerzer, J. Sellahewa, M. H. Nguyen, & R. Buckow (Eds.), *Food Engineering Innovations Across the Food Supply Chain* (pp. 131–148). Academic Press. https://doi.org/10.1016/B978-0-12-821292-9.00005-4

Emin, M. A., Quevedo, M., Wilhelm, M., & Karbstein, H. P. (2017). Analysis of the reaction behavior of highly concentrated plant proteins in extrusion-like conditions. *Innovative Food Science and Emerging Technologies*, *44*, 15–20. https://doi.org/10.1016/j.ifset.2017.09.013

Emin, M. A., & Schuchmann, H. P. (2017). A mechanistic approach to analyze extrusion processing of biopolymers by numerical, rheological, and optical methods. In *Trends in Food Science and Technology* (Vol. 60, pp. 88–95). Elsevier Ltd. https://doi.org/10.1016/j.tifs.2016.10.003

Emin, M. A., Teumer, T., Schmitt, W., Rädle, M., & Schuchmann, H. P. (2016). Measurement of the true melt temperature in a twin-screw extrusion processing of starch based matrices via infrared sensor. *Journal of Food Engineering*, *170*, 119–124. https://doi.org/10.1016/J.JFOODENG.2015.09.018

Ersch, C., ter Laak, I., van der Linden, E., Venema, P., & Martin, A. (2015). Modulating fracture properties of mixed protein systems. *Food Hydrocolloids*, *44*, 59–65. https://doi.org/10.1016/j.foodhyd.2014.09.009

Evans, A. J., Huang, S., Osborne, B. C., Kotwal, Z., & Wesley, U. (1999). Near infrared on-line measurement of degree of cook in extrusion processing of wheat flour. *Journal of Near Infrared Spectroscopy*, *7*(2), 77–84. https://doi.org/10.1255/jnirs.237

Fowler, S. M., Wheeler, D., Morris, S., Mortimer, S. I., & Hopkins, D. L. (2021). Partial least squares and machine learning for the prediction of intramuscular fat content of lamb loin. *Meat Science*, *177*, 108505. https://doi.org/10.1016/J.MEATSCI.2021.108505

Gaitán-Jurado, A. J., Ortiz-Somovilla, V., España-España, F., Pérez-Aparicio, J., & De Pedro-Sanz, E. J. (2008). Quantitative analysis of pork dry-cured sausages to quality control by NIR spectroscopy. *Meat Science*, *78*(4), 391–399. https://doi.org/10.1016/J.MEATSCI.2007.07.005

Garina, E. D., den Adel, R., van Duynhoven, J. P. M., Smith, G. N., Dalgliesh, R. M., Sztucki, M., & Bouwman, W. G. (2024). SANS and SAXS: A Love Story to unravel structural evolution of soy proteins and polysaccharide fibres during high moisture extrusion for meat alternatives. *Food Hydrocolloids*, *155*, 110121. https://doi.org/10.1016/J.FOODHYD.2024.110121

Giezen, F. E., Jansen, W. W. J. T., & Willemsen, J. H. A. (2014). *METHOD OF MAKING STRUCTURED PROTEIN COMPOSITIONS* (Patent US 2014/0127363 A1).

Godschalk-Broers, L., Sala, G., & Scholten, E. (2022). Meat Analogues: Relating Structure to Texture and Sensory Perception. *Foods 2022, Vol. 11, Page 2227*, *11*(15), 2227. https://doi.org/10.3390/FOODS11152227

Goi, A., Hocquette, J. F., Pellattiero, E., & De Marchi, M. (2022). Handheld near-infrared spectrometer allows on-line prediction of beef quality traits. *Meat Science*, *184*, 108694. https://doi.org/10.1016/j.meatsci.2021.108694

Good Food Institute. (2022). *2021 State of The Industry Report Plant-base meat, seafood, eggs and dairy*. https://gfi.org/wp-content/uploads/2022/03/2021-U.S.-retail-market-insights_Plant-based-foods-GFI.pdf

Grabowska, K. J., Tekidou, S., Boom, R. M., & van der Goot, A. J. (2014). Shear structuring as a new method to make anisotropic structures from soy-gluten blends. *Food Research International*, *64*, 743–751. https://doi.org/10.1016/j.foodres.2014.08.010

Grabowska, K. J., Zhu, S., Dekkers, B. L., De Ruijter, N. C. A., Gieteling, J., & van der Goot, A. J. (2016). Shear-induced structuring as a tool to make anisotropic materials using soy protein concentrate. *Journal of Food Engineering*, *188*, 77–86. https://doi.org/10.1016/j.jfoodeng.2016.05.010

Guy, R. C. E., Osborne, B. G., & Robert, P. (1996). The Application of Near Infrared Reflectance Spectroscopy to Measure the Degree of Processing in Extrusion Cooking Processes. *Journal of Food Engineering*, *27*(3), 241–258. https://doi.org/10.1016/0260-8774(95)00006-2

Guyony, V., Fayolle, F., & Jury, V. (2023). High moisture extrusion of vegetable proteins for making fibrous meat analogs: A review. *Food Reviews International*, *39*(7), 4262–4287. https://doi.org/10.1080/87559129.2021.2023816

Hageman, J. A., Westerhuis, J. A., & Smilde, A. K. (2005). Temperature robust multivariate calibration: An overview of methods for dealing with temperature influences on near infrared spectra. *Journal of Near Infrared Spectroscopy*, *13*(2), 53–62. https://doi.org/10.1255/jnirs.457

Högg, E., & Rauh, C. (2023). Towards a Better Understanding of Texturization during High-Moisture Extrusion (HME)—Part I: Modeling the Texturability of Plant-Based Proteins. *Foods*, *12*(10). https://doi.org/10.3390/foods12101955

Holman, B. W. B., Bailes, K. L., Meyer, R. G., & Hopkins, D. L. (2019). Effect of modified Soxhlet (Soxtec) and Folch extraction method selection on the total lipid determination of aged beef. *Journal of Food Science and Technology*, *56*(8), 3957–3961. https://doi.org/ 10.1007/s13197-019-03878-4

Hoving-Bolink, A. H., Vedder, H. W., Merks, J. W. M., De Klein, W. J. H., Reimert, H. G. M., Frankhuizen, R., van den Broek, W. H. A. M., & Lambooij, E. (2005). Perspective of NIRS measurements early post mortem for prediction of pork quality. *Meat Science*, *69*(3), 417–423. https://doi.org/10.1016/j.meatsci.2004.08.012

Hughes, R. K., Desforges, N., Selwood, C., Smith, R., Speirs, C. I., Sinnaeve, G., Gorton, P. G., Wiseman, J., Jumel, K., Harding, S. E., Hill, S. E., Street, V., Wang, T. L., & Hedley, C. L. (2001). Genes affecting starch biosynthesis exert pleiotropic effects on the protein content and composition of pea seeds. *Journal of the Science of Food and Agriculture*, *81*(9), 877–882. https://doi.org/10.1002/jsfa.856

Jaeger, S. R., Cardello, A. V., Jin, D., Ryan, G. S., & Giacalone, D. (2023). Consumer perception of plant-based yoghurt: Sensory drivers of liking and emotional, holistic and conceptual associations. *Food Research International*, *167*, 112666. https://doi.org/10.1016/J.FOODRES.2023.112666

Jaspe, J., & Hagen, S. J. (2006). Do protein molecules unfold in a simple shear flow? *Biophysical Journal*, *91*(9), 3415–3424. https://doi.org/10.1529/biophysj.106.089367

Ji, Y., Wang, Z., Deng, Q., Chen, J., He, Z., Zeng, M., Qin, F., & Pan, H. (2023). Soy Protein Hydrolysates Affect the Structural and Mechanical Properties of Soy Protein-Wheat Gluten Extrudates Using High Moisture Extrusion. *Foods 2023, Vol. 12, Page 912*, *12*(5), 912. https://doi.org/10.3390/FOODS12050912

Jia, R., Zhang, M., Yang, T., Ma, M., Sun, Q., & Li, M. (2022). Evolution of the morphological, structural, and molecular properties of gluten protein in dough with different hydration levels during mixing. *Food Chemistry: X*, *15*, 100448. https://doi.org/10.1016/J.FOCHX.2022.100448

Jia, W., Curubeto, N., Rodríguez-Alonso, E., Keppler, J. K., & van der Goot, A. J. (2021). Rapeseed protein concentrate as a potential ingredient for meat analogues. *Innovative Food Science & Emerging Technologies*, *72*, 102758. https://doi.org/10.1016/J.IFSET.2021.102758

Ju, Q., Yuan, Y., Wu, C., Hu, Y., Zhou, S., & Luan, G. (2023). Heat-induced aggregation of subunits/polypeptides of soybean protein: Structural and physicochemical properties. *Food Chemistry*, *405*, 134774. https://doi.org/10.1016/J.FOODCHEM.2022.134774

Kantanen, K., Oksanen, A., Edelmann, M., Suhonen, H., Sontag-Strohm, T., Piironen, V., Diaz, J. M. R., & Jouppila, K. (2022). Physical Properties of Extrudates with Fibrous Structures Made of Faba Bean Protein Ingredients Using High Moisture Extrusion. *Foods*, *11*(9), 1280. https://doi.org/10.3390/foods11091280

Kartakoullis, A., Comaposada, J., Cruz-Carrión, A., Serra, X., & Gou, P. (2019). Feasibility study of smartphone-based Near Infrared Spectroscopy (NIRS) for salted minced meat composition diagnostics at different temperatures. *Food Chemistry*, *278*, 314–321. https://doi.org/10.1016/j.foodchem.2018.11.054

Kendler, C., Duchardt, A., Karbstein, H. P., & Emin, M. A. (2021). Effect of oil content and oil addition point on the extrusion processing of wheat gluten-based meat analogues. *Foods*, *10*(4), 697. https://doi.org/10.3390/foods10040697

Kim, B. F., Santo, R. E., Scatterday, A. P., Fry, J. P., Synk, C. M., Cebron, S. R., Mekonnen, M. M., Hoekstra, A. Y., de Pee, S., Bloem, M. W., Neff, R. A., & Nachman, K. E. (2020). Country-specific dietary shifts to mitigate climate and water crises. *Global Environmental Change*, *62*, 101926. https://doi.org/10.1016/J.GLOENVCHA.2019.05.010

Kim, B., Park, J., & Yoon, W. (2005). Rheology and Texture Properties of Surimi Gels. *Surimi Technology*, 491–582. https://doi.org/10.1201/9781420028041.ch11

Kjeldahl, K., & Bro, R. (2010). Some common misunderstandings in chemometrics. *Journal of Chemometrics*, *24*(7–8), 558–564. https://doi.org/10.1002/cem.1346

Klaypradit, W., Kerdpiboon, S., & Singh, R. K. (2011). Application of Artificial Neural Networks to Predict the Oxidation of Menhaden Fish Oil Obtained from Fourier Transform Infrared Spectroscopy Method. *Food and Bioprocess Technology*, *4*(3), 475–480. https://doi.org/10.1007/s11947-010-0386-5

Koksel, F., & Scanlon, M. G. (2012). Effects of composition on dough development and air entrainment in doughs made from gluten-starch blends. *Journal of Cereal Science*, *56*(2), 445–450. https://doi.org/10.1016/J.JCS.2012.05.013

Krepper, G., Romeo, F., Fernandes, D. D. de S., Diniz, P. H. G. D., de Araújo, M. C. U., Di Nezio, M. S., Pistonesi, M. F., & Centurión, M. E. (2018). Determination of fat content in chicken hamburgers using NIR spectroscopy and the Successive Projections Algorithm for interval selection in PLS regression (iSPA-PLS). *Spectrochimica Acta Part A: Molecular and Biomolecular Spectroscopy*, *189*, 300–306. https://doi.org/10.1016/J.SAA.2017.08.046

Krintiras, G. A., Gadea Diaz, J., van der Goot, A. J., Stankiewicz, A. I., & Stefanidis, G. D. (2016). On the use of the Couette Cell technology for large scale production of textured soy-based meat replacers. *Journal of Food Engineering*, *169*, 205–213. https://doi.org/10.1016/j.jfoodeng.2015.08.021

Kucha, C. T., Liu, L., Ngadi, M., & Gariépy, C. (2022). Prediction and visualization of fat content in polythene-packed meat using near-infrared hyperspectral imaging and chemometrics. *Journal of Food Composition and Analysis*, *111*, 104633. https://doi.org/10.1016/J.JFCA.2022.104633

Kuhn, M. (2008). Building predictive models in R using the caret package. *Journal of Statistical Software*, *28*(5), 1–26. https://doi.org/10.18637/JSS.V028.I05

Kwon, H., Hwang, J., Cho, Y., & Lee, S. (2024). Machine learning-enabled hyperspectral approaches for structural characterization of precooked noodles during refrigerated storage. *Food Chemistry*, *450*, 139371. https://doi.org/10.1016/J.FOODCHEM.2024.139371

Kyriakopoulou, K., Keppler, J. K., & van der Goot, A. J. (2021). Functionality of ingredients and additives in plant-based meat analogues. *Foods*, *10*(3), 600. https://doi.org/10.3390/foods10030600

Laurens, L. M. L., & Wolfrum, E. J. (2013). High-throughput quantitative biochemical characterization of algal biomass by NIR spectroscopy; Multiple linear regression and multivariate linear regression analysis. *Journal of Agricultural and Food Chemistry*, *61*(50), 12307–12314. https://doi.org/ 10.1021/jf403086f

Lê, S., Josse, J., & Husson, F. (2008). FactoMineR: An R package for multivariate analysis. *Journal of Statistical Software*, *25*(1), 1–18. https://doi.org/10.18637/JSS.V025.I01

Létang, C., Piau, M., & Verdier, C. (1999). Characterization of wheat flour–water doughs. Part I: Rheometry and microstructure. *Journal of Food Engineering*, *41*(2), 121–132. https://doi.org/10.1016/S0260-8774(99)00082-5

Li, F., Zhang, Y., Guo, B., Wei, Y., Don, C., Pan, W., & Zhang, B. (2020). The mesoscopic structure in wheat flour dough development. *Journal of Cereal Science*, *95*, 103087. https://doi.org/10.1016/J.JCS.2020.103087

Liu, K. S., & Hsieh, F. H. (2007). Protein–Protein Interactions in High Moisture-Extruded Meat Analogs and Heat-Induced Soy Protein Gels. *Journal of the American Oil Chemists' Society*, *84*(8), 741–748. https://doi.org/10.1007/S11746-007-1095-8

Lumley, T. (20 10.32614/CRAN.package.leaps24). *leaps: Regression Subset Selection* (3.2). https://doi.org/10.32614/CRAN.package.leaps

Ma, J., Pu, H., & Sun, D. W. (2018). Predicting intramuscular fat content variations in boiled pork muscles by hyperspectral imaging using a novel spectral pre-processing technique. *LWT*, *94*, 119–128. https://doi.org/10.1016/j.lwt.2018.04.030

Ma, Y., Schlangen, M., Potappel, J., Zhang, L., & van der Goot, A. J. (2024). Quantitative characterizations of visual fibrousness in meat analogues using automated image analysis. *Journal of Texture Studies*, *55*(1), e12806. https://doi.org/10.1111/JTXS.12806

Macosko, C. W. (1994). Extensional Rheometry. In *RHEOLOGY Principles, Measurements and Applications* (pp. 285–336). Wiley-VCH.

Mæhre, H. K., Dalheim, L., Edvinsen, G. K., Elvevoll, E. O., & Jensen, I. J. (2018). Protein determination—method matters. *Foods*, *7*(1), 5. https://doi.org/10.3390/foods7010005

Maningat, C. C., Jeradechachai, T., & Buttshaw, M. R. (2022). Textured wheat and pea proteins for meat alternative applications. *Cereal Chemistry*, *99*(1), 37–66. https://doi.org/10.1002/cche.10503

Manski, J. M., van der Goot, A. J., & Boom, R. M. (2007). Formation of fibrous materials from dense calcium caseinate dipersions. *Biomacromolecules*, *8*(4), 1271–1279. https://doi.org/10.1021/bm061008p

Mateen, A., Mathpati, M., & Singh, G. (2023). A study on high moisture extrusion for making whole cut meat analogue: Characterization of system, process and product parameters. *Innovative Food Science & Emerging Technologies*, *85*, 103315. https://doi.org/10.1016/J.IFSET.2023.103315

Maung, T. T., Gu, B. Y., & Ryu, G. H. (2021). Influence of extrusion process parameters on specific mechanical energy and physical properties of high-moisture meat analog. *International Journal of Food Engineering*, *17*(2), 149–157. https://doi.org/10.1515/ijfe-2020-0042

Maurya, A. K., & Said, P. P. (2014). Extrusion Processing on Physical and Chemical Properties of Protein Rich Products-An Overview. In *Journal of Bioresource Engineering and technology* (Vol. 2, Issue 4). https://www.researchgate.net/publication/281839028

McClements, D. J., Weiss, J., Kinchla, A. J., Nolden, A. A., & Grossmann, L. (2021). Methods for Testing the Quality Attributes of Plant-Based Foods: Meat- and Processed-Meat Analogs. *Foods 2021, Vol. 10, Page 260*, *10*(2), 260. https://doi.org/10.3390/FOODS10020260

R

Meerts, M., Cardinaels, R., Oosterlinck, F., M. Courtin, C., & Moldenaers, P. (2017). The Interplay Between the Main Flour Constituents in the Rheological Behaviour of Wheat Flour Dough. *Food and Bioprocess Technology*, *10*(2), 249–265. https://doi.org/10.1007/s11947-016-1810-2

Mefleh, M., Pasqualone, A., Caponio, F., De Angelis, D., Natrella, G., Summo, C., & Faccia, M. (2022). Spreadable plant-based cheese analogue with dry-fractioned pea protein and inulin–olive oil emulsion-filled gel. *Journal of the Science of Food and Agriculture*, *102*(12), 5478–5487. https://doi.org/10.1002/JSFA.11902

Meng, A., Chen, F., Zhao, D., Wei, Y., & Zhang, B. (2022). Identifying changes in soybean protein properties during high-moisture extrusion processing using dead-stop operation. *Food Chemistry*, *395*, 133599. https://doi.org/10.1016/J.FOODCHEM.2022.133599

Meuser, F., & van Lengerich, B. (1984). System Analytical Model for the Extrusion of Starches. In P. Zeuthen, J. C. Cheftel, C. Eriksson, M. Jul, H. Leniger, P. Linko, G. Varela, & G. Vos (Eds.), *Thermal processing and quality of foods* (pp. 175–179). Elsevier Applied Science Publishers.

Mevik, B.-H., & Wehrens, R. (2007). The pls Package: Principal Component and Partial Least Squares Regression in R. *Journal of Statistical Software*, *18*(2). https://doi.org/10.18637/jss.v018.i02

Michel, F., Hartmann, C., & Siegrist, M. (2021). Consumers' associations, perceptions and acceptance of meat and plant-based meat alternatives. *Food Quality and Preference*, *87*, 104063. https://doi.org/10.1016/j.foodqual.2020.104063

Mishra, P., & Nikzad-Langerodi, R. (2021). A brief note on application of domain-invariant PLS for adapting near-infrared spectroscopy calibrations between different physical forms of samples. *Talanta*, *232*, 122461. https://doi.org/10.1016/j.talanta.2021.122461

Mishra, P., Verkleij, T., & Klont, R. (2021). Improved prediction of minced pork meat chemical properties with near-infrared spectroscopy by a fusion of scatter-correction techniques. *Infrared Physics and Technology*, *113*, 103643. https://doi.org/10.1016/j.infrared.2021.103643

Mourya, V., Kumar, V., Rani, A., Jain, M., & Husain, S. M. (2016). Near-Infrared Reflectance Spectroscopy for Protein Content in Soybean Flour and Screening of Germplasm Across Different Countries. *Agricultural Research*, *5*(1), 29–34. https://doi.org/10.1007/s40003-015-0196-0

Nasrollahzadeh, F., Roman, L., Swaraj, V. J. S., Ragavan, K. V., Vidal, N. P., Dutcher, J. R., & Martinez, M. M. (2022). Hemp (Cannabis sativa L.) protein concentrates from wet and dry industrial fractionation: Molecular properties, nutritional composition, and anisotropic structuring. *Food Hydrocolloids*, *131*, 107755. https://doi.org/10.1016/J.FOODHYD.2022.107755

Noguchi, A. (1989). Extrusion cooking of high-moisture protein foods. In C. Mercier, P. Linko, & J. M. Harper (Eds.), *Extrusion cooking*. American Association of Cereal Chemists, Inc.

O'Farrell, M., Bakke, K. A. H., Tschudi, J., & Wold, J. P. (2011). Near-infrared (NIR) interactance system for non-contact monitoring of the temperature profile of baked liver pâté. *Applied Spectroscopy*, *65*(12), 1372–1379. https://doi.org/10.1366/11-06277

Omohimi, C. I., Sobukola, O. P., Sarafadeen, K. O., & Sanni, L. O. (2014). Effect of Thermo-extrusion Process Parameters on Selected Quality Attributes of Meat Analogue from Mucuna Bean Seed Flour. *Nigerian Food Journal*, *32*(1), 21–30. https://doi.org/10.1016/s0189-7241(15)30092-8

Onwezen, M. C., Bouwman, E. P., Reinders, M. J., & Dagevos, H. (2021). A systematic review on consumer acceptance of alternative proteins: Pulses, algae, insects, plant-based meat alternatives, and cultured meat. *Appetite*, *159*, 105058. https://doi.org/10.1016/J.APPET.2020.105058

Opaluwa, C., Lott, T., Karbstein, H. P., & Emin, M. A. (2023). Encapsulation of oil in the high moisture extrusion of wheat gluten: Interrelation between process parameters, matrix viscosity and oil droplet size. *Future Foods*, *7*, 100222. https://doi.org/10.1016/J.FUFO.2023.100222

Osborne, B. G. (2000). Near-infrared spectroscopy in food analysis. In R. A. Meyers (Ed.), *Encyclopedia of Analytical Chemistry* (pp. 1–14). Wiley.

Osborne, B. G. (2006). Near-Infrared Spectroscopy in Food Analysis. In R. A. Meyers & R. J. McGorrin (Eds.), *Encyclopedia of Analytical Chemistry* (pp. 1–14). Wiley. https://doi.org/10.1002/9780470027318.a1018

Osen, R., & Schweiggert-Weisz, U. (2016). High-Moisture Extrusion: Meat Analogues. In *Reference Module in Food Science* (pp. 1–7). Elsevier. https://doi.org/10.1016/B978-0-08-100596-5.03099-7

Osen, R., Toelstede, S., Eisner, P., & Schweiggert-Weisz, U. (2015). Effect of high moisture extrusion cooking on protein–protein interactions of pea (Pisum sativum L.) protein isolates. *International Journal of Food Science & Technology*, *50*(6), 1390–1396. https://doi.org/10.1111/IJFS.12783

Osen, R., Toelstede, S., Wild, F., Eisner, P., & Schweiggert-Weisz, U. (2014). High moisture extrusion cooking of pea protein isolates: Raw material characteristics, extruder responses, and texture properties. *Journal of Food Engineering*, *127*, 67–74. https://doi.org/10.1016/j.jfoodeng.2013.11.023

Ozaki, Y., & Morisawa, Y. (2021). Principles and Characteristics of NIR Spectroscopy. In Y. Ozaki, C. Huck, S. Tsuchikawa, & S. B. Engelsen (Eds.), *Near-Infrared Spectroscopy* (1st ed., pp. 11–35). Springer Singapore. https://doi.org/10.1007/978-981-15-8648-4_2

Palanisamy, M., Franke, K., Berger, R. G., Heinz, V., & Töpfl, S. (2019). High moisture extrusion of lupin protein: influence of extrusion parameters on extruder responses and product properties. *Journal of the Science of Food and Agriculture*, *99*(5), 2175–2185. https://doi.org/10.1002/jsfa.9410

Pallone, J. A. L., Caramês, E. T. dos S., & Alamar, P. D. (2018). Green analytical chemistry applied in food analysis: alternative techniques. *Current Opinion in Food Science*, *22*, 115–121. https://doi.org/10.1016/J.COFS.2018.01.009

Pasquini, C. (2018). Near infrared spectroscopy: A mature analytical technique with new perspectives – A review. *Analytica Chimica Acta*, *1026*, 8–36. https://doi.org/10.1016/j.aca.2018.04.004

Peighambardoust, S. H., van der Goot, A. J., Hamer, R. J., & Boom, R. M. (2004). A new method to study simple shear processing of wheat gluten-starch mixtures. In *Cereal Chemistry* (Vol. 81, Issue 6). American Association of Cereal Chemists. https://doi.org/10.1094/CCHEM.2004.81.6.714

Peighambardoust, S. H., van der Goot, A. J., Hamer, R. J., & Boom, R. M. (2005). Effect of simple shear on the physical properties of glutenin macro polymer (GMP). *Journal of Cereal Science*, *42*(1), 59–68. https://doi.org/10.1016/j.jcs.2004.12.007

Pietsch, V. L., Bühler, J. M., Karbstein, H. P., & Emin, M. A. (2019). High moisture extrusion of soy protein concentrate: Influence of thermomechanical treatment on protein-protein interactions and rheological properties. *Journal of Food Engineering*, *251*, 11–18. https://doi.org/10.1016/j.jfoodeng.2019.01.001

Pietsch, V. L., Karbstein, H. P., & Emin, M. A. (2018). Kinetics of wheat gluten polymerization at extrusion-like conditions relevant for the production of meat analog products. *Food Hydrocolloids*, *85*, 102–109. https://doi.org/10.1016/J.FOODHYD.2018.07.008

Pietsch, V. L., Schöffel, F., Rädle, M., Karbstein, H. P., & Emin, M. A. (2019). High moisture extrusion of wheat gluten: Modeling of the polymerization behavior in the screw section of the extrusion process. *Journal of Food Engineering*, *246*, 67–74. https://doi.org/10.1016/j.jfoodeng.2018.10.031

Pietsch, V. L., Werner, R., Karbstein, H. P., & Emin, M. A. (2019). High moisture extrusion of wheat gluten: Relationship between process parameters, protein polymerization, and final product characteristics. *Journal of Food Engineering*, *259*, 3–11. https://doi.org/10.1016/j.jfoodeng.2019.04.006

Pommet, M., Morel, M. H., Redl, A., & Guilbert, S. (2004). Aggregation and degradation of plasticized wheat gluten during thermo-mechanical treatments, as monitored by rheological and biochemical changes. *Polymer*, *45*(20), 6853–6860. https://doi.org/10.1016/J.POLYMER.2004.07.076

Porep, J. U., Kammerer, D. R., & Carle, R. (2015). On-line application of near infrared (NIR) spectroscopy in food production. *Trends in Food Science & Technology*, *46*(2), 211–230. https://doi.org/10.1016/J.TIFS.2015.10.002

Prevolnik, M., Škrlep, M., Janeš, L., Velikonja-Bolta, Š., Škorjanc, D., & Čandek-Potokar-Potokar, M. (2011). Accuracy of near infrared spectroscopy for prediction of chemical composition, salt content and free amino acids in dry-cured ham. *Meat Science*, *88*(2), 299–304. https://doi.org/10.1016/j.meatsci.2011.01.007

Pu, H., Sun, D. W., Ma, J., Liu, D., & Kamruzzaman, M. (2014). Hierarchical variable selection for predicting chemical constituents in lamb meats using hyperspectral imaging. *Journal of Food Engineering*, *143*, 44–52. https://doi.org/10.1016/j.jfoodeng.2014.06.025

Puski, G., & Konwinski, A. (1976). *Process of making a soy-based meat substitute*. *19*, 7.

Quevedo, M., Kulozik, U., Karbstein, H. P., & Emin, M. A. (2020). Kinetics of denaturation and aggregation of highly concentrated β-Lactoglobulin under defined thermomechanical treatment. *Journal of Food Engineering*, *274*, 109825. https://doi.org/10.1016/J.JFOODENG.2019.109825

R Core Team. (2023). *R: A Language and Environment for Statistical Computing* (4.3.2). R Foundation for Statistical Computing.

Ramachandraiah, K. (2021). Potential Development of Sustainable 3D-Printed Meat Analogues: A Review. *Sustainability 2021, Vol. 13, Page 938*, *13*(2), 938. https://doi.org/10.3390/SU13020938

Ramos Diaz, J. M., Kantanen, K., Edelmann, J. M., Suhonen, H., Sontag-Strohm, T., Jouppila, K., & Piironen, V. (2022). Fibrous meat analogues containing oat fiber concentrate and pea protein isolate: Mechanical and physicochemical characterization. *Innovative Food Science & Emerging Technologies*, *77*, 102954. https://doi.org/10.1016/J.IFSET.2022.102954

Ranade, S. S., & Thiagarajan, P. (2017). Selection of a design for response surface. *IOP Conference Series: Materials Science and Engineering*, *263*, 022043. https://doi.org/10.1088/1757-899X/263/2/022043

Ranzan, C., Trierweiler, L. F., Hitzmann, B., & Trierweiler, J. O. (2015). NIR pre-selection data using modified changeable size moving window partial least squares and pure spectral chemometrical modeling with ant colony optimization for wheat flour characterization. *Chemometrics and Intelligent Laboratory Systems*, *142*, 78–86. https://doi.org/10.1016/J.CHEMOLAB.2015.01.007

Reis, M. G., Agnew, M., Jacob, N., & Reis, M. M. (2022). Comparative evaluation of miniaturized and conventional NIR spectrophotometer for estimation of fatty acids in cheeses. *Spectrochimica Acta Part A: Molecular and Biomolecular Spectroscopy*, *279*, 121433. https://doi.org/10.1016/J.SAA.2022.121433

Riaz, M. N. (2011). Texturized vegetable proteins. In G. O. Philips & P. A. Williams (Eds.), *Handbook of Food Proteins* (pp. 395–418). Woodhead Publishing. https://doi.org/10.1533/9780857093639.395

Riazi, F., Tehrani, M. M., Lammers, V., Heinz, V., & Savadkoohi, S. (2023). Unexpected morphological modifications in high moisture extruded pea-flaxseed proteins: Part I, topological and conformational characteristics, textural attributes, and viscoelastic phenomena. *Food Hydrocolloids*, *136*. https://doi.org/10.1016/J.FOODHYD.2022.108304

Roger, J. M., Palagos, B., Bertrand, D., & Fernandez-Ahumada, E. (2011). CovSel: Variable selection for highly multivariate and multi-response calibration. Application to IR spectroscopy. *Chemometrics and Intelligent Laboratory Systems*, *106*(2), 216–223. https://doi.org/10.1016/j.chemolab.2010.10.003

RStudio Team. (2020). *RStudio: Integrated Development for R* (2023.09.1). RStudio, PBC.

Samard, S., Gu, B. Y., & Ryu, G. H. (2019). Effects of extrusion types, screw speed and addition of wheat gluten on physicochemical characteristics and cooking stability of meat analogues. *Journal of the Science of Food and Agriculture*, *99*(11), 4922–4931. https://doi.org/10.1002/jsfa.9722

Samard, S., & Ryu, G. H. (2019). Physicochemical and functional characteristics of plant protein-based meat analogs. *Journal of Food Processing and Preservation*, *43*(10), e14123. https://doi.org/10.1111/jfpp.14123

Sandoval Murillo, J. L., Osen, R., Hiermaier, S., & Ganzenmüller, G. (2019). Towards understanding the mechanism of fibrous texture formation during high-moisture extrusion of meat substitutes. *Journal of Food Engineering*, *242*, 8–20. https://doi.org/10.1016/j.jfoodeng.2018.08.009

Sato, T., Takahashi, M., & Matsunaga, R. (2002). Use of NIR spectroscopy for estimation of FA composition of soy flour. *JAOCS, Journal of the American Oil Chemists' Society*, *79*(6), 535–537. https://doi.org/10.1007/s11746-002-0517-3

Savitzky, A., & Golay, M. J. E. (1964). Smoothing and Differentiation of Data by Simplified Least Squares Procedures. *Analytical Chemistry*, *36*(8), 1627–1639. https://doi.org/10.1021/ac60214a047

Schlangen, M., Ribberink, M. A., Taghian Dinani, S., Sagis, L. M. C., & van der Goot, A. J. (2023). Mechanical and rheological effects of transglutaminase treatment on dense plant protein blends. *Food Hydrocolloids*, *136*, 108261. https://doi.org/10.1016/J.FOODHYD.2022.108261

Schmid, E. M., Farahnaky, A., Adhikari, B., & Torley, P. J. (2022). High moisture extrusion cooking of meat analogs: A review of mechanisms of protein texturization. *Comprehensive Reviews in Food Science and Food Safety*. https://doi.org/10.1111/1541-4337.13030

Schreuders, F. K. G., Bodnár, I., Erni, P., Boom, R. M., & der Goot, A. J. van. (2020). Water redistribution determined by time domain NMR explains rheological properties of dense fibrous protein blends at high temperature. *Food Hydrocolloids*, *101*, 105562. https://doi.org/10.1016/j.foodhyd.2019.105562

Schreuders, F. K. G., Dekkers, B. L., Bodnár, I., Erni, P., Boom, R. M., & van der Goot, A. J. (2019). Comparing structuring potential of pea and soy protein with gluten for meat analogue preparation. *Journal of Food Engineering*, *261*(May), 32–39. https://doi.org/10.1016/j.jfoodeng.2019.04.022

Schreuders, F. K. G., Sagis, L. M. C., Bodnár, I., Boom, R. M., & van der Goot, A. J. (2022). Non-linear rheology reveals the importance of elasticity in meat and meat analogues. *Scientific Reports*, *12*(1), 1334. https://doi.org/10.1038/s41598-021-04478-z

Schreuders, F. K. G., Sagis, L. M. C., Bodnár, I., Erni, P., Boom, R. M., & van der Goot, A. J. (2021). Mapping the texture of plant protein blends for meat analogues. *Food Hydrocolloids*, *118*, 106753. https://doi.org/10.1016/j.foodhyd.2021.106753

Schreuders, F. K. G., Schlangen, M., Bodnár, I., Erni, P., Boom, R. M., & van der Goot, A. J. (2022). Structure formation and non-linear rheology of blends of plant proteins with pectin and cellulose. *Food Hydrocolloids*, *124*, 107327. https://doi.org/10.1016/j.foodhyd.2021.107327

Schreuders, F. K. G., Schlangen, M., Kyriakopoulou, K., Boom, R. M., & van der Goot, A. J. (2021). Texture methods for evaluating meat and meat analogue structures: A review. *Food Control*, *127*, 108103. https://doi.org/10.1016/j.foodcont.2021.108103

Sha, L., & Xiong, Y. L. (2020). Plant protein-based alternatives of reconstructed meat: Science, technology, and challenges. *Trends in Food Science & Technology*, *102*, 51–61. https://doi.org/10.1016/j.tifs.2020.05.022

Shand, P. J., Ya, H., Pietrasik, Z., & Wanasundara, P. K. J. P. D. (2008). Transglutaminase treatment of pea proteins: Effect on physicochemical and rheological properties of heat-induced protein gels. *Food Chemistry*, *107*(2), 692–699. https://doi.org/10.1016/j.foodchem.2007.08.095

Sharma, L. G., & Pandey, L. M. (2021). Thermomechanical process induces unfolding and fibrillation of bovine serum albumin. *Food Hydrocolloids*, *112*. https://doi.org/10.1016/j.foodhyd.2020.106294

Shaw, R. A., & Mantsch, H. H. (2006). Infrared Spectroscopy in Clinical and Diagnostic Analysis. *Encyclopedia of Analytical Chemistry*. https://doi.org/10.1002/9780470027318.A0106

Shen, F., Ying, Y., Li, B., Zheng, Y., & Hu, J. (2011). Prediction of sugars and acids in Chinese rice wine by mid-infrared spectroscopy. *Food Research International*, *44*(5), 1521–1527. https://doi.org/10.1016/J.FOODRES.2011.03.058

Shrestha, S., van 't Hag, L., Haritos, V., & Dhital, S. (2023). Rheological and textural properties of heat-induced gels from pulse protein isolates: Lentil, mungbean and yellow pea. *Food Hydrocolloids*, *143*, 108904. https://doi.org/10.1016/J.FOODHYD.2023.108904

Shrestha, S., van 't Hag, L., Haritos, V., & Dhital, S. (2024). Fate of pulse globulin proteins molecular Structure and composition on high moisture extrusion. *Food Hydrocolloids*, *149*, 109512. https://doi.org/10.1016/J.FOODHYD.2023.109512

Sivakumar, C., Chaudhry, M. M. A., & Paliwal, J. (2022). Classification of pulse flours using near-infrared hyperspectral imaging. *Lwt*, *154*, 112799. https://doi.org/10.1016/j.lwt.2021.112799

Skåra, T., Stormo, S. K., Skipnes, D., Kondjoyan, A., Sivertsen, A., Gins, G., van Derlinden, E., Valdramidis, V. P., & van Impe, J. F. M. (2014). Estimation of surface temperature and thermal load in short-time heat treatment of surimi through reflectance spectroscopy and heat transfer modeling. *Journal of Food Engineering*, *120*(1), 75–80. https://doi.org/10.1016/J.JFOODENG.2013.07.022

Skibsted, E. T. S., Boelens, H. F. M., Westerhuis, J. A., Smilde, A. K., Broad, N. W., Rees, D. R., & Witte, D. T. (2005). Net analyte signal based statistical quality control. *Analytical Chemistry*, *77*(22), 7103–7114. https://doi.org/10.1021/ac048138d

Snel, S. J. E., Amroussi, Y., van der Goot, A. J., & Beyrer, M. (2023). Rework Potential of Soy and Pea Protein Isolates in High-Moisture Extrusion. *Foods 2023, Vol. 12, Page 2543*, *12*(13), 2543. https://doi.org/10.3390/FOODS12132543

Snel, S. J. E., Bellwald, Y., van der Goot, A. J., & Beyrer, M. (2022). Novel rotating die coupled to a twin-screw extruder as a new route to produce meat analogues with soy, pea and gluten. *Innovative Food Science & Emerging Technologies*, *81*, 103152. https://doi.org/10.1016/j.ifset.2022.103152

Snel, S. J. E., Otto, K., Schlangen, M., Beyrer, M., & van der Goot, A. J. (2024). Type of pectin determines structuring potential of soy proteins into meat analogue applications. *Food Hydrocolloids*, *146*, 109262. https://doi.org/10.1016/J.FOODHYD.2023.109262

Squeo, G., De Angelis, D., Summo, C., Pasqualone, A., Caponio, F., & Amigo, J. M. (2022). Assessment of macronutrients and alpha-galactosides of texturized vegetable proteins by near infrared hyperspectral imaging. *Journal of Food Composition and Analysis*, *108*, 104459. https://doi.org/10.1016/J.JFCA.2022.104459

Ståhle, L., & Wold, S. (1989). Analysis of variance (ANOVA). *Chemometrics and Intelligent Laboratory Systems*, *6*(4), 259–272. https://doi.org/10.1016/0169-7439(89)80095-4

Stubbs, T. L., Kennedy, A. C., & Fortuna, A. M. (2010). Using NIRS to predict fiber and nutrient content of Dryland cereal cultivars. *Journal of Agricultural and Food Chemistry*, *58*(1), 398–403. https://doi.org/10.1021/jf9025844

Sun, D., Wu, M., Zhou, C., & Wang, B. (2022). Transformation of high moisture extrusion on pea protein isolate in melting zone during: From the aspects of the rheological property, physicochemical attributes and modification mechanism. *Food Hydrocolloids*, *133*, 108016. https://doi.org/10.1016/J.FOODHYD.2022.108016

Taghian Dinani, S., Allaire, N., Boom, R., & van der Goot, A. J. (2023). Influence of processing temperature on quality attributes of meat analogues fortified with l-cysteine. *Food Hydrocolloids*, *137*, 108422. https://doi.org/10.1016/J.FOODHYD.2022.108422

Taghian Dinani, S., Broekema, N. L., Boom, R., & van der Goot, A. J. (2023). Investigation potential of hydrocolloids in meat analogue preparation. *Food Hydrocolloids*, *135*, 108199. https://doi.org/10.1016/j.foodhyd.2022.108199

Taghian Dinani, S., Charles Carrillo, M. F., Boom, R., & van der Goot, A. J. (2023). Quality improvement of plant-based meat alternatives by addition of iota carrageenan to pea protein–wheat gluten blend. *European Food Research and Technology*, *1*, 1–18. https://doi.org/10.1007/s00217-023-04244-7

Taghian Dinani, S., de Jong, S., Vardhanabhuti, B., & van der Goot, A. J. (2024). Improving the quality of gluten-free plant-based meat analogs based on soy protein isolate with insoluble soy fibers and low acyl gellan gum. *European Food Research and Technology*, *250*(2), 389–408. https://doi.org/10.1007/s00217-023-04391-x

Tao, F., & Ngadi, M. (2018). Recent advances in rapid and nondestructive determination of fat content and fatty acids composition of muscle foods. *Critical Reviews in Food Science and Nutrition*, *58*(9), 1565–1593. https://doi.org/10.1080/10408398.2016.1261332

Teixeira Dos Santos, C. A., Lopo, M., Páscoa, R. N. M. J., & Lopes, J. A. (2013). A review on the applications of portable near-infrared spectrometers in the agro-food industry. *Applied Spectroscopy*, *67*(11), 1215–1233. https://doi.org/10.1366/13-07228

Tian, T., Ren, K., Cao, X., Peng, X., Zheng, L., Dai, S., Tong, X., Zeng, Q., Qiu, S., Wang, H., & Jiang, L. (2023). High moisture extrusion of soybean-wheat co-precipitation protein: Mechanism of fibrosis based on different extrusion energy regulation. *Food Hydrocolloids*, *144*, 108950. https://doi.org/10.1016/J.FOODHYD.2023.108950

Tøgersen, G., Arnesen, J. F., Nilsen, B. N., & Hildrum, K. I. (2003). On-line prediction of chemical composition of semi-frozen ground beef by non-invasive NIR spectroscopy. *Meat Science*, *63*(4), 515–523. https://doi.org/10.1016/S0309-1740(02)00113-4

Tolstoguzov, V. B. (1993). Thermoplastic extrusion-the mechanism of the formation of extrudate structure and properties. *Journal of the American Oil Chemists' Society*, *70*(4), 417–424. https://doi.org/10.1007/BF02552717

Townshend, A. (1987). Official methods of analysis of the association of official analytical chemists, 14th edn. In K. Helvich (Ed.), *Analytica Chimica Acta* (15th ed., Vol. 193). https://doi.org/10.1016/s0003-2670(00)86185-1

Uddin, M., Ishizaki, S., Okazaki, E., & Tanaka, M. (2002). Near-infrared reflectance spectroscopy for determining end-point temperature of heated fish and shellfish meats. *Journal of the Science of Food and Agriculture*, *82*(3), 286–292. https://doi.org/10.1002/JSFA.1032

Uddin, M., Okazaki, E., Ahmad, M. U., Fukuda, Y., & Tanaka, M. (2005). Noninvasive NIR spectroscopy to verify endpoint temperature of kamaboko gel. *LWT - Food Science and Technology*, *38*(8), 809–814. https://doi.org/10.1016/j.lwt.2004.10.008

Uddin, M., Okazaki, E., Ahmad, M. U., Fukuda, Y., & Tanaka, M. (2006). NIR spectroscopy: A non-destructive fast technique to verify heat treatment of fish-meat gel. *Food Control*, *17*(8), 660–664. https://doi.org/10.1016/j.foodcont.2005.04.009

van den Einde, R. M., Bolsius, A., van Soest, J. J. G., Janssen, L. P. B. M., van der Goot, A. J., & Boom, R. M. (2004). The effect of thermomechanical treatment on starch breakdown and the consequences for process design. *Carbohydrate Polymers*, *55*(1), 57–63. https://doi.org/10.1016/j.carbpol.2003.07.004

van der Sman, R. G. M., & van der Goot, A. J. (2023). Hypotheses concerning structuring of extruded meat analogs. *Current Research in Food Science*, *6*, 100510. https://doi.org/10.1016/j.crfs.2023.100510

van der Veen, M. E., van Iersel, D. G., van der Goot, A. J., & Boom, R. M. (2004). Shear-induced inactivation of α-amylase in a plain shear field. *Biotechnology Progress*, *20*(4), 1140–1145. https://doi.org/10.1021/bp049976w

van Staveren, D. (2020, February 24). *Benefits of NIR spectroscopy: Part 2*. https://www.metrohm.com/en_nl/discover/blog/20-21/benefits-of-nir-spectroscopy--part-2.html

Wang, H., Zhang, L., Pawel Czaja, T., Bakalis, S., Zhang, W., & Lametsch, R. (2022). Structural characteristics of high-moisture extrudates with oil-in-water emulsions. *Food Research International*, *158*, 111554. https://doi.org/10.1016/J.FOODRES.2022.111554

Wang, Z., Wu, Q., & Kamruzzaman, M. (2022). Portable NIR spectroscopy and PLS based variable selection for adulteration detection in quinoa flour. *Food Control*, *138*, 108970. https://doi.org/10.1016/J.FOODCONT.2022.108970

Wehrmaker, A. M., Zenker, H. E., de Groot, W., Sanders, M., van der Goot, A. J., Janssen, A. E. M., Keppler, J., & Bosch, G. (2022). Amino Acid Modifications During the Production (Shearing, Sterilization) of Plant-Based Meat Analogues: An Explorative Study Using Pet Food Production as an Example. *ACS Food Science & Technology*, *2*(11), 1753–1765. https://doi.org/10.1021/acsfoodscitech.2c00242

Wittek, P., Ellwanger, F., Karbstein, H. P., & Emin, M. A. (2021). Morphology development and flow characteristics during high moisture extrusion of a plant-based meat analogue. *Foods*, *10*(8), 1753. https://doi.org/10.3390/foods10081753

Wittek, P., Karbstein, H. P., & Emin, M. A. (2021). Blending proteins in high moisture extrusion to design meat analogues: Rheological properties, morphology development and product properties. *Foods*, *10*(7), 1509. https://doi.org/10.3390/foods10071509

Wittek, P., Walther, G., Karbstein, H. P., & Emin, M. A. (2021). Comparison of the rheological properties of plant proteins from various sources for extrusion applications. *Foods*, *10*(8), 1700. https://doi.org/10.3390/foods10081700

Wittek, P., Zeiler, N., Karbstein, H. P., & Emin, M. A. (2021). High moisture extrusion of soy protein: Investigations on the formation of anisotropic product structure. *Foods*, *10*(1), 102. https://doi.org/10.3390/foods10010102

Wold, J. P. (2016). On-line and non-destructive measurement of core temperature in heat treated fish cakes by NIR hyperspectral imaging. *Innovative Food Science and Emerging Technologies*, *33*, 431–437. https://doi.org/10.1016/j.ifset.2015.12.012

Wold, J. P., O'Farrell, M., Høy, M., & Tschudi, J. (2011). On-line determination and control of fat content in batches of beef trimmings by NIR imaging spectroscopy. *Meat Science*, *89*(3), 317–324. https://doi.org/10.1016/j.meatsci.2011.05.001

Wold, J. P., O'Farrell, M., Tschudi, J., Eskildsen, C. E., Andersen, P. V., & Ottestad, S. (2020). In-line and non-destructive monitoring of core temperature in sausages during industrial heat treatment by NIR interaction spectroscopy. *Journal of Food Engineering*, *277*, 109921. https://doi.org/10.1016/j.jfoodeng.2020.109921

Wold, S., Sjöström, M., & Eriksson, L. (2001). PLS-regression: A basic tool of chemometrics. *Chemometrics and Intelligent Laboratory Systems*, *58*(2), 109–130. https://doi.org/10.1016/S0169-7439(01)00155-1

Wolz, M., & Kulozik, U. (2015). Thermal denaturation kinetics of whey proteins at high protein concentrations. *International Dairy Journal*, *49*, 95–101. https://doi.org/10.1016/J.IDAIRYJ.2015.05.008

Wu, D., He, Y., Feng, S., & Sun, D. W. (2008). Study on infrared spectroscopy technique for fast measurement of protein content in milk powder based on LS-SVM. *Journal of Food Engineering*, *84*(1), 124–131. https://doi.org/10.1016/j.jfoodeng.2007.04.031

Xiaobo, Z., Jiewen, Z., Povey, M. J. W., Holmes, M., & Hanpin, M. (2010). Variables selection methods in near-infrared spectroscopy. *Analytica Chimica Acta*, *667*(1–2), 14–32. https://doi.org/10.1016/J.ACA.2010.03.048

Xu, X., Gao, B., Li, Y., Liu, J., Han, L., & Liu, X. (2023). The effect of temperature on the identification of NIR animal fats and oils species and its mechanism. *Vibrational Spectroscopy*, *124*, 103498. https://doi.org/10.1016/J.VIBSPEC.2023.103498

Zahari, I., Ferawati, F., Purhagen, J. K., Rayner, M., Ahlström, C., Helstad, A., & Östbring, K. (2021). Development and characterization of extrudates based on rapeseed and pea protein blends using high-moisture extrusion cooking. *Foods*, *10*(10), 2397. https://doi.org/10.3390/foods10102397

Zeaiter, M., Roger, J. M., & Bellon-Maurel, V. (2006). Dynamic orthogonal projection. A new method to maintain the on-line robustness of multivariate calibrations. Application to NIR-based monitoring of wine fermentations. *Chemometrics and Intelligent Laboratory Systems*, *80*(2), 227–235. https://doi.org/10.1016/j.chemolab.2005.06.011

Zhang, H., Zhang, S., Chen, Y., Luo, W., Huang, Y., Tao, D., Zhan, B., & Liu, X. (2020). Non-destructive determination of fat and moisture contents in Salmon (Salmo salar) fillets using near-infrared hyperspectral imaging coupled with spectral and textural features. *Journal of Food Composition and Analysis*, *92*, 103567. https://doi.org/10.1016/J.JFCA.2020.103567

Zhang, J., Guo, C., Cui, X., Cai, W., & Shao, X. (2019). A two-level strategy for standardization of near infrared spectra by multi-level simultaneous component analysis. *Analytica Chimica Acta*, *1050*, 25–31. https://doi.org/10.1016/J.ACA.2018.11.013

Zhang, R., Yang, Y., Liu, Q., Xu, L., Bao, H., Ren, X., Jin, Z., & Jiao, A. (2023). Effect of Wheat Gluten and Peanut Protein Ratio on the Moisture Distribution and Textural Quality of High-Moisture Extruded Meat Analogs from an Extruder Response Perspective. *Foods 2023, Vol. 12, Page 1696*, *12*(8), 1696. https://doi.org/10.3390/FOODS12081696

Zhang, X., Zhao, Y., Zhang, T., Zhang, Y., Jiang, L., & Sui, X. (2022). High moisture extrusion of soy protein and wheat gluten blend: An underlying mechanism for the formation of fibrous structures. *LWT*, *163*. https://doi.org/10.1016/j.lwt.2022.113561

Zhang, Z., Zhang, L., He, S., Li, X., Jin, R., Liu, Q., Chen, S., & Sun, H. (2022). High-moisture Extrusion Technology Application in the Processing of Textured Plant Protein Meat Analogues: A Review. *Food Reviews International*. https://doi.org/10.1080/87559129.2021.2024223

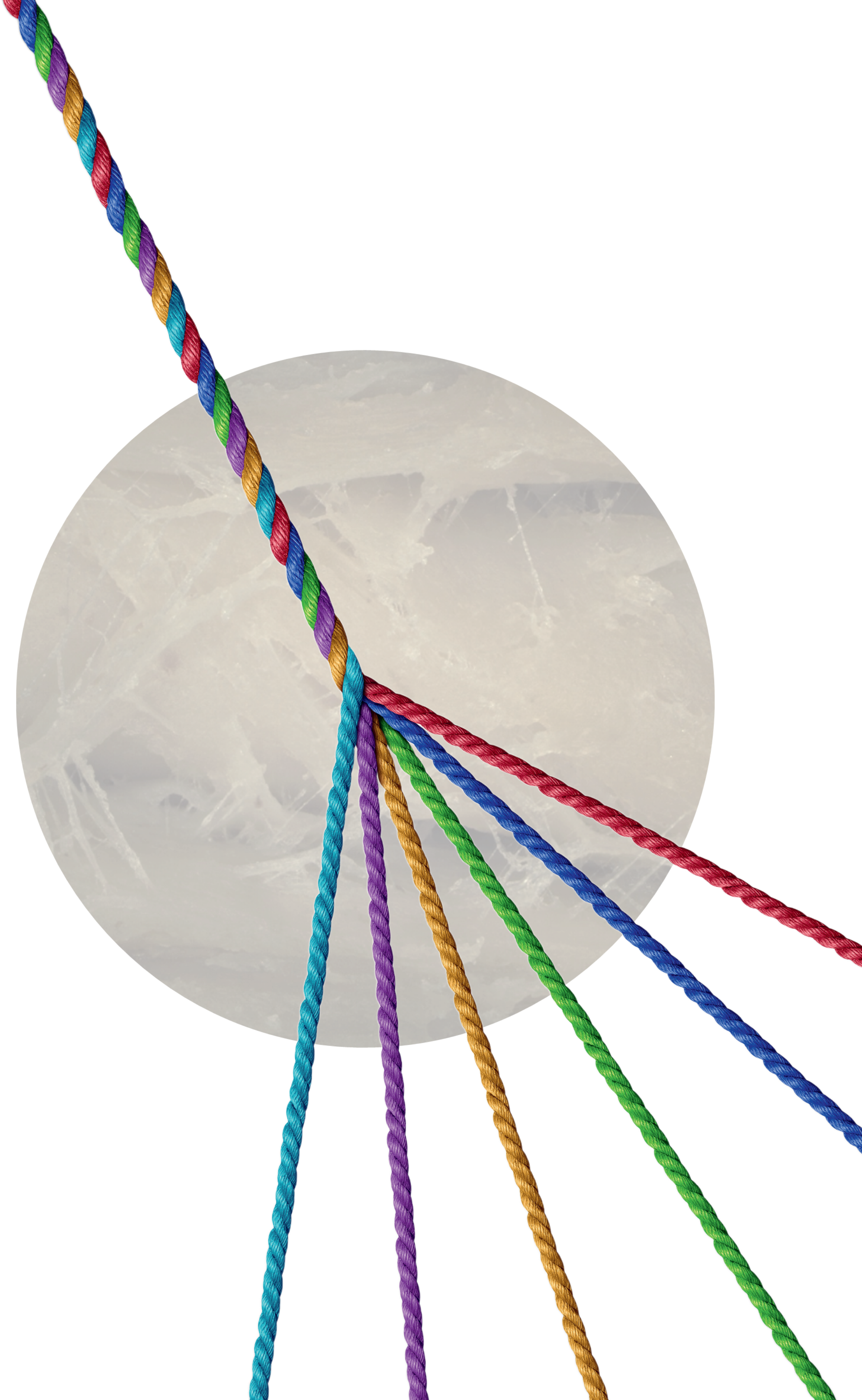

S

Summary &

Samenvatting

Meat analogues are one of the options to aid the consumer to transition from animal protein to plant-based protein, especially when these meat analogue products resemble the taste and texture of meat products. One of the characteristic properties of a meat is its fibrous structure, which is thus also a requirement for meat analogues. Plant-based products with a fibrous structure can be produced through extrusion. During this process the protein ingredient is transported through a heated barrel by two screws after which the material is cooled in a long cooling die. Extrusion is already researched since the 1990s, but there is no full consensus about the fibrous structure formation mechanism during this process. There are multiple reasons for this: first, it is difficult to study the extrusion process because the process is performed at high dry matter contents (>30%) and high temperatures (100 °C) and most measurement methods are designed to analyse products with low dry matter content and at ambient conditions. Additionally, the effects of the processing parameters are interlinked. The aim of this thesis was to gain more understanding of the effects of the processing conditions on the properties of dense plant-based products produced through HME.

To this end the high-temperature shear cell (HTSC) was used. The HTSC has similar processing steps as extrusion but does allow separate control over the processing parameters. In this thesis the HTSC was therefore used to study the effect of the processing parameters in **Chapters 2, 3 & 6.** Additionally, the potential of near-infrared spectroscopy to quantify the composition of dense plant-based products was studied in **Chapters 4 & 5**. This is particularly relevant because the current oil quantification methods require harmful chemicals and are laborious and time-consuming.

In **Chapter 2** we studied the effect of deformation during cooling in the HTSC on the final product properties. Deformation of the material in the cooling die during extrusion is often thought to be crucial for fibrous structure formation. Here, we found that shearing during cooling led to less fibrous products compared with products formed by shearing during heating. This indicates that a higher cooling die temperature might be beneficial for fibrous structure formation. Furthermore, we found that the most fibrous structures were created at the lowest rotational speed investigated and that too intensive mechanical treatment led to structural breakdown.

In **Chapter 3** the effect of mixing and hydrating of the proteinaceous doughs before HTSC processing on the final structural properties was studied. Hydrating had a limited effect on the final product structure compared with the effect of mixing. The effect of mixing depended on the type of protein ingredients that were used. For soy protein concentrate (SPC) and soy protein isolate (SPI)-wheat gluten (WG) mixing did not influence the rheological properties of the dough or the final product properties to a large extent. However, for pea protein isolate (PPI)-WG the strength of the product had a maximum at a certain mixing time.

In **Chapter 4** NIR spectroscopy was explored as a rapid and non-destructive quantification technique for oil and protein content in mixtures of PPI, water and sunflower oil. We showed that NIR spectroscopy was a suitable technique to measure the composition of these mixtures. A reduction of the wavelength range or wavelength selection improved the accuracy of the measurement. However, it is well-known that heating can affect the results of NIR spectroscopy. For this reason, the effect of heating conditions on the oil content quantification using NIR spectroscopy was studied in **Chapter 5**. In this chapter we showed that heating conditions indeed influenced the areas of the NIR spectra related to oil, but that wavelength selection can be used to reduce this effect. This means NIR spectroscopy is also a suitable tool for the measurement of oil content in meat analogues produced under varying heating conditions.

In **Chapter 6** we used the effect of heating on the NIR spectra to quantify the thermal process intensity during extrusion. To this end we first created a calibration curve based on NIR spectra of products processed at different temperatures in the HTSC. Subsequently, we used this calibration curve to calculate the so-called "equivalent shear cell temperature". This novel parameter is an indicator for the thermal process intensity of thermomechanical processing. This gave new insights in the effects of changes in barrel temperature, screw speed or screw profile during the extrusion process. The equivalent shear cell temperature could also be linked to the degree of texturization of the extrudates and therefore provides information about the processing conditions that allow the formation of an anisotropic structure.

Finally, **Chapter 7** provides an overview of the new insights gained in this thesis and suggestions for future research. In summary, it can be concluded that the use of the HTSC to study the extrusion of meat analogues is a fruitful approach and NIR spectroscopy is a suitable technique to measure the composition of dense plant-based protein products. Based on all results, it was concluded that all different processing steps contributed to the structural properties of the final product. Thus, the research described in this thesis confirms that fibrous structure formation occurs at multiple locations in the extruder and at multiple length scales.

Vleesvervangers helpen de consument bij het vervangen van dierlijke eiwitten door plantaardige eiwitten. Vleesvervangers zijn producten met een vergelijkbare structuur en smaak als vlees maar zijn gemaakt van plantaardige ingrediënten. In eerder onderzoek is gevonden dat het belangrijk is dat vleesvervangers zo veel mogelijk lijken op het vleesproduct dat ze proberen te vervangen om ze aantrekkelijk te maken voor vleeseters en flexitariërs.

Eén van de karakteristieke eigenschappen van vlees is de vezelige structuur. De ideale vleesvervanger is daarom ook vezelig. Zo’n vezelige structuur op basis van plantaardige eiwitten kan geproduceerd worden met extrusie. Tijdens extrusie worden de plantaardige ingrediënten gekneed door twee draaiende schroeven in een schroefhuis terwijl het materiaal verhit wordt. Hierna wordt het product door een gekoelde matrijs geperst. Extrusie wordt al sinds de jaren ’90 gebruikt, maar er is geen volledige consensus over het mechanisme achter de vorming van de vezelige structuur. Er zijn meerdere redenen waarom het zo lastig is om het extrusieproces te bestuderen. Ten eerste wordt de extrusie van vleesvervangers uitgevoerd bij hoge temperatuur (>100 °C) en hoge druk terwijl het drogestofgehalte meer dan 30% is Helaas zijn de meeste meetmethoden ontwikkeld voor producten met een veel lager drogestofgehalte en vinden metingen meestal plaats bij kamertemperatuur. Daarnaast is het effect van elke individuele procesinstelling afhankelijk van de andere procesinstellingen. Dit maakt het lastig om het effect van een individuele procesinstelling te onderzoeken.

Het belangrijkste doel van dit proefschrift was om meer inzicht te krijgen in het effect van de procescondities op de eigenschappen van geconcentreerde plantaardige producten. In **Hoofdstuk 2, 3 & 6** van dit proefschrift is de “shear cell” gebruikt om het effect van de procesinstellingen tijdens de extrusie van vleesvervangers te onderzoeken. In deze shear cell kunnen de procesinstellingen wel onafhankelijk van elkaar ingesteld worden, wat mogelijkheden biedt voor het bestuderen van het geïsoleerde effect van deze procesinstellingen. Daarnaast is nabij-infrarood (NIR) spectroscopie gebruikt om de hoeveelheid olie in geconcentreerde plantaardige producten te meten in **Hoofdstuk 4 & 5**. Het meten van de hoeveelheid olie in extrudaten is van belang omdat olie achter kan blijven in de extruder en dus niet alle olie die toegevoegd wordt ook in het uiteindelijke product belandt. Verder beïnvloedt het toevoegen van olie de textuur van het product.

In **Hoofdstuk 2** hebben we gekeken naar het effect van vervorming van het materiaal tijdens het koelen in de shear cell. Er wordt vaak gedacht dat deze vervorming in de koelmatrijs van de extruder bepalend is voor de vorming van de vezelige structuur. In dit hoofdstuk laten we echter zien dat vervorming tijdens koelen leidde tot minder vezelige producten. Daarnaast werden de meest vezelige producten gemaakt bij de laagste draaisnelheden. Dit is een indicatie dat te veel vervorming afbraak van de gevormde vezelige structuur kan veroorzaken.

In **Hoofdstuk 3** onderzochten we het effect van mixen en hydratatie van het eiwitrijke deeg voordat het in de shear cell behandeld werd op de structuur van het uiteindelijke product. De hydratatietijd van het deeg bleek weinig effect te hebben op de structuur van het eindproduct. Het effect van mixen hing af van de ingrediënten die werden gebruikt. Voor sojaeiwitconcentraat en een mengsel van sojaeiwitisolaat en gluten had mixen maar een beperkt effect op de reologische eigenschappen van het deeg en de structuur van het product. Mixen had wel een effect of de eigenschappen van het deeg en product voor een mengsel van erwteneiwitisolaat en gluten.

In **Hoofdstuk 4** is het gebruik van NIR-spectroscopie om de hoeveelheid olie en eiwit in een mengsel van erwteneiwitisolaat, water en zonnebloemolie te bepalen. Deze methode bleek succesvol en het gebruik van een kleiner deel van het nabije infrarood spectrum of het selecteren van specifieke golflengtes verbeterde zelfs de nauwkeurigheid van de metingen. Het is echter bekend dat verhitting een effect heeft op de NIR-spectra, wat de metingen van de productsamenstelling kan beïnvloeden. Daarom is in **Hoofdstuk 5** het effect van verhitten op het meten van olie met spectroscopie in het nabije infrarood spectrum onderzocht. Verhitting bleek inderdaad een effect te hebben op de NIR-spectra, maar door specifieke golflengtes te selecteren kon toch een betrouwbare kalibratielijn worden bepaald.

S

In **Hoofdstuk 6** is het effect van verhitten op de NIR-spectra gebruikt als informatiebron. Hier hebben we NIR-spectroscopie gebruikt om het gecombineerde effect van het veranderen van de verhittingstemperatuur, de schroefsnelheid en de schroefopzet op de mate van verhitting te meten. Hiervoor hebben we eerst een kalibratielijn gemaakt op basis van shear cell producten die verhit waren bij verschillende temperaturen. Door deze kalibratielijn toe te passen op extrudaten konden we de zogenaamde “equivalente shear cell temperatuur” berekenen. Deze equivalente shear cell temperatuur geeft informatie over de totale thermische procesintensiteit die een materiaal ervaart bij een combinatie van de verschillende procesinstellingen. Deze nieuwe parameter kon ook gelinkt worden aan de structurele eigenschappen van de extrudaten en is daarom geschikt om de juiste procescondities voor het maken van een vezelige structuur te bepalen.

Ten slotte geeft **Hoofdstuk 7** een overzicht van de nieuwe inzichten uit dit onderzoek en worden suggesties voor vervolgonderzoek gegeven. Samengevat laat dit proefschrift zien dat de shear cell een veelbelovende techniek is om de extrusie van vleesvervangers beter te begrijpen. Daarnaast kan NIR-spectroscopie gebruikt worden voor een snelle en betrouwbare bepaling van de samenstelling van geconcentreerde plantaardige producten. Tenslotte zagen we dat alle processtappen effect hadden of de structuureigenschappen van het eindproduct. We kunnen daarom concluderen dat structuurvorming op verschillende plaatsen in de extruder plaatsvindt en dat deze structuur op verschillende lengteschalen gevormd wordt.

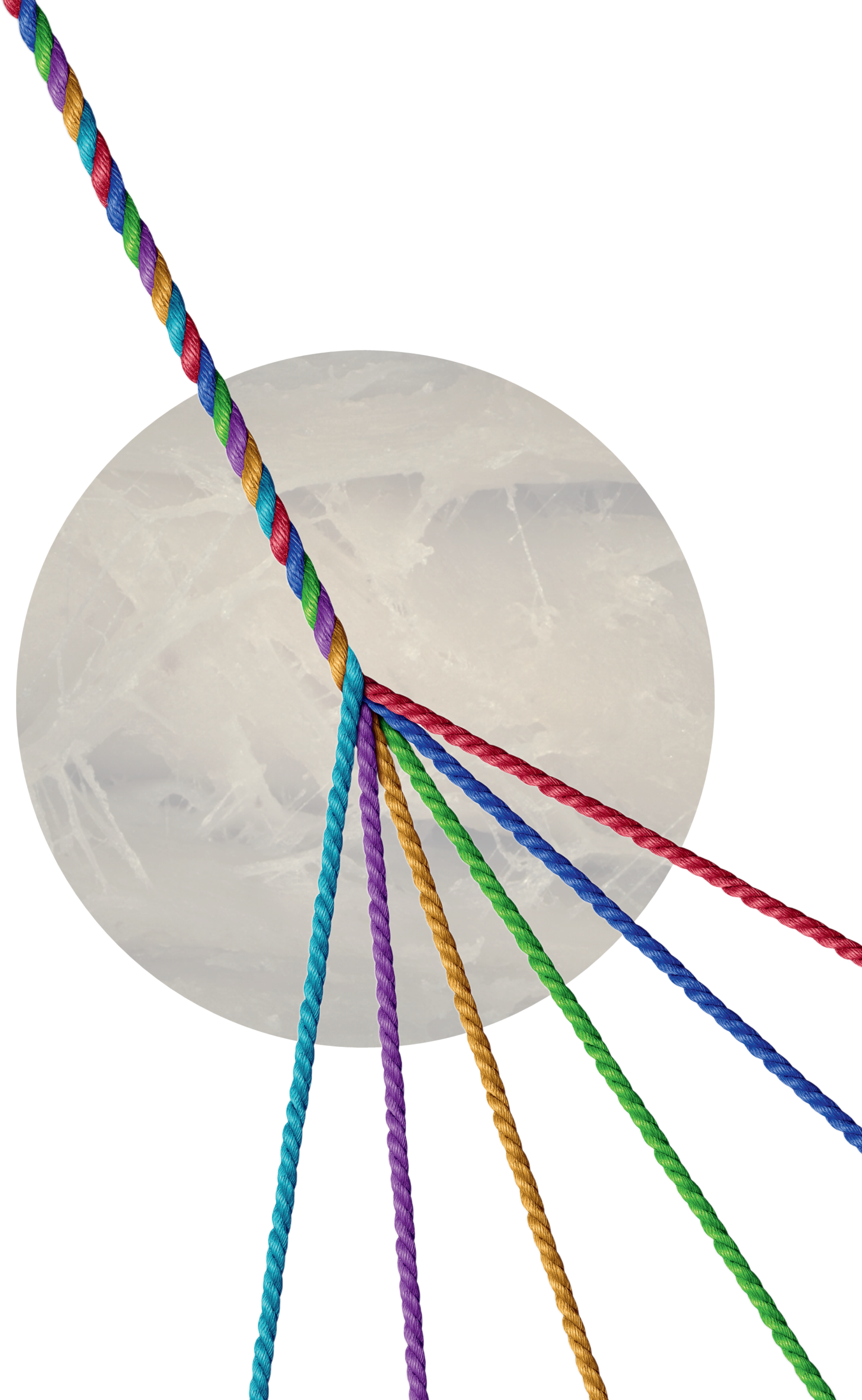

A

Appendices

Acknowledgements

I would like to take this opportunity to thank everyone who contributed to the booklet you are reading today.

First, I would like to thank my promotor, **Atze Jan,** and co-promotor, **Lu**. Thank you for giving me the opportunity to work on this project and believing in me when I did not believe in myself. I feel very lucky to have had you as my supervisors. The combination of your expertise and approaches to science was key to making this project a success. Thank you for helping me find the balance between thinking and doing, and for helping me grow as a person and independent scientist. And finally, thank you both for all the thorough and ridiculously fast feedback on all my manuscripts. **Atze Jan**, bedankt dat je me altijd uitdaagde om mijn eigen mening en ideeën over mijn project te uiten. **Lu**, thank you for your creativity when it comes to creating the clearest figures and for your encouraging words when I needed them.

This project was part of the **PlantPROMISE consortium**, and I want to thank all the partners for making this project possible and for their interest in my work. **Laurice, Jacqueline, and Walter**, thank you for all the organizational work for the PlantPROMISE consortium and your feedback during the monthly meetings in the first half of my PhD. **Jaap**, bedankt voor je hulp bij het gebruiken van de extruder.

Floor, bedankt dat je het estafettestokje na jouw PhD aan mij wilde doorgeven en voor al je hulp bij het opstarten van mijn PhD. To my other co-authors, **Puneet and Jos**, thank you for your help with the NIR data analysis. **Puneet**, thank you for showing me the way when it comes to analyzing NIR spectra and double-checking my work for two of the chapters of this thesis. **Jos**, bedankt voor je enthousiaste reactie toen ik je om hulp vroeg bij de data-analyse van hoofdstuk 5 en natuurlijk voor de chemometrie cursus.

I would also like to thank all technicians of FPE: **Kasia, Lyneth, Maurice, Martin, Jarno, Jos, and Wouter**. You are not only essential in keeping the labs organized and the equipment well maintained but also are the memory and social core of the group. Thank you for that. **Jarno**, bedankt voor alle hulp wanneer ik of een van mijn studenten problemen hadden met de shear cell en voor je hulp bij het werken met de extruder.

I would also like to thank my students: **Rozemarijn, Aline, Maarten, Lukas, Dieke, Imke, Punpun, Fahim, and Remy**. Thank you for your enthusiasm, critical questions about my

work, and your contribution to the lab work and initial data analysis for parts of this thesis. I enjoyed working with you and learned a lot from our collaborations.

To the **Food Structuring Group**: it was nice to be able to work together with people that understood my project beyond: “something with the shear cell and the extruder.” Also, thanks for the online coffee breaks when we were all working from home due to COVID at the start of my PhD. **Miek**, ik wil jou in het bijzonder bedanken voor je hulp bij het werken met de shear cell en CCR en voor je suggesties als daar rare resultaten uitkwamen. **Silvia**, het was leuk om jou af en toe tegen te komen en te kunnen sparren met iemand die nog veel meer extrusie ervaring heeft.

I want to thank **everyone in FPE** for the warm atmosphere in the group. Thank you for all the “gezelligheid” during lunch and coffee breaks, social and sportive events. **Koen en Sten**, bedankt voor het organiseren van een FPE-team voor de Veluweloop. Everyone in the borrel committee: **Katharina, Eric, Murat, Regina, Melanie, Kieke, Wouter, Anneloes, Sybren, Yifeng, Suzan, Martijn, Santi, and Danny**, thanks for all the good times during and outside of the borrels we organized together. **Yafei, Julia, Judith, Aadi, Solange, and Iris**, thanks for all the chats and shared laughter. **Martin, Maurice, Laurens, Sten, Loes, Nienke, Aadi, Lyneth, Koen, Ting, and Aryo**, thank you for organizing the PhD study trips to Singapore and the UK.

To my office mates: **Asif, Jolien, Nattawan, Nienke, and Yizhou**, thank you for all the nice office dinners and spontaneous breaks to discuss anything that comes along with doing a PhD at FPE. **Jolien en Nienke**, bedankt dat jullie mijn paranimfen willen zijn. **Nienke,** het was bijzonder om mijn tijd bij FPE van bachelor thesis tot PhD samen met jou te doorlopen. Ik ga het missen om zij-aan-zij met jou te werken.

Katha, Julian, Sophie, and Niels, thanks for all the board game and movie nights, and Niels for hosting most of them. It was great to see PhD life from a non-FPE perspective as well.

Pappa, mamma, en Thijs, bedankt dat jullie er altijd voor me zijn, voor alles. En dat ik bij jullie altijd een veilige haven vind om naar terug te keren. **Henk, Wanda, Lieke, en Roel**, bedankt voor jullie interesse in mijn onderzoek en alle gezelligheid.

Jaro, bedankt dat je me altijd blijft vertellen dat het allemaal wel goed komt. Voor al je liefde, warmte, humor, en nog zoveel meer. Alle enge avonturen die hierna nog komen durf ik samen met jou wel aan.

About the author

Nienke Köllmann was born on June 21, 1997, in Gorinchem, the Netherlands. She graduated cum laude from Het Baarnsch Lyceum in Baarn in 2015, with a double major in Nature and Health (Natuur en Gezondheid) and Nature and Technology (Natuur en Techniek).

Nienke pursued a bachelor's degree in food technology at Wageningen University from 2015 to 2018. During her studies, she spent a semester specializing in "Sustainable Development in Food Industries" at the Institut Supérieur d'Agriculture Rhône-Alpes (ISARA) in Lyon, France, in 2017. She completed her bachelor's degree cum laude in 2018, with a thesis on the influence of processing conditions on the rheological properties of oil-body mayonnaises, conducted at the laboratory of Food Process Engineering.

In 2018, Nienke began her master's in food technology with a specialization in Product Design at Wageningen University. Her master's thesis involved developing a regression model to predict the viscosity of pea-based ingredients based on their composition, also at the laboratory of Food Process Engineering. She completed her MSc in 2020, following an internship at Danone Nutricia Research in Utrecht, where she studied the properties of various dietary fiber ingredients and their effects on the quality of nutritional beverages.

Nienke started as a PhD candidate at the laboratory of Food Process Engineering in October 2020. Her research focused on understanding the formation of fibrous structures during high-moisture extrusion of meat analogues. The findings of this research are presented in this thesis.

List of publications

This thesis:

Köllmann, N., Schreuders, F. K. G., Zhang, L., & van der Goot, A. J. (2023). On the importance of cooling in structuring processes for meat analogues. *Journal of Food Engineering*, *350*, 111490. https://doi.org/10.1016/j.jfoodeng.2023.111490

Köllmann, N., Schreuders, F. K. G., Mishra, P., Zhang, L., & van der Goot, A. J. (2023). Near-infrared spectroscopy-based quantification of sunflower oil and pea protein isolate in dense mixtures for novel plant-based products. *Journal of Food Composition and Analysis*, *121*, 105414. https://doi.org/10.1016/J.JFCA.2023.105414

Köllmann, N., Sivakul, K., Zhang, L., & van der Goot, A. J. (2024). Effect of mixing and hydrating time on the structural properties of high-temperature shear cell products from multiple plant-based ingredients. *Journal of Food Engineering, 369,* 111911. https://doi.org/10.1016/J.JFOODENG.2023.111911

Köllmann, N., Vringer, R., Mishra, P., Zhang, L., & van der Goot, A. J. (2024). Near-infrared spectroscopy to quantify overall thermal process intensity during high-moisture extrusion of soy protein concentrate. *Food Research International*, *186*, 114320. https://doi.org/10.1016/J.FOODRES.2024.114320

Köllmann, N., Hageman, J., Groot Nibbelink, D., Zhang, L. & van der Goot, A.J. Wavelength selection enables robust oil content quantification with near-infrared spectroscopy in pea protein gels produced under varying heating conditions, submitted.

Other publications:

Romero-Guzmán, M. J., **Köllmann, N.**, Zhang, L., Boom, R. M., & Nikiforidis, C. v. (2020). Controlled oleosome extraction to produce a plant-based mayonnaise-like emulsion using solely rapeseed seeds. *LWT*, *123*, 109120. https://doi.org/10.1016/J.LWT.2020.109120

Lie-Piang, A., Möller, A. C., **Köllmann, N**., Garre, A., Boom, R., & van der Padt, A. (2022). Functionality-driven food product formulation – An illustration on selecting sustainable ingredients building viscosity. *Food Research International*, *152*, 110889. https://doi.org/10.1016/J.FOODRES.2021.110889

van der Sman, R. G. M., Chakraborty, P., Hua, N. P., & **Köllmann, N.** (2023). Scaling relations in rheology of proteins present in meat analogs. *Food Hydrocolloids*, *135*, 108195. https://doi.org/10.1016/J.FOODHYD.2022.108195

Overview of completed training activities

Discipline specific activities	**Organizer**	**Year**
Multivariate Analysis of Spectroscopic Data (online)	CAMO Analytics	2020
Emerging Meat Alternatives Conference 2nd and 3rd [a] edition (online)	AIChE	2020,2021
Science and Technology for Meat (and Dairy) Analogues Conference 2nd (online) and 3rd edition	WUR	2021, 2024
Chemometrics	VLAG	2021
HMEC Extrusion of Plant Based Meats (online)	Foodstream	2021
Rheology Do's and Don'ts	VLAG	2021
Food Structure and Functionality Symposium 4th (online), 5th [b] and 6th [b] editions	Elsevier and Food Structure and Functionality Forum	2021, 2022, 2024
Advanced Food Analysis[b]	VLAG	2022
European School on Rheology	KU Leuven	2022
Digital Food Processing event: Flexible and Controlled Food Processing using 3D Food Printing and beyond[b]	Digital Food Processing Initiative	2022
2nd Edible Soft Matter Conference & Workshop[b]	WUR	2022
21st Interational NIR Conference[a]	Austrian society of analytical chemistry	2023
Meat Analogues Technology &Science Course[a]	Wageningen Academy	2023

General courses	Organizer	Year
VLAG PhD week	VLAG	2021
Philosophy and Ethics of Food Science and Technology	WGS	2021
Scientific Writing	Wageningen In'to Languages	2021
PhD competence assessment	WGS	2021
Critical thinking and argumentation	WGS	2022
Un-box your PhD	WGS	2022
VLAG Midterm event: PhD on track	VLAG	2022
Career perspectives	WGS	2024

Other activities	Organizer	Year
Preparation of research proposal	WUR-FPE	2020
Weekly group meetings[a]	WUR-FPE	2020-2024
PhD study tours Singapore and UK[a,b]	WUR-FPE	2022, 2024

[a] Oral presentation

[b] Poster presentation

A

The studies presented in this thesis were performed within the framework of PlantPROMISE which is co-financed by Top Consortium for Knowledge and Innovation Agri& Food by the Dutch Ministry of Economic Affairs. The project is registered under contract number TKI-AF- LWV-19027.

Cover design by Nienke Köllmann with images by Lightspring
www.shutterstock.com/g/lightspring

Printed by ProefschriftMaken || www.proefschriftmaken.nl